Investigating the Kinetics and Structural Effects of Azo Dye Photochemistry Using NMR With *In Situ* Laser Irradiation and *Ab Initio* (DFT) Calculations

David Gibson

Doctor of Philosophy

2007

Abstract

Reversible *cis-trans* isomerisation of a series of commercially interesting yellow azo dyes has been studied using the technique of Nuclear Magnetic Resonance (NMR) spectroscopy with *in situ* laser irradiation. Photostationary state (PSS) spectra of the azo dyes, provided by coupling laser irradiation into the sample within the probe of the NMR spectrometer, have allowed observation of azo *cis* isomer species that would otherwise elude detection and characterisation by NMR due to their rapid thermal decay times.

The NMR results have been combined with geometry optimised structures obtained through *ab initio* (DFT) calculations in order to allow visualisation of the *trans* and *cis* isomer species, and explain NMR spectral features. In the majority of cases, these *in vacuo* calculated structures show a great deal of correlation with NMR observations of asymmetric, *cis-trans* isomerisation-induced chemical shift changes for protons adjacent to the azo bond. The *cis* isomer spectral pattern for substituted naphthyl group protons can hence be used as a diagnostic tool in determining the correct *cis* isomer conformation in molecules where more than one conformation may exist.

In addition to the aforementioned characterisation studies, *in situ* irradiation has provided the opportunity to undertake a thorough investigation of the kinetics of photo- and thermal isomerisation for the same yellow dye series. The results of these studies have been combined with previous work on similar systems to provide an extensive data set, and conduct analysis in a systematic fashion. Adding fibre-reactive groups, varying phenyl and chlorotriazine ring substituents, and altering naphthyl group sulfonation patterns have a profound effect on both the photochemical and thermal rates of isomerisation in these systems. In certain cases, the same structural calculations noted earlier have proved useful in rationalising the identified kinetic differences.

The presence of phenyl substituents *ortho* to the azo bond has been shown to increase the rate of thermal *cis* isomer decay. Additionally, substituents bonded to a fibre-reactive group distant from the azo bond have an appreciable effect on the barrier to thermal *cis-trans* isomerisation, but little effect on the photochemical characteristics of each isomer. Several sulfonated naphthyl group patterns have been studied, leading to

an observation that sulfonate groups positioned *ortho* to the azo bond assist in retarding thermal isomerisation, with sulfonate groups in other positions having a much smaller effect.

One particular molecule, a component of a currently available commercial dye, was studied for its interesting and previously unexplained behaviour, both photochemical and chemical. The dye demonstrated photoisomerisation at low concentrations only, with aggregation preventing formation of the *cis* isomer at higher concentrations. The *trans* isomer was found to undergo degradation to a product which did not photoisomerise. This product was identified as a benzotriazinium compound by multinuclear 2D correlation NMR spectroscopy, formed by a reversible cyclisation reaction involving the azo bond.

Declaration

I declare that the work presented in this thesis is my own unless otherwise stated by a reference.

David Gibson

Acknowledgements

I must express a huge vote of thanks to all the people that have helped me get to this stage. Firstly, to my supervisor Anita Jones, for arranging funding for the project from DyStar UK ltd, and providing me with good advice, input and direction during the course of the work. My other supervisors John Parkinson, Mike Hutchings and Warren Ebenezer for invaluable help and discussions at the various meetings over the course of the degree. I must also acknowledge the staff at DyStar UK for helping me with the synthetic work conducted at Manchester University. Without all their assistance I would not be writing this.

All occupants, past and present, of room 274 that have given me friendship and support must be thanked. I must say an extremely big thank you to Trish for providing technical and moral support during all the computational trials and tribulations associated with this project, and for being such an excellent officemate as I tied all this work together. And thank you to the people that have put up with me during the work and writing – Dilek for the smiley face, Ella for the cups of tea, Dave for the 7 Hills Challenge, are but a few people that need thanking. Whilst acknowledging the King's Buildings crowd, Max, Paul and Graham must be thanked for the frequent and entertaining tea breaks in JCMB – I feel this was a welcome, if not necessary, diversion for all!

Members of the Edinburgh University Sub Aqua Club require thanking for helping to satisfying my desire to immerse myself in freezing cold water of dubious quality throughout my time in Edinburgh. A special vote of thanks must go to all the 'Usual Suspects' for the friendship and memorable experiences that they helped create during the last three years. I look forward to many more. Amongst EUSACers, Graeme Kirk most certainly deserves a mention for putting me up when I had nowhere to live, and for the enthusiastic help in keeping the wheels of my car rolling whenever I was ready to sink it.

Outside of Edinburgh I must express thanks to Linzi for the occasional sanity check, and Amanda Hughes for an extremely encouraging, and effective, five minute chat in Manchester. Finally I must say thank you to my parents for making sure I was alive from time to time, and for encouragement and support during my time here.

Abbreviations

AM1	Austin Model 1
B3	Becke's 3-Parameter Exchange Funtional
CGTO	Contracted Gaussian Type Orbital
CIDNP	Chemically Induced Dynamic Nuclear Polarisation
COSY	Correlation Spectroscopy
CW	Continuous Wave
DFT	Density Functional Theory
DMSO	Dimethyl sulfoxide
FC	Franck Condon
FID	Free Induction Decay
FT	Fourier Transform
GS	Ground State
GTO	Gaussian Type Orbital
HF	Hartree-Fock
HMBC	Heteronuclear Multiple Bond Correlation
HSQC	Heteronuclear Single Quantum Correlation
IC	Internal Conversion
ISC	Intersystem Crossing
LYP	Lee-Yang-Parr Correlation functional
MO	Molecular Orbital
NDDO	Negelect of Differential Diatomic Overlap
NMR	Nuclear Magnetic Resonance
NOESY	Nuclear Overhauser Effect Spectroscopy
PES	Potential Energy Surface
PM3	Parameterised Model number 3
S_0	Ground state
S_1	First excited singlet state
STO	Slater Type Orbital
TMS	Tetramethyl Silane
TS	Transition State
UV-vis	Ultra violet and visible absorption spectroscopy
VR	Vibrational Relaxation

Table of Contents

Chapter 1

Introduction

The natural world honors our visual senses with an infinite display of colour. Throughout the years we have striven to apply these colours to fabrics and clothes by extracting them from natural sources. It was the advent of synthetic dyes during the 19th century that expanded the scope of the textile dye industry, allowing improved knowledge of chemical design to be exploited, and leading to a surge in the number of dyes available beyond those from natural sources. Amongst these new dyes, one of the very early contenders was the aromatic azo dye. Inexpensive and readily available starting materials, combined with the ease of the synthetic procedure, facilitated azo dyes in winning dominance in the commercial dye market in the early years. It is for the same reasons that azo dyes presently continue to be so successful within this industry, constituting 50% of worldwide dye production.[1,2]

Azo dyes are characterised by the presence of a N=N linkage, in most cases bridging two aromatic components. This allows for improved conjugation in the molecule, bringing with it enhanced charge distribution. In turn, the absorption characteristics shift into the visible region of the spectrum, providing the molecule with colouration, a property intrinsic to any dye. Variation of the aromatic groups, and substituents bonded to these groups, allows the dye chemist to tune the properties of the dye with scope for an abundance of colours to be derived. Hence, azo molecules can be used to cover the visual spectrum of dyes, an advantageous property complementing those highlighted earlier.

The success of an azo dye, or any dye for that matter, is governed by its ability to withstand the external physical and chemical influences to which it is subjected during its useable life. From a consumer viewpoint, it is unacceptable if the colour of a product fades over a normal period of ownership. Therefore, dye manufacturers must engineer their dyes to resist processes that influence the colour. If a dye is applied to a garment, it is likely to undergo repeated wear/wash cycles involving exposure to sunlight and

perspiration, along with the chemical action of washing powders and fabric conditioners. Needless to say, the dye must be robust in order to withstand these possible sources of degradation. The exposure to light can lead to both irreversible (bleaching) and reversible (photochromic) changes in the colour composition. Depending upon the dye structure, photochromism can occur through a number of mechanisms which, in the case of azo dyes, happens to be *cis-trans* isomerisation around the N=N bond.[3] Both of these processes have been studied extensively, and yet there is still only limited understanding of their exact mechanism.

Studies on the light-dependence of dyes have been conducted on dyed fabrics,[4–7] and in solution.[8–10] Light-induced fading studies on fabrics are often conducted by placing a strip of dyed fabric in a weatherometer for a long period of time. This instrument simulates an even distribution of light equivalent to average mid day sunlight in Florida.[7] The degree of fading can then be assessed in comparison to a control strip of the same fabric. Further analysis of photogenerated products is problematic as extraction of enough dye from the fibre is a difficult task. Moreover, this method precludes the observation of any intermediate species that may occur in the fading process. Solution-phase UV and visible (UV-vis) absorption spectroscopy is an extremely sensitive technique that has been used extensively to monitor colour changes.[4,8–10] However, usage is far from ideal since the spectra are often composed of broad overlapping absorption bands that yield little information on the molecular structure. It is more than likely that bands from any photo-induced species will overlap with those present from other components, leading to complication of the spectra and difficulties in interpretation. The only way to extract information in such situations is by a process of peak deconvolution, which is subject to errors in curve fitting.[11]

In a distinctly different approach to the problem of investigating azo dye fading, Tait *et al.* undertook a method of analysing samples using NMR spectroscopy with *in situ* irradiation.[12] The technique of NMR is extremely powerful for identifying and characterising species due to the high resolution of the spectra, and the detailed information conveyed within. In contrast to UV-vis, this allows information pertaining to each species present to be obtained separately and interpreted. Light delivery was simplified by coupling an optical fibre between the sample and a laser. This method has also seen use for other photochromic systems, again due to its high resolution for solution work compared to the available optical techniques.[13] The coupled nature of the apparatus allows real-time monitoring of the system under study, making kinetic information accessible to the analytical chemist.

The work presented in this thesis has extended the exploratory studies conducted by

Tait *et al.*, to achieve a systematic investigation of the influence of structural variation on the photoisomerisation of a series of sulfonated azo dyes. In Chapter 4, a series of yellow azo dyes is studied by NMR with *in situ* irradiation, and is presented alongside *ab initio* (DFT) calculated structures for both the thermally stable and photo-induced species. Chapter 5 goes on to examine the kinetics of photo and thermal isomerisation of the same yellow dye series, and discusses the results in combination with those from previous work. Chapter 6 presents an observation of uncharacteristic azo dye behaviour measured using NMR spectroscopy. Finally, Chapter 7 presents overall conclusions of the work in Chapters 4-6. Appendices of relevant observations, visualisations and cartesian coordinates of the optimised structures are available at the end of the thesis.

Chapter 2

Background and Theoretical Aspects

2.1 Photochemistry

2.1.1 The Interaction of Light With Matter

2.1.1.1 The Transition Dipole Moment

Photochemistry and photophysics are dependent upon the absorption of photons. For a molecule to interact with an electromagnetic field and absorb a photon, it must possess a dipole oscillating at the frequency of the field. This may be temporarily induced by the absorption of a photon if the frequency of the photon corresponds to the separation in energy of initial (i) and final (f) states of the transition. The excited molecule displays a charge separation and hence a dipole moment, where the energy of the final state is greater than the initial ($\mathrm{E}_f > \mathrm{E}_i$). This transient dipole is expressed quantum mechanically in terms of the transition moment between the initial and final states, μ_{fi}, and is described by Equation 2.1 where Ψ_i and Ψ_f^* are the time dependent wavefunctions of the initial and final states, and $\hat{\mu}$ is the dipole moment operator.

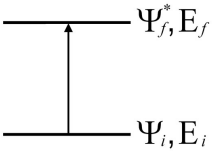

$$\mu_{fi} = \langle f|\mu|i\rangle = \int \Psi_f^* \hat{\mu} \Psi_i d\tau \tag{2.1}$$

In order for a transition to proceed, the amplitude of the transition moment must be non-zero, leading to a dipolar redistribution of charge. The intensity of the transition is proportional to the square of the transition moment $|\mu_{if}|^2$

2.1.1.2 The Franck–Condon Principle

Since nuclei are enormous in comparison to electrons, an electronic transition will take place far more rapidly (*ca.* 1×10^{-15} seconds) than the nuclei can respond through

nuclear and vibrational motion. This means the nuclear framework remains constant during electron excitation onto a higher energy surface, resulting in a state known as the Frank-Condon state. Since the geometry of the ground state molecule is projected onto an excited state potential energy surface, we can imagine this transition to be vertical. The vertical transition depicted in Figure 2.1 occurs from the centre of the ground state vibrational level and cuts through several vibrational levels in the electronically excited state. In this example, the transition is expected between the ground vibrational level in S_0, v"=0, and v'=3 in S_1. This is because the third vibrationally excited level of the S_1 state demonstrates the greatest integral overlap to v"=0 as the wavefunction is at maximum amplitude. However, it is not the only possible transition, since v'=2 demonstrates an appreciable overlap at the starting internuclear separation. Therefore a less intense transition from v"=0 to v'=2 will be present. This description holds for a diatomic molecule. For polyatomic systems, many transitions over a range of energies are possible, and these transitions merge leading to an absorption curve, the shape of which is governed by the relative intensity of the component transitions. This curve is often described as the Franck-Condon envelope.

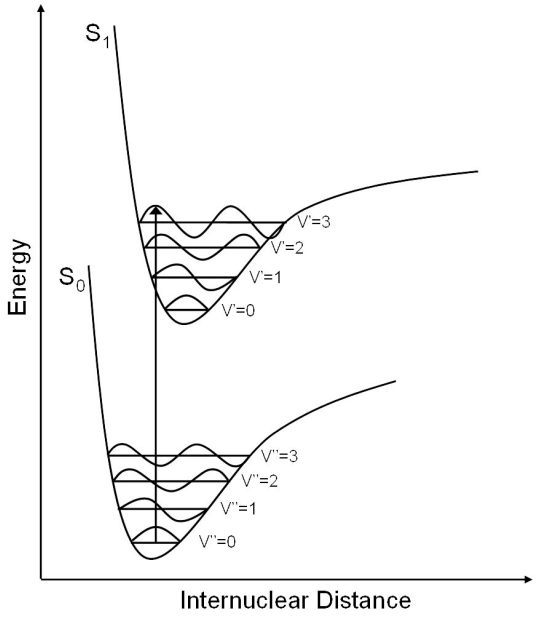

Figure 2.1: Illustration of the Franck-Condon Principle. In this example the 3-0 transition is most probable since it displays the greatest integral overlap.

2.1.1.3 The Beer-Lambert Law

The ratio of transmitted light (I) of a given wavelength to that of the incident light of the same wavelength (I_0) is described as transmittance, T. Empirical observations have shown that the intensity of transmitted light varies with the concentration of the absorbing species, c, and the pathlength through which it must pass, l. This is

represented in Equation 2.2.

$$\frac{I}{I_0} = 10^{-\epsilon cl} \tag{2.2}$$

In this equation, ϵ, known as the molar absorption coefficient (or extinction coefficient) is a constant characteristic of a particular sample for the wavelength of light studied. Larger values of ϵ indicate a greater ability for a sample to block the passage of light of a given frequency. To simplify this relationship, the term 'Absorbance' is introduced and is based on its relationship with inverse transmission. This is shown by Equation 2.3.

$$Abs = -\log_{10}\frac{I}{I_0} = \epsilon cl \tag{2.3}$$

2.1.2 Deactivation of Electronically Excited Molecules

Without participating in a photochemical reaction, several routes are available for an electronically excited molecule to lose its energy and relax to the ground state. Figure 2.2 is a simplified Jablonski diagram detailing the individual processes by which an arbitrary molecule, electronically excited from the ground to first excited singlet state, could be deactivated. Since this work is not concerned with radiative processes such as fluorescence and phosphorescence, no further discussion of these routes will be undertaken. However, the non-radiative routes are relevant in parts of this work, and are described briefly herein.

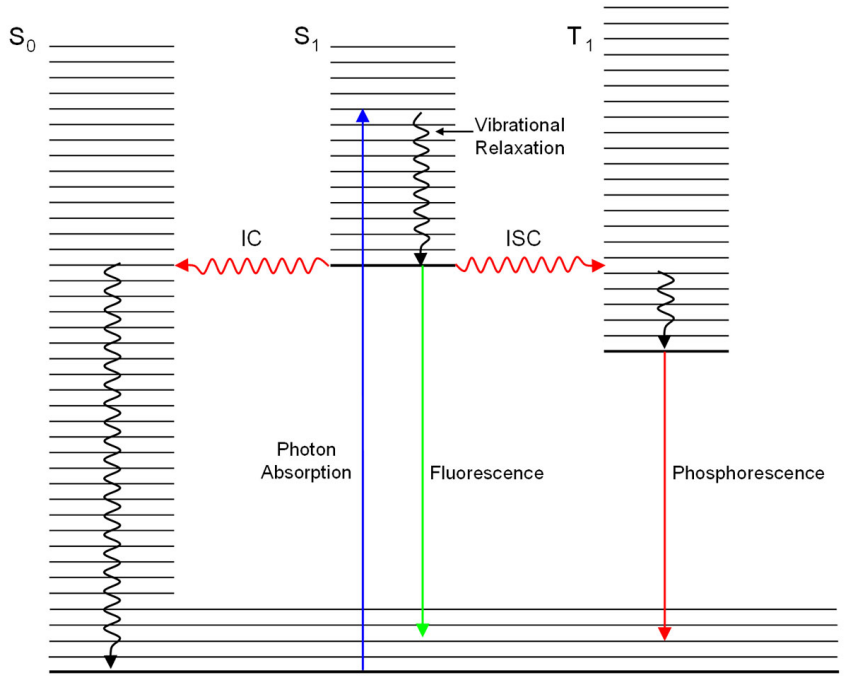

Figure 2.2: Jablonski diagram. Possible mechanisms for deactivation of an excited state species are listed in the figure.

2.1.2.1 Vibrational Relaxation

Vibrational relaxation is the most common non-radiative route in which an excited molecule loses its vibrational energy, and for most molecules it occurs very quickly ($< 1 \times 10^{-12}$ s). The process is enhanced through physical contact of the excited molecule with other molecules in the sample, be they molecules of the same species or the solvent. The energy is transferred through collisions with nearby molecules until the excited species reaches equilibrium with its environment.

2.1.2.2 Intersystem Crossing

Formation of a triplet state directly from photon absorption is highly improbable since both the orbit and spin of the excited electron would have to change simultaneously. Hence, a singlet electronic state is formed following absorption of light. However, the lifetime of the singlet state for some molecules is long enough to allow intersystem crossing (ISC), an isoenergetic, non-radiative transition to an electronic state with a different multiplicity. The spin of one electron must invert for this change to occur, and this forbidden transition is induced through spin-orbit coupling, an effect that is sometimes enhanced by a heavy atom in the sample or in the solvent. Spin-orbit coupling involves interaction of the electron spin and its motion around an atomic nucleus. This effect blurs the singlet and triplet states that the electron may occupy leading to a mixing of character and allowing an opportunity for the electron to change multiplicity rather than decaying through one of the spin-allowed pathways.

2.1.2.3 Internal Conversion

Internal conversion (IC) is an intramolecular non-radiative transition between two electronically excited states with the same multiplicity, for example the first excited singlet state (S_1) to the ground state (S_0). This form of deactivation, although non-radiative, differs from ISC since the spin state remains the same during the transition, and is therefore allowed. Following photon absorption into a singlet excited state, the molecule in a high lying state is likely to undergo IC to vibrationally excited levels of lower lying singlet states due to small energy differences in these high lying states. This is followed by rapid vibrational relaxation to the lowest vibrational level of the electronic state. The energy difference between S_1 and S_0 is greater than the gaps between higher electronically excited states, and therefore competing pathways of fluorescence, ISC, intermolecular deactivation and chemical reactions may occur. If IC occurs, the vibrationally excited molecule will release this energy to its surroundings through vibrational relaxation.

2.1.2.4 Quenching

Quenching is a form of intermolecular deactivation where the excited molecule, M^*, transfers its electronic energy to another species, Q.

$$M^* + Q \longrightarrow M + Q$$

Quenching is significant in solution phase experiments due to the great probability that M^* will collide with a solvent molecule. The energy imparted by these collisions is not generally enough to cause electronic excitation of the quenching molecule, instead leading to a change in the translational or vibrational excitation of the species.

2.1.2.5 Photochemical Isomerisation

Photochemical isomerisation (photoisomerisation) is the process by which a species changes its conformation following photon excitation. In contrast with purely photophysical phenomena, the initial and final physical states involved in photoisomerisation are chemically different. This is usually a reversible process, with examples including photo-induced rotation around a C=C or N=N bond. Taking the simple, and well characterised example of ethene, the process can be discussed in more detail. Ethene contains two sp^2 hybridised carbon atoms, joined by a double bond. Attached to each carbon atom are two hydrogen atoms. In the ground state this system has a planar geometry, any torsion of the double bond being highly unfavourable since bond scission is required to enable its occurrence, leading to a high energy structure. Hence, the geometry is locked.

Photo-excitation of an electron from the double bond will result in a transition of the ethene molecule from the ground state onto an excited state potential energy surface. Since this transition is from the HOMO π orbital to the LUMO π^* antibonding orbital, it is labelled as a $(\pi\pi^*)$ state. The initial geometry of this excited molecule will be unchanged from the ground state: a condition known as the Franck-Condon state. It is likely that the geometry will rapidly change on this new surface, an event directed by the shape of the excited state surface.

Figure 2.3 illustrates the potential energy diagram for the torsional potential of ethene in the ground, first excited singlet, and first excited triplet states, labelled S_0, S_1 and T_1. Plots of the potential energy of the structure across a 180° rotation of the CC bond for each state appear as an energy curve. In order to understand the behaviour of an excited ethene molecule, it is vital to understand the potential energy curves presented. This diagram highlights the aforementioned barrier to rotation in the ground state, showing an increase in energy until each end of the molecule is twisted at 90° to each

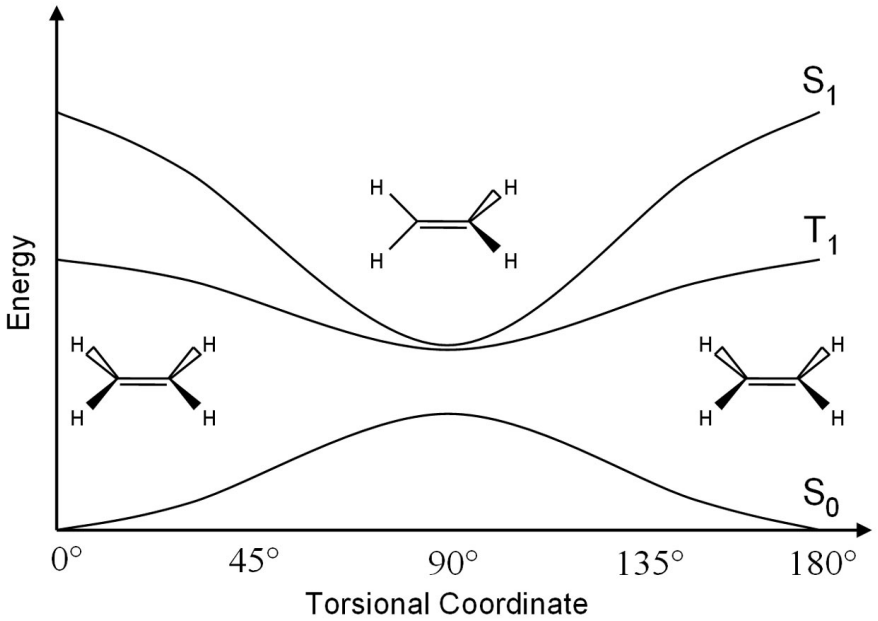

Figure 2.3: Illustration of the S_0, S_1 and T_1 potential energy curves for the C=C rotation in ethene.

other, where it reaches a maximum. However, the S_1 and T_1 states contain an electron in an anti-bonding orbital, reducing the order of the double bond. This change in bond character leads to preferred conformations in S_1 and T_1 that are twisted in order to reduce repulsion between the half-filled bonding and anti-bonding orbitals. At the minimum of these curves, where they are close to the maximum energy on the ground state, crossing may occur by internal conversion from S_1 or inter-system crossing from T_1, onto the S_0 potential energy curve. Relaxation may occur in either direction from this maximum, leading to the initial geometry, or a geometry that has rotated by 180°. In the case of ethene this will always appear as the same structure. When a substituent is added to each side of this double bond, the product of isomerisation is distinguishable.

2.1.3 Quantum Yield

The quantum yield, ϕ, simply defines the efficiency of a photo-induced event. This event may be anything that is observed after photo-excitation, such as fluorescence, phosphorescence, or isomerisation. It is described as:

$$\phi = \frac{number\ of\ events}{number\ of\ photons\ absorbed}$$

The closer ϕ is to 1, the more efficient a process will be since it reflects a high probability of an event occurring following the absorption of a photon.

2.2 NMR Spectroscopy

2.2.1 Introduction

Nuclear magnetic resonance (NMR) spectroscopy, first demonstrated in 1946, applies radio frequency (RF) radiation to the task of uncovering information pertaining to the structure of a given molecule. Nuclei with a spin quantum number other than zero will orientate themselves when placed in a magnetic field. A nucleus with a spin quantum number of 1/2 can orientate itself parallel or antiparallel to the external field. The energy difference between these two states is small, so the equilibrium is only shifted to a small extent in favour of the low energy orientation. Absorption of RF radiation bearing a frequency specific to the nucleus is possible, exciting the nuclear spin from the low energy state to a higher energy state. As the spin precesses back to its equilibrium state it can yield a great deal of information about the local environment, which can then be analysed and interpreted.

Early applications of NMR involved the physical study of the nucleus through measuring nuclear magnetic moments, important work that yielded a Nobel Prize in 1952 for physicists Bloch and Purcell. However, improvements in magnet homogeneity brought the technique into the view of chemists, and even further down the line the same principles were applied to medical imaging.

Magnetic fields were originally limited to the strength of bench electromagnets, and the experiments were performed by either sweeping the magnetic field, or sweeping the frequency of irradiation until a nucleus was brought into resonance. The continuous wave (CW) methods eventually gave way to methods using a static magnetic field with the RF radiation applied as a pulse covering the required frequency range. The free induction decay (FID) produced was processed through Fourier Transformation (FT) to give a spectrum equivalent to that obtained through traditional methods. However, it bore the advantages of speed and increased sensitivity through averaging the noise over multiple experiments. Introduction of superconducting electromagnets led to significant resolution improvements. The first two-dimensional experiment was performed and published in 1976,[14] causing explosive progress in this new and exciting field of NMR, and yielding the 1991 Nobel Prize in Chemistry for Richard Ernst. A further Nobel Prize in Chemistry was awarded to Wüthrich for the development of NMR spectroscopy aimed at extending the the capabilities of this technique for three-dimensional structural identification of biological macromolecules.

It is clear that NMR has developed from its initially crude form into a sophisticated technique capable of providing a huge variety of structural information, often through

the use of elegantly designed experiments. Its applications are so broad-ranging that few current chemical research laboratories lack a super-cooled magnet for conducting structural characterisation *via* this method. A number of experiments are available to the chemist, and can range from simple one dimensional (1D) ^{1}H and ^{13}C spectra of small molecules, to multidimensional, multinuclei spectra of protein samples, delivering distance and coupling information for the nuclei involved. The range of literature relating to the theory of this technique is vast, some examples existing in the cited references.[15–19] Sections that follow provide a brief examination of the relevant forms of NMR spectroscopy implemented in this work.

2.2.2 Basic Theory in One-dimensional NMR

As alluded to earlier, the spin of NMR-active nuclei will align to an applied magnetic field. Consider a nucleus with a spin quantum number, I, of $\frac{1}{2}$, *e.g.* a proton. The absence of an external magnetic field causes the states $m_{_I} = +\frac{1}{2}, -\frac{1}{2}$ to be degenerate. Application of a magnetic field causes two different energy states to become apparent: a low energy, N_α, state and a higher energy N_β state. This is illustrated in Figure 2.4.

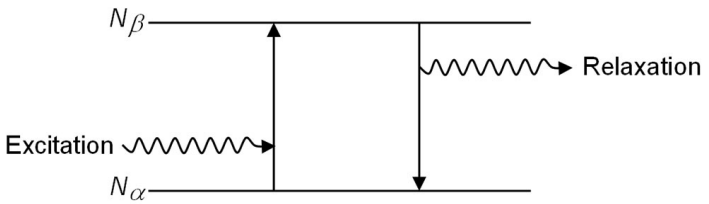

Figure 2.4: A simple energy level diagram for a system containing two two angular momentum spin states, N_α aligned with, and N_β aligned against, the applied magnetic field.

The energy difference between N_α and N_β (ΔE) is dependent upon the strength of the interaction between the nucleus and the magnetic field. To cause the nucleus of a proton to resonate, the correct frequency of radiation is required, and is defined by Equation 2.4, where h is Planck's constant, ν is the frequency of RF irradiation, $\gamma_{_H}$ is the gyromagentic ratio for a proton (relating the magnetic moment with the spin quantum number), and B is the applied magnetic field strength.

$$\Delta E = h\nu = \hbar\gamma_{_H} B \tag{2.4}$$

Although ΔE is principally related to the magnetic field strength and the type of nucleus studied, minute variations in the local electronic environment experienced by each nucleus lead to a difference in the energy at which each is brought into resonance. Therefore, identical nuclei in different environments can still be distinguished from one another.

Although modern NMR spectrometers boast large magnetic fields with a high power to resolve signals, this technology can stretch only so far in a single dimension. Following absorption of RF radiation, a nucleus will relax (from N_β to N_α, Figure 2.4). Considering a proton spectrum, as a molecule grows in size it is likely that more proton environments will be present, leading to a more cluttered spectrum. However, this potential problem is not the only one present for larger molecules. A molecule of significant size will tumble slowly in solution, at a rate that is inversely proportional to T_2, where T_2 is a measure of spin-spin relaxation. Hence, the slow tumbling rate of a large molecule leads to a fast rate of spin-spin relaxation. This is unfortunate, since the lineshape of a signal is proportional to $1/T_2$ leading to broad signals. As this work concentrates on small molecules, their tumbling rate is fast giving long T_2 relaxation times and therefore narrow lineshapes. The resulting one dimensional spectra presented in this thesis can be easily interpreted.

2.2.3 Interpretation of One-dimensional NMR Spectra

A Fourier transformed FID produces a plot of intensity versus frequency. Since the RF frequency at which a nucleus comes into resonance depends upon the magnetic field (Equation 2.4), comparison of results between different magnets is impossible without using a reference. To this end, results are reported as a chemical shift, δ, from a known reference signal, the units for which are parts per million (ppm). This is performed using Equation 2.5, where ν_s and ν_{ref} are the respective signal and reference frequencies, both quoted in Hz. For ^{1}H and ^{13}C nuclei, the reference frequency used is that of tetramethyl silane (TMS), an inert and volatile liquid at room temperature that does not interfere with the sample. TMS is quoted as zero on the chemical shift scale ($\delta(^1H) = 0$ ppm).

$$\delta = 10^6 \, \frac{\nu_s - \nu_{ref}}{\nu_{ref}} \tag{2.5}$$

Of use to the chemist is the sensitivity of the nuclear resonance frequency to the local electron environment, allowing nuclei to be brought into resonance at different chemical shifts. A small molecule with a limited number of protons in different environments should display discretely placed peaks in a ^{1}H NMR spectrum. The frequency range at which these peaks resonate helps characterise the local environment in which they are placed. For instance, aliphatic protons appear at a shielded position in the spectrum ($\delta(^1H) = 0$-5 ppm) close to the TMS reference, whereas aromatic proton signals appear more deshielded ($\delta(^1H) = 7$-9 ppm).

An example ^{1}H NMR spectrum from this research is presented in Figure 2.5. This spectrum highlights the high resolution of the NMR technique for small molecule work,

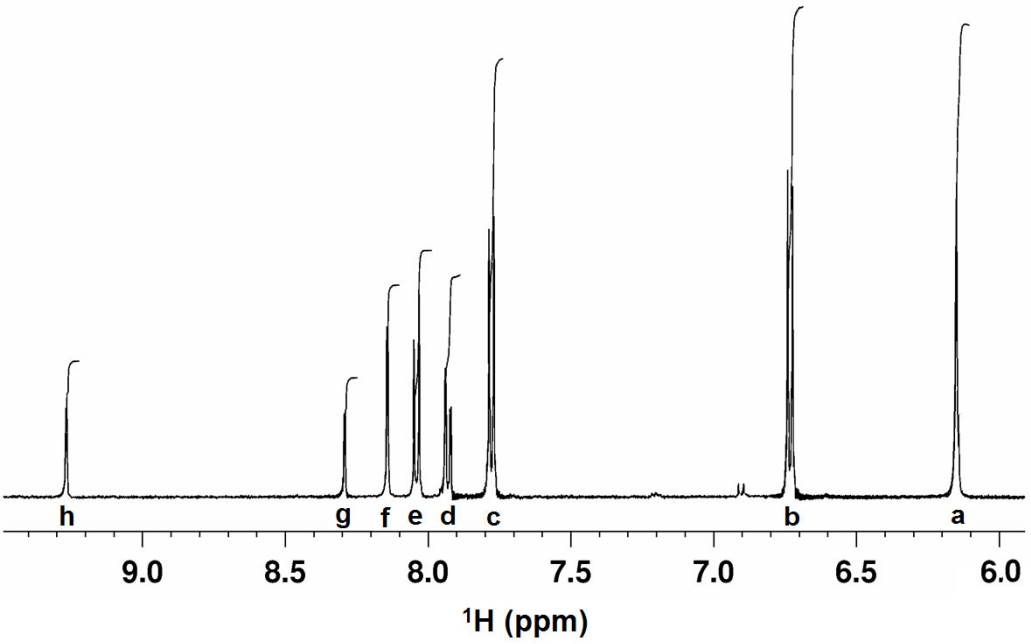

Figure 2.5: One dimensional ^{1}H NMR spectrum of a representative molecule. Quantitative peak integrals are shown.

and can be used to demonstrate some of the simple tools available for structural identification. The eight proton environments, clearly identified by the separate signals in the spectrum, are deshielded with their chemical shift indicating most protons are aromatic. However, it is not just the location of the signals on the chemical shift scale that identify the protons in the sample. Peak intensities provide important information on the relative number of protons defined by a given signal. In this case, integration of peak areas indicates peaks **a**, **b** and **c** as environments that each contain twice the number of protons as the other five environments.

Another critical feature of NMR that greatly aids structural determination is that of spin–spin coupling. The local magnetic environment of a proton can experience a short-range, through-bond interaction with another proton, causing a variation in the shielding experienced. The possible $m_I = +\frac{1}{2}, -\frac{1}{2}$ spins of a proton exhibit a subtle effect on a nearby proton environment, causing that proton to experience an increase or a decrease in the local shielding depending upon the spin with which it interacts. Essentially, a splitting of the main peak is observed, the fine-structure and spacing of the splitting depending heavily upon the nearby proton environments. This is clearly visible for peaks **b** and **c** in Figure 2.5, and the splitting, or coupling constant, of each is measured as 8.7 Hz. The magnitude of the coupling constant acts as an indicator as to the number of bonds between which the nuclei are coupled. This is indicative of a three bond proton coupling constant, suggesting the two peaks relate to protons on adjacent carbon atoms. The aromatic chemical shift, and double intensity indicate

they are most probably on a 1,4-asymmetrically substituted benzene ring creating two distinct proton environments.

Peaks **d** and **e** demonstrate a coupling constant of 9.16 Hz, again demonstrating a 3 bond coupling to one another. Furthermore, doublet **d** demonstrates additional splitting on the tip of each peak of 2.29 Hz, a small coupling constant that points towards a four-bond coupling. Peak **h** shows the same *meta* coupling constant to that of **d**. This pattern suggests **d** and **e** to be *ortho* coupled aromatic protons, with **d** *meta* to proton **h**. The remaining aromatic peaks **f** and **g** show coupling, suggesting the presence of up to three benzene rings, or one benzene ring and a higher fused ring system. Peak **a** is broader than the other signals suggesting the protons may be labile. The chemical shift suggests the protons are bonded to an electronegative element. This could quite possibly relate to an aromatic amine group. It is clear that a 1D NMR spectrum can yield a wealth of information about the proton environments present in a sample without prior knowledge of the sample's identity.

2.2.4 Two Dimensional NMR

The increase in molecular weight of a molecule often brings with it increasing complexity of the corresponding ^{1}H NMR spectrum. As mentioned in Section 2.2.2, this will not only lead to a greater number of peaks, but large molecules can exhibit particularly broad signals. An extremely powerful solution to this problem came in the form of two-dimensional NMR techniques. Adding a second dimension to the experiment greatly boosts the available resolution of the data, along with providing a route to obtaining data regarding the interaction of different types of nuclei in a single experiment.

Although two-dimensional experiments can vary to a great degree, they are based principally on the same four routine steps:

Preparation – Evolution – Mixing – Acquisition

The first step, preparation, involves a time delay allowing the nuclei to relax to equilibrium prior to the introduction of phase coherence *via* a 90° pulse. This phase coherence is allowed to develop over a period of time that is varied for each row of which the experiment is composed. Completion of this evolution period is marked with another pulse, causing transfer of phase coherence. This can either be a mixing pulse immediately followed by the acquisition of the FID, or a delay can be introduced prior to a final pulse and acquisition in order to allow the phase coherence to develop.

2.2.4.1 2D Correlation Spectroscopy (COSY)

In a 2D homonuclear Correlation Spectroscopy (COSY) experiment, magnetisation is allowed to transfer between two spin coupled nuclei. This occurs through the bonds *i.e.* through scalar coupling. A representation of a 2D COSY plot for a coupled two spin (AB) system is presented in Figure 2.6. For convenience, the two dimensional

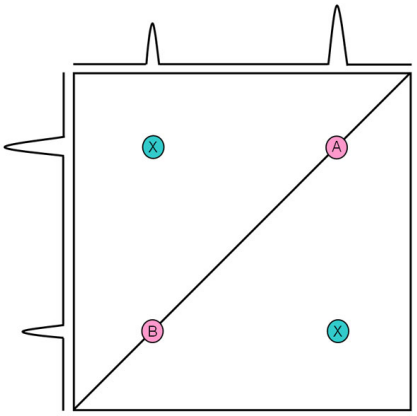

Figure 2.6: Simple representation of a 2D COSY spectrum of a coupled AB system.

plot is viewed from above, with two chemical shift axes plotted orthogonally. The one dimensional NMR spectrum is plotted on the diagonal between the two axes, although for ease of interpretation it is extremely helpful to plot this on one or both of the orthogonal axes. The two resonances shown in Figure 2.6, A and B, are coupled to one another. This is illustrated by the presence of a peak off the diagonal, known as a cross-peak. Usually, proton correlations up to three bonds apart are detected in the 2D spectrum. The power of this technique can be seen when overlapping signals, or signals hidden by a large solvent peak show cross-peaks: it is possible to resolve signals that would otherwise be unobserved in the corresponding 1D experiment. The information on 2D COSY detailed here is only for the simple cases used within this work. More complex COSY experiments for deriving heteronuclear cross-peaks are widely used but since they are not relevant to this work, they are not described here.

2.2.4.2 2D Nuclear Overhauser Effect Spectroscopy (NOESY)

Where COSY experiments work through the transfer of magnetisation through scalar coupling between nuclei, NOESY experiments work by transfer through dipolar couplings. In simple terms, NOESY detects interactions between nuclei in space, rather than through bonds. A NOESY experiment conforms to that shown in Figure 2.7, with transfer of magnetisation occurring during the mixing stage of the pulse sequence. The strength of the NOE bears a $1/r^6$ relationship, where r is the internuclear distance. Therefore, the interaction drops off rapidly with increasing distance leading to a typical

limit of detection of 5 Å.

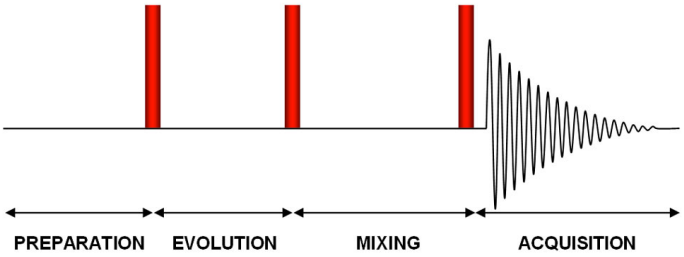

Figure 2.7: Basic representation of a two-dimensional pulse sequence.

The same format of a 2D plot to the COSY experiment (Figure 2.6) is formed, with the exception that the off-diagonal peaks show dipolar couplings. Similarities between the NOESY and COSY pulse sequences can lead to complication of the 2D NOESY experiment by magnetisation proceeding to give COSY-type artifacts in the spectrum. This undesirable feature not only complicates the spectrum, but may lead to overlap of cross-peaks for nuclei that demonstrate both scalar and dipolar couplings. A certain degree of optimisation must be performed to limit cross-peaks from the transfer of magnetisation appearing in the 2D NOESY spectrum. Using the procedure in the cited reference, the interference of COSY peaks can be eliminared from a NOESY spectrum.[20] NOE cross-peaks can be positive or negative, the sign depending upon the size of the molecule. The diagonal of the 2D NOESY spectrum is negative. For small molecules with slow relaxation times, the NOE peaks should be positive; large molecules with short relaxation rates producing negative cross-peaks.

2.2.5 Pseudo 2D NMR

As the name suggests, a pseudo 2D experiment only partially fulfills the characteristics of a two-dimensional investigation. Where a 2D experiment is performed with incremental evolution times in the second dimension, the pseudo 2D experiment involves a number of identical successive one-dimensional experiments. As modulation does not occur in the second dimension, the 2D file containing the FIDs is only processed in the first dimension. The end result is to produce a two-dimensional plot of a series of 1D experiments. The technique is effective at monitoring signal intensities over a time frame in which the sample being studied changes. Extraction of time-resolved data using software provides a method for accurate monitoring of the kinetics of a sample. In summary, such a pulse sequence allows for simple recording and extraction of kinetic data.

2.2.5.1 Definition of Integrals in Pseudo 2D Experiments

The integral is a measure of the number of nuclei associated with a particular signal. This is often used to to compare signals relative to one another during spectral assignment, to gain a representation of how many nuclei each peak corresponds to. In most cases, a small degree of variation in the measurement of each integral due to incomplete relaxation of the spin system is accepted, as it is not important overall. For the work conducted in Chapter 5, a comparison of the same peak between successive runs in a pseudo 2D experiment forms the basis of monitoring photochromic rates of a dye. For such work the integration must be both accurate and reproducible.

In order to gain the most points of a curve for modelling, the number of scans for each row of a pseudo 2D experiment must be optimised to give sufficient signal to noise without being too lengthy to avoid gathering insufficient data. The baseline noise from spectra acquired in this way can introduce unwanted noise in the resulting kinetic decay curve, which leads to error in the final fitted data. This becomes more apparent for low intensity signals such as those of a sample decaying to zero. It is possible to limit this effect through the accurate definition of the area that must be integrated in each spectrum. The baseline of each individual row must be corrected prior to integration, which leads to the noise being centred on the baseline. The integration is then performed at the discretion of the spectroscopist. Figure 2.8 shows two possible integrations of the same peak. In (a) some of the baseline noise on each side of the peak is included whilst the same peak in (b) has only been integrated above the baseline. This method produces a greater level of accuracy in peak definition when the same integration limits are applied to a series of spectra pertaining to a changing sample.

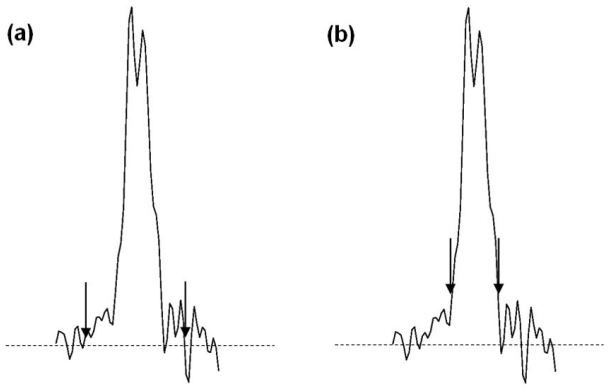

Figure 2.8: Two possible methods of defining peak integrals: (a) includes some of the baseline noise, (b) eliminates baseline noise. Dotted line represents the baseline and arrows define the integration limits.

2.3 NMR with *In Situ* Irradiation

The power of NMR for structural characterisation of samples lends itself well for studying samples that have been altered through the interaction of light. Although it is perfectly acceptable for characterising the reactants and products of photochemical reactions following *ex situ* irradiation,[21] the ability to study kinetic processes involving light are more difficult to achieve in the closed environment of an NMR probe. Several kinetic investigations of different multicomponent photochromic systems have been conducted using NMR spectroscopy with *ex situ* irradiation.[22–24] In the cited papers, thermal isomerisation following *ex situ* irradiation was monitored at low temperatures to limit any thermal changes in the sample whilst it was transferred to the probe of the NMR spectrometer. Where the thermal stability of the photo-induced species is high enough, a study of the photoisomerisation kinetics may also be conducted by acquiring NMR data between periods of sample irradiation. This will most certainly be subject to some error since transfer to and from the spectrometer is required between irradiation cycles. Two-photon irradiation has been used to invoke isomerisation of an azo dye that demonstrated a sufficiently long thermal decay to allow time to transfer the sample to an NMR spectrometer and record spectra.[25] Because of the static nature of the azo species on the time-scale used, details of the photoisomerisation rate could be obtained. *Ex situ* irradiation and NMR kinetic acquisitions like this are only applicable to dyes demonstrating such extended thermokinetic decays. Many systems exhibit thermal decays so rapid that the photo-induced species will decay prior to the sample reaching the probe of the spectrometer. For these studies another strategy must be adopted.

The ideal solution is to perform the irradiation *in situ*: with the sample inside the probe. However, difficult sample location, delicate electronics, and a high magnetic field do not lend themselves well to the integration of a light source with the probe of an NMR spectrometer. To approach this problem, the use of optical fibres, modified probes, and prism assemblies to guide open laser beams to the sample have been successfully implemented, each with their own merits and pitfalls. The advantage of the optical fibre method is that it does not require an open laser beam in the area, nor does it require complex or expensive modification of the NMR apparatus, ideal for spectrometers that are used by many individuals.[12,26–28] It also has the advantages of portability, assuming the laser in use is suitably portable. To improve homogeneity of sample illumination, Kurpov and Hore suggested a method of etching the optical fibre using an acid mixture (HF and H_2SO_4). In this case, a 1 mm optical fibre was dissolved in stages to give a stepped profile over 2 cm at the tip.[26] Insertion of this fibre into the probe region

allowed light to emit from each step of the fibre, providing more uniformity to the irradiation profile. However, the use of optical fibres with high power UV lasers can ultimately lead to distruction of the fibre, leading to questions of robustness over this method.[29]

Another method of non-intrusive light delivery is by guiding the beam of light from a laser on an optical bench through a focusing lens and a series of prisms. The final prism is mounted above the spectrometer, guiding the light down the bore of the magnet and into the sample solution.[29] In this case, the output of the laser will not be modified by an optical fibre, but introduces obvious safety concerns and the requirement of a dedicated laboratory. Additionally, the beam must pass through a proportion of the sample prior to reaching the detection region, where some of it will be absorbed. The final method involves modification of a probe to allow the laser beam to pass into the spectrometer and be directed to the sample using a prism.[13] This method of light delivery has the advantage of illuminating the sample from the side, so the laser beam does not get absorbed by sample that is not directly in the detection region of the NMR probe. However, this can be an expensive modification, and is less than user friendly in an environment where many users of the magnet are present, or the probe is often changed.

Of course, the advantages of NMR studies using *in situ* irradiation are numerous. When thermal decay measurements are being made, there is no requirement to transfer a sample from the irradiation source to the spectrometer. This is advantageous, especially for samples where thermal decay is rapid, since it allows results to be obtained that would otherwise be inaccessible. It can also be used to observe and characterise species that would otherwise be too short-lived to study. In a study of several azobenzene derivatives, Tait was able use an optical-fibre based method to observe and characterise short-lived azo *cis* isomers through continuous irradiation of the sample at the photostationary state (PSS).[12] In a later study, Tait examined more complex monoazo dyes, similar to those presented in later chapters.[30] A kinetic treatment of the photo and thermal kinetic processes occurring during irradiation of azo samples was also conducted. Delbaere *et al.* applied a modified probe to the problem of studying photochromic $3H$-naphthopyrans that could undergo interconversion between several isomeric forms *via* photochemical and thermal pathways.[13,31] In both cases, the high resolution of NMR provided accurate data pertaining to the concentration of different species within the same sample, and allowed the intensity of peaks related to each species to be followed over a period of time, yielding valuable data on which kinetic fits could be applied. This is in contrast with optical techniques such as UV-vis where deconvolution of the broad

bands in the spectrum is required, leading to a degree of ambiguity in any results.

One major use of NMR with *in situ* irradiation is the investigation of photo-generated chemically induced dynamic nuclear polarisation (photo-CIDNP). CIDNP describes the non-equilibrium spin state populations produced in chemical reactions that proceed through radical pair intermediates, and is detected by NMR spectroscopy as enhanced absorption or emission signals. CIDNP is used to detect transient radicals and investigate reaction mechanisms. In certain cases it can also be used to increase the sensitivity of NMR experiments. In the cited examples, CIDNP has been used for amplifying heteronuclear Overhauser effects,[27] and studying processes such as protein folding.[28,29] In the study of proteins, a sample containing the protein and a photosensitiser is irradiated, followed by detection of the nuclear polarisation. The signals of certain solvent-accessible aromatic amino acids (histidine, tryptophan and tyrosine) that can undergo radical pair reactions resulting in nuclear polarisation, will be enhanced by up to two orders of magnitude compared with other signals in the spectrum. This not only provides information on the accessibility of side-chains, but also provides a route for using lower concentrations for protein work.

The use of NMR with *in situ* irradiation evidently bears numerous applications to chemistry, from observing short-lived photo-induced species, to studying solvent accessible sites on proteins. The irradiation can also be implemented in a number of ways. The research contained in this thesis employs an optical fibre-based method for studying photo-induced *cis* isomers of azo dyes, and the kinetics of their formation and decay. Experimental details for these studies can be found in Chapter 3, and the results in Chapters 4, 5 and 6.

2.4 Computational Aspects

Extremely rapid advances in digital computing over the previous 40 years have brought about rapid advances in the field of computational chemistry. This section will provide a short summary of computational methods with relevance to the work presented in later chapters. Quantum chemical calculations are employed by chemists and physicists with the aim of solving the time-independent Shrödinger equation for a system. This yields useful information on the system that will either support current experimental findings, or make available properties that are inaccessible by experimental means. This is not a straightforward task since the Schrödinger equation can only be solved for a one-electron system. Moving any further within this field requires approximations to be applied to the problem.

The first approximation that must be considered relates to the interaction of nuclear and electronic motion. Because of the gross difference in mass between nuclei and electrons, the electrons are likely to respond instantanously to any changes in the nuclear framework. Therefore, the electrons are reliant upon the spatial position of the nuclei, but not on the nuclear motion. This assumption allows the terms for nuclear and electronic motion in a molecular wavefunction to be separated, and is known as the Born-Oppenheimer approximation. Following this assumption, the electronic Shrödinger equation for a fixed set of nuclear positions is shown in Equation 2.6a. $\Psi_{el}(r:R)$ is the electronic wavefunction and $E(r:R)$ is the electronic energy of the system, where r corresponds to the electronic positions, and R denotes the location of nuclei. The so-called clamped nucleus Hamiltonian describing this system follows in Equation 2.6b.

$$\hat{H}_{el}\Psi_{el}(r:R) = E(R)\Psi_{el}(r:R) \tag{2.6a}$$

$$\hat{H}_{el} = \hat{T}_e + \hat{V}_{en} + \hat{V}_{ee} + \hat{V}_{nn} \tag{2.6b}$$

Reviewing the terms in the Hamiltonian, $\hat{T}_e$ describes the kinetic energy of the system of electrons, $\hat{V}_{en}$ describes the Coulombic attraction between the nuclei and electron. The classical term for nuclear-nuclear repulsion energy, $\hat{V}_{nn}$, is conventionally added at the end of the calculation. The final term to mention is $\hat{V}_{ee}$, the electron-electron repulsion. This coupling of electronic motion prevents the facility of writing a many-body wavefunction as a combination of one-electron functions. This in turn makes the Schrödinger equation extremely difficult to deal with and, except for the most simple of systems, it has not been solved. In the approach to this problem, approximations must be applied to reach a solution. With any approximation, a certain degree of error will be present in the final solution and the amount of acceptable error must be decided upon by the computational chemist when embarking on a study. Two main considerations arise at this point:

(1) At what level of theory will the calculation be conducted.
(2) What basis set should be applied to the system in order to represent the electrons.

These two points are reviewed in the sections that follow.

2.4.1 Level of Theory

As alluded to earlier, it is the electron-electron repulsion term, $\hat{V}_{ee}$, in Equation 2.6b that obstructs solution of the Scrödinger equation for systems containing more than one electron. The theories that underpin computational chemistry must approach this by approximation. Firstly, consider the Pauli Exclusion Principle which infers that no two electrons can be characterised by the same four quantum numbers. Hence, the elec-

tronic wavefunctions must change sign whenever the coordinates of two electrons are interchanged. Exchange symmetry states that no observable physical quantity should change after exchanging two identical particles. In this case it is fulfilled, since observables are proportional to $|\Psi|^2$. Any electrons bearing the same spin quantum number occupy different orbitals, staying away from each other and experiencing reduced repulsion, termed the exchange energy. The Hartree-Fock (HF) method includes exchange energy by applying mean-field theory in the calculation, *i.e.* the electron under examination moves in an electric field generated by averaging all the other electrons and nuclei in the system. Treating all other electrons as a smooth distribution of negative charge is a simplification in the HF method that inevitably leads to calculated structures being higher in energy than experimentally determined values. This variation decreases as the accuracy of the basis set increases (Section 2.4.2) although, even with an infinite number of basis functions, the method will never achieve solution of the Scrödinger equation due to the approximations made with the mean-field approach. This is known as the Hartree-Fock limit.

Adaptation of the HF method is required in order to improve the accuracy of the results. The approximation of electron exhange included in HF theory partly represents electron correlation through avoiding electrons with parallel spins appearing at the same point in space. However, it does not consider the correlation of electrons with opposing spin, neglecting important Coulomb repulsion energy. Therefore, instantaneous repulsion between electrons is not considered. For improvement beyond the HF limit, the electron correlation must be considered within the calculation. Many expressions have been derived from HF theory to accommodate electron correlation. Two widely used methods are Configuration Interaction (CI) and Møller-Plesset (MP) perturbation theory. The CI method provides virtual orbitals that the electrons may occupy, effectively expanding the space the electrons can fill. This allows them to relax from the strict HF picture so they are better placed to avoid each other. The Møller-Plesset approach applies a perturbation to the HF system in order to represent electron correlation. The order of perturbation is generally quite small, and this theory is usually represented by MPn where n is the order of perturbation. The modifications apply an approximation of the electron configuration to the basic HF model, thus improving the accuracy. However, the increases in accuracy bear elevated computational costs due to the presence of two-electron integrals. The computational cost of experiments scales upwards from N^4, where N is the number of basis functions used.[32] As a result of this additional expense, these theories are generally applied to small systems only. As this work has exclusively used density functional theory (DFT) calculations, no further discussion of these methods will be presented. The benefits of DFT are discussed in Section 2.4.1.2.

2.4.1.1 Semi-empirical Methods

Simplification of the aforementioned *ab initio* methods, through the use of semi-empirical methods, can be used to calculate material properties at a much lower computational price. Semi-empirical methods are based on the HF formalism but are adapted to include parameters that fit experimental data in order to simplify the calculation. The Austin Model 1 (AM1) and Parameterised Model number 3 (PM3) are two of many semi-empirical methods, and are named here purely for example. Both methods are based on the Neglect of Differential Diatomic Overlap (NDDO) approximation,[33] which removes all 3 and 4 centre two-electron integrals. The difference between the two methods is that PM3 uses two Gaussian functions per core, and AM1 uses 1-4 depending on the atom. The numerical values of these parameters are also different: where AM1 uses spectroscopic data in its parameters, PM3 treats them as optimisable. Results of calculations may deviate distinctly from the true value if the molecule being studied does not resemble those in the database that was used to parameterise the method. Therefore, selecting an appropriate semi-empirical method will provide a computationally cheap method for calculating the properties of materials that are too costly to undergo formal *ab initio* calculations.

2.4.1.2 Density Functional Theory

The fundamental difference between Density Functional Theory (DFT) and other theories stems from the fact DFT optimises an electron density, rather than a wavefunction. The initial DFT theorum was published by Hohenberg and Kohn in 1964,[34] a pure observation that the ground state electron density and the ground state wavefunction could be mapped 1:1 in a many-particle system. Therefore, the total energy of a system of electrons at a given position in space, $E(r)$, is a function of the electron probability density at that exact position, $\rho(r)$. The total energy of the system becomes a functional of the electron probability density, denoted $E[\rho(r)]$.

The breakthrough came a year later, when Kohn and Sham formulated a method for calculating the ground state electron density by assuming the system of electrons was non-interactive in a static potential field.[35] For this fictitious system of non-interacting electrons, the electron density in the ground state will be the same as a real system where electronic interaction is present. Since the electron density determines the position and atomic numbers of the nuclei, these quantities must be the same in the real and fictitious systems. The total energy of the ground state is found by varying the electron distribution until a minimum is returned. This simplification reduces the calculation of electron density, ρ, to a series of one-electron densities that are composed of one-electron wavefunctions, Ψ_i. The exact ground state electron density, ρ at position

(r) is is given by Equation 2.7, where Ψ_i (i=1, 2, 3...n) are the Kohn-Sham orbitals for the n electron system.

$$\rho(r) = \sum_{i=1}^{n} |\Psi_i(r)|^2 \tag{2.7}$$

The total energy of a system is expressed in Equation 2.8.

$$E[\rho] = V_{en}[\rho] + T_{ni}[\rho] + V_{ee}[\rho] + E_{xc}[\rho] \tag{2.8}$$

The first term, V_{en}, describes the potential due to nuclear-electron attraction, T_{ni} is the kinetic energy of the non-interacting electron, V_{ee} is the Coulombic electron-electron repulsion, and the final term, E_{xc}, contains the electron exchange and correlation terms. Modelling the correlation and interaction is the difficult component of DFT, and approximations must be applied. The simplest answer to this is the Local-Density Approximation (LDA) which is based upon exact exchange, and fits to the correlation energy, for a homogeneous electron gas of constant density. The LDA is described by Equation 2.9, where $\epsilon_{xc}(\rho(r))$ is the exchange correlation energy of an electron in the uniform electron gas.

$$E_{xc}[\rho(r)] = \int \rho(r)\epsilon_{xc}(\rho(r))\, dr \tag{2.9}$$

Use of the LDA approximation will inherently lead to errors in the final result since a molecule will not contain a homogeneous distribution of positive or negative charge. Despite the approximation, LDA has been shown to give good results in solid state systems, but slightly less for molecular systems. Further improvements in DFT requires the inhomogeneity for a molecular system to be reviewed, which in turn requires approximations in the exchange and correlation energy to be modified. In acknowledgement of this inhomogeneity in a real system, non-local (gradient) correction can be applied to the parameterisation of the exchange correlation energy. Different forms of this are available, and are known as Generalised Gradient Approximations (GGA). The development of new GGA functionals in the late 80's and early 90's revolutionised the capabilities of DFT.[36,37] Hybrid models have been developed in addition to the noted GGA functionals. Combination of Becke's three parameter exact exchange functional (B3),[38], and the Lee-Yang-Parr (LYP) correlation functional,[39] allowed the B3LYP functional to be devised. Since this functional has been shown to be useful for a broad range of molecular systems, it has been used to perform all the DFT studies within this thesis.

2.4.2 Basis Sets

The accuracy of a calculation is reliant upon the number and type of function used to describe the electrons in the system being studied. The positions of nuclei and electrons

in a molecule are described by the molecular orbitals (Ψ_i). However, since the Born-Oppenheimer approximation demands the nuclei are static, the wavefunction need only consider electron motion in space. In quantum chemical calculations, the wavefunctions are constructed from a linear combination of a set of known one-electron functions: ϕ_n (x, y, z). Equation 2.10 describes the linear combinations of these functions, where ϕ_μ represents each one-electron basis function, and $c_{\mu i}$ is the coefficent for basis function ϕ_μ. These basis functions collectively form the basis set.

$$\Psi_i = \sum_{\mu=1}^{N} c_{\mu i}\phi_\mu \tag{2.10}$$

In an ideal world, the number of basis functions forming the basis set would be infinite in order to give an optimum description of the electron probability density. In reality it is not possible to make use of an infinite basis set. Instead, it must be composed of a finite number of functions, giving a truncated series. Keeping the number of basis functions to a minimum is computationally attractive. The functions used to represent the wavefunction must describe it well in order to be effective, *i.e.* they will have a large amplitude in the regions of space where electron probability density is high, and *vice versa*.

The accuracy of a calculation is dependent upon the mathematical form of the basis functions used. Given its resemblance to a hydrogenic atomic orbital, a Slater type orbital (STO) initially appears ideal for the modelling of a basis function. Unfortunately, an analytical solution to the general four-index integral of an STO does not exist. This poses a significant problem when using STOs for anything larger than three or more atoms. A solution to this problem comes in the form of a Gaussian type orbital (GTO) since the only required difference for the STO to be solved would be to change its radial decay from $e^{-\alpha r}$ to $e^{-\alpha r^2}$.[32] The solution to such a form is computationally tractable, allowing much larger systems to be studied. However, the utility of a GTO as a basis function is diminished with respect to STOs due to its poor fit when modelling the radial distribution. The GTO has zero slope at the nucleus, and falls off too rapidly as the distance from the nucleus increases. This unfortunate problem can be addressed through a linear combination of several different GTOs in order to represent the STO, the terminology for which is a contracted Gaussian type orbital (CGTO).

The early basis sets were called minimal basis sets. As a compromise between accuracy and computational cost, a CGTO composed of three primitive GTOs was found to model the STO orbital well. This basis set is formally named STO-3G (generally STO-NG where N = number of GTOs) and, as a result of its success in modelling the STO, basis sets have been defined for the majority of the periodic table using this method.

Although the computational costs involved are cheap, results using these primitive basis sets are generally not suitable for research publications. In most situations where molecular bonding occurs, it is principally the valence electrons that take part. The STO-NG basis sets contain the definition of a single basis function for all the core and valence orbitals. For a more accurate description, split-valence basis functions can be used. In a 3-21G basis set, the core consists of a CGTO comprising three GTOs, as for the STO-3G basis set. However, the valence functions are split, one basis function comprising two GTOs, the other a single GTO. Using two basis functions to describe an orbital can be described as a double-ζ basis set. The 3-21G basis set is split-valence with a single-ζ basis set describing the core, and double-ζ describing the valence electrons. This allows a greater degree of accuracy when modelling systems where the bonding is different in opposite directions, for example the carbon atom in H-C≡N.

When the basis functions are centered on the nucleus, there is insufficient mathematical flexibility for the wavefunction to describe the bonding in highly polar molecules. Additional flexibility can be achieved by applying basis functions with one quantum number of higher angular momentum than the valence orbitals. This allows for small displacements of the centre of electronic charge. Known as polarisation functions, these are often noted following the standard basis set nomenclature. For instance, 6-31G** (synonymous with 6-31G(d,p)) implies a set of d functions is added to polarise the p functions on first row atoms C, N, O and F, and a set of p functions is added to H and He.[40]

2.5 Azo Dyes

2.5.1 A Brief History of Dye Chemistry

The synthetic dyes we take for granted have only existed for a brief spell of time. Until the middle of the 19th century, colourants for textiles were all derived from natural sources, with the limited knowledge of chemical structure and reactions hampering progress towards synthetic dyes.[1,2] In 1856, whilst attempting to synthesise the anti-malarial drug quinine, William Perkin serendipitously discovered Mauveine. Through the reaction of a sample of aniline with potassium dichromate, Perkin produced a black sludge from which he could extract a purple solution using ethanol. Perkin recognised the potential in this discovery and submitted Mauveine crystals to a silk dyeworks, which reported a rich purple silk with reasonable fastness properties from the dye. After the process was patented, Perkin then went on to investigate a scale-up procedure for producing aniline from the reduction of nitrobenzene, not only providing a method of mass producing the dye, but more importantly kick-starting the organic chemicals

industry.

The most significant discovery following that of Mauveine was made in 1858 by Peter Griess. He demonstrated that the addition of nitrous acid with an aromatic amine yielded an unstable salt which, when reacted with certain chemicals, could be used in the preparation of differently coloured compounds with high tinctorial strengths. That salt was a diazonium salt, and the compounds were based around the dinitrogen (azo) linkage. The diazotisation reaction is singularly the most important discovery in the history of modern dyes as azo dyestuffs constitute such a great proportion of current commercial dyes.

Further progress in this area was significantly hampered since the structure of benzene was yet to be determined. Work performed by Kekulé predicting the ring structure of benzene allowed a great leap forward in both organic and, more specifically, dye chemistry, allowing results from earlier experiments to be interpreted in a new light. General organic chemistry reaped the benefits of this discovery, since chemical synthesis could be designed and conducted systematically with a more informed view of the structures involved. The dye industry indulged heavily in these discoveries.

As a consequence of Perkin's discovery of Mauveine, and the aforementioned discovery of the structure of benzene, a 50 year period allowed work on synthetic dyes to expand rapidly, taking a 90% share of the textile dyes sold. Azo dyes dominated this large share in the market. Since this time, new chromophores have been discovered and added to the textiles dyes market but azo dyes still hold a place on the shelf due to their vast range of colours, cheap synthetic routes and ease of dyeing and wastewater treatment. By the early years of the 20th century these dyes came into general use, enabling the dyer to produce an infinite palette of fast colours.

2.5.2 Synthesis of Azo Dyes

Pioneering work by Griess allowed azo dyes to be prepared through methods that remain in use today. The general preparative route is to react an aryl amine with nitrous acid ($NaNO_2$/HCl), making the unstable salt, prior to reacting it with another aromatic component. This is highlighted in the scheme below. The cheap, readily available nature of the starting materials, coupled with the aqueous nature of the process, allow azo dyes to remain a perfectly viable option in today's advanced dyes market.

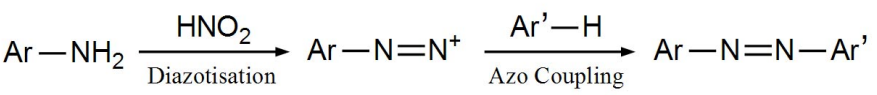

2.5.3 Hydrazo Dyes

Many commercial azo dyes feature a hydroxyl group *ortho* to the azo bond. This allows intramolecular hydrogen bonding with the azo bond, depicted below. The hydrogen bonding can lead to additional stability of the *trans* isomer of the azo dye, limiting unwanted light-driven isomerisation as described in Section 2.5.5.

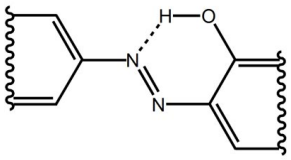

When a hydroxyl group is placed *ortho* or *para* to the azo bond, the effect of conjugation allows the dyes to exhibit tautomerism. Figure 2.9 shows the two possible tautomeric structures for a simple (a) *para* and (b) *ortho* substituted dye. This type of dye is classed as a hydrazo dye since it can take on different tautomers, proportions of which depend on whether the sample is a solid, or on the solvent in which it is dissolved. For 1-phenylazo-2-naphthol (Figure 2.9 b) there is strongly beneficial intramolecular hydrogen bonding in the hydrazone form compared with the azo tautomer leading to a predominance of the former.[2] This is not seen in the *para*-substituted isomer, which provides a good explanation as to why the stability of both tautomers is quite comparable. Interestingly, 3-phenylazo-1-naphthol exists exclusively as the azo tautomer due to instability of the hydrazo form caused by complete loss of naphthyl aromatic character. Furthermore, *ortho* and *para* phenol derived hydrazo dyes do not display tautomerism, the maintenance of conjugation in the phenyl ring being expected to outweigh the stability gain from tautomerism.

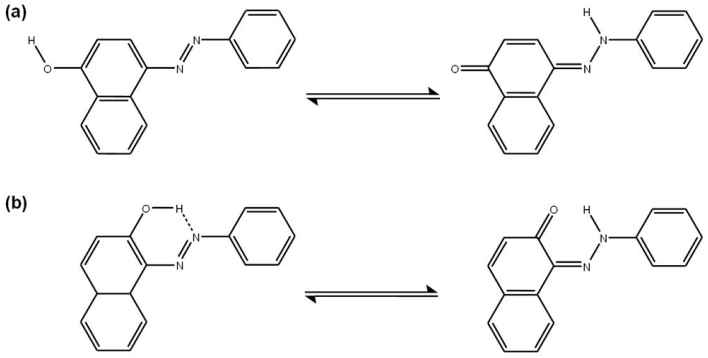

Figure 2.9: Azo, hydrazo tautomers of (a) 4-phenylazo-1-naphthol and (b) 1-phenylazo-2-naphthol.

2.5.4 Reactive Dyes

Reactive dyes, so named because they are engineered to chemically react with a textile material, form a covalent bond between a carbon and a hydroxy, amino, or thiol group on a fibre. Such application methods lead to superior washfastness when compared to traditional forms of dyeing, which rely on physical absorption or mechanical retention of the dye by the fibre. Rattee and Stephen discovered the first method for synthesising reactive dyes in 1954, which led to the introduction in 1956 of the first commercial reactive dyes for ICI.[41] The example shown below is illustrative of a reactive dye.

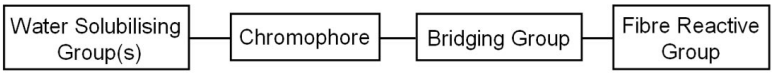

Reactive dyes must be water soluble for the dyeing process and it is often the chromophore that bears solubilising groups for this reason. The chromophore, the group that displays the colour, is then attached to the reactive group *via* a bridging group. For synthetic convenience, this is commonly derived from a terminal amine group to give a –NH– bridge. The first reactive dyes were formed by bonding cyanuric chloride to the chromophore, a successful strategy still widely in use today. This chlorotriazine group is susceptible to nucleophilic attack at the chlorine-bearing carbon atom due to the electron withdrawing nitrogen groups on either side of it.

The addition of the reactive group is what allows the dyes to form a covalent bond with a fibre. A cotton fabric is made up of cellulose chains, the repeating unit of which is shown in Figure 2.10. A reactive dye takes advantage of such a chain by forming a covalent bond with a hydroxyl group, anchoring the dye to the fibre. For this to occur, the activation of the cellulose (Cell–OH) to form Cell–O^- is performed using a mild alkaline solution. The cellulosic anions are nucleophilic and can attack the chlorotriazine group to form a covalent bond with the dye, liberating a chloride ion (Figure 2.11). Alternatively, the dye can be deactivated by the base which is also nucleophilic. Any deactivated dye must be washed away in the dyebase effluent, an environmental concern in itself.

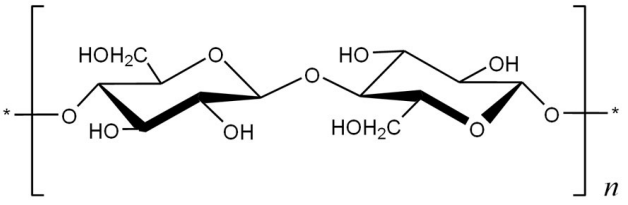

Figure 2.10: Structure of the repeating β-glucose units in a cellulose polymer.

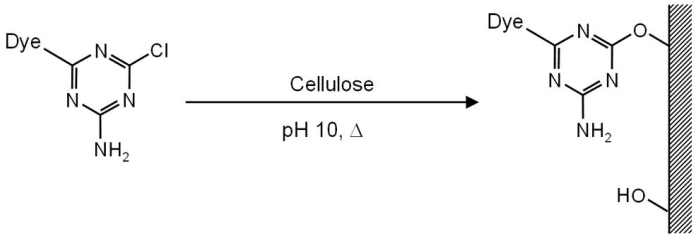

Figure 2.11: Scheme showing the reaction of a chlorotriazine reactive dye with a cellulose chain.

2.5.5 Photochromism of Azo Dyes

Photochromism is defined as the reversible interconversion of a chemical species between two states with different absorption spectra. Azo dyes can exhibit photochromism when they are subjected to light of a suitable frequency. An azo dye may exist as two separate isomers: *trans* and *cis*. The *trans* isomer is the thermally stable isomer. However, absorption of a photon can induce isomerisation to form a *cis* isomer. This geometrical change alters the absorption spectrum, giving rise to a change in colour. The *cis* isomer can also undergo photoisomerisation back to the *trans* isomer. If both the *trans* and *cis* isomer absorb light at the incident frequency, a photostationary state (PSS) where an equilibrium exists between each isomer can be generated. The *cis* isomer also exhibits thermal isomerisation to *trans*, meaning a sample left in darkness will always revert back to 100% *trans* isomer. These processes are summarised in Figure 2.12. An in-depth discussion of the mechanisms involved is conducted within Section 2.7.

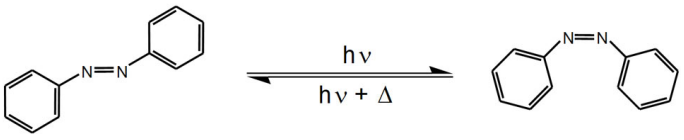

Figure 2.12: Scheme showing photochromism in a molecule of azobenzene.

Although *trans-cis* photoisomerisation is not destructive to the dye molecule since it will inevitably return to the *trans* geometry, it remains a highly undesirable feature. Not only is this problematic in terms of the change in colour, which in some cases may be so subtle as to go almost unnoticed, it is thought the *cis* isomer may be more susceptible to subsequent irreversible degradation effects compared with the *trans* isomer. Over the years, dye manufacturers have been able to minimise the degree of photochromism by engineering dyes that demonstrate a lower percentage of *cis* in the photostationary state, and a rapid rate of thermal decay. Despite engineering these dyes to be less susceptible to photochromism, the effect has not been ruled out fully and remains interesting for investigation through the use of NMR with *in situ* irradiation,

as described in this thesis.

2.5.6 Modern Applications of Azo Compounds

Section 2.5.5 touched on the photochromic nature of azo dyes. Azo molecules have seen a great deal of research invested in them for applications other than as dyes. The fascile geometric isomerisation around the azo bond, coupled with the cleanly reversible nature of the isomerisation, can be exploited to reversibly alter material properties. Studying the changes in the photoswitching and photomechanical response of materials leads towards addressing modern technological problems such as improving optical data storage capabilites. This is highlighted by the sheer number of articles on the subject, many of which have been summarised in review papers.[42–44]

Azo molecules have been incorporated into thin polymer films through doping or the addition of functionalised side-chains,[42–46] and in liquid crystals.[47] They have even been studied on a single molecule level using scanning tunnelling microscopy (STM). By placing the STM tip above a molecule, isomerisation could be induced by the transfer of energy to the molecule.[48] Inscription of polymer films can be initiated through irradiation, causing the free surface to deform as isomerisation takes place which in turn leads to a surface patterning in response to the incident light. The resulting surface relief grating can effectively be 'read' by light. The characteristics of the azo unit used allows the photoresponse of the film to be tuned. As opposed to the chemistry of a textile azo dye where minimal photoisomerisation to the *cis* isomer and rapid thermal reversion from this state are desirable features, functional materials demand the opposite characteristics. Research in the last two decades has strived towards meeting these criteria. One particular example used a film incorporating an azobenzene derivative to demonstrate the application of both photo and electrochemical techniques for high density information storage.[46] After the initial light-driven isomerisation process, the thermally unstable *cis* isomer was electrochemically reduced to a stable hydrazobenzene state. This could in turn be oxidised back to the *trans* isomer.

A number of other methods have been presented to try and combat the problems with thermal stability of the *cis* isomers on films. These usually involve strong hydrogen bonding forces or sterically hindered *cis* isomers in an attempt to limit the thermal reversal. Röttger *et al.* studied azobenzenophane, two azobenzene units linked by a functionalised 3 carbon chain at each end, which demonstrated a one year half-life in the *cis-cis* form.[49] More impressive still, Nagamani *et al.* demonstrated a 6 year half life for the *cis-cis* geometry of a xanthene-based cyclic azobenzene dimer, the system acting as a molecular hinge. Recent creation of azobenzene dendrimers has combatted some of

the problems present when using films, the monodisperse nature allowing precise control of molecular architecture in addition to desirable photoswitching properties.[44,50] One particularly elegant example utilised an azo unit with each end included in a cyclic peptide.[51,52] The *trans* isomers would self-organise through hydrogen bonding of the cyclic peptide rings. Upon isomerisation with UV irradiation, the intermolecular hydrogen bonding would be disrupted, with the *cis* isomer intramolecularly hydrogen bonding between the two available cyclic peptides. The *cis* geometry could be isomerised using visible radiation. This hydrogen bonding leads to a great deal of stability in each of the forms, a strong requirement in any funtional material. A simple diagram of this system is shown in Figure 2.13.

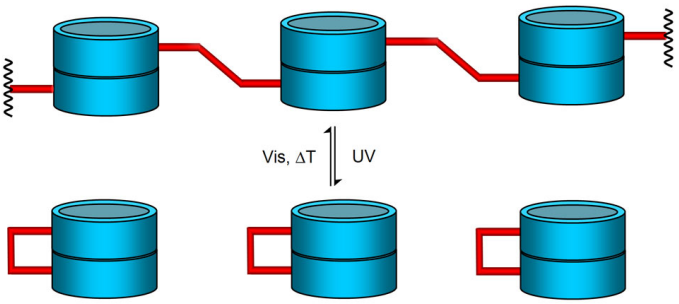

Figure 2.13: Simple representation of the hydrogen-bonded cyclic peptide system.

2.6 UV-Vis Spectroscopy of Azo Compounds

This section discusses the ultra violet and visible (UV-vis) spectra of azo molecules, knowledge of which is essential for understanding the photochemical isomerisation described later. Azo compounds have historically been categorised into three classes, namely azobenzene, aminoazobenzene, and pseudostilbene-type molecules. Spectroscopy of each type is discussed in the following sections.

2.6.1 Spectroscopy of Azobenzene

Two commonly accessible singlet states are present in the *cis* and *trans* isomers of azobenzene, which correspond to two absorption bands in the UV-visible spectrum.[53,54] These are best discussed with reference to the simple Molecular Orbital (MO) diagram shown in Figure 2.14.

The highest occupied, and lowest unoccupied π orbitals are shown, along with molecular orbitals n_a and n_b that represent the non-bonding electrons on each azo nitrogen atom. The π orbital in parentheses is present when a substituent, containing a lone pair of electrons able to conjugate with the delocalised π system, is added to one of the benzene rings.

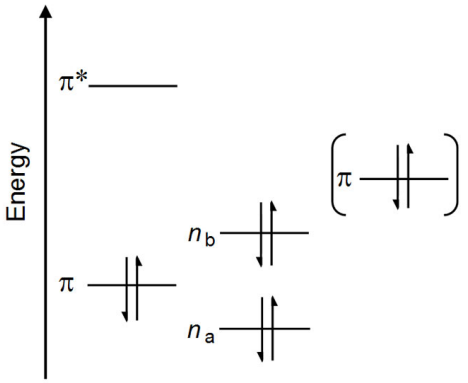

Figure 2.14: Simple illustration of the molecular orbitals of an azo group in azobenzene.[53] n_a and n_b are the lone electron pairs for each azo nitrogen atom. The π orbital in brackets is available when a substituent is present on, and conjugated with, the π-electron system.

The thermally stable (*trans*) isomer of azobenzene displays a low intensity visible band corresponding to a weak $n \rightarrow \pi^*$ transition (λ_{max}=440 nm, ϵ=440 moll^{-1}cm^{-1}).[54] Forber *et al.* reported that the *cis* isomer of azobenzene can be isolated by preparative TLC after irradiaiton of *trans* azobenzene at low temperature, allowing the less stable isomer to be characterised.[55] The $n \rightarrow \pi^*$ transition in the *cis* isomer is higher in intensity compared with the *trans* isomer (λ_{max}=437 nm, ϵ=1100 moll^{-1}cm^{-1}).[55] This lower energy transition is forbidden in the *trans* isomer (*t*-AB, C_{2h} symmetry), but allowed for the *cis* geometry (*cis*-AB, C_2 symmetry), explaining the weaker transition seen for *trans* azobenzene. The reason a band is observed for the *trans* isomer is due to vibronic coupling between the $n \rightarrow \pi^*$ transition and lower lying molecular states. This band is relatively unaffected by phenyl substituents, but a hypsochromic shift is apparent with increasing solvent polarity. The ground state is more polar than the excited state, with polar solvents increasing the ground state stability, raising the energy of the transition and leading to the observed shift in the band.[54]

A higher energy band in the UV region corresponding to the $\pi \rightarrow \pi^*$ transition is seen in both *trans* and *cis* azobenzene (*trans* λ_{max}=316 nm, ϵ=22,000 moll^{-1}cm^{-1}; *cis* λ_{max}=270 nm, ϵ=5,000 moll^{-1}cm^{-1}).[54,55] The pronounced difference in the intensities of the *trans* and *cis* isomer bands is due to non-planarity in the *cis* geometry disrupting conjugation of the π system. The result is an increase in energy in the *cis* isomer π^* orbital compared with the *trans* isomer, creating a higher energy $\pi \rightarrow \pi^*$ transition in the *cis* isomer. In this case, polar solvents stabilise the excited state with respect to the ground state, hence reducing the energy of the transition and producing a bathochromic shift.

2.6.2 Spectrosopy of Aminoazobenzenes and Pseudostilbenes

Aminoazobenzene-type molecules contain a group substituted on a phenyl ring *ortho* or *para* to the azo bond with a lone electron pair in conjugation with the azobenzene π system (see additional bracketed orbital in Figure 2.14). Introduction of this new high energy π orbital reduces the energy of the $\pi \rightarrow \pi^*$ transition, sometimes bringing it into the visible region to swamp the $n \rightarrow \pi^*$ band. The position of the $\pi\pi^*$ band is sensitive to the substituent that has been added. In general, the more electron donating the substiuent, the greater the bathochromic shift that is produced. For example, the energy of the $\pi\pi^*$ band of 4-aminoazobenzene will be greater than that of 4-(dimethylamino)-azobenzene, appearing at a shorter wavelength to that of the alkylamino equivalent. The bathochromic shift of the $\pi\pi^*$ band in the corresponding *cis* isomer is less pronounced since the electron donating groups are unable to fully conjugate across the entire molecule due to disruption of the π system. Azobenzene compounds containing an additional substituent become even more solvent dependent than the parent molecule, increased polarity causing a bathochromic shift in the absorption band.

Naturally, adding another substituent to the molecule will create even greater differences in the spectral characteristics. Pseudostilbene-type molecules are generally 4-(donor)-4'-(acceptor) substituted azobenzene molecules, the electron donating and accepting groups in resonance with the azobenzene π system. This is quite often enough to reduce the energy of the $\pi \rightarrow \pi^*$ transition below that of the $n \rightarrow \pi^*$ transition. The band maximum (λ_{max}) is strongly dependent upon both *para* substituents used. Unsurprisingly, their spectra are equally sensitive to polar solvents, as seen for aminoazobenzenes. This type of molecule is one of the most common types seen in commercial azo dyes.[54] A summary of these classifying structures is given in Figure 2.15.

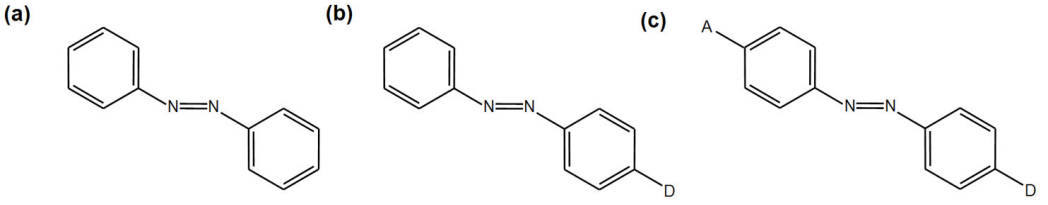

Figure 2.15: Classification of azo molecules: (a) azobenzene, (b) aminoazobenzene and (c) pseudostilbene. A and D represent Acceptor and Donor depending on the interaction with the π-electron system and may be substituted *ortho* or *para* to the azo bond.

2.7 Photochemistry of Azo Compounds

The most energetically favourable conformation of azobenzene is the *trans* geometry and, in darkness, it will always relax back to this form. However, upon irradiation using a suitable source of light, the *trans* isomer may isomerise to a *cis* isomer. This photoisomerisation of azobenzene is reversible, and widely considered to be one of the cleanest photochemical reactions.[53,54] The *trans* isomer is excited by illuminating the sample with a frequency of light corresponding to one of the absorption bands discussed in Section 2.6. Following photo-excitation to an excited state, the molecule will decay non-radiatively to the ground state potential energy surface, relaxing into either the *trans* or the *cis* geometry on S_0. A photo-excited *cis* isomer will decay in a similar manner to the *trans* isomer, again relaxing into either the *trans* or *cis* ground state geometry. A simple diagram of this is shown in Figure 2.16. The higher energy *cis* isomer may also decay thermally to the *trans* isomer. If both isomers absorb radiation incident upon a sample, it is likely that an equilibrium between the rates of each process will be established, otherwise known as the photostationary state (PSS).

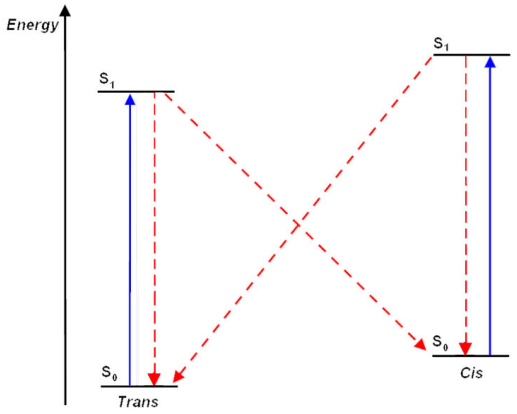

Figure 2.16: Simplified diagram of the excitation and decay routes for the *cis* and *trans* isomers of azobenzene.

The PSS comprises an equilibrium concentration of *trans* and *cis* isomers. The relative composition in this equilibrium is governed by the absorption of the incident radiation by the respective *trans* and *cis* isomers (ϵ_{trans} and ϵ_{cis}), and the quantum yield for the *trans*–*cis* and *cis*–*trans* isomerisation reactions ($\phi_{t\rightarrow c}$ and $\phi_{c\rightarrow t}$). Since this process is entirely intramolecular, sample concentration does not require consideration. By altering the wavelength at which the sample is irradiated, a degree of tuning for the PSS is possible. Irradiaiton in the visible band of azobenzene will produce a photostationary state reported to be composed of between 13 to 25% *cis* isomer.[12,56,57] Irradiation in the UV band, where the *cis* isomer displays a smaller molar absorption coefficient to the *trans* isomer, causes a reverse in the photo-isomerisation characteristics, with reports

of 82-91% *cis* isomer at the PSS.[56,57]

Since photoisomerisation of azobenzene is dominant over any other deactivation route available to the excited molecule, the process must be extremely rapid. The corresponding lifetimes of the first excited singlet state have been reported to be as short as 500 fs.[58] Although photoisomerisation is commonly stated as the only deactivation route available due to the short excited state lifetimes, azobenzene has been found to emit weak fluorescence, measured using steady state and time-resolved techniques.[58,59]

Placing an irradiated sample in darkness will lead to the eventual return of 100% *trans* isomer. This first-order rate is dependent upon the ground state potential energy barrier between the *cis* and *trans* isomers. For the parent azobenzene molecule, thermal *cis-trans* isomeriation is slow, taking approximately 119 hours in benzene.[60] Substituted azobenzenes tend to have more rapid thermal decay characteristics, those substituted with 4-donor-4'-acceptor substituents being extremely rapid. For instance, 4-(diethylamino)-4'-nitro-azobenzene is reported to have a *cis* half life of approximately 23 seconds at room temperature in benzene.[61]

2.7.1 Photoisomerisation Mechanism for Azobenzene

Section 2.1.2.5 commented on the photo-isomerisation mechanism of ethene which proceeds *via* rotation around the C=C bond. The azo functional group can isomerise by another pathway in addition to a torsional route: planar inversion at one of the nitrogen atoms. Each route seems perfectly plausible: rotation around the azo bond involves a reduction in bond order; the in-plane inversion of a phenyl ring at one of the two nitrogen atoms, leads to rehydridisation of an azo-nitrogen and only minor changes in the azo π bond. Both routes are illustrated in Figure 2.17. During the last few decades, this mechanism has been studied at length due to the numerous applications of azo molecules. In spite of the abundant research invested in determining the photo-isomerisation mechanism, the conclusion of many reports remain disparate. Although the majority of present day research is directed towards the use of azo molecules in functional systems (Section 2.5.6), the concepts remain highly relevant to research within the field of textile dyes.

The controversy regarding the mechanism can be summarised in three main points:
(**A**) The observation of different isomerisation quantum yields (ϕ_{isom}) after excitation to the S_1 and S_2 states is a violation of Kasha's rule, which assumes deactivation to the lowest excited state prior to other deactivation processes occuring. Average quantum yields of isomerisation in azobenzene have been reported as $\phi_{t\rightarrow c} = 0.25$, $\phi_{c\rightarrow t} = 0.52$ following S_1 excitation, and $\phi_{t\rightarrow c} = 0.11$, $\phi_{c\rightarrow t} = 0.44$ following S_2 excitation.[62,63]

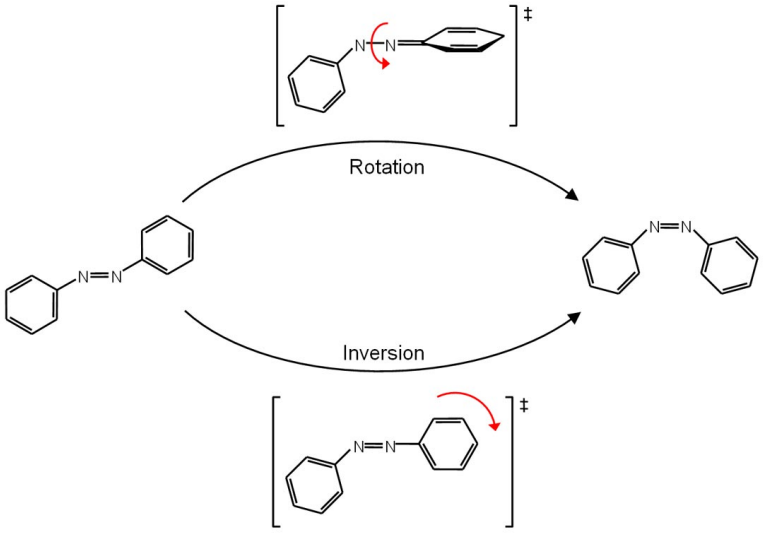

Figure 2.17: The two proposed mechanisms through which azobenzene can photoisomerise.

(**B**) Inhibiting the torsional coordinate by restraining the azobenzene molecule in a cyclophane structure cancels the wavelength dependence seen in point **A**, bringing the ϕ_{isom} from S_2 excitation in-line with S_1.[64]
(**C**) Efficient relaxation of S_2 to S_1 was observed for azobenzene with a planar equilibrium geometry.[58,65]

Many reports have been published containing attempts to explain points **A**-**C** above. The proposal of the two aforementioned mechanisms for photoisomerisation is meant to address point **A**, with inversion or rotation occuring after excitation to different electronically excited states. Inhibition of a rotational channel through incorporation in a cyclophane structure brings equality to ϕ_{isom} following excitation to each excited state, a fact interpreted as S_2 decaying onto the S_1 surface, followed by normal deactivation of S_1. This infers that S_1 deactivation proceeds *via* an inversion channel, satisfying point **C** . The existence of two mechanisms in free azobenzene appears to clarify the inequality in ϕ_{isom} in the excited states (Point **A**).

Early experimental work stimulated the use of quantum chemical calculations to model the ground and excited state potential energy curves for each isomerisation pathway. For a long time, potential energy diagrams of the inversion and torsional coordinates published by Monti *et al.* formed the basis for discussion in this area.[66] Using an early *ab initio* method with configuration interaction (CI), they were able to report calculated potential energy curves for the S_0, S_1 and S_2 states of azobenzene. Because they calculated a significant barrier to torsion on the S_1 curve, and a much shallower curve on the inversion coordinate containing a minimum half way between the *trans*

and *cis* isomers, rotation along S_1 was ruled out for many years in favour of an inversion mechanism. After excitation of each isomer to the S_2 state, only the rotational pathway provides an energetic downhill change, avoided crossings with the S_1 rotational pathway producing a minimum on both the *trans* and *cis* sides. These minima are postulated to undergo a bifurcation, the deactivation channelled 1:1 into the S_1 and S_0 states. This prediction that the S_1 state is partially bypassed correlates well with observations of smaller photo-isomerisation quantum yields ($\phi_{t\rightarrow c}$, $\phi_{c\rightarrow t}$) following S_2 excitation, satisfying point A.[62,63]

Access to experimental information regarding the excited states of azobenzene has recently been accessed through the use of ultrafast spectrosopic techniques. The following studies by Lednev *et al.* provide some support for previous experimental and computational work. The first study employed the use of femtosecond time-resolved UV-vis spectroscopy, observing transient absorptions at 370 to 450 nm.[67] A biexponential function fitted the decay, with fast and slow components (*ca.* 1 ps, 13 ps), which were attributed to the decay of a $^1(\pi\pi^*)$ state, and tentatively to a twisted bottleneck state of $^1(n\pi^*)$ or $^1(\pi\pi^*)$, respectively. The molecule could then decay to the ground state from this bottleneck state, with plausible formation of the *cis* isomer, through at least a partial rotational mechanism. The ground state was attained after 15 ps. Their conclusions supported the earlier studies that an inversion mechanism operates on the S_1 surface following $^1(n\pi^*)$ excitation, and rotation, at least in part, occurs following S_2 excitation. In a second study using the same technique, they examined an azocrown ether-capped azobenzene system where rotation was entirely restricted.[68] Large similarities were observed between the results obtained following UV excitation in this system, and those involving excitation to S_1 (rather than S_2) in azobenzene. The observations led them to suggest extremely fast (< 0.5 ps) internal conversion from S_2 to S_1 was occuring, avoiding the aforementioned bottleneck state and instead following inversion on the S_1 potential. This was taken as clear evidence that rotation occurs in azobenzene following excitation to the S_2 potential energy surface, and that inversion follows excitation to S_1, as predicted by the earlier studies in this area, and supporting point **A**.

Fujino and Tahara performed picosecond time-resolved Raman measurements on *trans*-azobenzene.[65] Observation of a N=N stretching frequency of 1428 cm^{-1} of a 410 nm transient assigned to the vibrationally excited S_1 state was consistent with that observed in the ground state (1440cm^{-1}). They concluded that isomerisation occurs through in-plane inversion of the azo bond, and questioned the rotational pathway. In further studies, Fujino *et al.* examined the time-resolved fluorescence spectra of *trans*-

azobenzene.[58,59] In spite of the very low fluorescence quantum yields, two fluorescence bands were observed, each a mirror image of the respective $S_2 \leftarrow S_0$ and $S_1 \leftarrow S_0$ absorption bands. They were assigned to fluorescence from the S_2 and S_1 states (lifetimes 110 fs and 500 fs respectively). Through comparison of the fluorescence quantum yields, internal conversion from S_2 to S_1 of almost unity was derived. Conclusions from the cited studies indicated a rotational pathway is unlikely to provide a significant contribution to photo-isomerisation, and that photo-isomerisation of azobenzene occurs through an inversion pathway on the S_1 potential, regardless of the initial difference in excitation.

Schultz *et al.* used the alternative methodology of time-resolved photoelectron spectroscopy with molecular dynamics simulations to try and elucidate the mechanism of azobenzene photoisomerisation.[69] They reported two optically bright states, one arising from the short-lived S_2 state, and one exhibiting different relaxation characteristics, ascribed to phenyl ring dynamics and assigned as $S_{3,4}$. They predicted this $S_{3,4}$ state to undergo relaxation that could possibly involve torsion, but back to the *trans*-azobenzene in the ground state. The decay of S_1 following relaxation of S_2 is expected to yield $\phi_{isom} \approx 0.25$ for the population of S_2, which would satisfy Kasha's rule.

Rapid advances in technology over the last two decades, along with improvements in the level of theory at which calculations can be conducted, have allowed computer modelling to become more commonplace amongst research facilities. This has brought with it a recent surge in theoretical work regarding the photoisomerisation mechanism of azobenzene,[70–75] allowing the early theoretical work by Monti,[66] to which many experimental studies refer, to be reviewed. The majority of groups have concentrated on the inversion and torsional pathways,[70–74] although Diau invoked the presence of a concerted inversion pathway.[75] Cattaneo and Perisco predicted that inversion is probably the preferred isomerisation route following S_1 excitation although, in contrast to the findings of Monti *et al.*, the rotational S_1 pathway does not show a significant maximum.[70] However, the majority of theoretical work now supports a rotational mechanism following excitation into S_1. The most recent studies have commented upon existence of a conical intersection between S_1 and S_0 halfway along the torsional potential,[71–73,75,76] leading to proposals that the inversion mechanism is far less likely to occur in S_1. One study backed up the proposed rotational mechanism by reporting a reduction in the calculated azo bond orders of the S_1 and S_2 states. These theoretical results all contradict Fujino's experimental Raman study of azobenzene.[65]

Theories regarding the mechanism of isomerisation following S_2 excitation are also varied and unclear. Ciminelli *et al.* calculated a conical intersection between S_2 and S_1 close to the *trans* azobenzene Franck-Condon region, which would lead to direct

relaxation of S_2 to S_1. Examining the torsional coordinate alone, Gagliardi *et al.* calculated the fourth excited singlet state ($(\pi^2\pi^{*2})$ labelled S_3) which, although high in energy at the Franck-Condon state geometries of the *cis* and *trans* isomers, has a deep minimum that intersects the S_2 and S_1 states.[74] This is expected to provide a fast, radiationless deactivation route for S_2 compared with a vertical transition from S_2 to S_1. Blocking the possibility of rotation in a cyclophane structure has shown the quantum yields following S_2 or S_1 excitation to be the same. In this case, blocking rotation would not allow the S_3 state to be accessed, thus eliminating a second decay pathway and providing a possible explanation of points A and B. Cembran *et al.* investigated this S_3 state, finding it to be higher in energy than Gagliardi reported.[73] Diau proposed an alternative mechanism open to the S_2 state, in the form of concerted inversion. This channel would produce a much higher proportion of *trans* than *cis* isomers, in part explaining the dispute over wavelength dependence of quantum yields.[75] Following up this work, Crecca and Roitberg found this mechanism would only be open to the parent azobenzene, with substituted azobenzenes proceeding *via* rotational pathways instead.[76]

Clearly a great deal of strong and suggestive evidence has been obtained with respect to the photo-isomerisation mechanism of azobenzene. However, groups remain in conflict over the exact mechanism that occurs following excitation. Advances in both experimental apparatus and computational theory have brought with them more advanced proposals that, all or in part, disagree with each other. Elucidation of the mechanism seems closer than ever, and yet just out of grasp. It is a hope that further experimental and theoretical investigations will shortly provide resolution of the controversy regarding the azobenzene photoisomerisation mechanism.

2.7.2 Thermal *Cis-Trans* Isomerisation Mechanism in Azobenzene

Given the controversy regarding the photochemical isomerisation mechanism of azobenzene, it is not surprising that a great deal of debate has been conducted regarding thermal isomerisation of *cis* azobenzene, which follows first order kinetics in homogeneous solution. Both rotation and inversion mechanisms have been proposed based on the varying experimental observations cited within. Groups have mainly used interpretations of the solvent and pressure effects to imply a mechanism, although they often disagree in their theories.

Very early work compared activation energies of *cis-trans* isomerisation in azobenzenes to stilbenes (which undergo exclusive rotation), and concluded the lower activation energies in azobenzenes must be due to a mechanism other than rotation, *i.e.* inversion.[77]

Such a simplistic view with little experimental support is not likely to satisfy most minds, and detailed studies on the mechanism followed. Examining simple azobenzenes, and parent azobenzene covalently linked to an azo-crown ether, Asano *et al.* inferred an inversion mechanism by measuring the activation volumes, $\Delta V^{\ddagger}$.[78] Only minor increases in $\Delta V^{\ddagger}$ were observed for simple azobenzenes, suggesting minimal disruption of the π-system, in-fitting with an inversion route. Sueyeshi *et al.* observed that *ortho* substituted azobenzenes display enhanced rates of thermal isomerisation. Based on the assumption that the rate of isomerisation relative to parent azobenzene should be retarded during rotation, they concluded an inversion mechanism was at work. Nishimura observed an increase in rate with increasing solvent polarity for donor/acceptor azobenzenes and also proposed an inversion route.[79,80] They argued that resonance stabilisation, only possible in the coplanar structures of an inversional transition state, could explain the increase in rate with solvent polarity.

Of course many people advocated the existence of a torsional pathway. Observations of a significant solvent effect on the rate of thermal isomerisation for some donor/acceptor azobenzenes led Wildes *et al.* to suggest the pathway was rotational,[61] the results indicative of a dipolar transition state befitting the reduced azo bond order required for CNNC torsion. In a later study, Schanze *et al.* came to the same conclusion.[81] Asano *et al.* found changes in $\Delta V^{\ddagger}$ with varying solvent polarity and suggested that the mechanism operating in a particular donor/acceptor azobenzene was subject to the effect of the solvent, changing from inversion in non-polar solvents to rotation as the solvent polarity increased.[78,82] In the parent molecule, Asano reported minimal sensitivity to the solvent polarity which was taken to imply inversion.

Naturally, theoretical studies have been conducted to try and shed light on the situation. Much of the current work suggests that an inversion mechanism operates for ground state isomerisation of *cis* azobenzene.[70,71,76] Crecca *et al.* investigated a concerted inversion mechanism on the ground state similar to that proposed by Diau for photoisomerisation,[75] and still concluded normal inversion was occuring.[76] In opposition to these studies, Cembran *et al.* proposed a rotational mechanism.[73] They calculated significant spin-orbit coupling between S_0 and T_1 states, with computed rotational potential energy curves for these two states crossing in the region of the twisted CNNC dihedral angle. This led them to propose the thermal *cis-trans* mechanism proceeds *via* a torsional route through S_0–T_1–S_0 crossing.

In spite of this process being simpler than those involving excited states, thermal *cis-trans* isomerisation remains complex enough to elude determination of a definite mechanism. It is more than likely that the two mechanisms exist, the type accessed depending

upon many variables including solvent properties and substituents. A single mechanism cannot be applied to either thermal or photochemical isomerisation when considering the broad range of systems that can be classed within the aromatic azo category.

Chapter 3

Experimental Methods

3.1 Introduction

This chapter outlines the chemicals, apparatus and procedures used to obtain the results discussed in chapters 4, 5 and 6. These include the use of NMR and UV-vis spectroscopy, the method employed for *in-situ* laser irradiation of NMR samples, and dye synthesis.

3.2 Materials

3.2.1 Solvents

Deuterium oxide (D_2O, Aldrich, 99.9 atom % D), dimethylsulfoxide (DMSO, Aldrich, spectrophotometric grade), d_6-dimethylsulfoxide (d_6-DMSO, Aldrich, 99.9 atom % D) vand water (Fisher, HPLC grade) were all used as supplied.

3.2.2 Chemicals

Anthracene ($C_{14}H_{10}$, Aldrich, 99%), sodium carbonate (Na_2CO_3, Fisons, anhydrous, >99.5%), sulfuric acid (H_2SO_4, Fisher, >98%), hydrochloric acid (HCl, Aldrich, 37%), morpholine (C_4H_9NO, Aldrich, 99+%) and diisopropanolamine ($C_6H_{15}NO_2$, Aldrich, 99%) were all used as supplied. Dye bases 269/52, 271/64, 283/26, 284/43, and reactive dyes 273/5 and 269/56 were supplied by Dr. Warren Ebenezer at DyStar UK Ltd. Other dyes were prepared by the author using the general methods described in Section 3.2.3).

3.2.3 Dye Synthesis

Outlined within this section are the general synthetic routes used for producing the yellow azo dyes studied in Chapters 4, 5 and 6. The reaction mixtures were sampled periodically to monitor reaction progress by HPLC. Products were confirmed by mass spectrometry and NMR spectroscopy. CHN microanalysis was used as a measure of

sample purity, which was taken into account when preparing samples for NMR and UV-vis.

3.2.3.1 Dye Base Synthesis

Sodium nitrite was added to an aqueous solution of the relevant aromatic amine, in all cases a substituted naphthalene ring, at pH 6. The resulting solution was added to a stirred solution of concentrated hydrochloric acid at 1–2°C and pH $\leq$ 2. The now diazotised aromatic molecule was added portionwise to a stirred suspension of the required coupling component in water at 1–2°C and pH 4–5. The resulting dyebase was then precipitated from solution using either sodium chloride or methylated spirits, collected, washed and dried.

3.2.3.2 Preparation of Reactive Dyes from Dye Bases

An aqueous solution of the dye base was added dropwise to a stirred solution of cyanuric chloride in acetone, regulated at pH 6 and a temperature less than 5°C. Once consumption of the dye base had been confirmed, excess aqueous ammonia was added at room temperature to complete the synthesis. The reactive dye was precipitated from solution using either sodium chloride or methylated spirits, collected, washed and dried.

3.2.3.3 Synthesis of Reactive Dyes With a 'Second Leg'

Several of the dyes discussed in Chapters 4 and 5 were modifications of the standard reactive dye structure: instead of the chlortriazine ring terminating with NH_2 an alternative amine group was used. The synthetic procedure follows the same route used for reactive dye preparation (Section 3.2.3.2) to the point of ammonia addition. Then the pH of the solution was raised to 10 using aqueous NaOH under stirring prior to the portionwise addition of the appropriate amine. This essentially gives rise to a 'second leg' on the chlorotriazine ring. HPLC was used to monitor the reaction progress. The product was precipitated from solution using either sodium chloride or methylated spirits, collected, washed and dried.

3.3 NMR Spectroscopy

3.3.1 Spectrometer

A Bruker DMX 500 NMR spectrometer operating at 500.13 MHz (^{1}H) was used to acquire all NMR data presented in this thesis. The spectrometer was equipped with a multinuclear TBI (^{1}H, ^{13}C, X) probehead which, unless otherwise stated in the text, was regulated at 298 K. The probehead was fitted with actively shielded z-gradient coils, capable of delivering pulsed field gradients. The Xwinnmr software package (Bruker,

version 3.6), installed on a PC running linux, was used to operate the spectrometer and process the data.

3.3.2 *In situ* Laser Irradiation

In situ irradiation of NMR samples was achieved using the setup shown in Figure 3.1. The laser source was a continuous wave Ar^+/Kr^+ mixed gas laser (Coherent INNOVA 70C Spectrum) providing lines at 647, 568, 530, 520, 514, 488 and 457 nm along with multiline emission from 351–364 nm. The laser light was coupled into an optical fibre (Elliot Scientific, FT-600-UMT, ⌀ 600 μm) using a lens mounted on a XY translation stage to facilitate alignment. One end of the fibre was connected to this mount via a standard SMA interface while the sample end was prepared with a flat cleave, allowing it to be pushed into the NMR tube. Using a 5 mm screw-capped tube (Wilmad, 528-TR-7) with an o-ring seal it was possible to securely attach and position the optical fibre within the sample (Figure 3.2). Prior to inserting the optical fibre, the transmitted laser power was measured and tuned to 30 mW (unless otherwise stated) using a power meter (Coherent, FieldMate with OP-2 VIS Head) to ensure consistency between sample measurements. Control of sample irradiation was provided by a simple ON/OFF shutter mechanism on the laser.

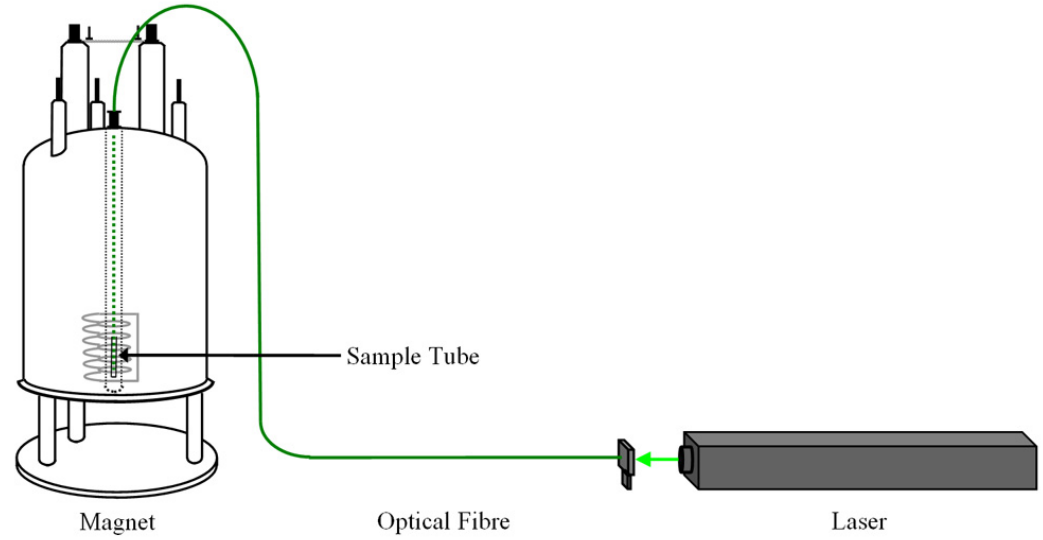

Figure 3.1: Schematic of the apparatus used for *in-situ* irradiation of NMR samples.

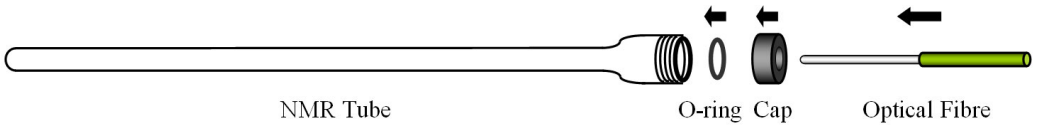

Figure 3.2: Components used to secure the optical fibre within the NMR tube.

3.3.3 Optical Fibre Position

A typical NMR sample consists of 500–600 μl of solution, leading to a sample depth of 5–6 cm in a 5 mm NMR tube. However, the technique requires the sample under observation to be perfectly homogenous. Therefore only a 200 μl region in the centre of the tube is monitored as other areas suffer from inhomogeneities, either from curvature at the base of the tube or surface effects near to the top. The sample section covered by the receiver coils, described as the detection volume, begins 21 mm from the base of the tube and is only 18 mm deep. For the purposes of a normal NMR study it is only necessary to add the correct volume of sample to the tube and run the experiment. In the case of NMR with *in situ* irradiation, especially with respect to ensuring consistency between kinetic measurements, it is vital that the fibre is placed in the same position for each experiment. Often the lifetime of the *cis* isomer is relatively short-lived so diffusion cannot be relied upon to transfer photoproducts into the detection volume. The ideal situation would be to generate new species at the position where they will be observed. Introducing the optical fibre into the detection volume has an adverse effect on the lineshape of the spectrum, caused by sample inhomogeneity. However, placing the optical fibre within the solution so that light exiting the fibre impinges directly on the sample area being monitored, without the optical fibre entering this area, did not appear to affect sample homogeneity as no detrimental effects were observed on the acquired spectra. Moreover, no light is absorbed prior to it reaching the detection volume, as illustrated in Figure 3.3. It was possible to align the optical fibre using a depth gauge.

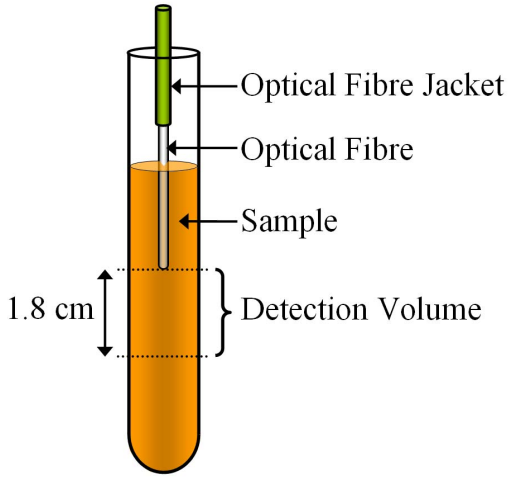

Figure 3.3: Aligning the cleaved end of the optical fibre to the top of the detection volume.

3.3.4 NMR Sample Concentration

For all of the dyes studied under irradiation it was essential to consider the sample concentration, as this is linked to the pathlength of light, i.e. the penetration depth of the laser. The laser had a number of visible lines (Section 3.3.2) but examining these wavelengths in a typical UV-vis spectrum for these dyes reveals strong absorption characteristics. This is unfortunate as the light will almost surely be absorbed around the fibre tip before any species are generated in the detection volume. Considering the Beer Lambert Law (Equation 2.3) which relates absorption to the molar absorption coefficient, sample concentration and pathlength, reveals irradiation must be applied at the long wavelength edge of the spectrum to allow a high enough sample concentration for NMR (minimum 100 μM). At these low concentrations many scans were often necessary to build up an adequate spectrum.

3.3.4.1 Constant Absorption Conditions

To allow comparison of the kinetic data for different dyes, it was critically important to ensure the amount of light irradiating each sample was constant. Each dye exhibited a different molar absorption coefficient at the chosen irradiation wavelength so it was necessary to tune the concentration of the solution using the Beer Lambert Law (Equation 2.2) to guarantee an identical pathlength for each dye. The pathlength of 50% transmission at 2 mm was used for each sample, as designated in previous work by KM Tait.[30] This length allowed photoconversion of the sample within the detection volume, whilst keeping the concentration of each sample within the limits for NMR. By keeping the conditions consistent with the previous studies it was possible to draw comparisons between results within this thesis and those presented by Tait.[30]

3.3.5 Acquisition of NMR Data

Most 1D ^{1}H NMR spectra presented within later chapters are of samples dissolved in d_6-DMSO. As such, it was necessary to suppress the water signal to increase the signal to noise ratio of the other signals in the spectrum. The water signal lies at much lower ppm than the majority of peaks for the aromatic azo dyes studied and therefore high selectivity of this suppression was not required. A simple presaturation pulse sequence was used, centred on the water peak between 3 and 5 ppm, and employing a 90° pulse prior to acquisition. The 1D NMR data were then acquired over a spectral width of typically 15 kHz into 36,000 data points (acquisition time = 1 second, relaxation delay 5 seconds). Most samples needed to be studied at low concentration (0.2 - 2 mM) for irradiation studies. For this reason up to 512 scans were used to collect an FID to give a high quality spectrum. Prior to Fourier transformation and phase correction, the data

were processed using a line broadening function of up to 0.5 Hz.

2D ^{1}H–^{1}H COSY and ^{1}H–^{1}H NOESY data sets were acquired with 16 scans (10 mM sample concentration) into 2048 data points (acquisition time = 0.2 seconds) over a spectral width of 6 kHz centred at 6.0 ppm. 512 t_1 increments were allowed giving a final digital resolution of 5.86 Hz/pt in F1. COSY data were processed using a sine squared window function prior to Fourier transformation in F1 and F2. The NOESY pulse program was phase sensitive (noesyph, Bruker), and the data processed using a shifted sine (cosine) squared window function prior to Fourier transformation.

For the kinetic results presented in Chapter 5 a pseudo 2D NMR pulse program was utilised. This improved the ease of acquisiton and processing of kinetic data. Pseudo 2D data were typically acquired with between 4 and 32 scans per FID, depending on the sample concentration and the rate of the process being measured. Water presaturation was built into this pulse program and the conditions for acquisition of 1D ^{1}H NMR samples were carried over and applied to the F2 dimension. The F1 dimension dictated the number of time increments and hence data points for kinetic fitting. This value was tuned to ensure the kinetic process was monitored to its full extent. The 2D data set was processed in the F2 dimension only, using a line broadening function of up to 0.5 Hz prior to Fourier transformation and phasing. The t1/t2 analysis function within the Xwinnmr package allowed extraction of peak intensity data *vs.* time, where it could then be processed by Microsoft Excel software using an iterative non-linear least squares fitting routine employing the solver function to minimise the sum of squares of the variables.

As the sample tube was coupled directly to the optical fibre, it was impossible to spin the samples in the spectrometer. This did not present a problem with inhomogeneity in the sample as modern probes are capable of recording high quality data without the necessity to spin.

3.4 UV-visible Absorption Spectroscopy

3.4.1 Spectrometer

A Varian Cary 300 UV-visible spectrophotometer capable of measurements from $190-900$nm was used for UV-vis absorption studies. Measurements were made using a matched pair of 10 mm pathlength fused silica cuvettes (Starna) and, unless otherwise specified in the text, regulated at 298 K through use of a peltier unit. The spectrometer was controlled from a PC with the Cary WinUV suite of software installed: spectra were obtained using the 'Scan' application; single point measurements using the 'Ad-

vanced Reads' application. A 2 nm bandwidth and subtraction of background solvent absorption was applied for all measurements.

3.4.2 *Ex-situ* Laser Irradiation for UV-vis Measurements

Where UV-vis measurements of the photostationary state of a dye were required, the sample was irradiated using the laser and optical fibre described in Section 3.3.2. An initial spectrum was recorded in darkness prior to irradiation. To limit any possible solvent evaporation, and hence concentration changes, a PTFE cap was used to cover the cuvette. This cap had a narrow hole drilled in the middle of it allowing the optical fibre to be inserted into the centre of the solution (Figure 3.4). A small magnetic stirrer bar was used to ensure adequate mixing of the sample. After a suitable period of time had elapsed, the sample was transferred (still under irradiation) from the stirrer plate to the UV-vis spectrometer. Following rapid removal of the optical fibre to allow the sample compartment to be closed, the absorption spectrum was recorded. This minimised the length of time and hence decay of the sample between irradiation and measurement. In many cases, single point measurements were conducted at λ_{ex} due to rapid *cis* isomer decay. Using thermal decay data derived from NMR experiments, it was possible to extrapolate a photostationary state molar absorption coefficient for the *cis* isomer from the acquired data (see Section 5.3.5). This was to correct for the time lapse between terminating the irradiation of the sample and taking a measurement, usually on the order of thirty seconds. Although there was often little difference between the measured and corrected values, it ensured a thorough treatment for samples displaying rapid *cis* isomer decay.

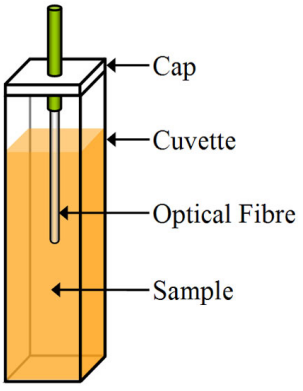

Figure 3.4: Setup used for irradiating UV-vis samples prior to measurement.

3.5 *Ab Initio* Quantum Chemical Calculations

Calculations were performed between a dual Intel Xeon-based PC, and an AMD Opteron-based cluster, each running the Gaussian 03 package[83] under Linux. Ge-

ometry optimisations were conducted by density functional theory using Becke's three paramter exchange functional[38] and the Lee-Yang-Parr correlation functional.[39] Calculations were performed at the 6-31G(d,p) basis set.[40] Every bond length, angle and dihedral angle for each structure was free of constraints and allowed to relax during the optimisation.

To investigate the possible structures for each dye it was necessary to explore the potential energy surface for local minima. This was done through geometry optimisations following the sequential adjustment of one of many possible torsional angles, shown in Figure 3.5. Firstly the torsion τ_{azo} was used to dictate whether the geometry would give a *cis* or *trans* structure, the angles being close to 0° or 180° respectively. Torsions τ_1 and τ_2 specify the orientation of the naphthalene and benzene ring components respectively, τ_3 and τ_4 specify where the chlorotriazine ring is arranged in space and, where applicable, τ_{u1} and τ_{u2} were used to investigate the effect of varying the ureido group orientation. Molecules containing a 'second leg' on the chlorotriazine complicated matters by adding further torsional variables, the number of which being dependent on the substituent under investigation. Each adjustment in to the necessary torsional angle was applied manually to the Guassian 03 input matrix prior to optimisation. Hence, the number of input structures was dependent on the number of torsional angles present in any given structure, increasing the amount of user intervention in the process. It must be stressed that all dihedral angles, including those adjusted, were allowed to relax during the optimisation. Following successful optimisation to a minimum energy geometry, the suitability of a structure was judged by the energy difference. In certain cases it was important to use experimental NMR data to judge the suitability of optimisation when multiple minima close to the global minimum were predicted.

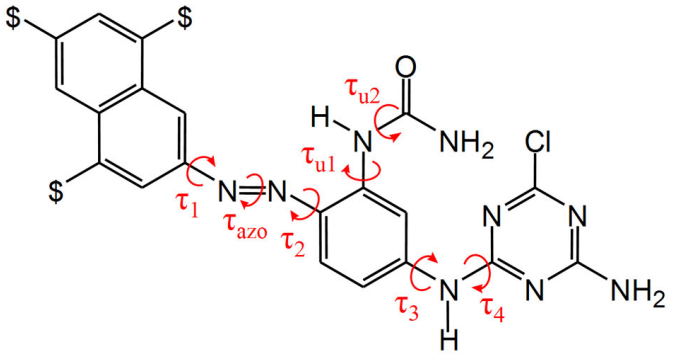

Figure 3.5: Torsions adjusted in search of potential energy minima.

The *cis* and *trans* structures presented later are the lowest energy local minima. Each structure was confirmed as a minimum on the potential energy surface by the absence

of any negative frequencies. The global minimum, a *trans* structure in all cases, was taken as the lowest energy local minimum. In all cases studied, the dyes contained multiple SO_3^- groups to aid solubility. In solution sodium counter ions will be present to balance the charge. The structures derived from the calculation represent an *in vacuo* isolated molecule. In reality, the molecules are solvated. Furthermore, calculations were performed by approximating the sulfonate ($SO_3^+Na^-$) groups to sulfonic acid groups (SO_3H). This strategy has been used in the past and has been shown to provide data more agreeable with experimental results than a charged species (see Section 4.4.1 for further details).[84] For each molecule it was important to ensure this extra proton did not take part in any interactions in the structure. Despite the approximation, the calculated structures demonstrated features highly consistent with the experimental NMR data, validating the approach taken. Structural figures presented in this thesis were created using UCSF Chimera.[85]

Chapter 4

NMR Spectra & Structures of the Photoisomers of a Series of Yellow Azo Dyes

4.1 Introduction

This chapter examines the ^{1}H NMR spectra of a number of sulfonated azo dyes built around a golden yellow chromophore. Studies on analogous dye molecules, structured around this chromophore, have been conducted previously.[30] Although the results were enlightening with respect to the influence of structural changes on the NMR spectra and photoisomerisation kinetics, they were not entirely conclusive. Large differences in the kinetic parameters were identified with minor structural changes to each dye. However, in some cases more than one change was engineered into the dye, making absolute determination of which structural feature impacted most on the photoisomerisation kinetics somewhat ambiguous. Despite this problem, strong conclusions were drawn from the studies.

The prediction that groups adjacent to the azo bond are the biggest culprits for introducing large differences in the photoisomerisation kinetics is a theory that carries well for small dyes. However, some kinetic observations have been made for more complex reactive dyes that seem counter-intuitive.[30] For instance, certain dyes with only minimal changes in the dye structures displayed extreme thermal persistence of photoinduced *cis* isomers, in some cases on the order of days. The use of geometry-optimised calculated structures has assisted explanation of these unexpected kinetic results, often highlighting interactions between two functional groups in the *cis* isomer that are normally remote in the *trans* isomer. Moreover, this chapter relies upon calculated structures to help explain differences in the chemical shift changes between *cis* and *trans* isomer protons in the NMR spectra. For this reason, structural calculations have been conducted for each of the dyes investigated in this chapter.

The pioneering use of NMR coupled with *in situ* laser irradiation for this type of study

investigated simple, disperse monoazo molecules to verify that the technique was suitable to the purpose.[12] Through observation and characterisation of the *cis* isomer, and monitoring thermal decay of the observed *cis* signals back to *trans*, the study proved that reversible *cis-trans* isomerisation was the exclusive photoinduced process occurring. It was a concern that the application of this technique to the more complex reactive dyes would lead to additional photoinduced processes, producing crowded spectra that were difficult to assign unequivocally. Fears were displaced by studies conducted on these yellow azo dyes. The *cis* isomer was observed as the exclusive product of illumination by visible light. Additionally, the proton peaks in both *trans* and *cis* isomers were often well resolved from one another, enabling simple assignment of the spectra.

The dyes studied in this chapter are listed in Figure 4.1. This work has focused upon differences in benzene ring substitution, and the introduction of a 'second leg' onto the chlorotriazine ring. The dyebases, not dyes themselves but precursors to the reactive dyes, are included to examine the effects of adding the chlorotriazine ring to the chromophore. In addition, a new sulfonate group pattern labelled **ACF** in Figure 4.1 has been investigated along with **AC** and **BD** patterns. Engineering these differences into the golden yellow chromophore not only yields important new information, but allows a closer examination of previously published data,[30] effectively filling in some gaps and helping to further our understanding of the impact of structural modifications. In Chapter 5 the kinetic observations are discussed and allow a global comparison of these new data with the previously published results.

The sulfonated reactive dyes have been known to display undesirable photochromic effects when bound to a cellulose substrate. By investigating kinetic differences effected by systematic structural changes, it is hoped that the design strategy of yellow dyes can be improved with a view toward limiting, or eliminating, photochromic behaviour. It is necessary to assign the ^{1}H NMR spectra in order to conduct an investigation of the photoisomerisation kinetics. This ensures that signals corresponding to the *cis* and *trans* isomers are reliably assigned, and that no other processes are occurring in the sample under investigation. Furthermore, the composition of the photostationary state can be determined through measurement of *cis* and *trans* peaks relating to the same proton in a molecule.

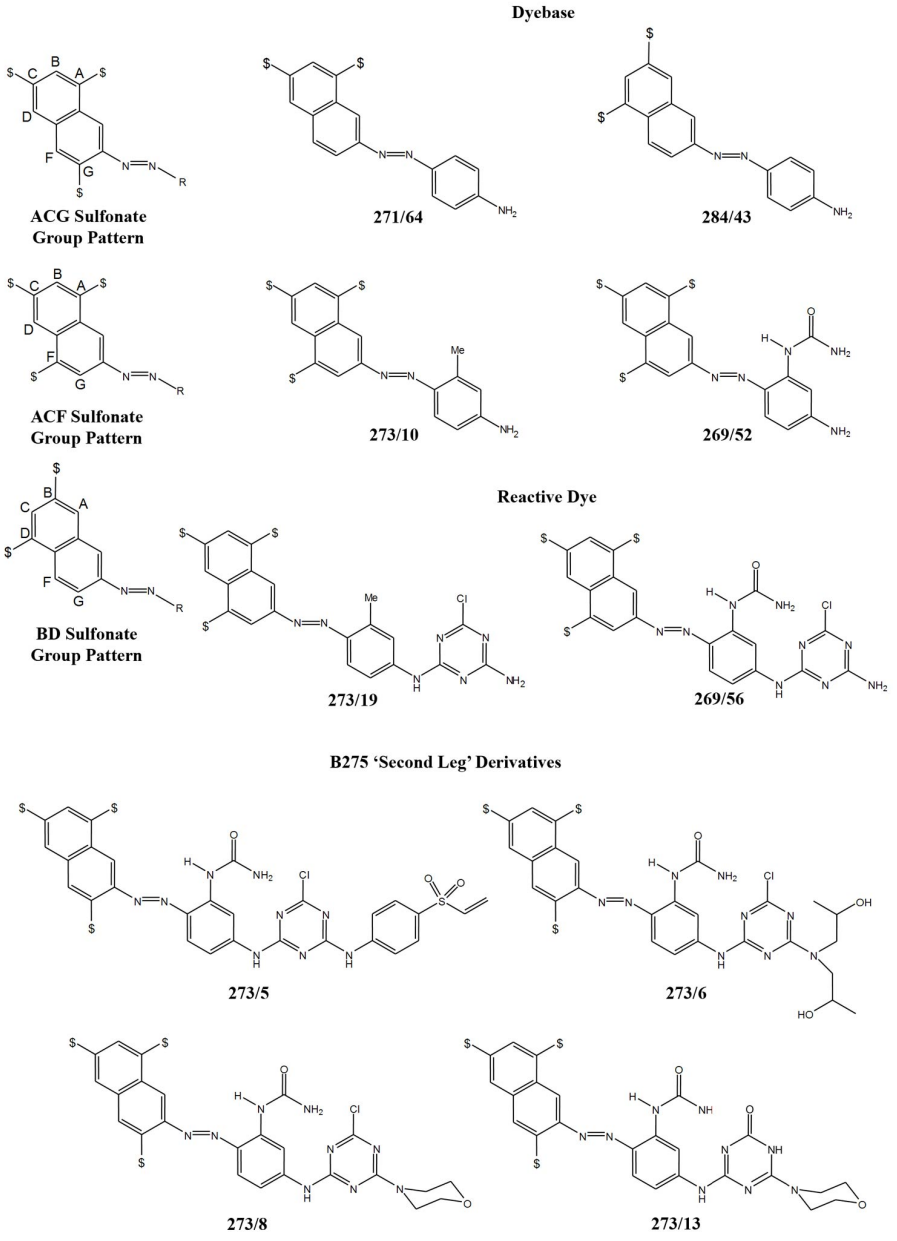

Figure 4.1: *Trans* isomer structures of the yellow azo dye series investigated. $\$=SO_3^-$

4.2 Experimental Conditions

4.2.1 Choice of Solvent

Previous work investigating the *cis-trans* isomerisation of disperse azo dyes utilised non-polar, aprotic solvents to limit the rate of thermal *cis* isomer decay.[12] This is not possible for reactive dyes: they are deliberately designed to be water-soluble in order to make the synthetic and dyeing processes economical. As such, the molecules are very polar and require the use of a polar solvent. Dimethyl sulfoxide (DMSO) was used

due to the exceptional solubility of reactive dyes in this medium. Despite using a dry solvent, the ionic nature of the dyes, along with the preparative routes employed, led to a certain amount of water being associated with the samples, even when oven-dried. ^{1}H NMR spectra of the dyes therefore contained a significant water signal. Since the aromatic region was the interesting zone of the NMR spectra for these dyes, the water peak was selectively supressed to increase the signal to noise ratio of the other peaks. The use of DMSO is consistent with the previous study conducted on these yellow azo dyes, allowing comparisons to be drawn between NMR spectra, and with the kinetic data in Chapter 5.

4.2.2 pH of Dyebase Samples

The dyebases, and sample 273/13 (hydrolysed 273/8), were all isolated under mildly acidic conditions and therefore required a pH adjustment before any isomerisation experiments could be conducted. Prior to each experiment, a 5 μL aliquot of a 0.1 M aqueous solution of Na_2CO_3 was added to the dyebase sample and the pH measured to ensure the conditions were basic. Making this adjustment had no adverse effects on the NMR spectrum.

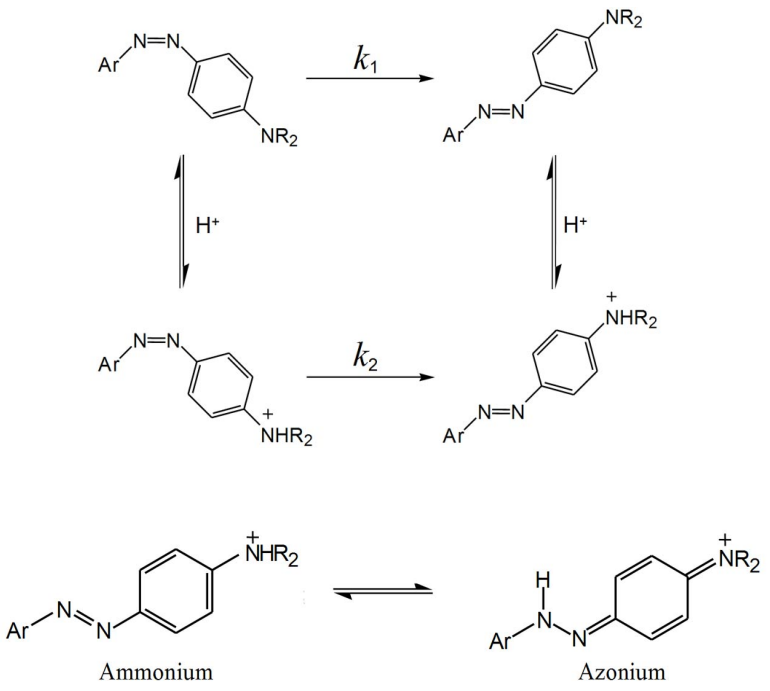

Figure 4.2: The proposed mechanism regarding the effect of pH on thermal *cis-trans* isomerisation.[86]

The necessesity to adjust sample pH in order to observe the *cis* isomer of these dyes was realised by Tait.[30] Isomerisation of the dyes was not observed under acidic conditions.

Furthermore, the presence of *cis* isomers observed to be long-lived was disrupted by altering the sample pH through addition of an aliqout of acidic solution, resulting in rapid thermal decay to the *trans* isomer. A protonated substrate will display tautomerism between ammonium and azonium forms. This tautomeric equilibrium is highlighted in Figure 4.2.2, with a mechanism to explain the observation. In the azonium tautomer, the azo bond will be significantly weaker, facilitating the rapid decay observed experimentally. The barrier to thermal isomerisation is reduced in this tautomer by reducing the pH of the sample, providing a rapid alternative route to thermal isomerisation. Experiments have confirmed that $k_2 \gg k_1$.[86–88]

4.2.3 Selecting a Suitable Irradiation Wavelength

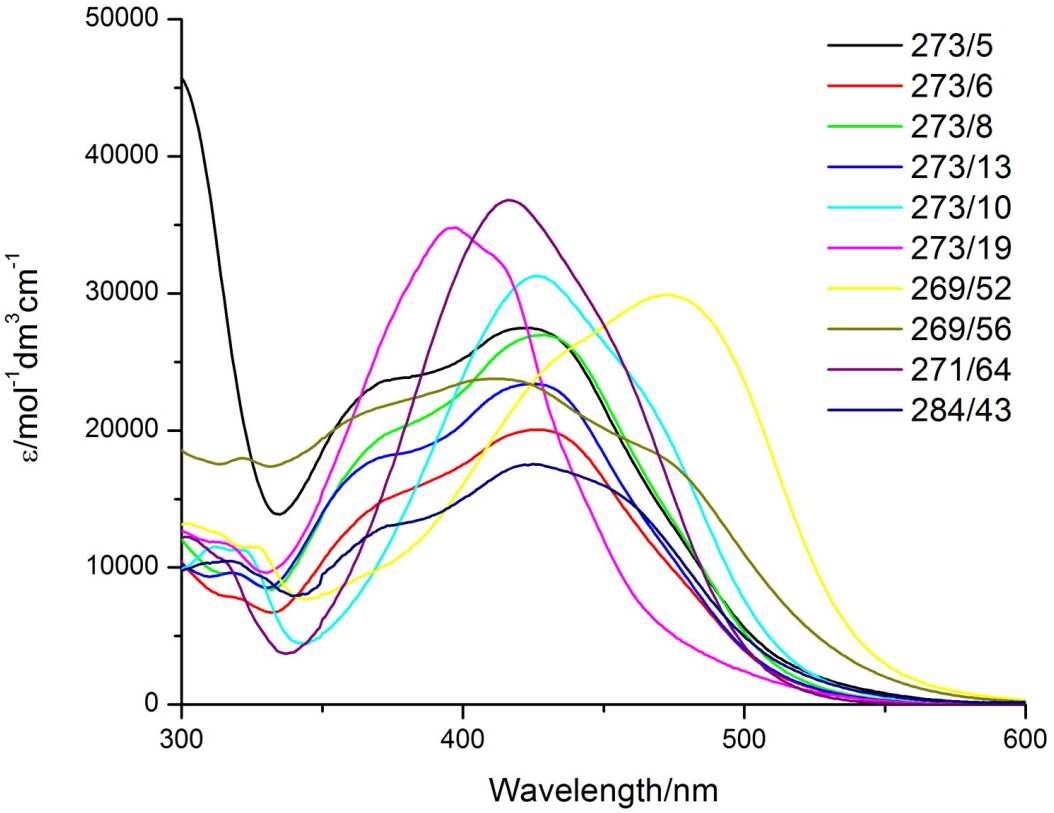

Figure 4.3: The UV-visible absorption spectrum for the *trans* isomers of dyes depicted in Figure 4.1.

Figure 4.3 shows the UV-visible absorption spectrum for each of the dyes depicted in Figure 4.1. As mentioned in Section 3.3.2, a limited number of visible wavelengths are available for use. It was necessary to optimise the concentration of the NMR samples to allow a spectrum of sufficient quality to be obtained while at the same time enabling light to penetrate the sample. For kinetic studies, it was crucial that the same intensity of light was delivered to all samples to allow for rigorous comparison of kinetic data. To meet these criteria, wavelengths on the long-wavelength edge of the absorption

spectrum were used. Table 4.1 summarises the chosen conditions for each dye.

	Irradiation Wavelength, λ_{irr}/nm	Molar Absorption Coefficient, ϵ_{irr}/mol^{-1}lcm^{-1}	Concentration/mM
273/10†	530	1620	0.93
273/19	530	730	2.06
269/52†	530	7950	0.19
269/56	530	4333	0.35
271/64†	530	1522	1.00
284/43†	530	520	2.90
273/5	530	1788	0.84
273/6	530	916	1.64
273/8	530	1073	1.40
273/13	530	930	1.62

Table 4.1: The irradiation wavelengths, molar absorption coefficients at these wavelengths, and calculated NMR sample concentrations for constant absorption. † – dyebase spectra were acquired under basic conditions.

4.2.4 Numbering Scheme for Proton Assignment

The structures examined in this chapter are variations upon a generic yellow azo dye chromophore. They are based upon a naphthyl unit linked to a phenyl group through an azo bond. In the case of dyebases, the benzene ring terminates with an amine group. The reactive dyes are bound to cotton through a chlorotriazine group, normally terminating with an amine. In most cases the benzene ring will be substituted in one position, and the naphthalene unit will carry sulfonate groups to aid water solubility of the dye. In an attempt to make proton numbering consistent between molecules, hence simplifying the comparison of assignments, the numbering scheme in Figure 4.4 was devised. Each position where a proton could theoretically be placed is assigned a number. Hence, in the following assignment section, the numbering of protons will not be continuous, but the same position on analogous structures will have the same number.

4.3 ^{1}H NMR Spectra Before and After Irradiation and Their Interpretation

This section will concentrate on the assignment of the NMR spectra for each of the dyes depicted in Figure 4.1. It is necessary to make the assignments for the dyes investigated to confirm the identity of the molecule under study is correct, and to prove that the *cis* isomer is the sole photo product generated upon irradiation of the *trans*

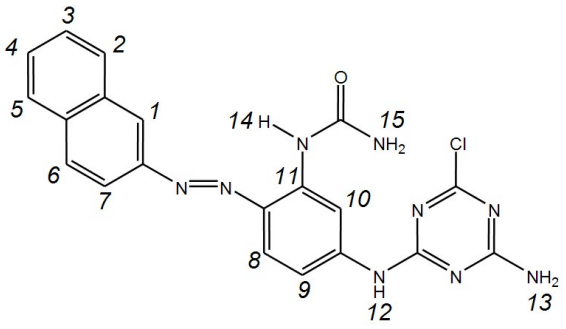

Figure 4.4: The proton numbering scheme imposed onto the general golden yellow azo dye structure to assist comparison of assignments.

sample. Direct measurement of signals relating to the same proton in both the *trans* and *cis* isomers allows the composition of the photostationary state to be measured. An accurate determination of this value is not only useful as a measure of how much *cis* isomer is present, but is vital for use in the isomerisation kinetic studies performed in Chapter 5.

4.3.1 Dyebases 271/64 and 284/43

Dyebases 271/64 and 284/43 are assigned first since they are the simplest molecules studied. Observations relating to the chemical shifts of the *trans* isomer naphthyl group protons allow for an intuitive assignment of the tri-sulfonated naphthyl molecules described in later sections.

4.3.1.1 Assignment of 271/64

Examining the *trans* isomer spectrum of 271/64 in d_6-DMSO (basic), Figure 4.5 (a), eight proton environments, labelled **a**-**h**, can be identified. Signals **a**, **b** and **c** all integrate to two protons, with the remaining signals each integrating to one. Doublets **b** and **c** must form the *ortho* coupled protons of the benzene ring ($^3J_{HH}$ = 8.71 Hz), characteristic of a *para*-disubstituted phenyl group. The electron withdrawing nature of the azo bond will cause the adjacent protons of the phenyl ring to appear at higher ppm than the pair *ortho* the amine group. Hence, peak **c** can be assigned to protons 8/11. As the coupled partner to **c**, peak **b** must belong to protons 9/10 of the phenyl ring. Signal **a** must therefore belong to terminal amine protons 12, its singlet nature indicating the group is able to rotate freely on the NMR time-scale.

The remaining signals must belong to the five protons of the naphthalene ring. Peaks **d** and **e** show vicinal coupling to one another ($^3J_{HH}$ = 9.16 Hz) and must comprise protons 6 and 7. Since signal **d** shows additional fine-structure of 2.29 Hz it must be assigned to proton 7, which is expected to couple with *meta* proton 1. Therefore **e** is

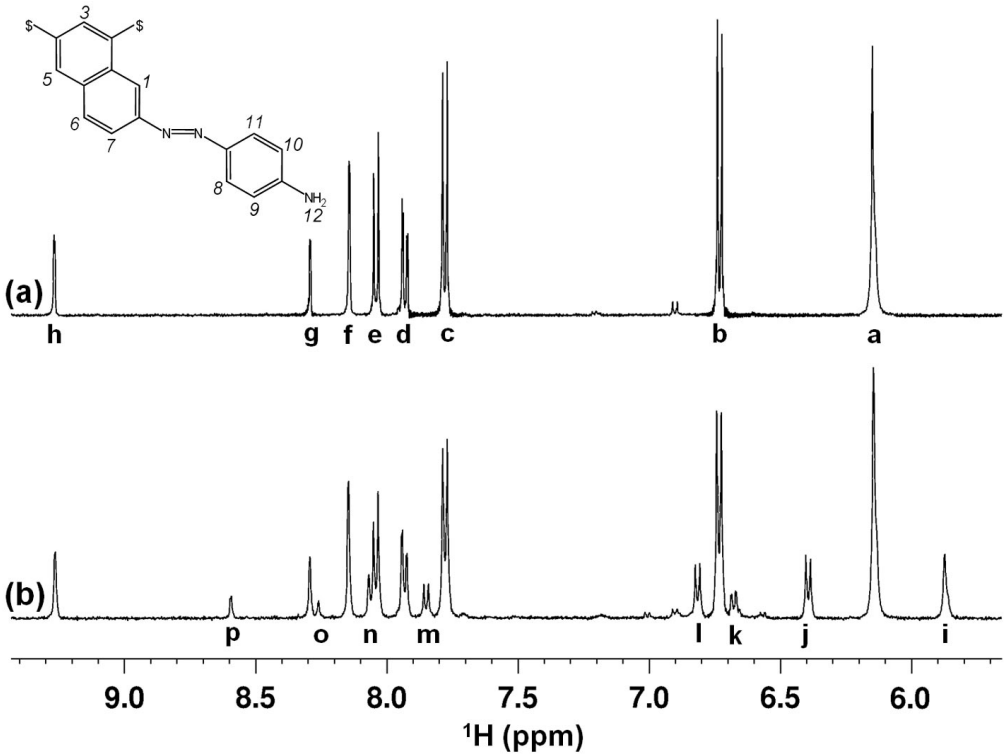

Figure 4.5: The ^{1}H NMR Spectra of 271/64 (1.00 mM) in d_6-DMSO (a) prior to irradiation and (b) during irradiation at the 530-nm PSS.

proton 6. The most deshielded signal, **h**, must belong to proton 1 due to its location adjacent to the azo bond compared with the other possible candidates, **f** and **g**, which belong to protons 3 and 5. Peak **g** displays *meta* coupling, but peak **f** instead displays a slightly broad top to the peak. This loss of fine-structure is often apparent for peaks demonstrating small coupling constants. The combined electron withdrawing effects of the **A** and **C** sulfonate are likely to produce a signal for proton 3 at slightly higher ppm than that for proton 5. For this reason proton 3 is assigned to signal **g** and proton 5 to remaining signal **f**.

Figure 4.5 (b) is the 530-nm photostationary state spectrum of 271/64, recorded after a sufficient period of continuous irradiation to guarantee an equilibrium was present. In addition to the assigned *trans* signals of Figure 4.5 (a), a further eight photo-induced signals labelled **i-p** are present. As with the *trans* signals, three *cis* signals (**i**, **j** and **l**) integrate to twice those of the other five. Singlet **i** may confidently be assigned to amine protons 12 forming a *cis*/*trans* pair with peak **a** ($\Delta\delta$ = 0.28 ppm). Coupled peaks **j** and **l** ($^{3}J_{HH}$ = 8.71 Hz) belong to protons 8/11 and 9/10. Since the *cis* isomer proton is always expected to be more shielded than the *trans* proton, **c** and **l** must form a *trans*/*cis* pair ($\Delta\delta$ = 0.96 ppm). This leads to the assignment of **b** and **j** as *trans*/*cis* a pair ($\Delta\delta$ = 0.34 ppm). These assignments tie in with theory as the protons *ortho* to the azo bond are expected to demonstrate the greatest difference in chemical shift.

Cis peaks **m** and **k** show vicinal coupling ($^3J_{HH} = 9.16$ Hz) confirming them as napthalene protons 6 and 7. With additional coupling of 2.29 Hz, signal **k** can be paired with *trans* peak **d** as proton 7 ($\Delta\delta = 1.25$ ppm). As a result, **e** and **m** can be paired together as proton 6 ($\Delta\delta = 0.19$ ppm). The remaining three peaks may easily be assigned on the principle that no *cis* peak will appear with a larger chemical shift than the *trans* equivalent. Therefore **h** and **p**, **g** and **o**, and **f** and **n** form *trans*/*cis* pairs for protons 1, 3 and 5 respectively ($\Delta\delta = 0.68$, 0.03, 0.08 ppm respectively), each assignment supported by the expected changes in chemical shifts, and fine-structure displayed by the peaks. Using the integrals from selected *trans*/*cis* pairs it is possible to measure the photostationary state composition as 22% *cis* . The *cis* and *trans* isomer assignments are listed in Table 4.2.

Trans Signal	*Cis* Signal	Proton Assignment	$\Delta\delta$/ppm
a	i	12	0.28
b	j	9/10	0.34
c	l	8/11	0.96
d	k	7	1.25
e	m	6	0.19
f	n	5	0.08
g	o	3	0.03
h	p	1	0.68

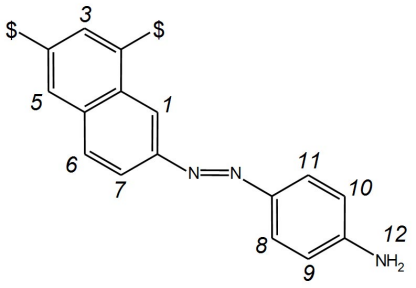

Table 4.2: ^{1}H NMR assignments for the *trans* and *cis* isomers of 271-64 in d_6-DMSO, and the difference in chemical shift between *cis* and *trans* isomers, $\Delta\delta$.

4.3.1.2 Assignment of 284/43

Figure 4.6 (a) is the *trans* isomer spectrum of dyebase 284/43 in d_6-DMSO (basic). Eight signals, labelled **a**-**h**, are observed. All peaks integrate to one proton equivalent, apart from **a**-**c**, each of which integrates to two protons. Singlet **a** must belong to protons 12 since doublets **b** and **c** show *ortho* coupling characteristic of the benzene ring protons. The more electron withdrawn peak **c** is assigned to protons 8/11 *ortho* to the azo bond, indicating protons 9/10 must be represented by peak **b**. Signals **d** and **h** demonstrate *ortho* coupling characterisitcs of protons 6 and 7 of the naphthalene ring. Peak **d** displays *meta* coupling of 1.83 Hz in addition to the *ortho* coupling and can be reliably assigned to proton 7, leaving peak **h** to be assigned as proton 6. Of the three remaining signals, only **g** shows any sign of splitting with a *meta* coupling constant of 1.83 Hz. The two remaining signals, **e** and **f**, do not demonstrate coupling. This indicates signal **g** to belong to proton 1, coupled with proton 7. Although the difference

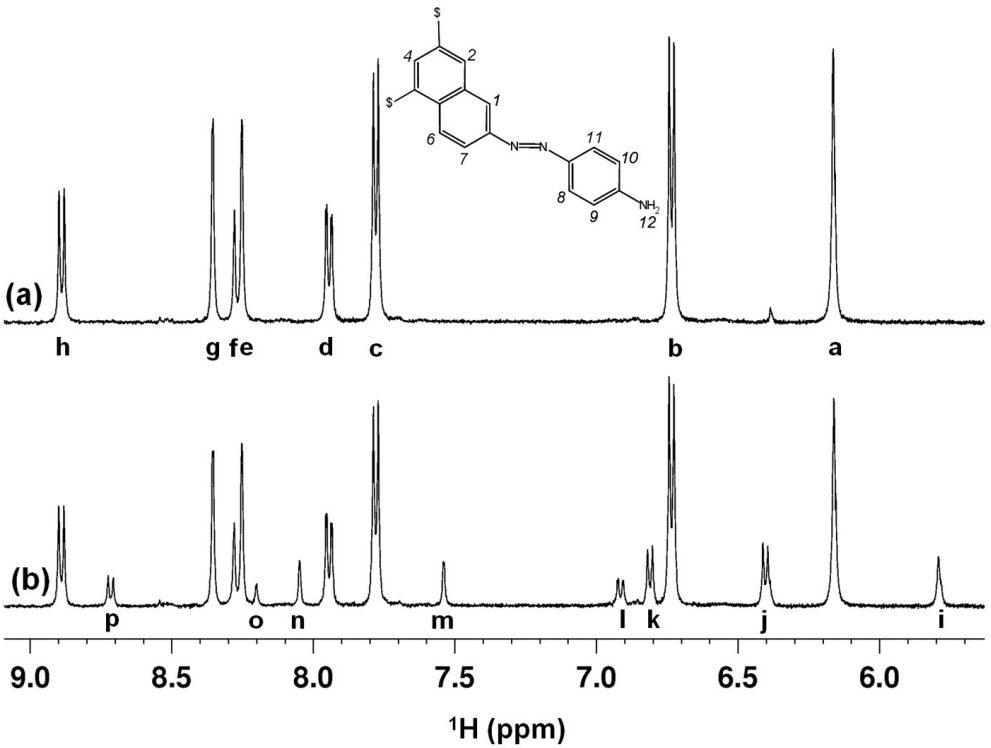

Figure 4.6: The ^{1}H NMR Spectra of 284/43 (2.90 mM) in d_6-DMSO (a) prior to irradiation and (b) during irradiation at the 530-nm PSS.

is marginal, it is anticipated that the combined electron withdrawing effect of the two sulfonate groups would cause proton 4 to have a higher chemical shift to proton 2. For this reason, signal **f** is assigned to proton 4 and **e** to proton 2.

Figure 4.6 (b) is the photostationary state spectrum of dyebase 284/43, irradiated at 530 nm. Eight new peaks labelled **i-p**, in addition to those identified as *trans* isomer signals, are apparent for the *cis* isomer of 284/43. Due to its intensity, multiplicity, and location as the only peak more shielded than *trans* **a**, **i** can be assigned to amine protons 12 ($\Delta\delta = 0.37$ ppm). Doublets **j** and **k**, at twice the intensity of the remaining *cis* isomer peaks, must belong to the benzene ring protons. Since no *cis* peak is expected to show a shift to a greater chemical shift than its *trans* partner, **j** can be reliably paired with **b** as protons 9/10 ($\Delta\delta = 0.34$ ppm), and **k** with **c** as protons 8/11 ($\Delta\delta = 0.97$ ppm). The greater magnitude of the chemical shift change for protons 8/11 is consistent for protons directly adjacent to the azo bond. Using a similar strategy for assignment, doublet **p** must be paired with peak **h** forming the *trans*/*cis* pair for proton 6 ($\Delta\delta = 0.18$ ppm). The coupling partner of this *cis* doublet, peak **l**, demonstrating an additional 1.83 Hz *meta* coupling, can be assigned with *trans* peak **d** as proton 7 ($\Delta\delta = 1.03$ ppm). The *trans* protons represented by peaks **e** and **f** are not close to the point of greatest geometry change upon isomerisation. Therefore, they are not expected to demonstrate

a great deal of difference in the *cis* isomer, and can be paired with *cis* peaks **n** and **o** respectively, the relative peak shape providing a clue to the assignments ($\Delta\delta = 0.20$ and 0.08 ppm). The final peak to be assigned, **m**, must pair with peak **g** as proton 1, peak fine-structure supporting this observation ($\Delta\delta = 0.81$ ppm). Using the integrals from selected *trans*/*cis* pairs it is possible to measure the photostationary state composition as 21% *cis* . The *cis* and *trans* isomer assignments are listed in Table 4.3.

Trans Signal	*Cis* Signal	Proton Assignment	$\Delta\delta$/ppm
a	i	12	0.37
b	j	9/10	0.34
c	k	8/11	0.97
d	l	7	1.03
e	n	2	0.20
f	o	4	0.08
g	m	1	0.81
h	p	6	0.18

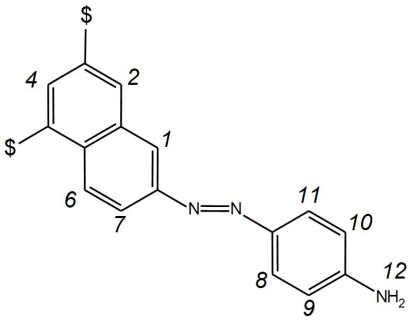

Table 4.3: ^{1}H NMR assignments for the *trans* and *cis* isomers of 284-43 in d_6-DMSO, and the difference in chemical shift between *cis* and *trans* isomers, $\Delta\delta$.

4.3.1.3 Discussion of *Trans* Isomer Naphthyl Assignments

The assignment of the naphthyl group protons for the *trans* isomer of each dyebase provides a significant amount of detail regarding the effect of sulfonate group position on proton chemical shift. Due to the *ortho* and *meta* coupling observations, protons 1, 6 and 7 can be unequivocally assigned for each molecule. Observations made for the chemical shifts of these protons assist with assignment of the tri-sulfonated dyes studied herein. Figure 4.7 (a) and (b) shows the chemical shifts for the *trans* isomer naphthyl protons in both the **AC** and **BD** sulfonated dye.

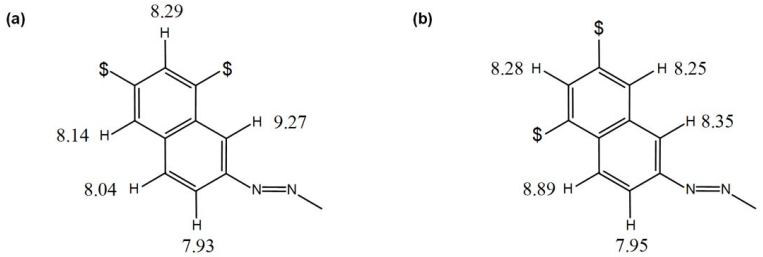

Figure 4.7: **AC** and **BD** sulfonated naphthyl groups for dyebases (a) 271/64 and (b) 284/43. Protons are labelled with *trans* isomer chemical shifts. \$=SO_3^-.

Despite its position adjacent to the azo bond, proton 7 demonstrates the lowest chemical shift in each case, the position of the two sulfonate groups showing minimal influence on

this proton environment. Proton 1 does show a dependence on the sulfonation pattern. In the **AC** molecule, the chemical shift is the greatest of the five protons. However, movement of the **A** sulfonate to the **B** position has the effect of reducing the chemical shift of proton 1 by approximately 1 ppm. Moreover, the movement of sulfonate **C** to **D**, causes an increase of 0.85 ppm in proton 6 on the adjacent ring, inducing the largest chemical shift in the **BD** dye. This suggests the location of a sulfonate group in the **A** position causes deshielding of proton 1, with the **D** sulfonate having the same effect on proton 6. This effect is greater than the electron withdrawing effect of an *ortho* sulfonate. It is conceivable that a sulfonate in the 1 or 6 proton position would affect the respective 2 and 5 protons in a similar manner.

The proton located between the two sulfonate groups does not show a significant change in chemical shift between the **AC** and **BD** dyes, the local effect of the sulfonates appearing more important. This is reflected when it changes to the *cis* geometry, this proton demonstrating the smallest $\Delta\delta$ each time, presumably because of the surrounding sulfonate groups and its situation so remote from the azo bond.

The information gathered from analysis of the changes in *trans* isomer chemical shift with respect to sulfonation patterns **AC** and **BD** can be effectively applied to the **ACF** and **ACG** sulfonate patterns discussed later in this section.

4.3.2 Dyebase 273/10 and Reactive Dye 273/19

4.3.2.1 Assignment of 273/10

The spectrum of dyebase 273/10 (basic) presented in Figure 4.8 is assigned first, because it has a simpler ^{1}H NMR spectrum when compared to the corresponding reactive dye 273/19. Examining Figure 4.8 (a), the spectrum of the *trans* isomer, it is clear the molecule gives a clean spectrum containing separate and well resolved signals for each of the 8 different proton environments. With the exception of peak **a**, all signals integrate to one proton equivalent. Signal **a** integrates to two protons and can therefore be assigned to protons 12 of the NH_2 group. The sharp singlet nature of this peak implies the group is freely rotating on the NMR timescale.

The benzene ring protons display distinctive splittings allowing simple assignment of these peaks. Signal **b** is a double doublet that shows *ortho* coupling of 8.71 Hz and *meta* coupling of 2.29 Hz. It must therefore be assigned to proton 9, *ortho* to proton 8 and *meta* to proton 10. Signal **d** is a doublet with a coupling constant of 8.71 Hz, a splitting that could only be produced in this molecule from vicinal coupling of proton 8 with 9. Hence **d** is assigned to proton 8. The coupling between signals **b** and **d** is confirmed by a 500 MHz 2D [^{1}H, ^{1}H] COSY NMR spectrum (data not shown). Peak

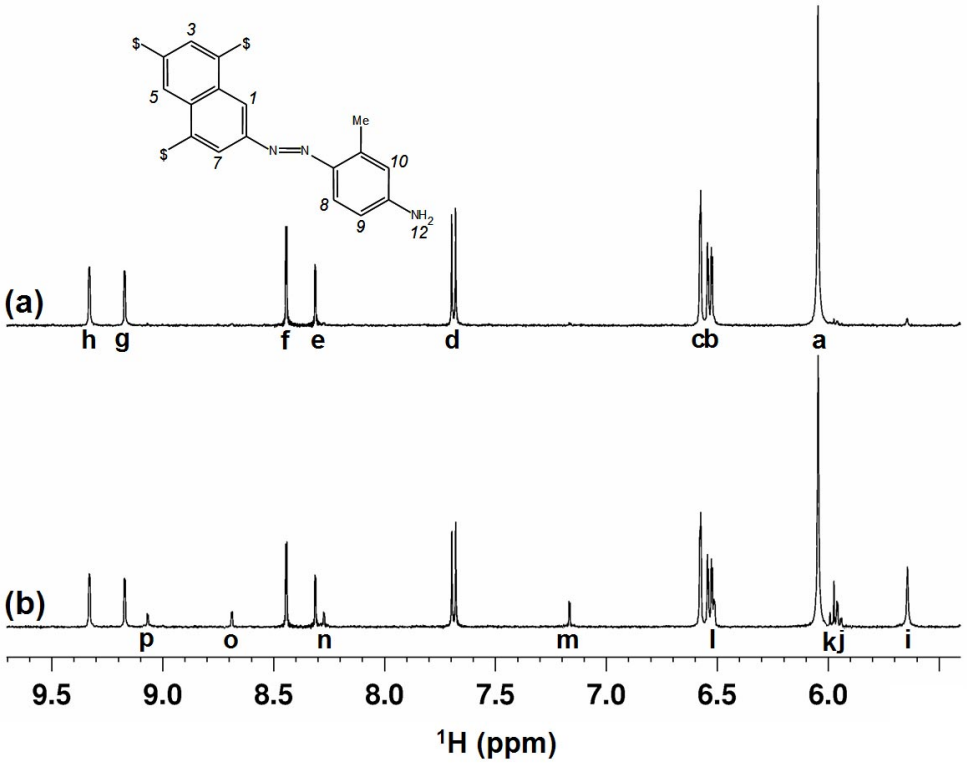

Figure 4.8: The ^{1}H NMR Spectra of 273/10 (0.93 mM) in d_6-DMSO (a) prior to irradiation and (b) during irradiation at the 530-nm PSS.

c is the only signal to display a *meta* coupling constant of 2.29 Hz, this value being a clear indication that it is proton 10.

Signals labelled **e**, **f**, **g** and **h** form the characteristic pattern of protons on a naphthalene ring substituted in this manner.[89] Assignment of these signals is not as straightforward as those examined thus far. A 500 MHz 2D [^{1}H, ^{1}H] COSY NMR spectrum of the *trans* isomer gives weak crosspeaks betweeen signals **h** and **f**, and between **g** and **e**. Signal **h** is the most deshielded proton of the naphthalene ring. Observations made regarding the **AC** and **BD** sulfonation pattern assist in assigning peaks **f** and **h** to the correct protons. When a sulfonate group is present in the **A** or **D** position, the nearest proton on the adjacent ring experiences further electron withdrawal relative to when a proton is present in place of that sulfonate. Hence, proton 1 is expected to display a higher ppm value than proton 7, despite the sulfonate group adjacent to proton 7. Therefore, proton 1 is assigned to signal **h**. It follows that signal **f**, demonstrating *meta* coupling ($^4J_{HH}$ = 1.83 Hz) to signal **h**, is assigned to proton 7. Signals **e** and **g** remain. Of the two peaks, **e** displays a 1.83 Hz *meta* coupling constant whilst, although precedent suggests it should, **g** does not show *meta* coupling. Coupling of nuclei results in broadening of the signals involved, and for signal **g** this appears to prevent observation of any finestructure. Since the presence of an **A** or **D** sulfonate is

expected to increase electron withdrawal of protons 1 or 6 respectively, addition of a sulfonate group in the **F** position should be expected to affect proton 5 on the adjacent ring to a similar extent. In 271/64, protons 3 and 5 display very similar chemical shifts in the *trans* isomer. A difference of 0.9 ppm between protons 3 and 5 is present following addition of a sulfonate in the **F** position. This almost certainly identifies signal **g** as proton 5. The remaining naphthalene signal **e**, which displays a chemical shift comparable to protons 3/5 in 271/64 and therefore only a small dependence on the **F** sulfonate introduced in 273/10, can be assigned to proton 3.

Figure 4.8 (b) is the ^{1}H NMR spectrum of the 530-nm photostationary state of 273/10 in d_6-DMSO. It was recorded after a sufficient period of continuous irradiation had been applied to the sample to ensure equilibrium existed between the *cis* and *trans* isomers. Eight *cis* isomer signals, labelled **i**–**p**, can be identified. Hence, all *cis* signals are accounted for. Each *cis* signal integrates to one proton equivalent, with the exception of signal **i**, which integrates to two. Peak **i** can be assigned to protons 12 of the NH_2 group in the *cis* isomer, with a difference in the chemical shift between *cis* and *trans* signals, $\Delta\delta$, of 0.41 ppm. As with the *trans* isomer, the *cis* signal is a singlet demonstrating the protons are equivalent on the NMR timescale. The double doublet character of signals **j** and **b** make it possible to assign them as a *cis*/*trans* signal pair ($\Delta\delta = 0.58$ ppm). Likewise, through coupling constants, signal **k** can be assigned as the *cis* partner to *trans* **d** ($\Delta\delta = 1.71$ ppm). *Meta* coupling of 2.29 Hz implies that signals **c** and **l**, partially overlapping with double doublet **b**, form a *trans*/*cis* pair, assigned to proton 10 ($\Delta\delta = 0.07$ ppm).

The four *cis* signals from the naphthalene ring remain to be assigned. Previous studies[12,30,90] demonstrate that the protons adjacent to the azo linkage are most likely to experience the largest change in chemical shift between *cis* and *trans* isomers on account of the new geometry placing the protons in a significantly different shielding environment. This has already been observed in 273/10 for proton 8 ($\Delta\delta = 1.71$ ppm). All current research has reported the *cis* isomer protons to appear at lower ppm than the *trans* protons, making it unlikely that we will see any *cis* isomer peaks with larger chemical shifts than the *trans* equivalents.[12,30,90] For this reason it is clear that **o** and **p** must derive from *trans* peaks **g** and **h**. The *cis*/*trans* chemical shift difference in proton 1, adjacent to the azo bond, will be decidedly greater than that of proton 5. For this reason *trans* signal **h** is paired with *cis* peak **o** ($\Delta\delta = 0.64$ ppm). Assigned by default, **g** and **p** must form a *trans*/*cis* pair for proton 5 ($\Delta\delta = 0.11$ ppm). The two remaining *cis* signals, **m** and **n**, belong to protons 7 and 3 of the naphthalene ring. The greatest $\Delta\delta$ of the two will be observed for proton 7, *ortho* to the azo bond, and there-

fore signals **f** and **m** can be associated as a *trans*/*cis* pair ($\Delta\delta$ = 1.27 ppm). Through elimination of all other assignments, *trans* signal **e** and *cis* signal **n** form the final pair ($\Delta\delta$ = 0.04 ppm). The methyl group present in the aliphatic region of the spectrum (not shown) also undergoes a change in the chemical shift induced by isomerisation ($\Delta\delta$ = 0.16 ppm). Using the integrals from selected *trans*/*cis* pairs it is possible to measure the photostationary state composition as 22% *cis*. The *cis* and *trans* isomer assignments are listed in Table 4.4.

Trans Signal	*Cis* Signal	Proton Assignment	$\Delta\delta$/ppm
a	i	12	0.41
b	j	9	0.58
c	l	10	0.07
d	k	8	1.71
e	n	3	0.04
f	m	7	1.27
g	p	5	0.11
h	o	1	0.64
Me	Me	Me	0.16

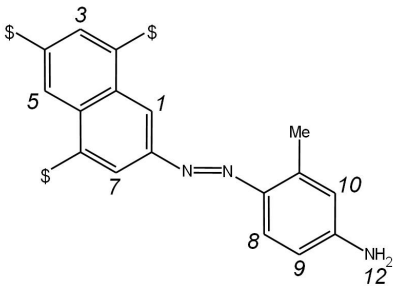

Table 4.4: ^{1}H NMR assignments for the *trans* and *cis* isomers of 273/10 in d_6-DMSO and the difference in chemical shift between *cis* and *trans* isomers, $\Delta\delta$.

4.3.2.2 Assignment of 273/19

Figure 4.9 is the ^{1}H NMR spectrum of reactive dye 273/19 in d_6-DMSO, (a) before and (b) during irradiation at the 530-nm PSS. Nine proton environments labelled **a**-**i**, are observed for the *trans* isomer in Figure 4.9 (a). Signals **e**, **f**, **g** and **h** form the recognisable naphthalene substitution pattern noted for 273/10. From the previous assignment of 273/10, it is possible to assign signal **e** to proton 3, signal **f** to proton 7, signal **g** to proton 5 and signal **h** to proton 1. To support this assignment, signals **f** and **h** demonstrate a 1.83 Hz *meta* coupling. Although signal **e** shows the same *meta* coupling, its expected *meta* coupled partner **g** does not, instead showing broadening at the top of the peak, most probably from line broadening associated with the *meta* coupling.

Signal **a** is a very broad singlet, integrating to two protons. The only possible assignment could be protons 13 of the terminal amine. The broad nature of the peak suggests a degree of exchange with water to be occurring, and could also indicate the rotation of the group as slow on the NMR timescale. Signals **b** and **c** are beginning to merge, showing a distortion typical for NMR of a coupled AB system. Closer examination

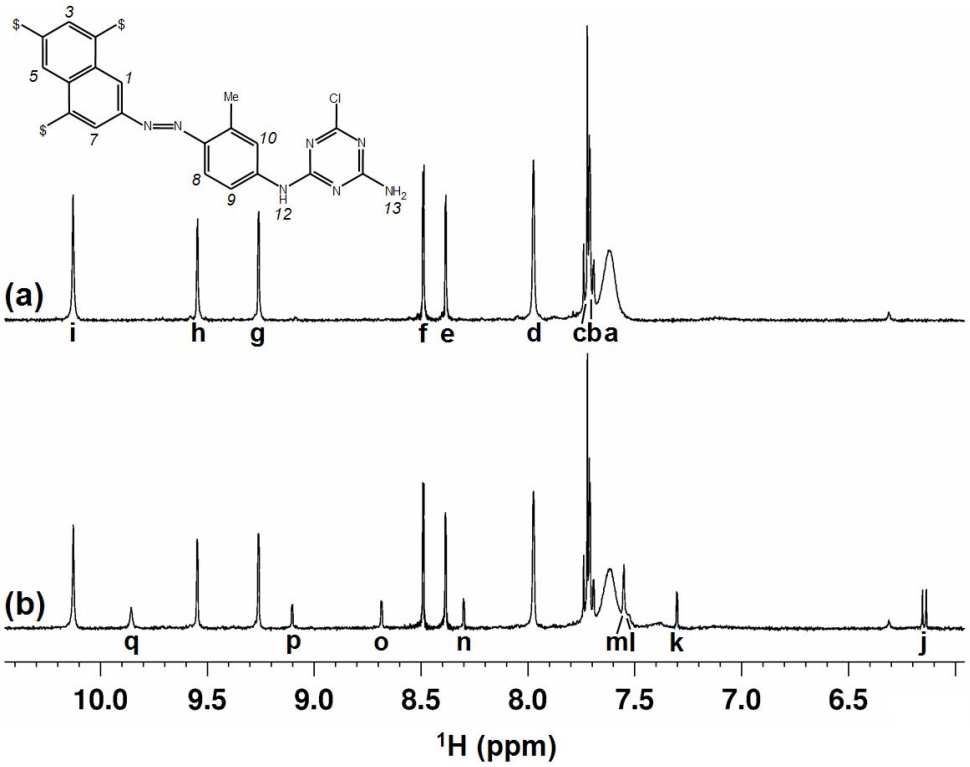

Figure 4.9: The ^{1}H NMR Spectra of 273/19 (2.06 mM) in d_6-DMSO (a) prior to irradiation and (b) during irradiation at the 530-nm PSS.

highlights signal **b** as a double doublet ($^3J_{HH}$ = 8.71, $^4J_{HH}$ = 2.29 Hz), and signal **c** as a doublet ($^3J_{HH}$ = 8.71 Hz). Clearly, **b** and **c** can be assigned to *ortho* coupled protons 9 and 8 respectively. Peak **i**, appearing as the most deshielded proton, is likely to be amine proton 12. The position of this amine group is subject to the influence of strong electron withdrawl from both the benzene and chlorotriazine groups on each side and as such, the proton will have a large chemical shift. The remaining peak in the *trans* spectrum of 273/19, **d**, can be assigned to proton 10 through elimination of all other signals.

Figure 4.9 (b) is the photostationary state ^{1}H NMR spectrum of 273/19 in d_6-DMSO, undergoing irradiation at 530 nm. Eight of the nine expected photo-induced *cis* signals can be identified. Due to its similarity with 273/10, comparable $\Delta\delta$ values are expected between the corresponding *trans* and *cis* protons of the naphthalene unit. Indeed a similar pattern of *cis* signals is visible in Figure 4.9 (b). This consistency of the *trans* and *cis* naphthalene group signals should allow for straightforward assignment of *cis* protons in this dye, and other azo dyes containing the same group, assuming the same *cis* isomer conformation is generated. Protons 3 and 5 are expected to have the smallest chemical shift changes from *trans* to *cis*. *Trans* signal **e** can be paired up with *cis* signal **n** as proton 3 ($\Delta\delta$ = 0.08 ppm). Peaks **g** and **p** form the *trans*/*cis* pair of

signals corresponding to proton 5 ($\Delta\delta = 0.15$ ppm). Signal **h**, assigned earlier to proton 1, must be paired with *cis* peak **o** ($\Delta\delta = 0.86$ ppm). The remaining naphthalene *cis* peak **k**, with a *meta* coupling constant of 1.83 Hz, can be assigned to proton 7 as the partner of *trans* signal **f** ($\Delta\delta = 1.19$ ppm).

Of the remaining peaks, **j** can be unambiguously assigned to proton 8, adjacent to the azo bond, due to the observed *ortho* coupling ($^3J_{HH} = 8.7$ Hz). This means **c** and **j** form a *trans*/*cis* pair ($\Delta\delta = 1.58$ ppm). Due to its deshielded nature, the location of peak **q** demands it be partnered with *trans* peak **i** as proton 12 on the linking amine ($\Delta\delta = 0.26$ ppm). The only singlet *trans* signal to have not been paired with a *cis* isomer signal is **d**. Therefore, using lineshape, signals **d** and **m** form a *trans*/*cis* pair for proton 10 ($\Delta\delta = 0.42$ ppm). The only remaining *cis* signal is unresolved peak **l**. This appears to be a broad singlet, merged with peak **m**. Using lineshape it can be assigned to protons 13 of the terminal amine, partnered with *trans* peak **a** ($\Delta\delta = 0.09$ ppm).

Surprisingly, a *cis* signal for proton 9 is not observed in Figure 4.9 (b). Not a single new peak in the PSS spectrum demonstrated the characteristic splitting associated with this proton. It is not unfeasible that the *cis* peak is hidden under *trans* signal **a**. Removing the light source allows the new signals observed in Figure 4.9 (b) to decay and the *trans* signals to increase in intensity. Despite the missing peak for *cis* proton 9, it is safe to assume that the *cis* isomer of 273/19 is the species being observed. Through measurement of the appropriate peaks, the fraction of *cis* isomer at the photostationary state was estimated to be 17%. The assignments made for 273/19 are listed in Table 4.5.

4.3.3 Dyebase 269/52 and Reactive Dye 269/56

The structural difference between dyebases 269/52 and 273/10, and dyes 269/56 and 273/19, originate from the substition of the methyl group with a ureido group. This alternative functionality introduces additional amine signals into the aromatic region of the ^{1}H NMR spectrum. In the absence of any other changes between the dye and dye base structures, influence of the benzene ring substituents on the ^{1}H NMR spectra of these molecules may be examined. Additionally, a study of this influence on the isomerisation kinetics is conducted in Chapter 5.

4.3.3.1 Assignment of 269/52

Figure 4.10 is the ^{1}H NMR spectrum of 269/52 (basic) in d_6-DMSO, (a) prior to and (b), irradiated to the photostationary state at 530 nm. Due to a large absorption co-

Trans Signal	*Cis* Signal	Proton Assignment	$\Delta\delta$/ppm
a	l	13	0.09
b	†	9	†
c	j	8	1.58
d	m	10	0.42
e	n	3	0.08
f	k	7	1.19
g	p	5	0.15
h	o	1	0.86
i	q	12	0.26
Me	Me	Me	0.36

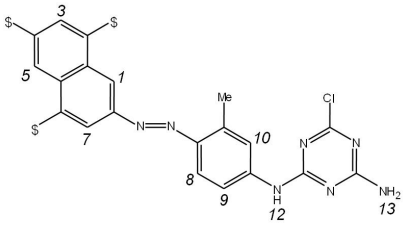

Table 4.5: ^{1}H NMR assignments for the *trans* and *cis* isomers of 273/19 in d_6-DMSO, and the difference in chemical shift between *cis* and *trans* isomers, $\Delta\delta$.
† Unobtainable.

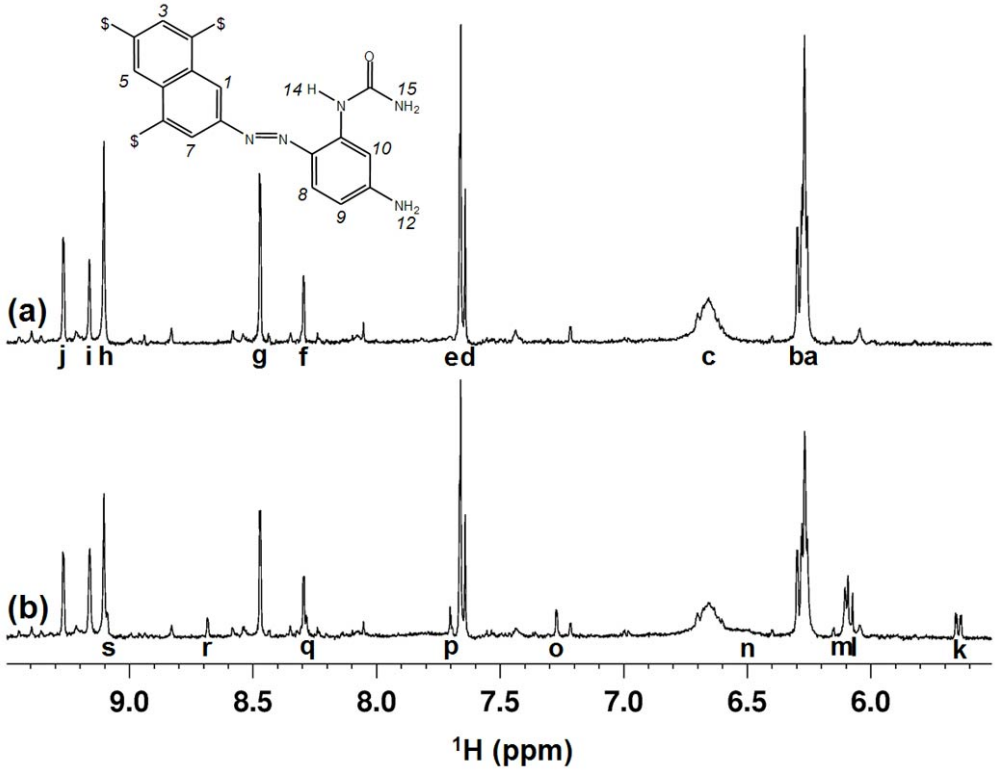

Figure 4.10: The ^{1}H NMR Spectra of 269/52 (0.19 mM) in d_6-DMSO (a) prior to irradiation and (b) during irradiation at the 530-nm PSS.

efficient, a low sample concentration was required and consequently a large number of scans was employed to achieve adequate signal to noise for analysis. The spectrum clearly contains some low level impurity signals which must not be mistaken for *cis* peaks during assignnment of the PSS spectrum. Ten proton environments, labelled **a-j** are present in the spectrum of the *trans* isomer, Figure 4.10 (a). Each of these signals

integrates to one proton equivalent, except for peaks **a** and **c**, which integrate to two. On account of its characteristic ^{1}H NMR fingerprint, the naphthalene group demonstrates the simplest set of protons to assign initially. Through the use of assignments made previously for molecules 273/10 and 273/19 (Section 4.3.2), signals **f**, **g**, **i** and **j** are identified as naphthalene protons and can be attributed to protons 3, 7, 5 and 1 respectively. The usual observations of peak fine-structure are also consistent with the earlier dye and dyebase studied, each showing *meta* coupling of 1.83 Hz apart from signal **i**, which instead displays a broad and rounded top to the peak.

An additional peak, **h**, is observed at $\delta(^1\text{H}) = 9.1$ ppm in the region of the two most deshielded naphthyl signals. This peak does not feature in the ^{1}H NMR spectrum of 273/10 (Figure 4.8) and is likely to be one of the amine signals of the ureido group bonded to the benzene ring of 269/52. A previous study of a dye with a near identical structure, albeit using an **AF** substitution pattern compared to the **ACF** pattern under study, revealed a peak with the same chemical shift and assigned it to the single NH proton of the ureido group.[30] Given the location of the NH proton, adjacent to an amide group and bound to an aromatic ring close to the azo linkage, a large chemical shift would be anticipated as a result of significant electron withdrawl. The lack of other unassigned signals in this electron deficient area of the spectrum, and the previously reported result, make it appropriate to assign signal **h** to proton 14.

Ignoring the two signals that integrate to two proton equivalents, **a** and **c**, the three remaining signals **b**, **d** and **e** must belong to the protons of the benzene ring. Signals **d** and **e** contain some overlap with one another, and signal **b** is merging into signal **a**. Despite the lack of perfect signal resolution, assignment remains straightforward. The magnitude of the coupling constants of signals **b** and **d** ($^3J_{HH} = 8.71$ Hz) indicate them to be *ortho* coupled protons 8 and 9. Although overlapping with signal **a**, **b** displays further splitting of 2.29 Hz indicating it belongs to proton 9. Hence, signal **d** is proton 8. Remaining signal **e** must be attributed to proton 10, an assignment supported by a *meta* coupling constant of 2.29 Hz matching that of double doublet **b**. Two signals remain, relating to the two NH_2 groups on the molecule. The chemical shift and sharp nature of signal **a** is very similar to that observed in 273/10 for the terminal amine of the benzene group, protons 12. Signal **c** is particularly broad suggesting a slow rotation on the NMR timescale, an observation made in previous studies due to possible hindering from groups on the opposing naphthyl ring, making it highly likely to be the terminal amine of the ureido amide group, protons 15.[30]

Figure 4.10 (b) is the photostationary state spectrum of 269/52. Nine photo-induced signals, labelled **k** to **s**, have been detected in addition to the previously assigned *trans*

signals. Signal **k** immediately stands out as a double doublet ($^3J_{HH}$ = 8.70 Hz, $^4J_{HH}$ = 2.29 Hz) and can immediately be placed as proton 9, forming a partnership with *trans* **b** ($\Delta\delta$ = 0.64 ppm). Peak **l**, starting to overlap with **m**, demonstrates *ortho* coupling ($^3J_{HH}$ = 8.70 Hz) and is therefore paired with *trans* d as proton 8 ($\Delta\delta$ = 1.57 ppm). Signal **m** can be partnered with *trans* peak **a** as protons 12 due to its lineshape and intensity ($\Delta\delta$ = 0.17 ppm). Using the same methodology, and bearing in mind *cis* peaks always shift to lower ppm to the *trans* equivalent, signal **n** which is barely detectable and very broad can be paired with broad *trans* signal **c** as ureido NH_2 protons 15 ($\Delta\delta$ = 0.13 ppm). Peak **o**, displaying a *meta* coupling constant of 2.29 Hz and existing as the one peak at lower ppm than *trans* **e** must form a *cis*/*trans* pair with **e** as proton 10 ($\Delta\delta$ = 0.40 ppm).

Four *cis* isomer signals remain to be assigned for the five *trans* isomer peaks of the naphthyl group and the ureido NH proton. *Trans* signal **f** can be paired with *cis* signal **q** as proton 3 ($\Delta\delta$ = 0.01), the coupling constants of these protons matching each other and the small change in chemical shift representative of a proton more distant from the large geometry change and protected by the sulfonate groups. The large change in chemical shift expected for proton 7, *trans* signal **g**, is found in *cis* **p**, with a matching coupling constant and a change in chemical shift of 0.76 ppm. This $\Delta\delta$ value is smaller than the equivalent proton found in dyebase 273/10 and dye 273/19, indicating a different shielding environment, possibly derived from a difference in orientation of the naphthyl and phenyl rings in this *cis* isomer to the other molecules. The *cis* isomer signal for proton 1 may be assigned to **r**, a splitting of 1.83 Hz indicative of the relationship with *trans* **j** as the other nearby *trans* signals do not demonstrate splitting. The chemical shift difference of 0.59 ppm derived from this assignment is also similar to studies of 273/10 and 273/19. The remaining *trans* napthalene peak to be paired up, **i**, is in an area close to ureido peak **h**, and should not display a large change in chemical shift. Peak **s** is the only new *cis* peak in this area and is only partially resolved, overlapping with signal **h**. However, due to the lack of other nearby *cis* signals, **s** could also be assigned as the *cis* partner of *trans* **h**. Indeed recent work has shown that the chemical shift of proton 14 on a similarly substituted naphthalene ring will not greatly differ upon isomerisation[30]. The *cis* signal for proton 3 may in fact be completely masked by the intense *trans* peak of proton 14, with signal **s** being the *cis* partner for *trans* **h**. It is not possible to confidently assign peaks **h** or **i** with a definite *cis* partner.

Despite the lack of a complete *cis* assignment, it does not detract from the evidence that reversible *trans-cis* photoisomerisation and thermal *cis-trans* isomerisation is taking

place in this molecule. Through measurment of appropriate *trans* and *cis* signals it is possible to determine the composition of the photostationary state as 20%. The assignments and $\Delta\delta$ values are available in Table 4.6. The fact the *trans* proton pattern of the naphthalene group is similar to other **ACF** dyes, yet the *cis* isomer is not, suggests a different orientation of the *cis* isomer. This is explored more fully in later sections through the use of calculated minimum energy structures.

Trans Signal	*Cis* Signal	Proton Assignment	$\Delta\delta$/ppm
a	m	12	0.17
b	k	9	0.64
c	n	15	0.13
d	l	8	1.57
e	o	10	0.40
f	q	3	0.01
g	p	7	0.76
h	†	14	†
i	†	5	†
j	r	1	0.59

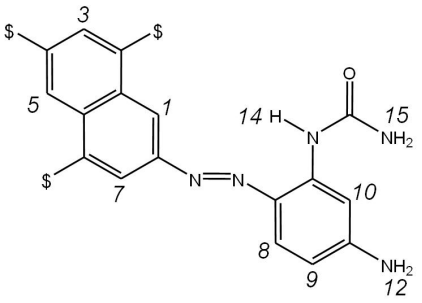

Table 4.6: ^{1}H NMR assignments for the *trans* and *cis* isomers of 269/52 in d_6-DMSO, and the difference in chemical shift between *cis* and *trans* isomers, $\Delta\delta$.
† Unobtainable.

4.3.3.2 Assignment of 269/56

Figure 4.11 is the ^{1}H NMR spectrum of 269/56 in d_6-DMSO. This spectrum demonstrates some very broad signals and for some assignments it was necessary to elevate the temperature at which the spectrum was recorded in order to to improve lineshape and expose some of the signal fine-structure required for a complete assignment of the dye. Examining the *trans* isomer spectrum, Figure 4.11 (a), the diagnostic proton fingerprint for a naphthalene ring substituted in this manner can be identified in protons **e**, **f**, **i** and **j**. As expected, each of the signals demonstrate *meta* coupling apart from the second most deshielded of these protons, **i**, where this is unresolved. Using previous assignments of the **ACF** substituted molecules, signals **e**, **f**, **i** and **j** can be assigned to protons 3, 5, 7 and 1 respectively.

Of the remaining signals, **h** appears particularly deshielded, a likely candidate for this peak being proton 14, the electron withdrawn environment induced by the adjacent amide functional group and nearby azo bond. The same proton in the assignment of the dyebase appears at an identical chemical shift, supporting this proposition. Broad signal **a** appearing at $\delta(^1\text{H})$ 6.6 ppm has a much smaller chemical shift than the other

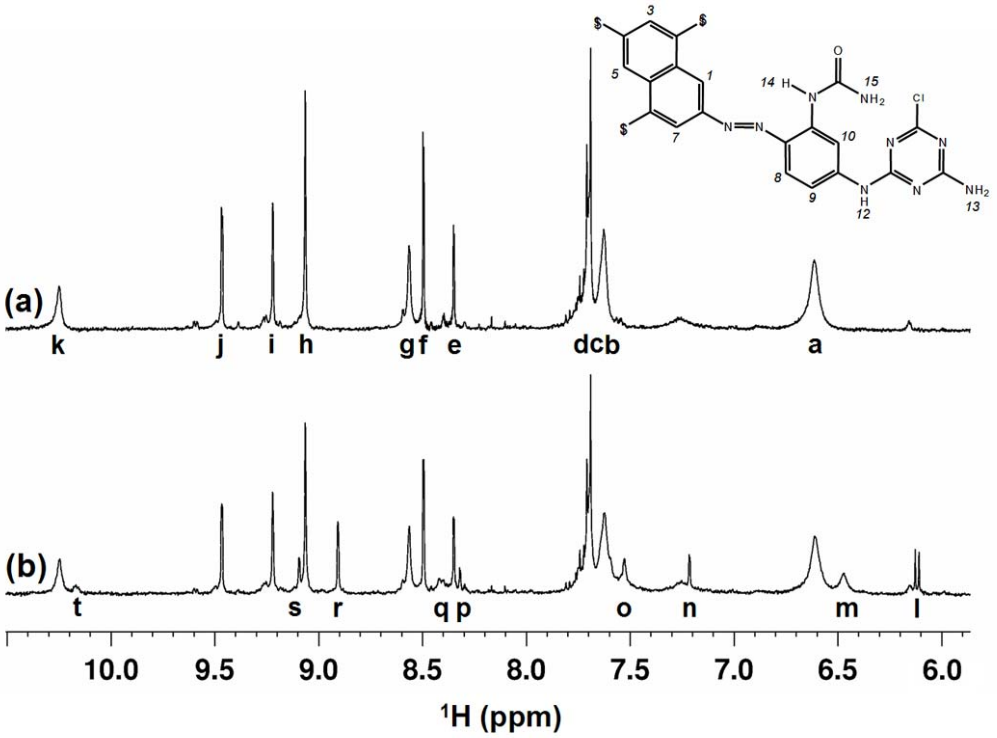

Figure 4.11: The ^1H NMR Spectra of 269/56 (0.35 mM) in d_6-DMSO (a) prior to irradiation and (b) during irradiation at the 530-nm PSS. Spectra recorded at 298 K.

signals and is doubly intense. Figure 4.9, the ^{1}H NMR spectrum of 273/19 is similar to that of 269/56 although it lacks *trans* signals in the area where peak **a** appears in Figure 4.11. It is logical this signal belongs to terminal amine protons in the ureido group present on 269/56. Therfore peak **a** is assigned to protons 15.

Signals **b**, **c** and **d** appear broad and overlap a great deal. To resolve these signals, and assist in the assignment, a spectrum was recorded at higher temperature and is presented as Figure 4.12. At 328 K the signals resolve to a doublet ($^3J_{HH}$ = 8.70 Hz), a second, broader doublet ($^3J_{HH}$ = 8.70 Hz), and a large, broad singlet. The first *ortho* coupled doublet, **d**, can be assigned to proton 8, expected to be the most electron withdrawn signal of the doublets due to its proximity to the azo bond. As the second doublet is broad, it is conceivable that the fine-structure anticipated for the double doublet of proton 9 has broadened out to give this doublet. Additionally it would appear at a lower chemical shift than proton 8 as it is further from the azo bond. Comparing this reactive dye to the dyebase spectrum, there is an additional peak in the naphthalene fingerprint region at $\delta(^1$H) 8.6 ppm. This has broadened out to an extent and could be expected as the *meta* coupled partner of proton 9. The fact this peak has a higher chemical shift than that of the equivalent dyebase, 269/52, can be explained by the introduction of the electron withdrawing chlorotriazine ring on that end of the molecule, a structural modification that has also affected proton 9 in the

same way. Hence, peak **g** is assigned to proton 10. The remaining peak, **b**, exposed in the higher temperature spectrum of 269/56 can be assigned to the terminal amine of the chlorotriazine ring, its broad nature indicating quite slow rotation of the amine group.

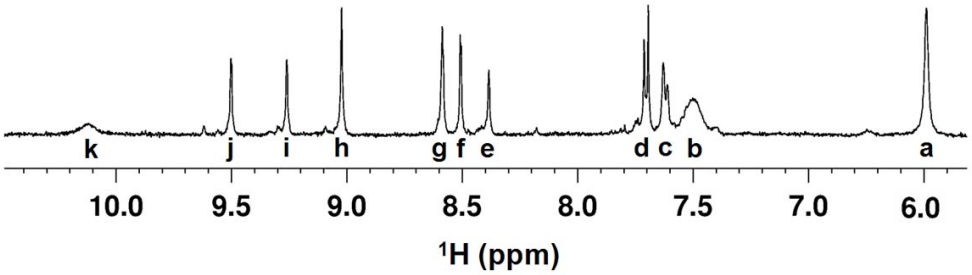

Figure 4.12: The ^{1}H NMR Spectrum of 269/56 (0.35 mM) in d_6-DMSO, recorded at 328 K.

Figure 4.11 (b) is the 530-nm photostationary state spectrum of 269/56 in d_6-DMSO. Nine new peaks can be identified in this spectrum, alongside the original *trans* signals. Starting with the simple assignments, peak **l**, a doublet ($^3J_{HH}$ = 8.70 Hz) can be identified as proton 8, the large change in chemical shift from *trans* peak **d** showing the typical characteristics of isomerisation for a proton directly adjacent to the azo bond($\Delta\delta$ = 1.58 ppm). Peak **t** forms a *cis*/*trans* pair with signal **k** for proton 12 ($\Delta\delta$ = 0.08 ppm). This is due to the similar broad nature of the peaks, the fact that only a small change is expected for a proton so far from the largest isomerisation-induced geometry change, and the lack of other *trans* signals at high enough ppm to induce a *cis* signal in this area. Signal **m** can be paired with **a** on account of lineshape and intensity ($\Delta\delta$ = 0.14 ppm).

Concentrating on the naphthalene group, the *cis* isomer protons of the **ACF** substituted group for the previous three dyes have shown a variation in chemical shift differences from the *trans* signals, and care must therefore be taken assigning the spectrum. Protons 3 and 5 of the naphthalene group should show no significant chemical shift change upon isomerisation, the $\Delta\delta$ value typically being much less than 0.2 ppm. Peak **e**, corresponding to *trans* proton 3, matches *cis* peak **p** in terms of signal splitting, and with a chemical shift change within the expected range, and no other *cis* protons in the expected area, they can be solidly assigned as a *trans*/*cis* pair ($\Delta\delta$ = 0.03). Two new peaks are detected near signal **i**: peak **s** and the much more intense **r**. It is most likely peak **s** is the *cis* partner to **i** as the only alternative would be for it to pair with **j**, forming a chemical shift change uncharacteristically small for proton 1. Therefore **i** and **s** are paired together as proton 5 ($\Delta\delta$ = 0.12 ppm). Signal **n** at $\delta(^1$H) 7.2 ppm,

demonstrating *meta* coupling of 1.83 Hz, is expected as the partner to *trans* **f** due to excellent chemical shift coincidence with each of the other **ACF** dyes studied. The chemical shift difference of 1.28 ppm derived from this pair compares well to proton 7 in molecules 273/10 and 273/19, and the lack of any other *cis* signals in this area of the spectrum suggest the assignment is firm. The final naphthalene signal, **j**, should be paired with *cis* peak **r** as this is the area of the spectrum the new peak would be expected. However, a signal for *cis* 14 would also be expected in this area. Peak **r** is unexpectedly intense to be either *cis* 1 or 14. It appears that the two are superimposed upon one another. Elevating the temperature to 313 K caused the signal to separate into two peaks, one remianing at the same chemical shift, the second peak moving lower to 0.05 ppm at 313 K (data not shown). Therefore signals **j** and **r**, and **h** and **r** form *trans*/*cis* pairs ($\Delta\delta = 0.56$ and 0.15 ppm respectively).

A signal is not observed for the *cis* isomer of proton 13. The very broad and unresolved nature of the *trans* signal in the 298 K spectrum could easily be hiding a *cis* peak, especially since this pair of protons did not demonstrate a large change on isomerisation in the similar 273/19 molecule. Unfortunately, a 328 K spectrum could not be obtained to assist with the assignment: the *cis* isomer was not observed at this temperature, suggesting a rapid thermal decay rate for this molecule. As a compromise, a spectrum was recorded at 313 K (data not shown). This assisted in confirming the identity of peak **o** as proton 9. Although fine structure is not observed at 313 K, the lineshape and chemical shift change from *trans* c suggest the assignment to be correct ($\Delta\delta = 0.14$ ppm). The remaining broad signal **q** forms a *trans*/*cis* pair with **g** for proton 10, the chemical shifts observed at 313 K matching up ($\Delta\delta = 0.14$ ppm).

Through measurement of the intensity of selected *trans*/*cis* pairs, the composition of the photostationary state can be estimated as 20% *cis* isomer. The assignments have been tabulated in Table 4.7.

Trans Signal	*Cis* Signal	Proton Assignment	$\Delta\delta$/ppm
a	m	15	0.14
b	$*$	13	$*$
c	o	9	0.14
d	l	8	1.58
e	p	3	0.03
f	n	7	1.28
g	q	10	0.14
h	r†	14	0.15
i	s	5	0.12
j	r†	1	0.56
k	t	12	0.08

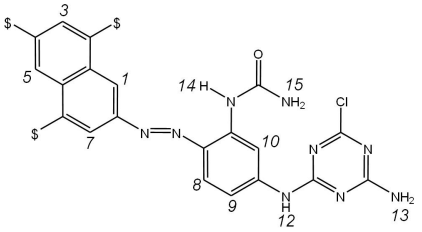

Table 4.7: ^{1}H NMR assignments for the *trans* and *cis* isomers of 269-56 in d_6-DMSO at 298K, and the difference in chemical shifts between the *cis* and *trans* isomers, $\Delta\delta$.
$*$ Unobtainable.
† Superimposed *cis* signals.

4.3.4 ^{1}H NMR Spectra of a Series of 'Second Leg' B275 Derivatives

B275, depicted in Figure 4.13, is a commercial yellow azo dye. This dye was rigourously studied and assigned by Tait.[30] When the dye is bound to a cellulose substrate it attaches *via* the triazine component, chlorine acting as a good leaving group for the bond to form with a cellulose hydroxyl group. Through additon of a second leg on the triazine group, larger than the terminal amine present in B275, it was hoped that a variation in the kinetic processes would be observed. The four second leg dyes are depicted in Figure 4.1. Each of these should have a similar ^{1}H NMR spectrum of the aromatic region as they all derive from B275. For one of the dyes, 273/5, new peaks from the aromatic component of the 'second leg' should also be visible in this region of the spectrum, the other second leg compounds displaying aliphatic signals for the new group. Only the aromatic regions were assigned for use in kinetic measurements, due to the good signal separations and characteristic signals. Although the *cis* isomer spectrum of B275 was not fully assigned from first principles, the assignments based on a series of analogues suggest the assignments to be a fair representation of the isomerisation. Discussion of these assignments, alongside the calculated structures, is conducted in Section 4.4. Dye 273/5 is a commercial dye that was recrystallised to try and remove some formulating agents. After this process a small amount appear to remain, so the other dyes with similar proton signals are assigned prior to this dye.

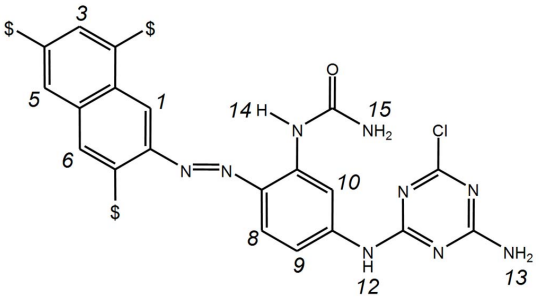

Figure 4.13: The structure of reactive dye B275. Proton numbering is applied as defined in Section 4.2.4.

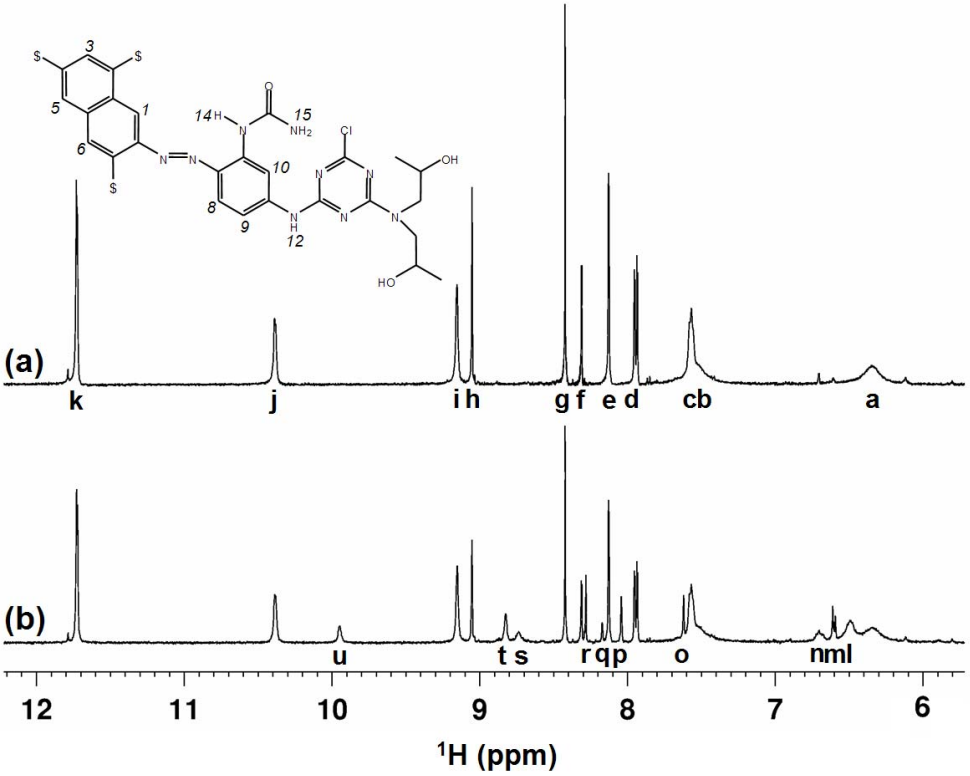

Figure 4.14: The ^{1}H NMR Spectra of 273/6 (1.64 mM) in d_6-DMSO (a) prior to irradiation and (b) during irradiation at the 530-nm PSS.

4.3.4.1 Assignment of 273/6

Figure 4.14 is the ^{1}H NMR spectrum of 273/6 in d_6-DMSO (a) prior to and (b) during irradiation at 530 nm after the photostationary state had been attained. The *trans* isomer in Figure 4.14 is studied first. Signals **e**, **f**, **g** and **h** form a reliable pattern of signals associated with an **ACG** sulfonated naphthyl group. Singlet **h**, more deshielded than the other three peaks can be reliably assigned to proton 1, the chemical shift matching up with observations made earlier on the **AC** and **BD** dyes. Proton 6, adjacent to the **G** sulfonate, is expected to be the next most deshielded proton, and is assigned to signal **g**. Of the two remaining signals, **f** displays *meta* coupling whereas

e shows a degree of broadening anticipated to hide the small coupling constant. The chemical shifts of peaks **e** and **f** are coincidental with those of **f** and **g** in 271/64, assigned to protons 5 and 3 respectively. The **G** sulfonate would not be expected to influence the chemical shift of these two protons significantly, and for this reason **e** is assigned to proton 5, and **f** to proton 3. Peak **k**, at an extremely deshielded region of the ^{1}H NMR spectrum, is distinctive of ureido NH proton 14. Furthermore, peak **j**, at $\delta(^{1}\mathrm{H})$ 10.4 ppm isolated from the other signals in the spectrum, is indicative of proton 12 on the secondary amine linking the benzene and chlorotriazine components of the molecule. The two broad peaks **a** and **b** can be attributed to the non-equivalent protons of the ureido terminal amine, 15.

The remaining peaks, **c**, **d** and **i** belong to the protons on the benzene ring. Signal **d** is sharp and shows *ortho* coupling ($^{3}J_{HH}$ = 8.70 Hz) characteristic of proton 8. The two remaining signals relating to protons 9 and 10 are broader than those in B275, surely indicating the large group now attached to the chlorotriazine ring is having an influence on these protons. Signal **c**, overlapping with **b**, is anticipated to be proton 9, its broad nature hiding the double doublet fine-structure that is normally observed for this proton. Peak **i** is less shielded than its B275 equivalent but can still be reliably assigned to proton 10 of the benzene ring, making a complete assignment for the aromatic signals of 273/6. The di-isopropanolamine group attached to the triazine ring contains several aliphatic protons. Some of these appear to merge with the water peak that is suppressed during the NMR acquisition. This part of the molecule was not studied further: it can not be reliably used to secure NMR assignments of the *cis* and *trans* isomers and therefore is no help for determining the photostationary state composition, or for following the kinetic processes described in Chapter 5.

Figure 4.14 (b) is the photostationary state spectrum of 273-6. An additional 10 peaks are present amongst the signals from the *trans* isomer, labelled **l** to **u**. The assignments can be based upon the spectrum of B275, the protons displaying characteristic chemical shift changes assigned first. Signal **u** is typical of the *cis* signal of proton 12. Due to its location it could also be assigned as the partner of *trans* **k**, but this is extremely unlikely since a large change in chemical shift is not expected in proton 12. Hence signals **j** and **u** are assigned as a *trans*/*cis* pair for proton 12 ($\Delta\delta$ = 0.44 ppm). As signal **h** is expected to undergo a large change upon isomerisation from previous observations, it is conceivable that signals **s** and **t** are the *cis* protons for *trans* **i** and *trans* k. The lineshape of these signals indicate **k** and **t** form a *trans*/*cis* pair as proton 14 ($\Delta\delta$ = 2.89 ppm), and signals **i** and **s** form a pair of signals relating to proton 10 ($\Delta\delta$ = 0.43 ppm). The new *ortho* coupled doublet **m** can be designated as proton 8, paired with

trans signal **d** ($\Delta\delta$ = 1.34 ppm).

A further two signals, **l** and **n**, have been generated close to the new *cis* doublet of proton 8. The intensity and shape of signal **l** is indicative of the broad, two-proton singlet formed for *cis* isomer protons 15, merging from the *trans* signals **a** and **b** ($\Delta\delta$ = -0.13 and 1.05 ppm). *Cis* peak **n** appears as a broad signal demonstrating no signs of fine-structure: it appears in a location expected for *cis* proton 9, and given the lack of other signals at lower ppm to *trans* **c**, coupled with the broad and unresolved nature of the *trans* peak, it is plausible that **n** can be paired with **c** as a *cis*/*trans* pair for proton 9 ($\Delta\delta$ = 0.87 ppm).

The four remaining signals, **o**, **p**, **q** and **r** are the *cis* protons of the naphthalene ring. Through a process of comparing the lineshape, fine-structure and relative intensities of the signals, the following peaks have been assigned as *trans*/*cis* pairs: **e** and **p** as proton 5 ($\Delta\delta$ = 0.09 ppm); **f** and **q** as proton 3 ($\Delta\delta$ = 0.15 ppm); **g** and **r** as proton 6 ($\Delta\delta$ = 0.15); and **h** and **o** as proton 1 ($\Delta\delta$ = 1.43 ppm). All *trans* peaks have been assigned a *cis* partner for this molecule. By measuring selected *trans*/*cis* pairs of peaks it was possible to estimate the photostationary state composition for 273/6 as 29% *cis*. A summary of the assignments discussed earlier is presented in Table 4.8.

Trans Signal	*Cis* Signal	Proton Assignment	$\Delta\delta$/ppm
a	l	15	-0.13
b	l	15	1.05
c	n	9	0.87
d	m	8	1.34
e	p	5	0.09
f	q	3	0.15
g	r	6	0.15
h	o	1	1.43
i	s	10	0.43
j	u	12	0.44
k	t	14	2.89

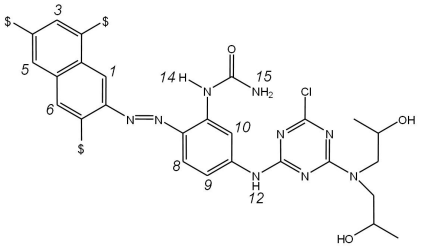

Table 4.8: ^{1}H NMR assignments for the *trans* and *cis* isomers of 273-6 in d_6-DMSO, and the difference in chemical shift between *cis* and *trans* isomers, $\Delta\delta$.
$*$ Unobtainable.

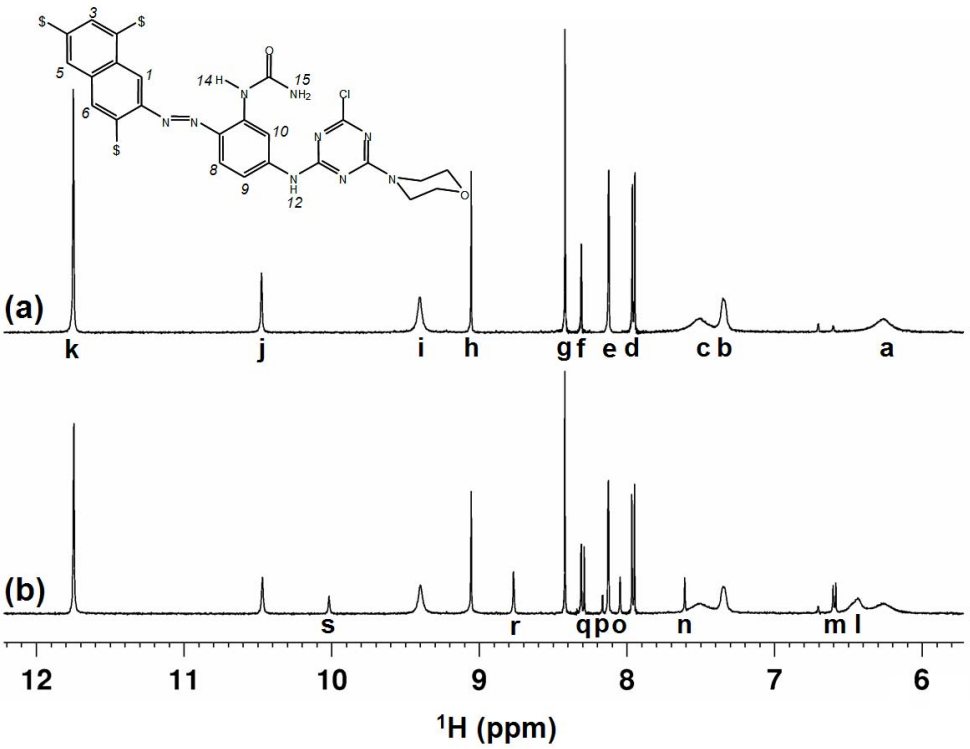

Figure 4.15: The ^{1}H NMR Spectra of 273/8 (1.40 mM) in d_6-DMSO (a) prior to irradiation and (b) during irradiation at the 530-nm PSS.

4.3.4.2 Assignment of 273/8

Figure 4.15 is the ^{1}H NMR spectrum of 273/8 (a) prior to irradiation and (b), during irradiation at the 530-nm photostationary state. The *trans* spectrum of 273/8 contains 11 proton peaks and is comparable to that of B275, although broadening is apparent in certain peaks. Assignment of this spectrum can be applied quite simply from the B275 fingerprint discussed during the assignment of 273/6. Signal **k** demonstrates the extremely electron withdrawn environment identified for proton 14 of the ureido group. Similarly signal **j** can be assigned to proton 12, the bridging proton between the benzene and chlorotriazine groups. Broad singlets **a** and **c**, each integrating to one proton equivalent, are the expected pair of signals for the ureido NH_2 protons 15, demonstrating inequivalence on the NMR timescale. The sharp signals **e**, **f**, **g** and **h** form the characteristic pattern of the **ACG** naphthalene group and from this fingerprint can be assigned to protons 5, 3, 6 and 1 respectively.

The remaining signals must belong to the benzene group protons 8, 9 and 10. Doublet **d** ($^{3}J_{HH}$ = 8.70 Hz) can be assigned to proton 8. Signals **b** and **i**, pertaining to the two reminaing benzene ring protons, are particularly broad compared to peak **d**, and to those in the original B275 spectrum. Neither of the signals show the fine-structure

of a double doublet expected for proton 9. Despite this, the signals are well removed from one another, signal **b** appearing at $\delta(^1\text{H})$ 7.35 ppm and **i** at 9.4 ppm. This means there is no ambiguity in the assignments, and signal **b** can be assigned to proton 9, and signal **i** to proton 10, sandwiched between the linking amine and the electron deficient ureido group.

Figure 4.15 (b) is the photostationary state spectrum of 273/8 under irradiaition at 530 nm. Amongst the assigned *trans* signals, 8 new proton environments labelled **l** to **s** are identified. As with the previous assignments based upon B275, some *trans*/*cis* pairs may be defined straightforwardly. The new *ortho* coupled doublet labelled **m** can safely be paired with *trans* peak **d** as proton 8, the large change in chemical shift characteristic of this proton adjacent to the azo bond ($\Delta\delta$ = 1.36 ppm). Signal **k** is expected to demonstrate a massive change in chemical shift of the order of 3 ppm. Signal **r** is the likely candidate for this proton, given the expected shift and the lack of other new *cis* peaks in this area ($\Delta\delta$ = 2.98 ppm). The smaller change expected of proton 12, and the lack of any other peaks in a wide area around *trans* peak **j** mean **s** can be reliably paired with **j** ($\Delta\delta$ = 0.45 ppm). The two inequivalent peaks observed in the *trans* spectrum for protons 15 are expected to appear as a single peak in *cis* isomer and are identified as peak **l**, at slightly higher ppm than **a** but significantly lower than **c** ($\Delta\delta$ = -0.13 and 1.08).

The remaining four *cis* signals can be assigned to the naphthyl protons. Examining these peaks, and the pattern expected from assignment of 273/6, **h** can be paired with signal **n** as proton 1 ($\Delta\delta$ = 1.45 ppm), **g** can be paired with **q** as proton 6 ($\Delta\delta$ = 0.13 ppm), **f** is paired with **p** as proton 3 ($\Delta\delta$ = 0.14 ppm) and signal **e** with **o** as proton 5 ($\Delta\delta$ = 0.07 ppm). No *cis* signals are present for protons 9 and 10 of the benzene ring, the *trans* signals of which were particularly broad when compared to B275 itself. Upon elevation of the sample temperature to 328 K a new signal starts to rise at $\delta(^1\text{H})$ 8.88 ppm, and another very broad and noisy signal begins to uncover at 6.59 ppm. These could possibly be the two signals that are not observed at room temperature. The fact that the *trans* peaks of 9 and 10 were broad, and that it was necessary to raise the temperature of the spectrum to reveal these *cis* peaks, suggests that conformational averaging may be slowing down to produce such an observation.

The aliphatic region of the spectrum was broad and beginning to merge with the large water signal, making this area difficult to assign. This broadening is caused by the eight different protons of the morpholine group, and the varying conformations that the six membered ring can take. No useful information is discernible from the spectrum with respect to specific *cis* and *trans* peaks: the data can not be used for deriving the

composition of the photostationary state, nor can it be followed in the kinetic treatment performed later. Signal assignments are presented in Table 4.9. Through measurement of selected *trans* and *cis* peak pairs, the photostationary state composition can be estimated as 19% *cis* isomer.

Trans Signal	*Cis* Signal	Proton Assignment	$\Delta\delta$/ppm
a	l	15	-0.13
b	*	9	*
c	l	15	1.08
d	m	8	1.36
e	o	5	0.07
f	p	3	0.14
g	q	6	0.13
h	n	1	1.45
i	*	10	*
j	s	12	0.45
k	r	14	2.98

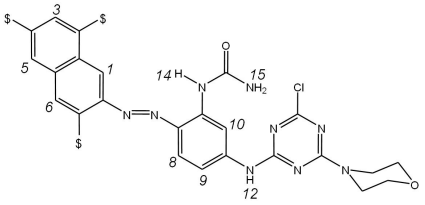

Table 4.9: ^{1}H NMR assignments for the *trans* and *cis* isomers of 273-8 in d_6-DMSO, and the difference in chemical shift between *cis* and *trans* isomers, $\Delta\delta$.
* Unobtainable.

4.3.4.3 Assignment of 273/5

Figure 4.16 is the ^{1}H NMR spectrum of 273/5 in d_6-DMSO (a) prior to irradiation and (b) at the photostationary state of 530 nm. The spectrum appears with some very broad signals apparent around $\delta(^1\text{H})$ 8 ppm which could be attributed to formulating agents still present after recrystallisation. Fourteen proton environments can be clearly identified. Some of these peaks are easy to place after examining the assignments made for similar proton environments in the other 'second leg' dyes. The signal appearing at $\delta(^1\text{H})$ 11.7 ppm (peak **n**) can be assigned to ureido NH proton 14. For all the reactive dyes studied that contain proton 12 on the amine bridge, a chemical shift between $\delta(^1\text{H})$ 10.0-10.5 ppm has been observed. The lack of other signals in this area of the spectrum allows signal **m** to be assigned to proton 12. The low intensity of this signal suggests a certain amount of exchange with water in the solvent. The suppression of the water peak employed in the NMR pulse program has the effect of reducing the intensity of this peak compared to that observed without water suppression. A high concentration (10 mM) spectrum of the *trans* isomer of this dye recorded without suppressing the water present in the DMSO solvent shows a more intense signal, which is actually two broad singlets merging (data not shown). The environments of protons 12 and 16 are

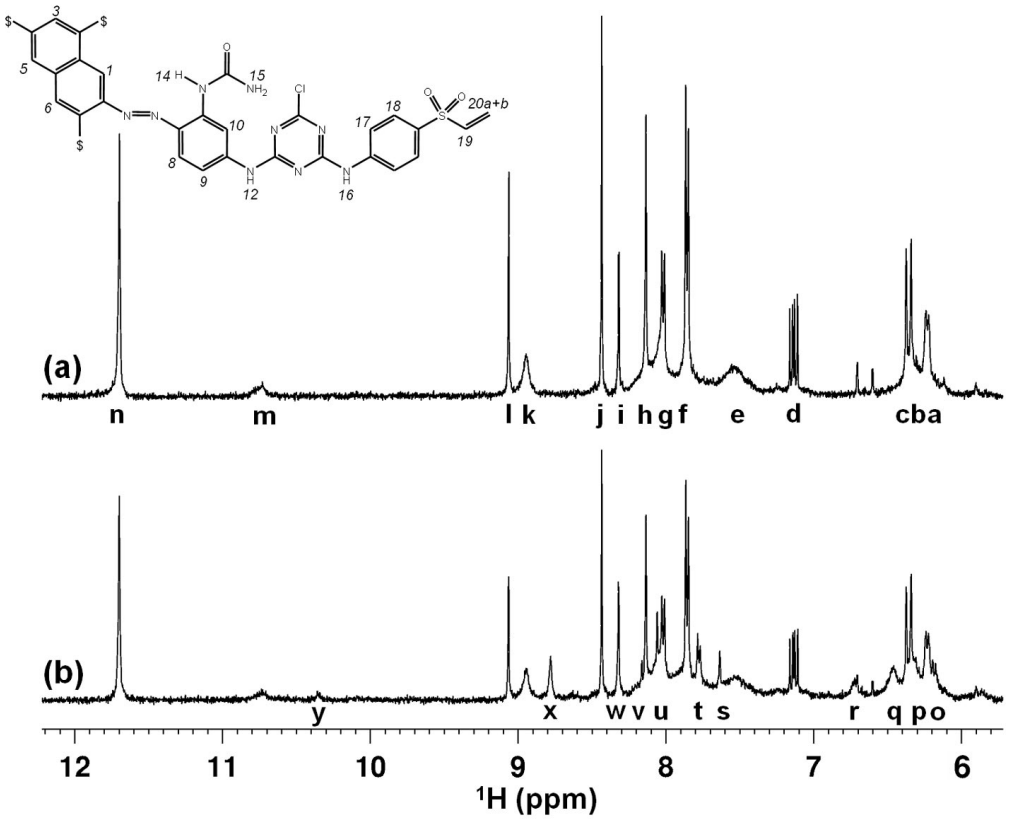

Figure 4.16: The ^{1}H NMR Spectra of 273/5 (0.84 mM) in d_6-DMSO (a) prior to irradiation and (b) during irradiation at the 530-nm PSS.

expected to be roughly similar compared with other protons in the sample, and so the two peaks present, that appear as weak signal **n** in the water-suppressed spectrum shown in Figure 4.16 (a) comprise these two protons.

The four sharp signals **h**, **i**, **j** and **l** form the chemical shift pattern identified for the previous 'second leg' dyes as the **ACG** sulfonated naphthyl group, and can be assigned to protons 5, 3, 6 and 1 respectively. Examining the signals at the more shielded end of the spectrum, certain details can be extracted from peaks **a** – **e**. Signal **b**, a broad singlet underneath **a** and **c** is characteristic of one of the two ureido terminal amine protons. Peak **e** can be paired with **b** as the two signals expected for protons 15 on the ureido group. Signal **c** demonstrates a coupling constant of 16.5 Hz, which identifies it as one of the alkene protons 20, placed *trans* to proton 19, since a coupling constant this large could only arise from such a proton in this dye. Since **d** displays double doublet character (J_{HH} = 16.5 Hz, 9.6 Hz) with an obvious relationship to the *trans* alkene proton, it can be reliably assigned to proton 19. Signal **a** displays a 9.6 Hz coupling constant and is attributed to alkene proton 20, *cis* to proton 19. The terminal alkene protons will be labelled 20_E and 20_Z for the respective *trans* and *cis* protons.

The remaining signals in the *trans* isomer spectrum relate to phenyl ring protons and

are more difficult to assign definitively. Broad peak **k** is characteristic of proton 10 in these dyes. Only two peaks remain to be assigned. Peaks **f** and **g** appear as two broad *ortho* coupled doublets ($^3J_{HH}$ = 8.7 Hz) for the *para* substituted benzene ring present in the molecule. The chlorotriazine group is likely to withdraw electron density from the ring more than the vinyl sulfone group, and therefore signal **g** is assigned to protons 17 and **f** to protons 18. Doublet **g** contains a shoulder which is likely to be an unresolved signal for one of the phenyl resonances 8 or 9. Given prior observations for dyes 273/6 and 273/8, it is more likely to relate to proton 8 due to the region in the NMR spectrum. Proton 9 appeared at 7.6 ppm in the previous two dyes, but does not appear in this spectrum. The presence of some broad resonances and more aromatic signals in this NMR spectrum could well be hiding the peak for proton 6. However, the assignment of all other peaks with this spectrum are consistent with the structure of 273/5.

Figure 4.16 (b) is the photostationary state ^{1}H NMR spectrum of 273/5 recorded under 530 nm irradiation. In addition to the signals oberserved in the *trans* isomer spectrum, eleven proton environments can be identified. Observations from previous dyes assist with identifying which signals relate to which protons here. Signals **n** and **x** can be paired together, giving the now characteristic change in chemical shift for proton 14 of 2.92 ppm. Signal **y** is in the correct region to pair with proton 12. Since proton 16 is also present in *trans* signal **n**, **y** cannot be definitively assigned to one resonance or the other. It may in fact comprise both signals. A characteristic pattern for the *cis* isomer naphthyl group protons can be identified amongst the signals. Minimal reduction in the intensity of peak **i** following irradiation of the sample suggests a *cis* peak is coincident with *trans* peak. This peak is identified as **w** and can be paired with *trans* **j** as proton 6 ($\Delta\delta$ = 0.12 ppm). *Cis* peak **v**, can be paired with *trans* **i** as proton 3 ($\Delta\delta$ = 0.16 ppm). Rising from *trans* signal **g**, *cis* signal **u** is in a location characteristic of *cis* proton 5 for this sulfonation pattern, showing a change in chemical shift of 0.08 ppm from its *trans* partner **h**. Proton 1, always displays a significant increase in the shielding of the *cis* isomer compared with the *trans* signal. This is no different for 273/5, signal **l** pairing with *cis* **s** for proton 1 ($\Delta\delta$ = 1.44 ppm). Whilst using the previously assigned dyes as a template to assist for this dye, the two signals for the terminal ureido resonances of the *trans* isomer, **b** and **e**, match well with *cis* peak **q**, giving expected changes in chemical shift ($\Delta\delta$ = -0.12, 1.09 ppm).

Of the remaining *cis* isomer peaks, doublet **t** closely resembles *trans* peak **f** and is paired as protons 18 of the benzene ring ($\Delta\delta$ = 0.10 ppm). A second doublet for protons 17 does not appear to resolve. Two *cis* signals remain. Signal **o** shows the same coupling

constant as *trans* peak **a**, indicating it to be proton 20_Z of the alkene ($\Delta\delta = 0.03$ ppm). Neither of the remaining two *trans* alkene protons display a *cis* isomer equivalent. The remianing *cis* signal, labelled **r**, does not match up to any of the other *trans* signals remaining to be assigned. Although it displays a coupling constant of 8.71 Hz, the intensity is too low to be the *cis* partner of *trans* **g**. It was noted earlier that a *trans* isomer peak looked to be obscured by **g**, which could possibly be a signal for proton 8 due to the location when compared with the other dyes in this study. *Cis* signal **r** could well be the signal for proton 8, since a movement to this location from the unresolved peak under **g** would induce a chemical shift change of approximately 1.3 ppm, highly consistent with that observed in 273/6 and 273/8. *Cis* isomer signals for protons 9 and 10 are not observed in this spectrum.

Unfortunately it is not possible to further assign the *cis* isomer spectrum of 273/5. However, the photoinduced signals coupled with the thermal reversibility of the process, and the agreement with features of the ^{1}H NMR spectra of other **ACG** dyes assigned in this study, are solid indicators that photoinduced *trans-cis* isomerisation is occurring. The measurement of integrals of *trans* and *cis* isomer peak pairs had to be highly selective due to the uneven baseline and overlapping nature of many peaks. They indicated that 22% *cis* isomer was present at the photostationary state.

Trans Signal	*Cis* Signal	Proton Assignment	$\Delta\delta$/ppm
a	o	20_Z	0.03
b	q	15	-0.12
c	*	20_E	*
d	*	19	*
e	q	15	1.09
f	t	18	0.10
g	*	17	*
h	u	5	0.08
i	v	3	0.16
j	w	6	0.12
k	*	10	*
l	s	1	1.44
m	y	12/16	0.38
n	x	14	2.92

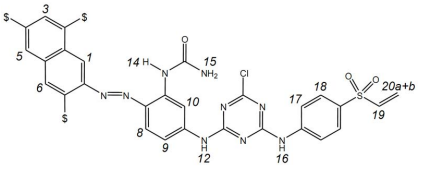

Table 4.10: ^{1}H NMR assignments for the *trans* and *cis* isomers of 273-5 in d_6-DMSO, and the difference in chemical shift between *cis* and *trans* isomers, $\Delta\delta$.
* Unobtainable.

4.3.4.4 Assignment of 273/13

Dye 273/13 has a very similar structure to 273/8, the only difference being the hydrolysis of the chlorotriazine group. Although this would substitute the chlorine with a hydroxyl group, the proton of this new group is expected to exist on one of the chlorotriazine ring nitrogen atoms in a tautomeric form. This modification was introduced to investigate the influence of the chlorine atom on the isomerisation kinetics.

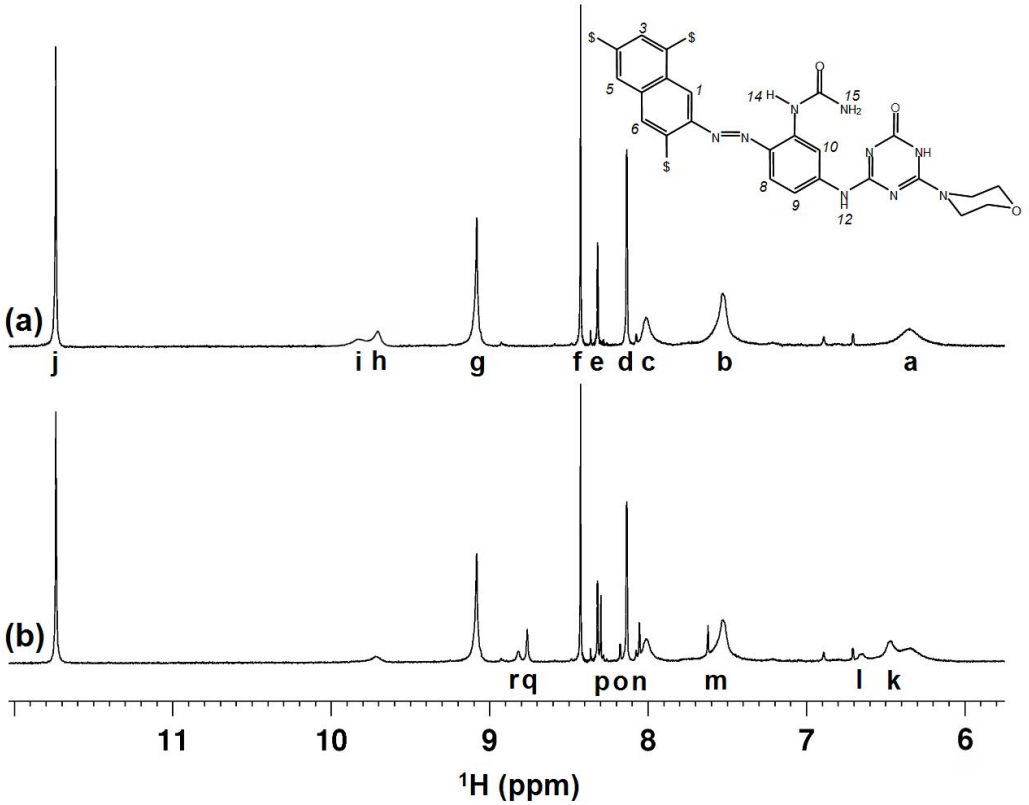

Figure 4.17: The ^{1}H NMR Spectra of 273/13 (1.62 mM) in d_6-DMSO (a) prior to irradiation and (b) during irradiation at the 530-nm PSS.

Figure 4.17 is the ^{1}H NMR spectrum of 273-13 in d_6-DMSO, (a) for the *trans* isomer prior to irradiation and (b), for the sample undergoing continuous irradiation at 530 nm. Ten peaks can be identified in *trans* isomer spectrum, and are labelled **a** to **j**. The majority of peaks are particularly broad, and initially the signals do not all appear to be present. Peak **j** is indicative of ureido proton 14. Additionally, peaks **d**, **e**, **f** and **g** form the characteristic pattern of signals for **ACG** naphthyl protons 5, 3, 6 and 1, although signal **g** is unusually broad. Peak **h** can be assigned to proton 12 of the amine linking group due to its characteristic location. Alongside this peak, low intensity signal **i** at $\delta(^1\text{H})$ 9.85 ppm is also identified. As no other peaks were observed in this region of the 273/8 ^{1}H NMR spectrum, this must be the tautomeric proton attached to one of the chlorotriazine ring nitrogens. The low intensity of both peaks **h** and **i** suggest

they are labile and exchanging with the water that is present in the solvent.

For the assignment of 273/8 (Section 4.3.4.2), elevating the temperature at which the spectrum was acquired allowed broadened peaks to resolve some of their fine structure, and the missing *cis* isomer peaks of protons 9 and 10 to begin appearing. Raising the temperature at which 273/13 was recorded proved beneficial for assignment of the *trans* isomer. Figure 4.18 is a progression of NMR spectra as the sample temperature is elevated in 10 K increments. As the temperature is raised, several features of the 298 K spectrum become clearer to comprehend. Broad peak **g** has separated into two separate peaks, and peaks **b** and **c** have sharpened into a double doublet ($^3J_{HH}$ = 8.70, $^4J_{HH}$ = 1.83 Hz) and a doublet ($^3J_{HH}$ = 8.70 Hz) respectively, a clear indication that **b** is proton 9 and **c** is proton 8. As the temperature is increased, signal **a** disappears, at 338 K a new broad, low intensity peak centred at $\delta(^1\text{H})$ 6.8 ppm beginning to rise from the baseline. This suggestes that **a** is coalescing with another signal. Since **a** is normally attributed to one of the two ureido protons labelled 15, it is reasonable to assume the increase in temperature has given the terminal amine group enough energy to rotate fast enough on the NMR time-scale to appear as a single resonance. The fact that coalescence appears to be occurring suggests that signal **b** comprises one of the broad peaks expected for proton 15, along with the aforementioned proton 9 and explains the larger size observed for this signal.

Figure 4.17 (b) is the photostationary state of 273-13 in d_6-DMSO at 530 nm, recorded at 298 K. Eight new proton peaks can be identified. Peaks **r** and **q** appear in a location typical for the *cis* protons 10 and 14. Since proton 10 is combined with 1 as *trans* peak **g** making it particularly broad, we would expect the equivalent *cis* proton to be broad. Moreover, the sharp nature of ureido proton 14 should produce a sharp *cis* resonance. Therefore, peaks **j** and **q** form a *trans*/*cis* pair for proton 14 ($\Delta\delta$ = 2.98 ppm), and peak **g** can be paired with **r** ($\Delta\delta$ = 0.26 ppm). Peaks **m**, **n**, **o** and **p** form the usual pattern identified for the *cis* **ACG** sulfonated naphthyl group identified in 273/6 and 273/8. Through studying the chemical shifts and changes between the *trans* and *cis* isomers of the previously assigned second leg dyes, the following pairs may be simply assigned: **g** and **m**, demonstrating the typical large chemical shift change expected for proton 1 ($\Delta\delta$ = 1.44 ppm); **f** and **p** for proton 6 ($\Delta\delta$ = 0.13 ppm); **e** and **o** as proton 3 ($\Delta\delta$ = 0.15 ppm); and **d** and **n** as proton 5 ($\Delta\delta$ = 0.08 ppm).

Following this assignment, two signals labelled **k** and **l** remain. Signal **k**, overlapping with *trans* **a**, is broad and more intense than **l**, and is expected to be the combined signals of the terminal amine group protons, 15 that present themselves as *trans* **a** and part of **b** ($\Delta\delta$ = -0.13 and 1.06). The remaining *cis* peak has a chemical shift that

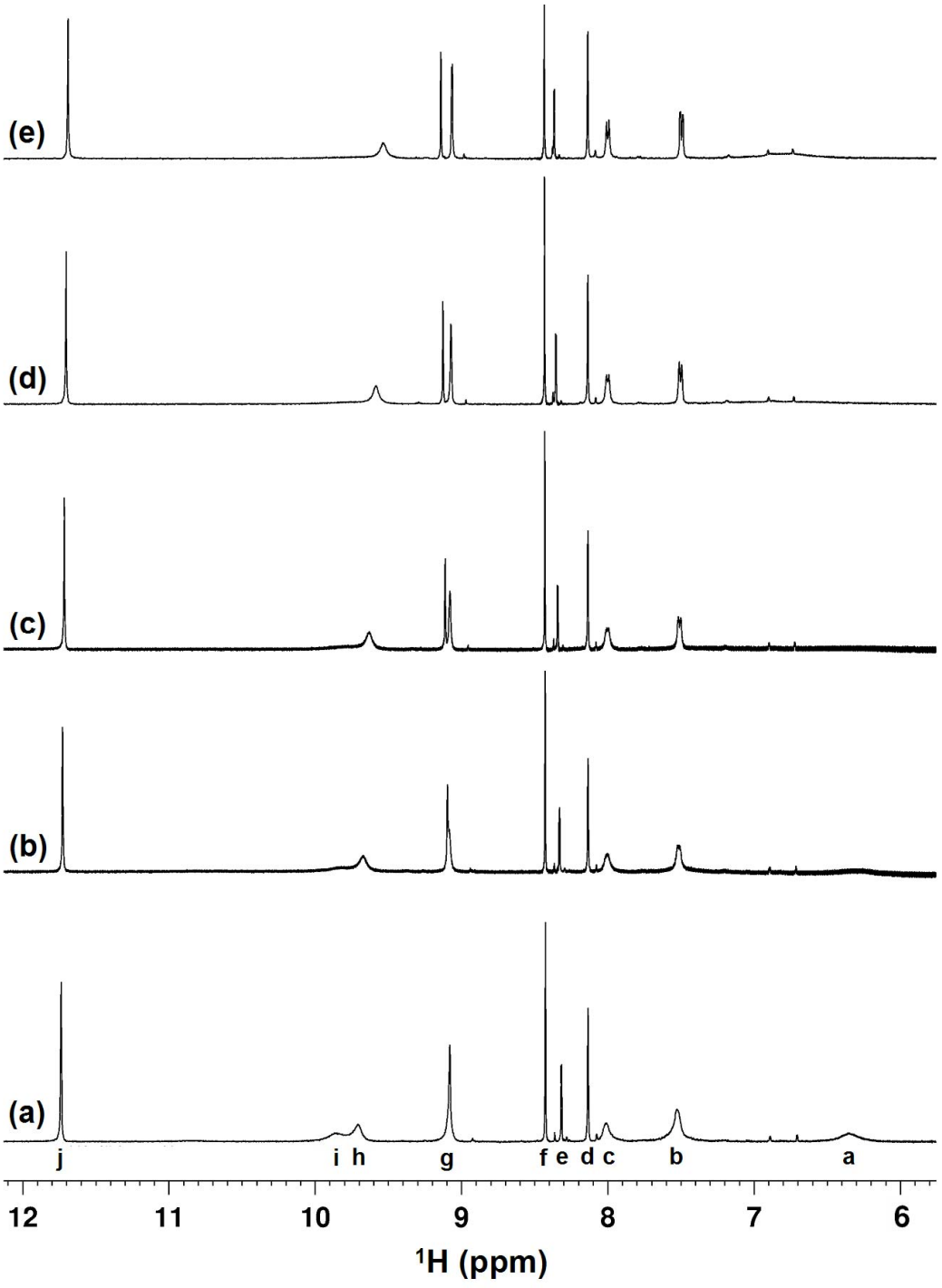

Figure 4.18: The ^{1}H NMR Spectra of 273/13 (1.62 mM) in d_6-DMSO. Spectra recorded at (a) 298 K (b) 308 K, (c) 318 K, (d) 328 K and (e) 338 K.

could be generated from proton 8 or 9. In 273/8 a *cis* signal was not observed for proton 9 suggesting the observed signal will relate to proton 8. However, the lack of any distinguishing features in the *trans* and *cis* peaks do not allow a conclusion to be drawn. *Cis* signals are also missing for proton 12 and the proton expected to move as the molecule undergoes tautomerism. It is assumed the low intensity of signals **h**

and **i**, noted earlier, is preventing their detection in the *cis* isomer. Despite the lack of certain assignments, and the broad nature of some of the peaks, it remains clear that photoisomerisation is occurring, and since the signals observed in the *cis* isomer revert to *trans* signals under thermal conditions, this remains the only process occurring. The composition of the photostationary state can be estimated as 18% *cis* . Assignments have been compiled in Table 4.11.

Trans Signal	*Cis* Signal	Proton Assignment	$\Delta\delta$/ppm
a	k	15	-0.13
b	k	15	1.06
	*	9	*
c	*	8	*
d	n	5	0.08
e	o	3	0.15
f	p	6	0.13
g	m	1	1.44
	r	7	0.26
h	*	12	*
i	*	OH/NH	*
j	q	14	2.98

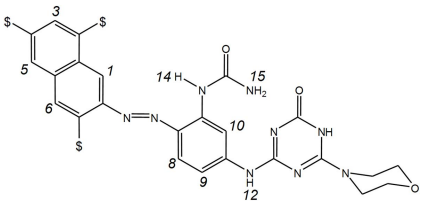

Table 4.11: ^{1}H NMR assignments for the *trans* and *cis* isomers of 273-13 in d_6-DMSO, and the difference in chemical shift between *cis* and *trans* isomers, $\Delta\delta$.
* Unobtainable.

4.3.5 Discussion of *Trans* Isomer Naphthyl Assignments

Figure 4.19 shows five different sulfonated naphthyl azo systems with the chemical shifts for the *trans* isomer protons labelled. The **AF** group (Figure 4.19 (e)) is derived from measurements conducted previously by Tait.[30] Initial observations regarding the the **AC** and **BD** dyes established a certain level of understanding regarding the effect of sulfonate groups adjacent to protons on the same ring, and on the second fused ring (Section 4.3.1.3). Extending this knowledge first to the **ACF** dyes allowed for straightforward assignment. Positioning of the additional **F** sulfonate caused a decrease in the shielding of proton 7, resulting in a rise of 0.5 ppm for the signal. An approximate rise of 1 ppm was observed for proton 5 on the adjacent fused ring, a change mirrored by the effect on proton 1 of the **A** sulfonate. For the **ACG** dyes, the additional sulfonate group *ortho* to the azo bond raises the chemical shift of proton 6 relative to that in the **AC** dyebase by 0.35 ppm. Comaparing Figure 4.19 (c) and (e), removal of the **C** sulfonate provides additional shielding for proton 3, a decrease of 0.35 ppm being

observed. Furthermore, a 0.3 ppm reduction in the chemical shift of proton 5 is seen after removal of this sulfonate. It is quite clear that a sulfonate adjacent to a proton on the same ring will cause the proton to experience less shielding, but the effect on the nearest proton on the other fused ring is even more profound.

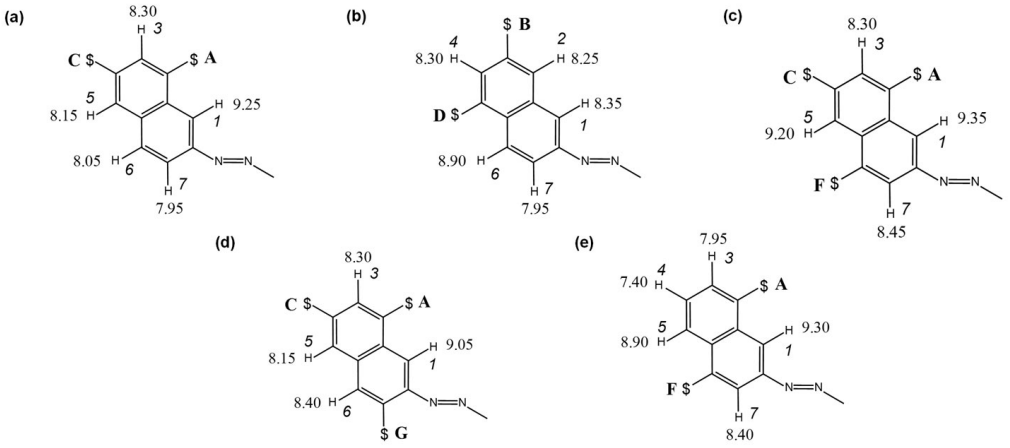

Figure 4.19: Observed *trans* isomer chemical shifts for four sulfonated naphthyl groups (a) **AC**, (b) **BD**, (c) **ACF**, (d) **ACG** and (e) **AF** (corrected). Chemical shifts are rounded to the nearest 0.05 ppm.

4.3.5.1 Correction of Previous Assignments

During the detailed analysis of the ^{1}H NMR spectra for the *trans* isomers of several sulfonated naphthyl groups performed in this research, it has become apparent that assignments presented by KM Tait for the **AF** sulfonated dyes contain some errors.[30] The chemical shifts depicted in Figure 4.19 (e) have been corrected in light of the present work. Tait studied only **ACG** and **AF** dyes. During the analysis of the **AF** dyes, proton 7 and proton 1 were assigned the wrong way round based on the assumption that proton 7, between the azo and a sulfonate group, would experience less shielding than proton 1. The doublets observed for protons 3 and 5 were also assigned wrongly, since the sulfonate adjacent to proton 3 would be expected to produced a more electron deficient environment, causing the peak to display at higher ppm. It is clear from the earlier discussion that the assignment of dyebases 271/64 and 284/43 has helped to prove that the adjacent sulfonate on the neighbouring fused ring has a greater influence on the proton environment than directly adjacent sulfonate groups. As a result, tables of Tait's four **AF** dyes are presented with reassigned proton values in Appendix A.

4.4 Correlating Experimental Observations With Calculated Structures

Ab initio DFT calculations of the ground state *trans* and *cis* isomer geometries have been conducted to assist in explaining experimental observations made using NMR spectroscopy. In this chapter the computational work is concerned with identifying the geometries of the isomers, and how these geometries are affected by structural changes to the basic yellow dye chromophore. Additionally, these calculated structures are used in Chapter 5 to help rationalise results derived from a kinetic analysis of the photoisomerisation processes for each dye.

This section is divided into a detailed examination of the minimum energy structures, followed by an examination of features in the NMR spectra, and how the structures relate to the spectral observations.

4.4.1 Calculation Method and Approximations

All dyes presented herein are geometry optimised structures calculated using the B3LYP/6-31G(d,p) level of theory/basis set. The method for deriving the optimised structures is defined in Section 3.5. For the larger dyes, further torsions to those defined in Figure 3.5, relating to the 'second leg' were adjusted where necessary to ensure the potential energy surface was thoroughly probed for minimum energy structures. The sulfonate groups present in all molecules were approximated by sulfonic acid groups. This is a common approximation to make for charged species. Abbott *et. al.* investigated the use of density functional theory calculations for the hydrazo dye Orange II, and derivatives thereof.[84] Orange II is a small dye, consisting of a *para*-sulfonated benzene ring joined by an azo bond to an *ortho*-hydroxynaphthyl group.
In solution, the charge on each SO_3^- is balanced by a Na^+ counter ion. For the purposes of the calculation, which refer to isolated gas-phase molecules, sulfonic acid groups to approximate the $–SO_3Na$ groups. DFT calculations were performed on structures containing: no sulfonate group; a negatively charged SO_3^- group; or an SO_3H group. Compared with experimental results for dye molecules containing SO_3Na groups (X-ray structures and spectral properties of Orange II in solution), calculations on structures with SO_3H groups gave the best match with the experimental results indicating this structure provides the best model for the dye. Additional studies have used sulfonic acid groups in chemical calculations, again reporting poor fit to experimental data when using charged sulfonate groups.[91,92] Furthermore, similar tactics have been used to model carboxylate groups, the protonated equivalents providing results more consistent with experimental observations.[93] This evidence means approximating the $–SO_3Na$

groups to sulfonic acid is justified in the following study.

Section 3.5 describes the method of varying bond angles and torsions undertaken in this research to search for minimum energy structures. To illustrate the necessity of probing the potential energy surface for minima, four mininum energy structures of molecule 273/10 are presented in Figure 4.20. Each structure is a minimum on the potential energy surface (verified by the absence of any negative frequencies), yet they all have different energies. It is clear that adjusting two torsional angles, τ_1 and τ_2 in Figure 3.5, can produce four different minima for the *trans* isomer of this dye. The energies of each conformation are presented in Table 4.12, where structure **(b)** is identified as the lowest energy *trans* structure, and the global minimum on the ground state potential energy surface.

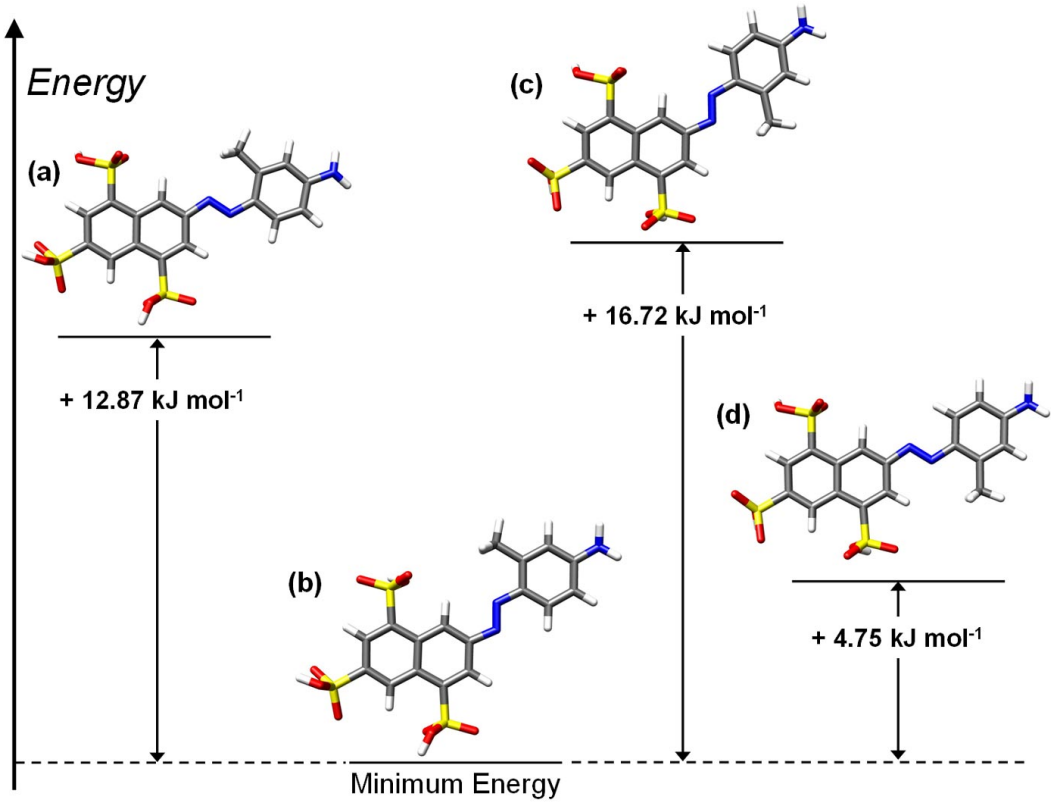

Figure 4.20: Four structures corresponding to potential energy minima of *trans* 273/10.

It follows that there is unlikely to be only one potential well for the *cis* isomer. Features of each NMR spectrum can be interpreted in this light: the sharp nature of the peaks in the spectrum indicate that either one structure, or a rapid exchange between more than one conformational structure, for each (*trans* or *cis*) isomer is present. Where the energy difference between two minimum energy structures is small, it is feasible fast exchange will be present. Structures presented in this section have been derived using

Minimum Energy Structure	Absolute Energy/ Hartrees	Relative Energy/ kJ mol^{-1}
a	-2692.47326692	+12.87
b	-2692.47816796	0.00
c	-2692.47179829	+16.72
d	-2692.47635881	+4.75

Table 4.12: Calculated data for the four structures of *trans* 273/10, depicted in Figure 4.20; structure (b) is identified as the global minimum. Calculations were performed at the B3LYP/6-31G(d,p) level of theory.

the aforementioned experimental procedure, through varying specified torsional angles and allowing all bond lengths, angles and dihedrals to relax. Calculating minimum energy structures of the second leg dyes proved computationally expensive due to the size of the molecules. The new groups often contained many degrees of freedom and a great deal of user interaction was required in order to explore the different minima on the potential energy surface, along with substantially increased demand on the processor. Molecules of this size are certainly at the limit current computational resources can handle when using the method outlined for these dyes. In certain cases, experimental data from ^{1}H NMR studies can be used intuitively in searching for the minimum energy structure, cases of which can be seen in this section.

4.4.2 Structural Analysis

A general discussion of the calculated structures is presented in this section. Due to the number of structures, they are split between two figures and discussed in turn. Figure 4.21 shows the calculated structures for the *trans* and *cis* isomers of dyes 273/19 and 269/56, and their respective dyebases, along with the two additional dyebases. For the purpose of comparison, structures are presented with the **ACF** sulfonated naphthyl ring in the same orientation for all of the *trans* structures, and similarly for the *cis* isomer. Each structure has been labelled with intramolecular distances <3 Å in black, and proton numbers in red. A summary of the calculated energy difference between the *cis* and *trans* isomers, and dipole moments for each isomer can be found in Table 4.13. Additional data regarding selected bond lengths, angles and torsions are available in Table 4.14.

Examining the *trans* isomer structures first (Figure 4.21 **a**, **c**, **e**, **g**, **i** and **k**), shows that the molecules do not all adopt the same orientation around the azo linkage. Dyebase **a** and its respective reactive dye **c** take on different orientations with respect to torsion about the naphthyl C–N bond, whereas dyebase **e** and dye **g** have the same torsional conformation. Furthermore, the two dyebases **i** and **k** which are less complicated by

Molecule	Energy Difference kJ mol^{-1}	*Trans* Dipole Moment/ Debye	*Cis* Dipole Moment/ Debye
273/10	64.3	8.9	6.0
273/19	64.7	5.6	3.5
269/52	82.0	5.5	4.7
269/56	81.2	6.0	6.3
271/64	46.0	6.7	9.4
284/43	45.6	9.3	5.6
273/5	93.3	9.4	7.5
273/6	65.8	6.6	4.0
273/8	60.8	3.9	6.0
273/13	61.1	5.0	9.7

Table 4.13: Calculated energy differences and dipole moments for the *trans* and *cis* isomers of the dye and dyebases.

		Length/Å			Angle/degrees		Torsion/degrees
		C_n–N	N=N	N–C_p	C_n–N=N	N=N–C_p	C_n–N=N–C_p
273/10	*Trans*	1.412	1.271	1.389	113.581	116.401	179.239
	Cis	1.423	1.257	1.409	124.440	124.799	-14.442
273/19	*Trans*	1.412	1.267	1.400	113.975	115.746	-179.885
	Cis	1.427	1.253	1.417	124.061	124.415	-13.093
269/52	*Trans*	1.405	1.280	1.365	111.704	119.461	-176.931
	Cis	1.415	1.264	1.389	124.752	127.589	-14.361
269/56	*Trans*	1.411	1.274	1.374	111.677	119.266	-177.266
	Cis	1.419	1.257	1.400	125.799	127.579	12.383
271/64	*Trans*	1.412	1.269	1.397	114.036	115.474	180.000
	Cis	1.425	1.254	1.418	124.960	124.795	-12.039
284/43	*Trans*	1.413	1.268	1.398	113.988	115.606	180.000
	Cis	1.427	1.253	1.420	125.156	125.015	11.160

Table 4.14: Selected bond lengths, angles and torsions for the *trans* and *cis* isomers shown in Figure 4.21. C_n is naphthyl ring carbon adjoining the azo bond, and C_p the phenyl ring carbon.

ortho phenyl substituents take on the same naphthyl-azo conformation seen in **c**. Upon closer inspection, **e** and **g** appear to gain some stability from interactions of the ureido group that is present on the benzene ring. The terminal amine reaches over towards the **A** sulfonate in both cases, forming a hydrogen bonding interaction of 2.2 Å between the amine protons and the sulfonate group oxygen. This also brings the NH proton (proton 14) of the ureido group close to the phenyl side azo nitrogen, with a distance of 2.11-2.12 Å. In contrast to this, no hydrogen bonding interactions between phenyl and naphthyl substituents are observed for the methyl-containing *trans* isomers (**a** and **c**),

and the lack of conformation locking through intramolecular interactions is reflected in the alternative geometries around the azo bond. In both the dye and dyebase structure, this methyl group is closer to the phenyl azo nitrogen, with higher energies expected if

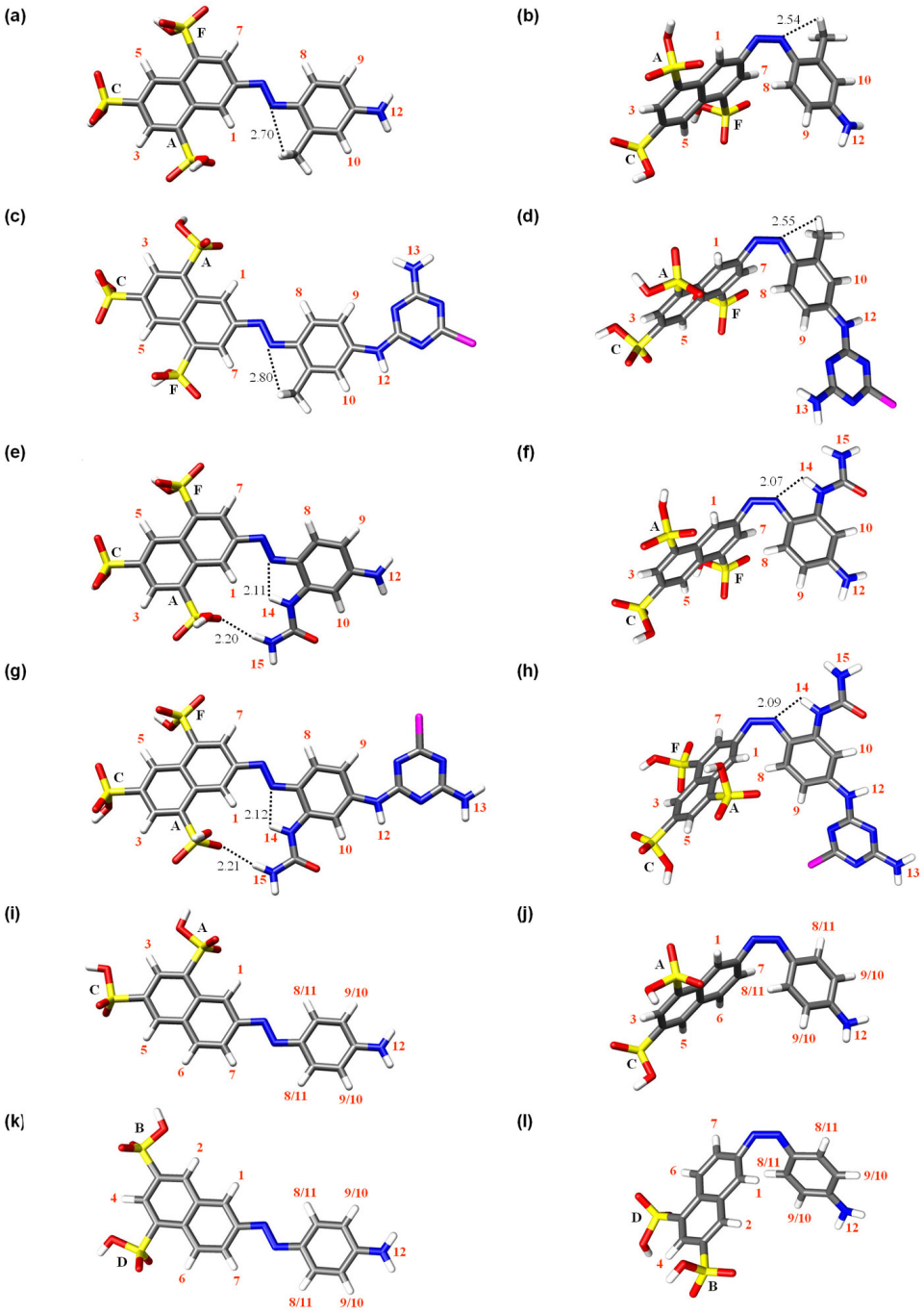

Figure 4.21: Minimum energy stuctures of the dye and dyebases (a) *trans* 273/10, (b) *cis* 273/10, (c) *trans* 273/19, (d) *cis* 273/19, (e) *trans* 269/52, (f) *cis* 269/52, (g) *trans* 269/56, (h) *cis* 269/56, (i) *trans* 271/64, (j) *cis* 271/64, (k) *trans* 284/43, (l) *cis* 284/43. Distances (Å) are presented for interactions < 3 Å. Proton numbers are labelled in red.

the molecules were to orientate themselves with the methyl close to the naphthyl azo nitrogen (*c.f.* Figure 4.20). Lack of any *ortho* substituents also allows these dyebases to take the most stable conformation, not governed by intramolecular interactions. For the reactive dyes (**c** and **g**), the chlorotriazine ring remains roughly co-planar with the benzene ring, with a deviation of less than 3°.

In the interests of comparability, Figure 4.21 displays the *cis* isomers with the azo linkage aligned identically in each case, allowing a comparison of the naphthyl and phenyl ring arrangements for each *cis* isomer. The *cis* structures contain azo dihedral (C–N=N–C) angles from 11-15° (see Table 4.14). Conjugation across this bond present in the *trans* isomer will be diminished in the *cis* isomer due to disruption of the extended π system, and is evidenced by a lengthening of the C_p–N and C_n–N bonds, and shortening of the azo bond. In all cases the phenyl ring is orientated with the *ortho* substituent away from the naphthalene ring, to avoid a steric clash, and proton 8 points towards the naphthyl component.

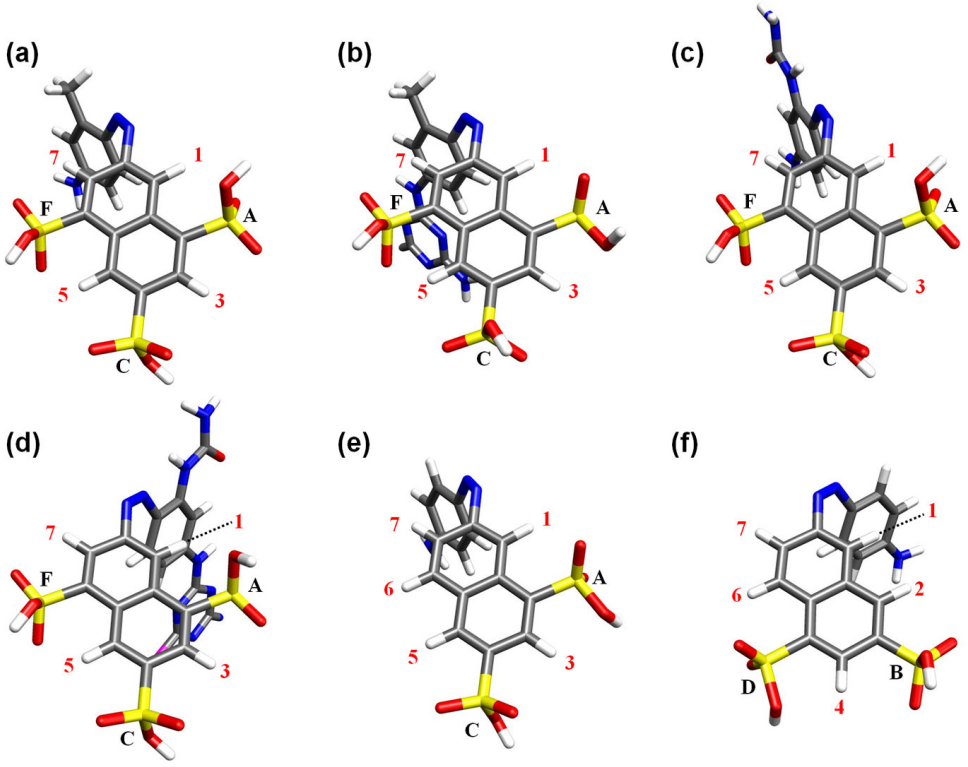

Figure 4.22: *Cis* isomer structures of molecules (a) 273/10, (b) 273/19, (c) 269/52, (d) 269/56, (e) 271/64, (f) 284/43. Proton numbers are labelled in red.

Some features of the *cis* isomers may be visualised more clearly in Figure 4.22. Although the angle of torsion in the azo bond is similar for each of the *cis* isomers shown, the sign of this torsion is not. For molecules **a**, **b**, **c** and **e** the angle of twist from zero

is in the opposite direction to that of **d** and **f**. In the latter two molecules (269/56 and 284/43) the phenyl ring is orientated differently to that seen in the other dyes. In the *cis* isomers of 273/10, 273/19, 269/52, and 271/64 (**a**, **b**, **c** and **e**) orientation of the phenyl ring causes proton 7 to point towards the ring to a greater degree than proton 1. An alternative conformation is seen in the other two molecules, with proton 1 approaching the phenyl ring more than proton 7.

Further to the aforementioned studies of **AC**, **BD** and **ACF** sulfonated dyes, the 'second leg' dyes presented in Figure 4.23 are examined here. Calculating minimum energy structures of the dyes was more computationally expensive due to the size of

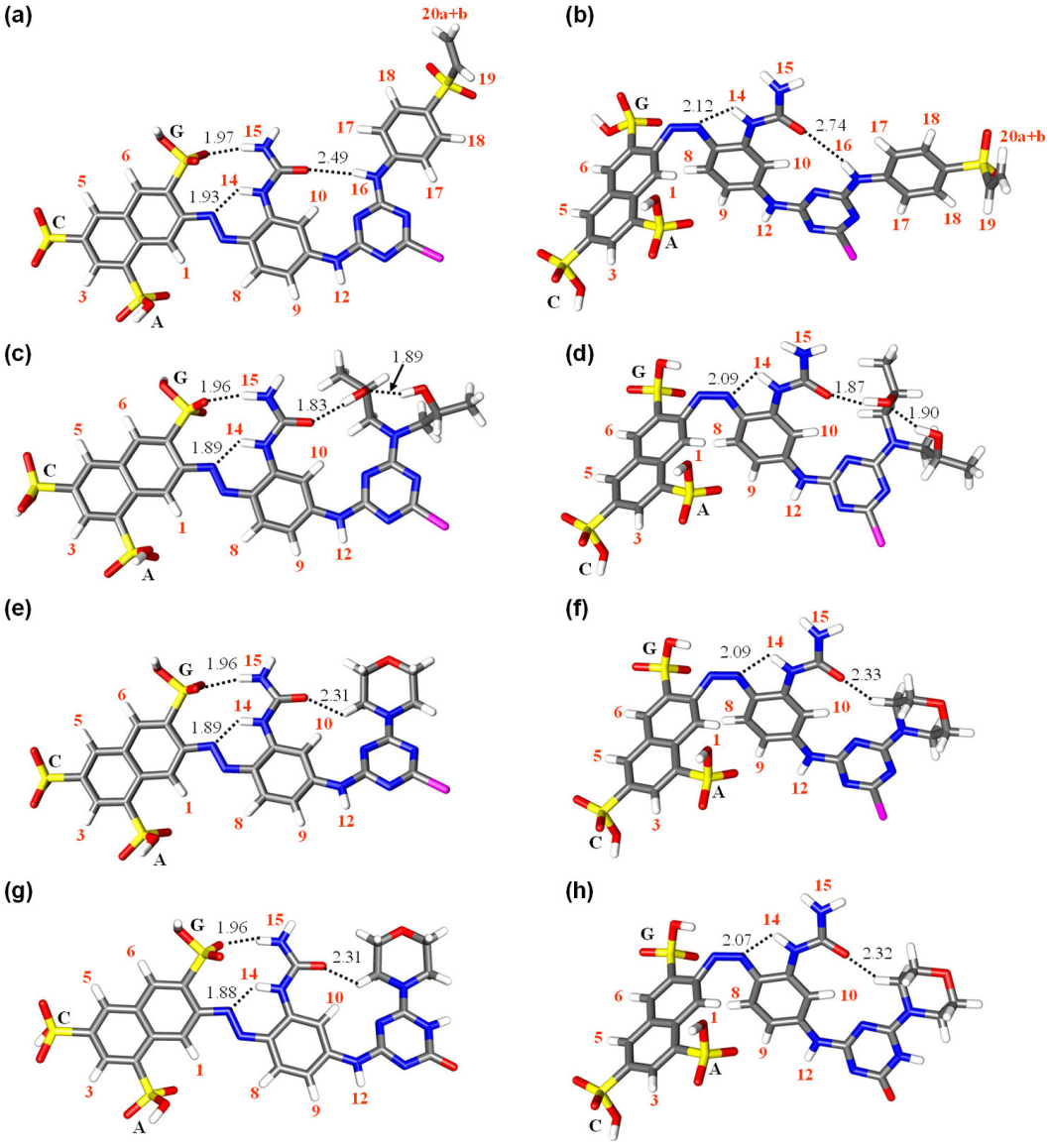

Figure 4.23: Minimum energy stuctures of the 'second leg' dyes (a) *trans* 273/5, (b) *cis* 273/5, (c) *trans* 273/6, (d) *cis* 273/6, (e) *trans* 273/8, (f) *cis* 273/8, (g) *trans* 273/13, (h) *cis* 273/13. Distances (Å) are presented for interactions <3 Å.

the molecules. As noted earlier, dyes of this size are at the extreme limits of what is possible using the computational resources employed for these studies. Further details relating to azo bond lengths and angles are presented in Table 4.15.

		Length/Å			Angle/degrees		Torsion/degrees
		C_n–N	N=N	N–C_p	C_n–N=N	N=N–C_p	C_n–N=N–C_p
273/5	*Trans*	1.406	1.281	1.371	113.295	119.396	176.240
	Cis	1.416	1.256	1.396	126.135	126.799	14.468
273/6	*Trans*	1.406	1.282	1.370	113.209	119.995	-177.101
	Cis	1.423	1.264	1.385	126.544	127.429	15.699
273/8	*Trans*	1.405	1.282	1.369	113.168	120.093	176.453
	Cis	1.422	1.265	1.383	126.488	127.165	16.252
273/13	*Trans*	1.403	1.284	1.367	113.151	120.164	176.527
	Cis	1.421	1.267	1.381	126.472	127.294	16.644

Table 4.15: Selected bond lengths, angles and torsions for the *trans* and *cis* isomers shown in Figure 4.23. C_n is naphthyl ring carbon adjoining the azo bond, and C_p the phenyl ring carbon.

Comparing the *trans* isomers for the four dyes studied here shows the structural arrangement is very similar across the naphthalene and benzene ring components. In each case the ureido, as for the *trans* isomers of **ACF** molecules 269/52 and 269/56, hydrogen bonds *via* the terminal amine protons, to the oxygen on a sulfonate group. The difference in structural arrangement between the *trans* **ACF** and **ACG** pattern occurs in the proximity of the interaction. The **G** sulfonate causes an alteration in the arrangement of the benzene and naphthalene rings around the azo bond when compared to the **ACF** dyes examined earlier. The *ortho* sulfonate allows closer interaction between a sulfonate and the amine protons, with O···H distances of 1.96 Å compared with ≈2.20 Å for the **ACF** dyes. The new orientation brings the ureido NH proton close to the naphthyl azo nitrogen, with a distance of approximately 1.9 Å, compared to the *ca.* 2.1 Å distance between this proton and the phenyl azo nitrogen in the **ACF** dyes.

The orientation of the linking group amine proton and chlorotriazine ring is consistent across structures **a**, **c**, **e** and **g** in Figure 4.23, as is the orientation of the chlorine and 'second leg' of the dye, relative to the remainder of the structure. Where the chlorine group was not present in 273/13, the same conformation was observed with an oxygen atom in its place. There is a stabilising interaction between the second leg of each dye, and the ureido group. Molecule 273/5 orientates itself so the proton on the amine group bridging the chlorotriazine ring and 'second leg' benzene ring points towards the carbonyl oxygen of the ureido group. For *trans* 273/6 (**c**), the most favourable

orientation allows the hydroxyl groups of the second leg to hydrogen bond with each other, and with the ureido carbonyl oxygen. Both 273/8 (**e**) and 273/13 (**g**) display close proximity of the morpholine ring to the ureido carbonyl group. This interaction is substantially weaker than that of the hydroxyl proton of 273/6. However, this conformation has a lower energy than conformations where the second leg was allowed to stretch away from the rest of the structure by switching it with the chlorine atom.

The *cis* isomer structures of the 'second leg' dyes (Figure 4.23 **b**, **d**, **f** and **h**) are presented with identically aligned azo linkages to ease comparison between structures. In constrast to the simpler dye and dyebase *cis* isomers discussed earlier, the orientation of the naphthyl and phenyl rings are locked to one conformation for all of these dyes. Closer examination suggests that steric hindrance from the *ortho* naphthyl sulfonate is directing this conformation. The molecules orientate themselves so the bulky substituents face away from the opposing ring system. This means proton 1 and proton 8 always point towards each other to give the minimum energy structure. If the alternative conformations are considered, we could expect the large sulfonate or ureido group to cause a degree of steric hindrance with the facing aromatic ring, raising the energy of the structure. In the *cis* isomers of the ureido-containing **ACF** molecules, the NH proton remained close to the nearest azo nitrogen, with a distance of approximately 2.09 Å. A similar conformation of the ureido group exists in the **ACG** dyes presented here. This also encourages the interaction of the carbonyl oxygen with the 'second leg' as noted for the *trans* isomer structures. In all of the cases studied, the lowest energy *cis* isomer has the same conformational arrangement for the phenyl, chlorotriazine and 'second leg' to that displayed in the corresponding *trans* isomer. This implies that isomerisation only occurs through a geometrical rearrangement at the azo bond, and does not induce any other geometric changes in the *cis* isomer conformation to bring about the minimum energy structure.

4.4.3 Matching Experiment With Theory

This section concentrates on identifying correlations between calculated structures and experimental NMR observations. For ease of comparison, features relating to the NMR spectra are identified separately, for instance by naphthalene substitution pattern, or for ureido group observations. In an earlier piece of work, Tait demonstrated that chemical shifts of small disperse azo dyes could be calculated, and compared well to experimental NMR chemical shifts.[90] However, this work was conducted using the B3LYP/6-311G+(2d,2p) method. This large basis set was necessary to fully optimise the structures for the calculation of chemical shifts. Due to the size of the molecules presented in this work, and their demand on computing power and time, such calcula-

tions are far beyond the scope of the research. However, it is possible to use the NMR spectra to validate the calculated structures, and likewise use the structures to explain particular features of the NMR spectra.

4.4.3.1 ACF Sulfonated Naphthyl Proton Pattern

Across the four **ACF** molecules studied, the *trans* isomer pattern for protons 1, 3, 5 and 7 in the ^{1}H NMR spectra appear consistent. Referring to the structures in Figure 4.21 (**a**, **c**, **e** and **g**) not all *trans* isomers exhibited the same orientation around the azo bond. Due to the planarity of the structures, the protons on the naphthyl group are not expected to interact with any other parts of the structure in the *trans* geometry, and only experience the circulating ring current of the naphthyl group. Since no other intramolecular influences are present, this indicates that although a different azo bond orientation is present in 273/19 to the other three molecules, it is unlikely this difference would be apparent in the ^{1}H NMR spectrum of the *trans* isomer.

The *cis* isomer signals deviate from the *trans* isomer signals, allowing direct observation of the two different species in the NMR spectrum. This difference is due to shielding effects, the protons being placed in a different environment to that experienced in the *trans* isomer. The difference in the chemical shifts for the **ACF** dye protons is summarised in Table 4.16.

Proton	273/10 $\Delta\delta$	273/19 $\Delta\delta$	269/52 $\Delta\delta$	269/56 $\Delta\delta$
1	0.64	0.86	0.59	0.56
3	0.04	0.08	0.01	0.03
5	0.11	0.15	†	0.12
7	1.27	1.19	0.76	1.28
8	1.71	1.58	1.57	1.58
9	0.58	†	0.64	0.14
10	0.07	0.42	0.40	0.14
12	0.41	0.26	0.17	0.08
13	∗	0.09	∗	†
14	∗	∗	†	0.15
15	∗	∗	0.13	0.14
Me	0.16	0.36	∗	∗

Table 4.16: $\Delta\delta$ values for **ACF** substituted dye and dyebas pairs.
∗ Not applicable.
† Unobtainable.

If the *cis* isomer proton pattern were a fingerprint, as in the *trans* isomer, the change

in chemcial shift, $\Delta\delta$ for protons 1, 3, 5 and 7 should be fairly consistent across the molecules studied. For protons distant from the azo bond, *i.e.* 3 and 5, only very small changes in the chemical shifts from their *trans* equivalent is expected since the shielding environment is not anticipated to undergo a great deal of change. However, $\Delta\delta$ for the protons *ortho* to the azo bond is not the same for all molecules. A consistent change in chemical shift for proton 7 in molecules 273/10, 273/19 and 269/56 indicates this proton benefits from a similar degree of shielding in these *cis* isomers. The change in proton 1 shows the amount of additional shielding received is less than for proton 7. Adding a reactive group to the methyl substituted dyebase results in a marginal change in the shielding experienced by protons 1 and 7 in the *trans* and *cis* isomers, as evidenced by small changes in $\Delta\delta$ for each proton. Larger changes in $\Delta\delta$ are apparent between the dyebase and reactive dye of the ureido **ACF** molecules. Dyebase 269/52 displays different characteristics in the *cis* isomer spectrum, leading to a reduction in $\Delta\delta$ for proton 7 of approximately 0.5 ppm compared with the other three molecules. This evidence alone is indicative that the *cis* isomer of dyebase 269/52 takes on a different conformation to that of the other three **ACF** molecules, an experimental observation not reflected in the calculated structure.

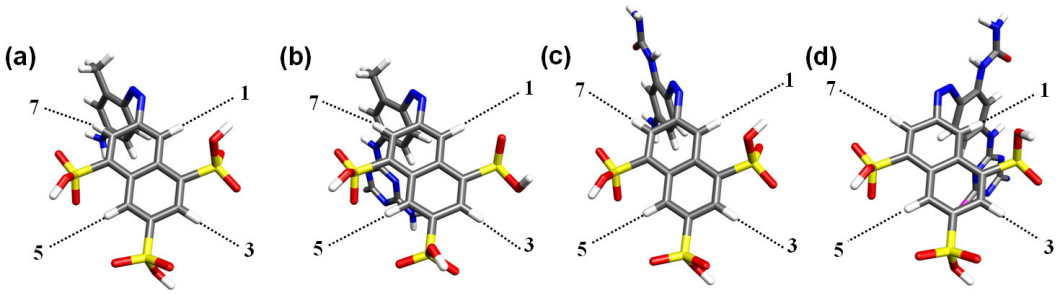

Figure 4.24: *Cis* isomer structures of **ACF** molecules (a) 273/10, (b) 273/19, (c) 269/52, (d) 269/56. Naphthyl protons are labelled.

Figure 4.24 shows the *cis* isomers for the four **ACF** dyes studied, with the naphthyl protons labelled. Structural calculations for *cis* 273/10 and 273/19 are consistent with the NMR measurements; however, structures for *cis* 269/52 and 269/56 shown in Figure 4.21 (**f** and **h**) appear inconsistent. The *cis* isomers of molecules 273/10 and 273/19 are orientated so that proton 7 points towards the shielding cone of the phenyl ring. This explains the asymmetry in the chemical shift differences for these protons, with proton 7 experiencing a greater degree of shielding to proton 1. In all cases, the isomerisation-induced change in chemical shift for proton 7 is greater than that for proton 1. The changes in chemical shift for the **ACF** dyes are quite comparable for these two protons, apart from dyebase 269/52, where $\Delta\delta$ is lower in proton 7 and slightly higher in proton

1. From the NMR observations, it is logical to expect that *cis* 269/56 would display a similar orientation of the aromatic rings to the methyl substituted dyes. Figure 4.25 provides a rationalisation of these observations. Structures **a** and **b** are two minimum energy structures for *cis* 269/56, with **a** predicted as the lowest energy *cis* structure. However, **b** is only 1.8 kJ mol^{-1} higher in energy, and is consistent with the experimental results. The NMR data represent an average of all populated forms of the structure. Since the NMR signals are sharp for the *cis* isomer species of each dye, the data suggest that interconversion between any conformers is rapid. Hence, the equilibrium between these structures is likely to lie towards that of (b) in the figure, according to the NMR data. Dyebase 269/52, with a reduced $\Delta\delta$ for proton 7 and increase in proton 1 to expectation, can also take on the minimum energy structure shown in Figure 4.25 (d), a mere 0.25 kJ mol^{-1} higher in energy than (c). It is likely an equilibrium between these structures will shift more towards (d) compared with the other dyes, bringing about these differences in the asymmetry of $\Delta\delta$. This is an indication that where there exist minimum energy conformations very close in energy, the lowest energy structure *in vacuo* (calculation) may not correspond to that observed experimentally. However, it is notable that these are the only cases where a discrepancy between calculated structures and NMR observations have been found.

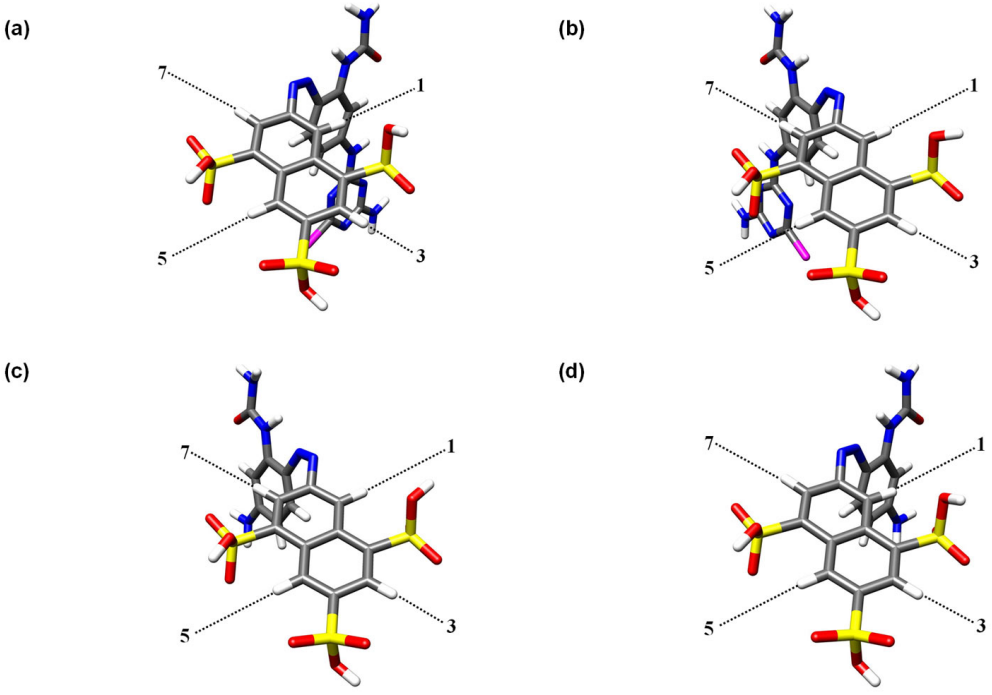

Figure 4.25: Calculated structures for the *cis* isomers of dye 269/56 (a) predicted *cis* minimum, (b) higher energy *cis* minimum, and dyebase 269/52 (c) predicted *cis* minimum, and (d) higher energy *cis* minimum. Appropriate proton numbers are identified.

4.4.3.2 ACG Sulfonated Naphthyl Proton Pattern

Each ^{1}H NMR spectrum for the *trans* isomer of the **ACG** sulfonated dye demonstrated a highly consistent pattern. As noted for the **ACF** dyes in Section 4.4.3.1, the influence from other structural components across the azo bond is unlikely to demonstrate a profound effect on the chemical shifts of the *trans* isomer naphthyl protons since the structure is expected to be planar, preventing intramolecular interactions. This explains the consistency of NMR signals despite alterations to the chlorotriazine substituents between dyes. Examination of the *trans* isomer structures in Figure 4.23 provides additional support for these observations. The structures are relatively planar, and although an intramolecular interaction is present between the ureido group and the *ortho* sulfonate, it occurs in all cases and is unlikely to affect the naphthyl proton environments significantly. This interaction effectively locks the naphthyl and phenyl rings around the azo bond to the same conformation for each **ACG** dye studied.

Table 4.17 contains the available $\Delta\delta$ values for the four **ACG** dyes studied here. All changes in chemical shift are very similar across the four dyes, indicating a high degree of consistency between both the *cis* and *trans* structures. Unlike the *cis* isomer proton patterns in the **ACF** naphthyl group, only a single *cis* isomer pattern is found for these dyes. An examination of the *cis* isomer structures in Figure 4.23 supports this finding, with all structures displaying the same conformation of naphthyl and phenyl rings around the azo bond. Proton 1 demonstrates a large isomerisation-induced change in chemical shift and must experience a large degree of shielding from facing into the shielding cone of the phenyl ring in the *cis* isomer. This is also true of proton 8, where present, facing into the shielding cone of the naphthyl ring with a chemical shift change similar to that experienced by proton 1. Protons 3, 5 and 6, further from the geometrically altered azo bond and opposing phenyl ring, are relatively unaffected.

The consistency of the $\Delta\delta$ values for the four 'second leg' dyes in Table 4.17, and the good correlation of these NMR chemical shift changes with the calculated structures supports the validity of the structures presented in Figure 4.23.

4.4.3.3 AC and BD Sulfonated Naphthyl Proton Patterns

The *trans* isomer protonation pattern for dyebases 271/64 and 284/43 were discussed earlier in Sections 4.3.1.3 and 4.3.5, to assist the assignment of protons on the **ACF** and **ACG** sulfonated groups. The observed changes of chemical shift, and how these relate to calculated structures are examined here. Calculated minimum energy structures for the *trans* and *cis* isomers of these dyes are presented in Figure 4.21, with the related changes in chemical shift available in Table 4.18. Only protons 1, 6 and 7 of the

Proton	273/5 $\Delta\delta$	273/6 $\Delta\delta$	273/8 $\Delta\delta$	273/13 $\Delta\delta$
1	1.44	1.43	1.45	1.44
3	0.16	0.15	0.14	0.15
5	0.08	0.09	0.07	0.08
6	0.12	0.15	0.13	0.13
8	$\approx$1.3†	1.34	1.36	$*$
9	$*$	0.87	$*$	$*$
10	$*$	0.43	$*$	0.26
12	0.38	0.44	0.45	$*$
14	2.92	2.89	2.98	2.98
15	-0.12 1.09	-0.13 1.05	-0.13 1.08	-0.13 1.06

Table 4.17: Changes in chemical shift for the **ACG** substituted 'second leg' dyes.
$*$ Unobtainable.
†Estimated from partially resolved signals.

naphthyl group may be compared due to structural differences in sulfonation pattern of the second fused ring. The calculated structures indicate the *trans* isomers to take on the same conformation around the azo bond. The difference in the *trans* isomer naphthyl chemical shifts can be attributed to the movement in sulfonate groups noted earlier, since no other intramolecular effects are present.

Proton	271/64 $\Delta\delta$	284/43 $\Delta\delta$
1	0.68	0.81
2	N/A	0.20
3	0.03	N/A
4	N/A	0.08
5	0.08	N/A
6	0.19	0.18
7	1.25	1.03
8/11	0.96	0.97
9/10	0.34	0.34
12	0.28	0.37

Table 4.18: $\Delta\delta$ values for **AC** and **BD** sulfonated molecules.

The larger changes in chemical shift anticipated for protons directly adjacent to the azo bond (1, 7, 8/11) can be seen in these two molecules, with smaller changes for protons more distant from the azo linkage. An asymmetry in the chemical shift changes of protons 1 and 7 suggests a different conformation around the azo bond in the *cis*

isomer may be present. Compared to the **AC** sulfonated dyebase, the **BD** dyebase displays an increase in additional shielding for proton 1, and an associated decrease for proton 7, somewhat similar to that observed in **ACF** dyebase 269/52 when compared to the other three **ACF** molecules.

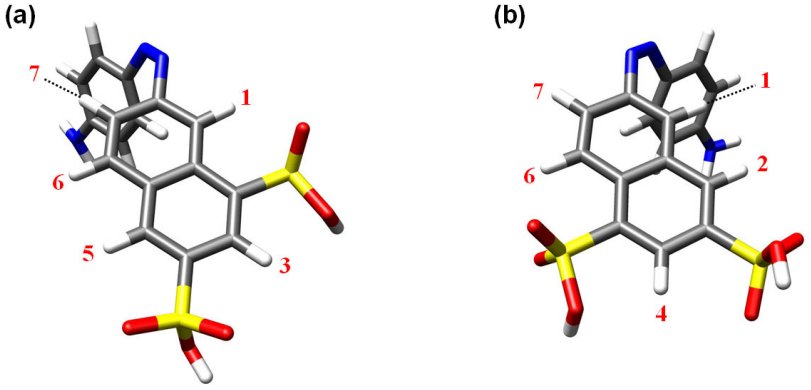

Figure 4.26: Calculated minimum energy structures for the *cis* isomers of (a) 271/64 and (b) 284/43.

The minimum energy structures for the *cis* isomers of these two dyebases, reproduced in Figure 4.26, clearly show the two *cis* isomers to have different conformations around the azo bond. On closer inspection, proton 7 of 271/64 appears closer to the shielding cone of the nearby phenyl ring compared with proton 1, an observation expected from the magnitude of the $\Delta\delta$ values. In constrast, dyebase 284/43 shows a smaller $\Delta\delta$ for proton 7 and an increase for proton 1 when comapared with dyebase 271/64. It has already been demonstrated that chemical shift changes for protons that take on the same conformation around the azo bond are highly consistent. This difference is an indication that the signal corresponding to the average of the populated *cis* isomer forms in solution is somewhere in between the minimum energy structure and an alternative, with proton 7 pointing towards the shielding cone of the phenyl ring. It is interesting that the calculated minimum energy structure has produced this conformation around the azo bond, since the NMR data certainly demonstrate a difference in the chemical shifts between the **AC** and **BD** sulfonated molecules.

4.4.3.4 Ureido Group

In molecules containing a ureido group, the calculated structures can provide a valuable insight into the changes in chemical shift observed. It was noted during the analysis of the structures that the conformations of each *trans* isomer was locked in place by favourable hydrogen bonding interactions between the ureido terminal amine protons and the sulfonate oxygen atoms. This involved a different orientation of the aromatic

systems around the azo bond for the **ACF** and **ACG** sulfonate patterns as shown in Figure 4.27.

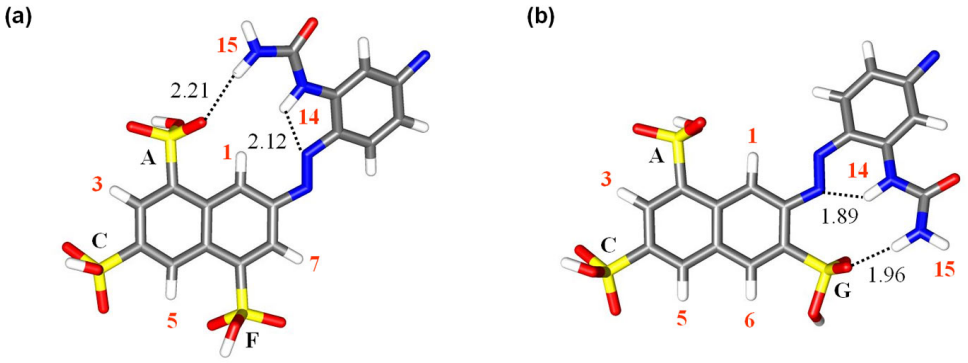

Figure 4.27: Comparing portions of **ACF** and **ACG** dyes (a) 269/56 and (b) 273/6. Distances (Å) are presented for interactions < 3 Å. Proton numbers are labelled in red.

A summary of relevant information for one **ACF** and one **ACG** sulfonated azo dye containing a ureido group is presented in Table 4.19. A difference becomes very clear in the ^{1}H NMR spectra. At *ca.* 11.7 ppm, proton 14 in the **ACG** dye differs significantly to that of the **ACF** dye, which is approximately 9.1 ppm. The distinctly different nature of these chemical shifts is indicative of a very different environment, with more electron withdrawal from this proton for **ACG** dyes. For the **ACF** dyes, proton 14 is close to the nearest azo nitrogen with a distance of 2.12 Å – close enough to hydrogen bond. For the *ortho* sulfonated dye, the nitrogen is forced close to the naphthyl-side azo nitrogen, with a shorter distance of 1.89 Å. The 0.20 Å reduction in distance is clearly enough to have a large electron withdrawing effect on the proton giving rise to such a deshielded signal in the spectrum. Another interesting observation can be derived for the terminal amine protons. In the **ACG** dye two broad singlets are present, indicating a slow rotation of the group on the NMR timesscale. The alternatively substituted dye shows one broad singlet for the *trans* isomer. This is reflected in the distances observed in calculated structures. Co-ordination with the *ortho* sulfonate group occurs with a distance of 1.96 Å, whereas co-ordination to the **A** sulfonate displays a distance of 2.21 Å. The extra 0.2 Å distance allows the rotation to speed up enough for the peaks to coalesce as one broad peak.

Structures of the *cis* isomers are broadly similar to one another, the only interaction being proton 14 with the nearer azo nitrogen. For the **ACF** dyes this produces little change in the chemical shifts, with the NH proton continuing to hydrogen bond with the phenyl azo nitrogen, with a similar hydrogen bonding length. However, for the **ACG** dye there is a very large change in chemical shift of this proton on isomerisation.

	ACF *trans*	**ACF** *cis*	**ACG** *trans*	**ACG** *cis*
NH_2 – Sulfonate **A**/Å	2.21	N/A	N/A	N/A
NH_2 – Sulfonate **G**/Å	N/A	N/A	1.96	N/A
NH – Azo N (Phenyl)/Å	2.12	2.09	N/A	2.09
NH – Azo N (Naphthyl)/Å	N/A	N/A	1.89	N/A

	ACF $\Delta\delta$/ppm	**ACG** $\Delta\delta$/ppm
Proton 14	0.15	2.98
Proton 15	0.14	-0.13 1.08

Table 4.19: Selected information relating to intramolecular bonding distances, and chemical shift differences, in the *cis* and *trans* isomers of **ACF** and **ACG** dyes (269/56 and 273/6).

Examination of features of the predicted structures (Table 4.19) shows that on isomerisation the hydrogen bond interaction shifts from the naphthyl azo to the phenyl azo nitrogen, with a corresponding increase in the hydrogen bond length from 1.89 to 2.09 Å. The two signals for the **ACG** ureido terminal amine protons have combined to form a single peak in the *cis* isomer, indicating a movement from this locked environment to a structure where the group may rotate. Again, chemical shifts for this signal in the *cis* isomer are consistent to those of *cis* isomers of the **ACF** dye. This gives a strong indication that no interaction between the groups on the two aromatic systems is present in the *cis* isomer, as reflected in the calculated structures.

4.5 Conclusions

The studies conducted have further demonstrated the ability of NMR spectroscopy with *in situ* laser irradiation to monitor more or less transient photoinduced species. The high resolution that underpins NMR spectroscopy provides a route to characterising the *cis* isomer in the presence of more dominant signals from the *trans* isomer. This feature of NMR also allows the proportions of each species to be measured, yielding valuable data for kinetic analyses to be performed later. The assignment of the *trans* isomer, and photo-generated signals characteristic of a geometry change to the *cis* isomer, combined with the thermally reversible nature of the process, contribute to a clear message that reversible *trans-cis* photoisomerisation and thermal *cis* decay are the only processes involved during irradiation of each dye presented here.

Analysis of the ^{1}H NMR spectra of azo molecules containing a di-sulfonated naphthyl ring has allowed a greater appreciation of the effect of sulfonation on the chemical shift of nearby protons. This has led to a definitive assignment of the **ACF** sulfonated

naphthyl protons and has brought about cause to acknowledge faults in the assignment of **AF** dyes presented in a previous publication.[30] The different sulfonation patterns display a characteristic fingerprint in each *trans* isomer. This is generally reflected in the *cis* isomer. However, inconsistencies in the chemical shift differences between similar dyes have suggested different conformations around the azo bond to be present in certain *cis* isomers. Variants of golden yellow dye B275, made through modification of the chlorotriazine ring by the addition of a large group, have been analysed. Varying degrees of signal broadening have been observed to occur through these structural modifications, mainly relating to the phenyl ring protons. Changing the nature of the triazine group by hydrolysis of the chlorine has demonstrated a further broadening of the signals observed in the complementary chloro-substituted dye. In 273/5, additional aromatic groups were noted to begin complicating the spectrum, although not to the extent of preventing detection of the *cis* isomer.

Correlation of theoretical and experimental work has assisted in explaining empirical observations made in the ^{1}H NMR spectra, often highlighting intramolecular interactions that may not be anticipated from the NMR spectrum alone. Geometry optimised structures have also helped in providing an insight into curious NMR results, giving direction for the explanations. Many of the experimental NMR results are reflected in the calculated molecular geometries, establishing the coherence between *in vacuo* calculated structures, and the structures present in solution. However, in two cases the calculated *cis* isomer structures were observed to be inconsistent with the structure predicted by NMR data, proving calculations on such large structures should not be relied upon without structural NMR data to support them. For the two *cis* isomers where an inconsistent structure was predicted, an equilibrium with alternative structures that correlated with the experimental data is expected. These alternative structures were calculated within 2 kJ mol^{-1} of the predicted minimum, and could well represent the difference between a zero kelvin gas phase calculation of an idealised molecule, and a solvated system. The general consistency of theoretical and experimental data supports the assumptions, based on prior work, that simplifying a sodium sulfonate group to sulfonic acid is an appropriate strategy.

Chapter 5

Kinetics of the Photoisomerisation of a Series of Yellow Azo Dyes

5.1 Introduction

The success of a commercial dye is dependent upon several factors, one especially important feature being the ability to chemically withstand all potentially damaging influences sustained throughout its useful life. Azo dyes are particularly susceptible to reversible light-induced fading, or photochromism, and this concern must be addressed by a dye manufacturer before the release of an azo product can be actioned. Kinetic investigations of photochromism help to indicate how resistant a dye is to this unwanted process. Ideally, a dye will not suffer from photochromism at all. However, this expectation is unrealistic and acceptable limits must be settled upon. A dye should demonstrate a slow photochemical *trans-cis* isomerisation rate (k_1) to retard the formation of the *cis* isomer, and rapid rates of both photochemical and thermal *cis-trans* isomerisation (k_{-1}) to ensure rapid decay of any *cis* isomer formed. If $k_{-1} > k_1$ then the percentage of *cis* isomer observed at the photostationary state will be low, and any undesirable colour change of a dye limited by the dominance of the *trans* isomer. Hence, with a view to engineering superior dyes, it is important to understand the factors that influence the rates of isomerisation.

Relatively little work has been published regarding the rates of photochemical isomerisation in commercial azo dyes. This is due to hydrazo chromophores currently dominating the commercial dye market (refer to Section 2.5.3 for an explanation of hydrazo dyes). Through trial and error in synthesis, the level of photochromism in azo dyes has been minimised by dye manufacturers. However, a substantial amount of research relating to the rate of thermal *cis* isomer decay in azo molecules is available.[4,30,61,78–80,82,94,95] Amongst this work, groups have studied the effects of solvent,[4,30,61,80] pressure,[78,80,82] and substituents,[30,79,80,94,96] often with the desire to elucidate the mechanism by which the *cis* isomer converts back to the more stable *trans* isomer, be that *via* inversion or

rotation. Additional studies regarding degradation of hydrazo dyes by light exist in abundance in the literature,[4,6,7,97,98] often in attempts to gain more insight into irreversible fading effects, either to limit this problem, or to devise methods for industrial wastewater treatment.

For the most part, published rates have been determined spectrophotometrically, the technique used being dependent on whether the dye is in solution or on a substrate. Solution measurements are conducted using UV-vis, studying the time dependence of the recovery of a *trans* isomer absorption band after it is bleached by a period of irradiation,[78–80,94–97,99] whilst flash photolysis allows more transient species to be monitored.[61,79,80,94] Reflectance spectroscopy is used to monitor bleaching of dyes on substrates such as cellulose fibres or silk during the irradiation process.[6,7,97] Studying the photofading of dyes on substrates can provide important information on how the dye interacts with its surroundings. Although the use of these techniques is widespread, they are all lacking in resolution, often relying on the ability to deconvolute spectra into component peaks in an effort to gain kinetic data for fitting. This can lead to varying degrees of uncertainty in the results. Despite this problem, few alternative techniques have been used to study *cis-trans* azo isomerisation.[30,95] Using the apparatus and conditions described in Section 3.3, Tait was able to perform studies using ^{1}H NMR spectroscopy, gaining results that were not limited by the poor resolution typical of absorption based techniques.[30] An accurate measure of concentration dependence with respect to time, essential for successful fitting of kinetic data, could be obtained by monitoring proton peak integrals specific to the individual species. This eliminates some of the aforementioned uncertainty seen in the usual analytical methods. Furthermore, *in situ* irradiation allows the photoisomerisation kinetics of a dye to be studied, in addition to thermal isomerisation rates.

As stated earlier, this work is focused on dye structure, with this particular chapter looking at how substituents govern the isomerisation kinetics. An examination of literature relating to this follows. It is widely accepted that adding a *para* substituent to azobenzene will increase the rate of thermal *cis* decay, irrespective of the nature of the substituent. This effect is additive, leading to a further increase in the rate when a *para*' group is added. Early work by Nishimura and Sueyoshi highlighted the effect of adding methyl groups *ortho* to the azo bond of *para*-dimethylaminoazobenzene using spectrophotometry.[79,94] They found a 2-methyl substituent accelerated thermal *cis* decay, whilst the equivalent 2'-methyl substitution resulted in little change in the rate. Symmetrical substitution, creating a 2,2'-dimethyl compound gave a thermal *cis–trans* rate somewhere between those of 2- and 2'- methylation. *Para*-donor/*para*'-acceptor substi-

tuted azobenzenes demonstrated dramatic acceleration in the rate of *cis* isomer thermal decay following addition of an *ortho* methyl group. Nishimura and Sueyoshi later went on to investigate the kinetics of 4-dimethylamino-4'-nitroazobenzene (NDAAB) finding 2-methyl and 2'-chloro groups cause an increase in the rate of thermal *cis-trans* isomerisation compared to the parent dye, with 2'-methyl and 2-chloro causing the opposite effect.[80] They concluded that the rate of thermal isomerisation is governed mainly by the electronic effect of substituents, with small perturbations due to solvation and steric factors. Yoshida *et al.* presented work on phenylazo-1-naphthalenes substituted in various positions.[96] Results showed 4- and 4'- substitutions enhanced the rate of thermal *cis-trans* isomerisation, in accordance with previous observations. The use of *ortho* methoxy groups on the aryl or naphthyl rings retarded thermal *cis* decay, the explanation for which came from steric hindrance, in an inversional transition state, between the *ortho* substituents and the two nitrogen lone electron pairs. Recent studies, conducted by NMR spectroscopy with *in situ* irradiation, examined the role of substituents on the kinetics of dyes based on a golden yellow dye chromophore.[30] Unexpectedly large variations in rates were observed for small structural changes. However, these modifications were not systematic, rendering some of the results open to interpretation. To avoid repetition, these results are discussed later in Section 5.6, where they are used to corroborate data from the current study.

A kinetic analysis of the dyes presented in Chapter 4 is presented herein. To assist the reader, the structures based upon the standard golden yellow chromophore have been reproduced in Figure 5.1. The work undertaken aims to examine the kinetic properties of dyes that contain engineered differences in the sulfonation pattern, benzene ring substitution, addition of a chlorotriazine group, and further adaptation of the latter reactive component. Geometry optimised structures are presented in parallel with the experimental results to assist explanation of the observations. It is possible to draw on previous studies by Tait[30] and present these alongside the new results, allowing an extensive set of kinetic data for the yellow azo dyes to be analysed. This enables the effect of location and nature of substituents to be examined systematically. It is hoped that this research will provide informative data to the dye industry, and inspire further work in this area.

5.2 Experimental Procedures

5.2.1 Acquiring Kinetic Data by NMR

A pseudo 2 dimensional pulse program was used to acquire the kinetic data presented in later sections. This type of pulse program has, amongst other applications, been applied

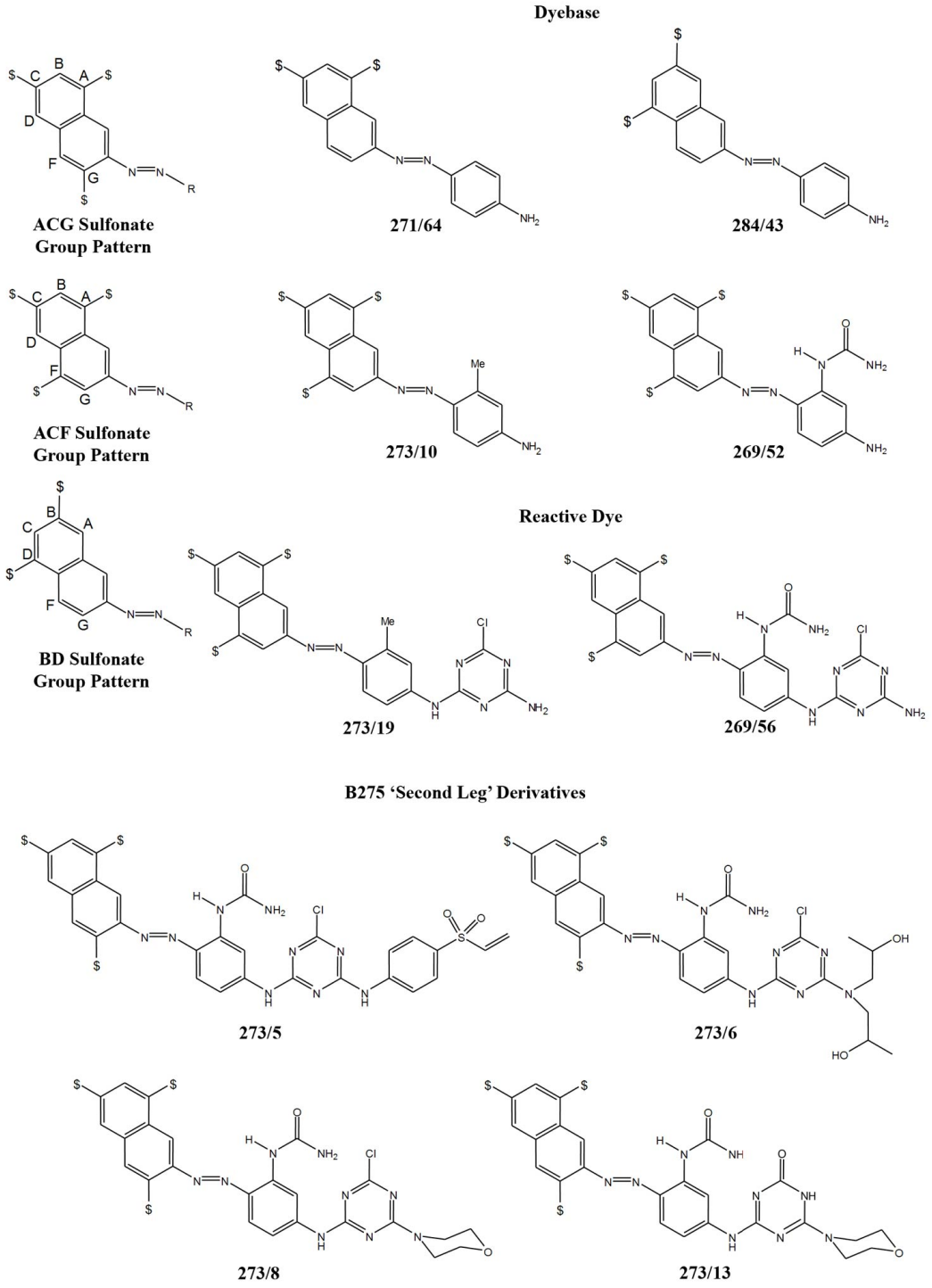

Figure 5.1: *Trans* isomer structures of the yellow azo dye series investigated. $\$=SO_3^-$

to liquid chomatography coupled with NMR (LC-NMR), the nature of the acquisition minimising user input when components of a mixture are eluted from a column at different times. The F2 domain of the NMR spectrum was acquired as for a normal 1D spectrum using a presaturation pulse centred on the water peak, depicted in Figure

5.2. The F1 domain was simply the time interval between successive 1D experiments. Changes in peak intensity between experiments can be followed and the data extracted and fitted. Although this method is used primarily for t1/t2 relaxation experiments in NMR, this pulse program is ideally suited to the kinetic experiments reported within this chapter.

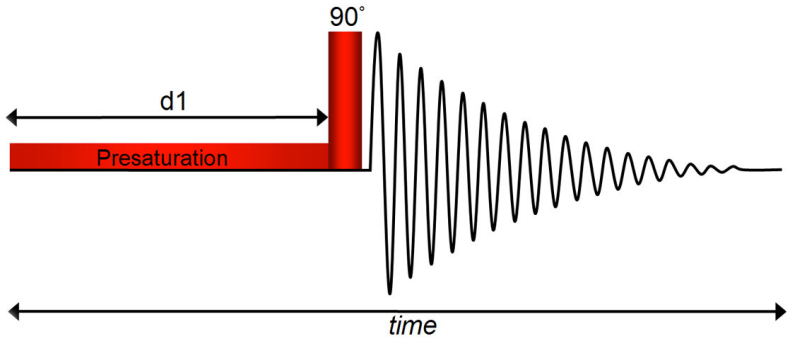

Figure 5.2: Pulse program used in the acquisition of each row of the pseudo 2D ^{1}H NMR spectrum.

Figure 5.3 is a simple scheme of the experimental procedure employed for each dye when acquiring the spectra presented in Chapter 4, and the kinetic results presented in this chapter. Samples were made up and allowed to stand in darkness overnight, remaining in darkness until attaching the optical fibre to the NMR tube and placing the sample in the NMR probe, where no light could reach it. In doing so, it was guaranteed that the *trans* isomer would be the only species present in the sample at the start of the experiment. An initial spectrum of this *trans* isomer was recorded and conditions for the pseudo 2D experiment optimised to bring about sufficient signal to noise in as short a time interval as possible. In monitoring the rise to the photostationary state (Figure 5.3 (a)), the first row of the data set, t_0, was acquired in darkness. Upon completion of this scan, the laser shutter was opened allowing light to be delivered to the sample *via* the optical fibre, and successive spectra of the sample undergoing irradiation to be recorded. Rows of the 2D data set were periodically extracted and compared until no further changes were observed, ensuring that the full time course of the photochemical process had been recorded.

During continuous irradiation at the photostationary state (Figure 5.3 (b)), conditions were optimised and a high quality spectrum of the PSS recorded, prior to monitoring thermal decay of the *cis* isomer. The first row of the 2D spectrum was recorded under irradiation to mark t_0 of the decay, after which the irradiation was terminated allowing the *cis* isomer to decay in darkness (Figure 5.3 (c)). Periodic monitoring of the decay was conducted to guarantee the entire process was recorded for later fitting.

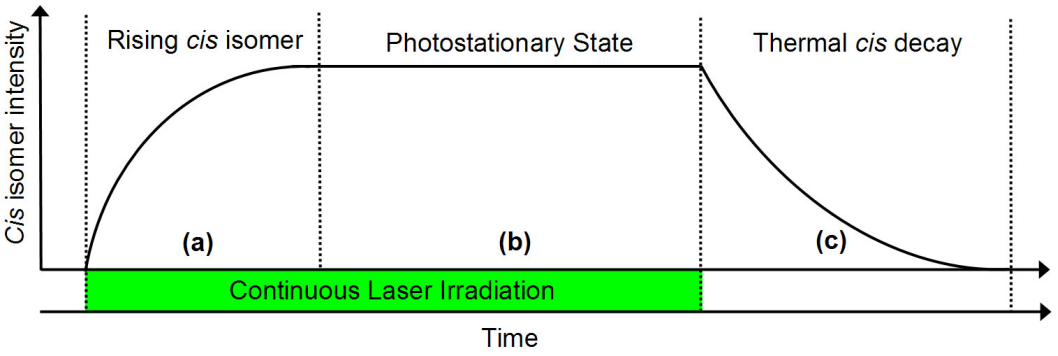

Figure 5.3: Schematic representation of the time course of an *in situ* experiment to monitor the isomerisation kinetics of a dye.

Each dye yielded two pseudo 2D data sets, one following the rise of the *cis* isomer and decay of *trans* to the photostationary state, the other tracking the *cis* decay and rise of *trans* back to 100% *trans* isomer. Both data sets were processed in the same manner. In contrast to a standard 2 dimensional experiment, the data were Fourier transformed in the F2 dimension only, F1 being the time dimension. The time interval is simply taken as the time elapsed during the acquisition of each row. After transformation of F2, the same phasing and baseline correction parameters were applied to each row of the dataset. A 1D spectrum containing both *trans* and *cis* isomer signals was extracted from the pseudo 2D file. *Trans* and *cis* isomer signals were picked and the area of each peak defined. With these parameters defined, the Xwinnmr software was able to extract the size of the integral for the same peak in sequential rows of the 2D spectrum, giving an output suitable for applying mathematical fitting functions. These functions, and their application for fitting these data, are described in Section 5.3.

5.2.2 Standardised Conditions for Measurements

As far as possible, experiments were conducted to allow maximum comparability between the final results. As solvent effects have been shown to affect the rate of thermal isomerisation,[4,61,80] all studies were conducted in d_6-DMSO, ensuring the rates were derived under the same solvent conditions. Throughout all experiments, the NMR probe temperature was regulated at 298 K. Furthermore, the samples were prepared to a concentration that would allow 50% light transmission at a 2 mm depth. This was performed by applying the Beer Lambert Law (Equation 2.3) with the known path-length and molar absorption coefficient of the *trans* isomer, ϵ_{trans}, in Equation 5.1. The sample conditions for each dye are presented in Table 5.1, reproduced from Chapter 4.

$$\frac{\log 0.5}{0.2\epsilon} = concentration \tag{5.1}$$

The optical fibre was inserted so the tip aligned with the top of the detection region using an external depth gauge. Prior to insertion, the output power of the laser from the optical fibre was regulated to 30 mW to maintain identical intensity between studies.

	Irradiation Wavelength, λ_{irr}/nm	Molar Absorption Coefficient, ϵ_{irr}/mol^{-1}lcm^{-1}	Concentration/mM
273/10†	530	1620	0.93
273/19	530	730	2.06
269/52†	530	7950	0.19
269/56	530	4333	0.35
271/64†	530	1522	1.00
284/43†	530	520	2.90
273/5	530	1788	0.84
273/6	530	916	1.64
273/8	530	1073	1.40
273/13	530	930	1.62

Table 5.1: The irradiation wavelengths, molar absorption coefficients at these wavelengths, and calculated NMR sample concentrations for constant absorption.
†Dyebase spectra were acquired under basic conditions.

5.2.3 Calculated Structures

Where appropriate, calculated ground state structures have been included in the text to assist in the interpretation of the observed rate constants. A full description of how these structures were obtained can be found in Chapter 4. All structures were optimised to the B3LYP/6-31G(d,p) level of theory/basis set. Section 4.4 showed the *in vacuo* calculated structures correlate well with features of the ^{1}H NMR spectra. In Section 5.6 the structures presented for dyes studied by Tait were calculated by Dr. P.R. Richardson (School of Chemistry, Edinburgh University) to the aforementioned level of theory, ensuring complete comparability with the present work.

5.3 Processing the Kinetic Data

When an azo dye is subjected to irradiation, several processes will occur, namely reversible photochemical *trans-cis* isomerisation, and thermal *cis-trans* isomerisation. The rates of these processes are summarised as:

$$trans \underset{k_{-1}(h\nu) + k_{-1}(\Delta)}{\overset{k_{1}(h\nu)}{\rightleftharpoons}} cis$$

These rates must be determined to gain a full understanding of both *trans-cis* and *cis-trans* photo-induced isomerisation, and thermal *cis-trans* isomerisation. The intensity data extracted from the pseudo 2D file will give two separate sets of data to fit, one for the *trans* isomer integrals and one for the *cis* isomer. Data were imported into Microsoft Excel and summed, before using an iterative non-linear least squares fitting routine employing the 'solver' function to minimise the sum of squares of the variables. Data were fitted using integrated rate laws given in the equations below. The rate constants for the *trans* and *cis* isomer could then be compared to ensure the data were in agreement. This process was conducted on two separate pseudo 2D files, one following the kinetics involved during irradiation, and one in darkness to determine the thermal decay rate constant.

5.3.1 Fitting Kinetic Data for the Rise to the Photostationary State

The rise to the photostationary state can be modelled by first order equilibrium kinetics. Equation 5.2a can be applied to the change in *cis* isomer intensity to model the rise to the photostationary state. Likewise, equation 5.2b can be applied to the *trans* isomer to yield the same result. Clearly only one rate constant for the equilibrium process, k_{obs}, is yielded from fitting these data despite the presence of three processes as the system proceeds towards equilibrium. This can later be deconstructed into component rate constants for each of the contributing processes (Section 5.3.3). Figure 5.4 shows (a) the decay of the *trans* isomer and (b) the rise of *cis* isomer for dyebase 273/10 at 298 K. The fitted function clearly describes the experimental data well, validating the kinetic model for use on this type of data.

$$\frac{[cis]_{PSS} - [cis]_t}{[cis]_{PSS} - [cis]_0} = e^{(k_{obs})t} \tag{5.2a}$$

$$\frac{[trans]_t - [trans]_{PSS}}{[trans]_0 - [trans]_{PSS}} = e^{(k_{obs})t} \tag{5.2b}$$

5.3.2 Fitting Kinetic Data for the *Cis* Isomer Decay

When the irradiation source is removed from the sample, the photochemical processes terminate allowing thermal decay of the *cis* isomer, and recovery of the *trans* isomer, to be monitored. Many studies have indicated that the rate of this thermal process in monoazo compounds proceeds *via* a first order decay.[4,30,61,78–80,95,99] The change in *cis* and *trans* isomer intensity of NMR peaks has been modelled using Equations 5.3 (a) and (b), yielding the rate constant for thermal decay, $k_{-1}(\Delta)$. Figure 5.5 shows (a) data for the *trans* isomer recovery, and (b) the *cis* isomer decay for dyebase 273/10

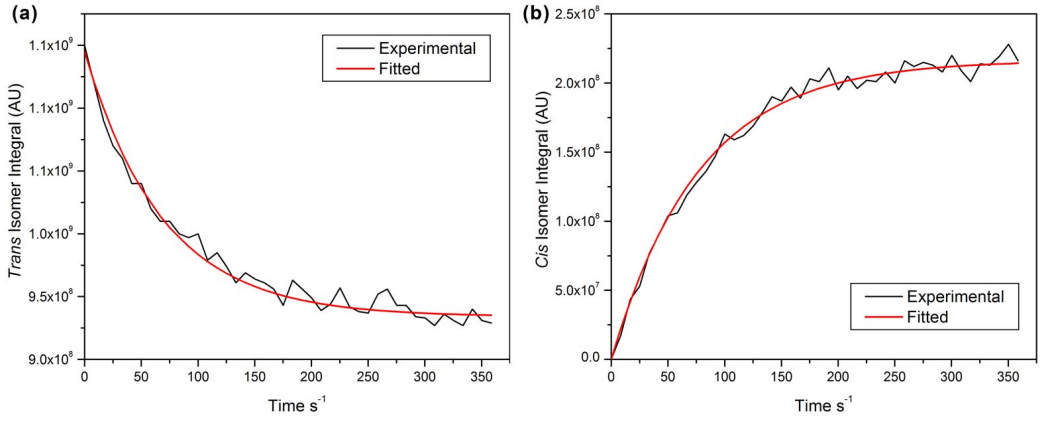

Figure 5.4: Time dependence of the isomers undergoing irradiation starting from a 100% *trans* solution at $t = 0$. (a) corresponds to the *trans* isomer and (b) the *cis* isomer.

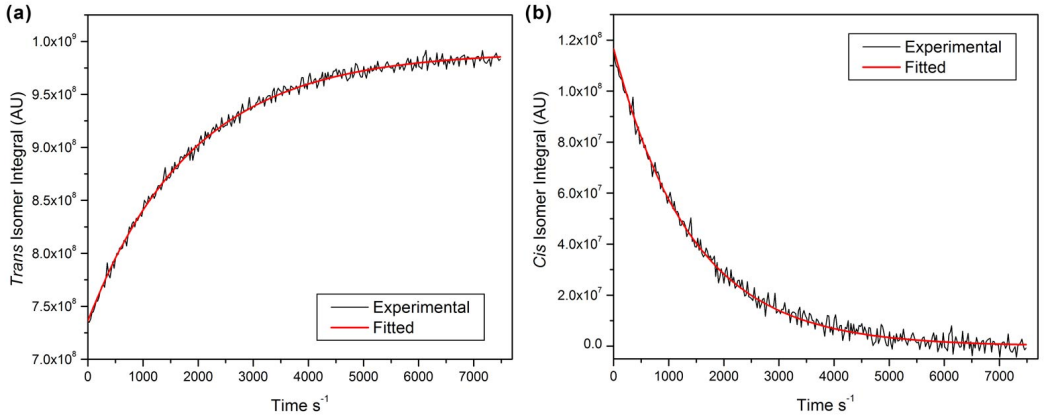

Figure 5.5: Time dependence of the isomer concentration after light is terminated at the photostationary state. (a) corresponds to the *trans* isomer and (b) the *cis* isomer.

at 298 K. The quality of fit of the function to these data demonstrates a first order concentration dependence for the decay.

$$[cis]_t = [cis]_{PSS} e^{-k_{-1}(\Delta)t} \tag{5.3a}$$

$$[trans]_t = [trans]_{PSS} + [cis]_{PSS}(1 - e^{-k_{-1}(\Delta)t}) \tag{5.3b}$$

Table 5.2 shows the extracted values for dyebase 273/10. For the irradiated system, and for the system undergoing thermal *cis* isomer decay, there are two rate constants; one derived from fitting *cis* isomer peaks, and one from *trans*. The two results for k_{obs}, and for $k_{-1}(\Delta)$, were consistent proving peak intensities for both isomers could be used to derive the same result. Therefore, rate constants stated in the results derive from the average of the two fitted rate constants, k_{obs} and $k_{-1}(\Delta)$.

k_{obs} /$10^{-4}s^{-1}$ ***Trans* Decay**	k_{obs} /$10^{-4}s^{-1}$ ***Cis* Rise**	$k_{-1}(\Delta)$ /$10^{-4}s^{-1}$ ***Trans* Rise**	$k_{-1}(\Delta)$ /$10^{-4}s^{-1}$ ***Cis* Decay**
125	134	6.99	6.39

Table 5.2: Kinetic data extracted and fitted for the rise to the PSS and thermal decay for dyebase 273/10.

5.3.3 Separating the Data Into Component Rate Constants

The rate constant extracted from the NMR data recorded whilst the sample is under irradiation, k_{obs}, is a combination of three separate rate constants, $k_1(h\nu)$, $k_{-1}(h\nu)$, and $k_{-1}(\Delta)$. To determine the component values, initally consider the observed rate constant as the sum of the forward and reverse processes:

$$k_{obs} = k_1(h\nu) + k_{-1}(h\nu + \Delta) \tag{5.4}$$

The two constituent rate constants, k_1 and k_{-1}, drive the isomerisation of *trans-cis* and *cis-trans* towards an equilibrium in solution (the photostationary state). Through measurements made in Chapter 4, the ratio of *cis* and *trans* isomers in this equilibrium state are available. The relative concentrations of *trans* and *cis* isomers are used in Equation 5.5, allowing the equilibrium constant, K, to be derived. Calculation of k_1 and k_{-1} from the total rate constant k_{obs} is then possible.

$$K = \frac{k_1(h\nu)}{k_{-1}(h\nu + \Delta)} = \frac{[cis]_{PSS}}{[trans]_{PSS}} \tag{5.5}$$

The value k_1 requires no further attention since this is the measured photochemical *trans-cis* rate constant, $k_1(h\nu)$. The reverse rate constant, k_{-1}, which comprises the photochemical and thermal *cis-trans* processes, $k_{-1}(h\nu)$ and $k_{-1}(\Delta)$, can be broken down further. Since $k_{-1}(\Delta)$ is derived directly from measuring the thermal decay (Section 5.3.2) it can be subtracted from k_{-1} to give $k_{-1}(h\nu)$. To understand the thermal kinetic decay results from a more 'real world' viewpoint, they are also presented in this work as a half-life for the *cis* isomer. This was made possible using Equation 5.6.

$$\frac{\ln 2}{k_{-1}(\Delta)} = t_{\frac{1}{2}cis} \tag{5.6}$$

Continuing the analysis of dyebase 273/10, the reported rates in Table 5.2 have been averaged to give two rate constants. From the NMR results presented in Chapter 4, the concentration of *cis* isomer at the PSS was determined to be 22%. This can be used to give an equilibrium rate constant, K, of 0.282. Table 5.3 shows the rate constants formed from using the equilibrium constant and the half-life of the *cis* isomer. All data were processed in this manner to give the results presented in later sections.

k_{obs} /$10^{-4}s^{-1}$	%*Cis* PSS	*K*	$k_{-1}(\Delta)$ /$10^{-4}s^{-1}$	$k_1(h\nu)$ /$10^{-4}s^{-1}$	$k_{-1}(h\nu)$ /$10^{-4}s^{-1}$	$t_{1/2}$ *cis* /s
129	22	0.282	36	86	6.7	1040

Table 5.3: Details used in separating k_{obs} into component rate constants for dyebase 273/10.

5.3.4 Correcting the Kinetic Data To Allow Comparison

Thermal decay rate constants, $k_{-1}(\Delta)$, require no further correction as they depend only on the temperature, maintained in all cases at 298 K. However, the photochemical rate constants, $k(h\nu)$, are dependent upon the intensity of irradiation, I_{irr}, the molar absorption coefficent ϵ, and the quantum yield for isomerisation, ϕ_{isom}. For all experiments involving irradiation, the laser power was adjusted to 30 mW to make certain I_{irr} was constant. Since the two photochemical rate constants were dependent upon ϵ, $k_1(h\nu)$ was divided by ϵ_{trans} at λ_{irr} and therefore $k_{-1}(h\nu)$ required division by ϵ_{cis}. It was necessary to obtain ϵ_{cis} to thoroughly compare the photochemical rate constants for *trans-cis* and *cis-trans* isomerisation. The resulting corrected rate constants, $k_1(h\nu)/\epsilon_{trans}$ and $k_{-1}(h\nu)/\epsilon_{cis}$, allude to the relative quantum yields for photoisomerisation which ultimately depends upon the ground and excited state potential energy surfaces for a molecule.

5.3.5 Obtaining the Molar Absorption Coefficient of the *Cis* Isomer

The molar absorption coefficient of the *cis* isomer, ϵ_{cis}, must be obtained *via* UV-vis spectroscopy. Although it was impossible to measure a spectrum of 100% *cis* isomer, the composition of the photostationary state for each dye has been measured accurately by NMR spectroscopy. Therefore comparing ϵ_{obs}, the molar absorption coefficient of the PSS at the wavelength being measured, with ϵ_{trans}, and using the composition of the PSS obtained from NMR experiments (where x = decimal fraction of *cis* isomer), it is possible to acquire ϵ_{cis} using Equation 5.7.

$$\epsilon_{cis} = \frac{\epsilon_{obs} - (1-x)\epsilon_{trans}}{x} \tag{5.7}$$

The spectrometer used to gather UV-visible spectra did not allow *in-situ* irradiation of the samples while spectra were collected. This did not pose a problem for dyes with slow *cis* decay times as it was assumed the samples could be transferred promptly enough between the irradiation source and the UV-vis spectrometer to avoid thermal decay in the transition. Hence, the previous study by Tait has only stated $k_{-1}(h\nu)/\epsilon_{cis}$ for dyes with sufficiently long-lived *cis* isomers.[30] For dyes with a small *cis* half life the cuvette was irradiated in the spectrometer *via* an optical fibre. After irradiation

over a sufficient period of time to attain the PSS, the light was terminated, optical fibre extracted, the light-tight hatch on the spectrometer closed, and single wavelength absorption readings acquired at the required wavelength, λ_{irr}. Although this procedure is rapid, false values may be obtained for rapidly decaying samples due to thermal *cis-trans* isomerisation that occurs during the short period of time in darkness. However, since the thermal decay of the sample has been determined from NMR experiments, it can also be used to work backwards from a molar absorption coefficient gathered t seconds after irradiation is terminated, to obtain a time-corrected value of ϵ_{obs}. An absorption measurement on a given system containing both *trans* and *cis* isomers may be described by Equation 5.8, where Abs_{total} is the total absorbance at the wavelength under investigation, ϵ_{trans} and ϵ_{cis} are the molar absorption coefficients of the respective *trans* and *cis* isomers, $[trans]$ and $[cis]$ are the concentrations of each isomer in the solution at a given time, and path length l, described in the Beer Lambert law, is 1 cm and therefore not included for simplicity.

$$Abs_{total} = \epsilon_{trans}[trans] + \epsilon_{cis}[cis] \tag{5.8}$$

The absorption of the sample at time t after irradiation is demonstrated by Equation 5.9a, and rearranged to form 5.9b.

$$Abs_{total} = \epsilon_{trans}\Big([trans]_{PSS} + \Big([cis]_{PSS} - [cis]_t\Big)\Big) + \epsilon_{cis}[cis]_t \tag{5.9a}$$

$$Abs_{total} = \epsilon_{trans}\Big([trans]_{PSS} + [cis]_{PSS}\Big) + (\epsilon_{cis} - \epsilon_{trans})[cis]_t \tag{5.9b}$$

Since $[trans]_{PSS} + [cis]_{PSS} = [trans]_0$ at all times, the overall term may be simplified, as shown in Equation 5.10a, which rearranges to allow derivation of the *cis* isomer molar absorption coefficient at any given time (Equation 5.10b).

$$Abs_{total} = \epsilon_{trans}[trans]_0 + (\epsilon_{cis} - \epsilon_{trans})[cis]_t \tag{5.10a}$$

$$\epsilon_{cis} = \frac{Abs_{total} - \epsilon_{trans}\Big([trans]_0 + [cis]_t\Big)}{[cis]_t} \tag{5.10b}$$

The thermal decay of the *cis* isomer was noted earlier in Equation 5.3(a). It allows the value of $[cis]_t$ to be substituted, creating Equation 5.11 that allows calculation of ϵ_{cis} at any time, t, after irradiation from known parameters. Therefore ϵ_{cis} is available for all dyes in this study, not only dyes with long *cis* isomer half-lives.

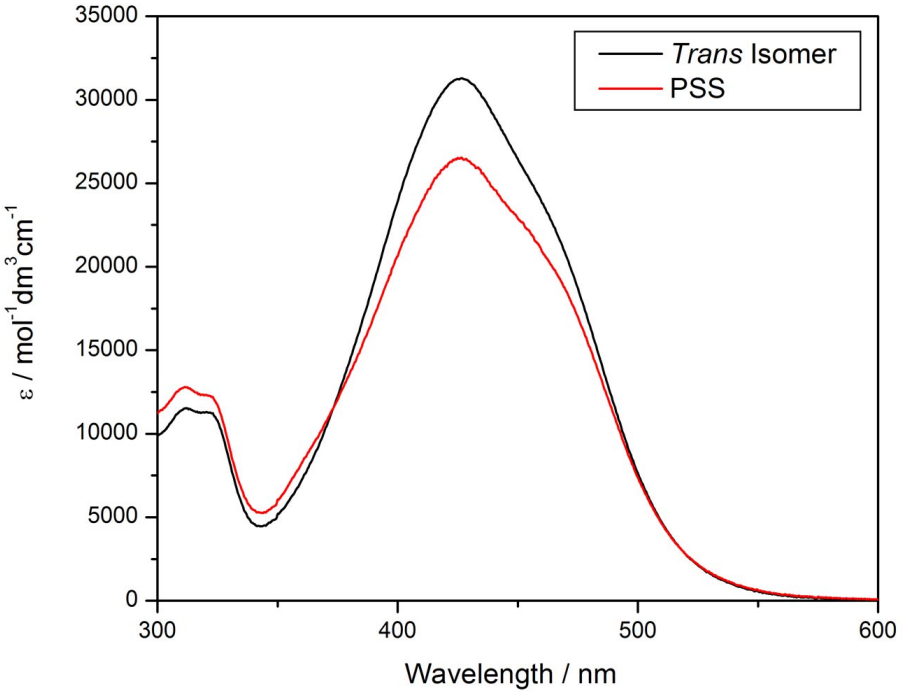

Figure 5.6: UV-vis spectra of 273/10 (a) *trans* isomer only (b) after irradiation at 530 nm. The sample was made basic using aqueous sodium carbonate as for the NMR sample.

$$\epsilon_{cis} = \frac{Abs_{total} - \epsilon_{trans}\left([trans]_0 + [cis]_{PSS}e^{-k_{-1}(\Delta)t}\right)}{[cis]_{PSS}e^{-k_{-1}(\Delta)t}} \tag{5.11}$$

Where the thermal decay of the *cis* isomer was lengthy enough to allow, a scan of wavelengths was performed to look at the spectrum of the irradiated species rather than a single point. In all cases, as expected for these systems, a bleaching of the dye sample was apparent at the wavelength of maximum absorption, λ_{max}. This is expected since λ_{max} *cis* is not likely to be equal to λ_{max} *trans* , leading to the reduction of ϵ_{obs} at λ_{max} observed in the UV-vis spectrum of 273/10 in Figure 5.6.

The *cis* isomer molar absorption coefficients for each dye, ϵ_{cis}, have been obtained and presented alongside ϵ_{trans} values in Table 5.4. For most molecules, ϵ_{trans} and ϵ_{cis} are similar since the measurement was made at 530 nm at the tail end of the spectrum where bleaching is not pronounced. It is clear that some of the molecules in the table do exhibit a change in ϵ, with ϵ_{cis} elevated compared to ϵ_{trans}. Depending on the relative positions of the *cis* and *trans* spectra, ϵ_{cis} may be less than, the same as, or greater ϵ_{trans} at λ_{irr}. On closer inspection of Figure 5.6, the $trans_0$ and PSS UV-vis traces for 273/10, an isosbestic point can be identified at 517 nm for the *trans* isomer and PSS traces. Therefore, on the tailing end of the UV-vis spectrum where the PSS trace has crossed the *trans*, there is marginally higher absorption which is amplified

when the value is scaled to 100% *cis*. This is responsible for the larger difference in values observed for five of the molecules cited in Table 5.4. The implication of differing *trans* and *cis* molar absorption coefficients at λ_{irr} is considered in Section 5.3.6.

	Irradiation Wavelength, λ_{irr}/nm	Molar Absorption Coefficient, ϵ_{trans}/mol^{-1}lcm^{-1}	Molar Absorption Coefficient, ϵ_{cis}/mol^{-1}lcm^{-1}
273/10†	530	1620	2122
273/19	530	730	1157
269/52†	530	7950	10810
269/56	530	4333	4229
271/64	530	1520	2340
284/43	530	520	1080
273/5	530	1788	1620
273/6	530	916	847
273/8	530	1073	1028
273/13	530	930	922

Table 5.4: The irradiation wavelengths and molar absorption coefficients for the *trans* and *cis* isomers at these wavelengths † – dyebase spectra were acquired under basic conditions.

5.3.6 The Photokinetic Factor

Consider the simple case where species A photochemically converts to form species B.

$$A \xrightarrow{h\nu} B$$

The rate law of this photochemical reaction is reliant upon the quantum yield, the photon flux, the concentration of the photosensitive substrate and the photokinetic factor. The photokinetic factor, F, is used to correct the other terms when defining the rate and is expressed below, where *Abs* is the total absorbance of the solution.

$$F = \frac{1 - 10^{-Abs}}{Abs} \tag{5.12}$$

If the absorbance of the solution changes over a period of time, *i.e.* $\epsilon_A \neq \epsilon_B$ at λ_{irr}, then F will be time dependent. Equation 5.13 may be used to described the rate of the reaction, assuming F remains constant. In this term, I_0 is the total intensity of light, $\phi_{A\rightarrow B}$ is the quantum yield for conversion of A to B, and ϵ_A is the molar absorption coefficient of species A.

$$\frac{-d[A]}{dt} = I_0 F \phi_{A\rightarrow B} \epsilon_A [A] \tag{5.13}$$

In systems where no difference is apparent in the molar absorption coefficients of the initial and final species, the *cis* and *trans* species in the case of this work, the photokinetic factor will not be time-dependent and therefore a standard treatment of the kinetic data can be undertaken. Examining the data in Table 5.4, most of the dyes bear similar ϵ_t and ϵ_c values. However, the first three dyes listed demonstrate sizable differences in the coefficients. The inequality of these values may have a detrimental effect on the fit to the data obtained using the first order equations stated in Section 5.3.1. However, given the reatively small percentage of *cis* isomer present in the irradiated sample, the change in ϵ_{obs} during the reaction is small. The photokinetic factor has been neglected in our treatment of the data due to these small changes, and is borne out by the success of a first order rate equation in fitting the data. To ensure this treatment was correct, F was calculated at $t = 0, PSS$ to look at the variation in the photokinetic factor at the start of the experiment, and when it reaches equilibrium. The method of calculating these results is defined in Section 5.3.6.1. For dyebase 273/10, the photokinetic factor changes from 0.979 at 100% *trans* to a PSS value of 0.984. This small change in F does not appear to impact on the results at all, the excellent fit seen in Figure 5.4 supporting this observation. Even in the most extreme case of change between ϵ_t and ϵ_c at λ_{irr}, seen in molecule 284/43, the photokinetic factor changes from 0.979 at 100% *trans* to a PSS value of 0.992. It is assumed from this point onwards that this does not impact on the knetic treatment used for these dyes.

5.3.6.1 Deriving the Photokinetic Factor For Azo Photoisomerisation

Considering the simple AB system defined in Section 5.3.6, the rate defined in Equation 5.13 can be simplified further. Using the Beer Lambert relation (Equation 2.2), the total intensity of light absorbed by the solution, I_{Abs}, can be defined as $I_0(1 - 10^{-Abs})$. Additionally, the total intensity of light absorbed by A can be calculated as the fraction of I_{Abs}, and related to F (assuming a pathlength of 1 cm).

$$I_A = \frac{\epsilon_A[A]}{Abs} I_{Abs} = \epsilon_A I_0 F \tag{5.14}$$

This leads to the following simplification of Equation 5.13, where k is the first order rate constant providing I_A is constant throughout the reaction, *i.e.* $\epsilon_A = \epsilon_B$:

$$\frac{-d[A]}{dt} = I_A \phi_{A \rightarrow B} = k[A] \tag{5.15}$$

Of course a photochromic dye system, where reversible light-induced effects are also present, is not this simple. The reversible *trans-cis* photoisomerisation observed in this study can be summarised in the following manner:

$$trans \underset{h\nu + \Delta}{\overset{h\nu}{\rightleftharpoons}} cis$$

The overall rate of this system is described in Equation 5.16, where $\phi_{t\rightarrow c}$ and $\phi_{c\rightarrow t}$ are constant and unknown; ϵ_t and ϵ_c, the molar absorption coefficent of the *trans* and *cis* isomers, are constant and known; I_0 is constant; and F may be time dependent.

$$-\frac{d[trans]}{dt} = I_0 F\Big(\phi_{t\rightarrow c}\epsilon_t[trans] - \phi_{c\rightarrow t}\epsilon_c[cis]\Big) - k_\Delta[cis] \tag{5.16}$$

At $t = 0$, $\epsilon_{obs} = \epsilon_{trans}$. At the photostationary state $\epsilon_{obs} = (1-x)\epsilon_{trans} + x\epsilon_{cis}$. i.e. the total absorption will be the sum total of *trans* and *cis* isomer absorption at any point. If we assume a 1 cm pathlength for simplicity, the photokinetic factor for this reversible system can be described as:

$$F = \frac{1 - 10^{-\left(\epsilon_t[trans] + \epsilon_c[cis]\right)}}{\epsilon_t[trans] + \epsilon_c[cis]} \tag{5.17}$$

In terms of the NMR rate constants described earlier in this chapter, $k_1 = I_0 F(\phi_{t\rightarrow c}\epsilon_t)$ and $k_{-1} = I_0 F(\phi_{c-t}\epsilon_{cis}) + k_{-1}(\Delta)$. At any time, the concentration of *cis* isomer may be related to the concentration of *trans* as $[cis] = [trans]_0 - [trans]$. Applying this to the above equation, and rearranging the terms allows F to be simplified.

$$F = \frac{1 - 10^{-\left((\epsilon_{trans} - \epsilon_{cis})[trans] + \epsilon_{cis}[trans]_0\right)}}{\left((\epsilon_{trans} - \epsilon_{cis})[trans] + \epsilon_{cis}[trans]_0\right)} \tag{5.18}$$

This term can be used to calculate F for the reversible photochromic azo dye systems studied. Calculation of values where ϵ_t and ϵ_c are significantly different has proved this not be a big factor in these studies due to the low concentrations of *cis* isomer present at the photostationary state.

5.4 Reproducibility of the Data

In order to ensure the validity of the results, it is necessary to test the procedure for acquiring the kinetic data to investigate the error associated with performing measurements, and fitting the data. It is expected that greater error will be associated with the data acquired whilst the sample is under irradiation due to possible variations in placing the optical fibre and the short pathlength employed. Furthermore, the error associated in measuring the composition of the photostationary state, and its impact on measuring the equilibrium constant, was included in the estimate for the photoisomerisation kinetics. Other variables including data extraction are expected to be minimal. The comparison of results obtained by Tait[30] demanded that a study of one of the dyes from the latter work was conducted to confirm the consistency between the two studies.

5.4.1 Reproducibility of Optical Fibre Position

Dyebase 273/10 was used to test how reproducible the data were across a series of repeat measurements. Five experiments were conducted back to back, following both photochemical and thermal processes. Between successive runs the sample was removed from the NMR spectrometer, optical fibre taken out of the sample and replaced. This was deemed a suitable test to investigate the error involved in placing the optical fibre correctly within the sample using the external depth guage. The pseudo 2D files were processed identically for each data set, and peak integrals extracted and fitted by the process described in Section 5.3. The ten values for each of the k_{obs} and $k_{-1}(\Delta)$ rate constants for the five successive runs are presented in Table 5.5. The standard deviation was observed to be 1.50×10^{-3} s^{-1} in k_{obs}, and 2.99×10^{-5} s^{-1} in $k_{-1}(\Delta)$, corresponding to 12% and 5% standard deviations respectively. As anticipated, due to uncertainty in fibre position, the rise to the photostationary state incurs additional error compared to thermal decay. The error in measuring peak integrals for both isomers and relating them to equilibrium constant K was propagated into this error. Error in K for this sample was estimated at 6% leading to an overall 18% error in the photoisomerisation rate constants.

Repeat	k_{obs} /10^{-4}s^{-1} ***Trans* Decay**	k_{obs} /10^{-4}s^{-1} ***Cis* Rise**	$k_{-1}(\Delta)$ /10^{-4}s^{-1} ***Trans* Rise**	$k_{-1}(\Delta)$ /10^{-4}s^{-1} ***Cis* Decay**
1	122.1	143.0	6.4	6.2
2	120.6	143.5	7.0	6.4
3	114.6	142.5	6.9	7.1
4	109.3	139.5	6.4	6.6
5	118.2	151.8	6.4	6.6

Table 5.5: Comparison of the kinetic values for five successive photochemical and thermal studies of dyebase 273/10. The optical fibre was removed and replaced between successive runs.

5.4.2 Correlating New Data with Previously Obtained Results

In Section 5.6, the kinetic data obtained in this study are compared with those previously obtained on similar dye systems. To ensure compatability of the results, and validity of any conclusions that are derived from the comparison, it was necessary to conduct a repeat study for one of the dyes studied by Tait. Dye B275, the structure of which is shown in Figure 5.7, was used for this purpose. Table 5.6 shows the values of k_1 and k_{-1} obtained from the original study and the repeat. Repeatability studies conducted by Tait showed errors of 18% standard deviation for the photochemical rate

constants, and 7% for thermal rate constants. Although the error estimate for the photoisomerisation rate constants presented in this study is identical, the error analysis conducted by Tait only relied upon the reproducibility and did not include other sources of error. Not only are the values are in agreement within the bounds of these stated errors, they are within the tighter treatment of error determined for reproducability in this study. It can be assumed that cross-comparison of the kinetic data obtained in each study can be safely conducted.

Study	k_{obs} /$10^{-4}s^{-1}$ *Trans* Decay	k_{obs} /$10^{-4}s^{-1}$ *Cis* Rise	$k_{-1}(\Delta)$ /$10^{-4}s^{-1}$ *Trans* Rise	$k_{-1}(\Delta)$ /$10^{-4}s^{-1}$ *Cis* Decay
Tait[30]	52.3	54.4	1.98	1.94
Repeat	55.8	56.6	2.06	2.00

Table 5.6: Comparison of the kinetic values obtained by Tait for compound B275, and those derived from a repeat experiment on this dye.

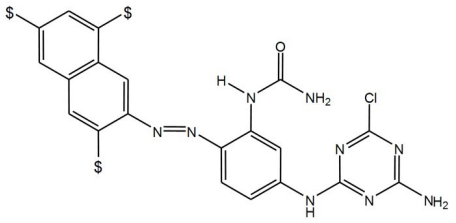

Figure 5.7: The structure of dye B275 used in the repeatability study to ensure data consistency.

5.5 Results and Discussion

In this section the kinetic parameters for dyes presented in Chapter 4 are examined and explained. In Section 5.6, the present results are assimilated with previous results, to provide a more comprehensive picture of the effect of molecular structure on the rates of isomerisation, both photo and thermal. The kinetic data for the dyes studied are presented in Table 5.7. Results for the two dyebase/dye pairs are shown, followed by results for the two di-sulfonated dyebases, then the 'second leg' dyes. In later discussions, portions of the table are reproduced and arranged in a suitable way to make comparison of the results straightforward. It should be noted that the photochemical rate constants used during later analysis are those that have been corrected by the molar absorption coefficient of the *trans* or *cis* isomer, presented in Table 5.4. A discussion of how these values are treated follows, prior to an examination of the overall data set in subsequent sections.

Molecule/Structure	ϵ_{t}^{irr} /$M^{-1}cm^{-1}$	$^{a}k_1(h\nu)$ /$10^{-4}s^{-1}$	$^{a}k_1(h\nu)/\epsilon_{t}^{irr}$ /10^{-6} $s^{-1}moll^{-1}cm$	$^{a}k_{-1}(h\nu)$ /$10^{-4}s^{-1}$	$^{a}k_{-1}(h\nu)/\epsilon_{c}^{irr}$ /10^{-6} $s^{-1}moll^{-1}cm$	$^{b}k_{-1}(\Delta)$ /$10^{-4}s^{-1}$	$^{b}t_{1/2}$ Cis /s
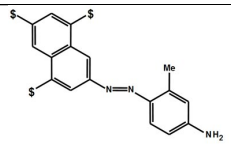 273/10	1620	36	2.3	86	4.1	6.7	1040
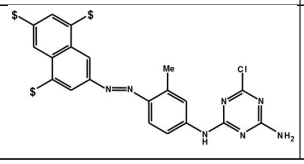 273/19	730	42	5.8	162	14.0	1.2	5800
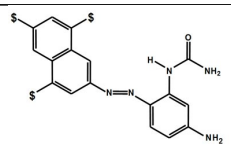 269/52	7950	64	0.8	116	1.1	74.7	90
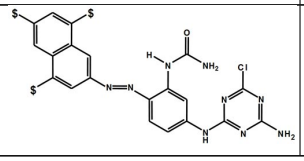 269/56	4333	106	2.5	307	7.3	11.2	620
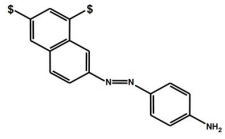 271/64/	1520	51	3.3	128	5.5	1.6	4500
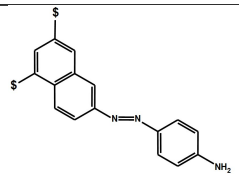 284/43	520	44	8.5	121	8.5	1.1	6300
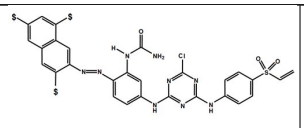 273/5	1788	53	2.9	123	7.6	11.1	620
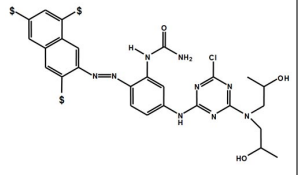 273/6	916	33	3.6	46	5.4	1.1	6200
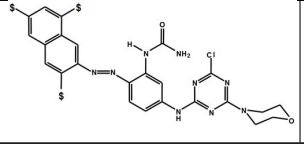 273/8	1073	25	2.4	78	7.6	4.1	1700

Table 5.7 – continued overleaf

Continued from previous page

Molecule/Structure	ϵ_t^{irr} /$M^{-1}cm^{-1}$	$^a k_1(h\nu)$ /$10^{-4}s^{-1}$	$^a k_1(h\nu)/\epsilon_t^{irr}$ /10^{-6} $s^{-1}moll^{-1}cm$	$^a k_{-1}(h\nu)$ /$10^{-4}s^{-1}$	$^a k_{-1}(h\nu)/\epsilon_c^{irr}$ /10^{-6} $s^{-1}moll^{-1}cm$	$^b k_{-1}(\Delta)$ /$10^{-4}s^{-1}$	$^b t_{1/2}$ Cis /s
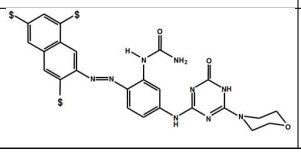 273/13	930	24	2.5	73	7.9	10.8	640

Table 5.7: Rates constants for isomerisation for each of the photoisomers in the series, grouped by dyebase/dye pairs, and 'second leg' structures. Observed *trans-cis* and *cis-trans* photochemical rate constants – $k_1(h\nu)$ and $k_{-1}(h\nu)$; photochemical rate constants corrected by ϵ_t and ϵ_c at λ_{irr} – $k_1(h\nu)/\epsilon_t$ and $k_{-1}(h\nu)/\epsilon_c$; thermal *cis* isomer decay rate constant – $k_{-1}(\Delta)$; half life for $k_{-1}(\Delta)$ – $t_{1/2}$ *cis*.
^{a}standard deviation = 18%. ^{b}standard deviation = 5%.

5.5.1 Relating Photoisomerisation Rate Constants to the Quantum Yield

Correcting the photochemical rate constants with the molar absorption coefficient allows for cross-comparison of the two values k_1/ϵ_t and k_{-1}/ϵ_c. Indeed, further comparison between other dyes may also be undertaken using these values. However, the rates of these processes also provide information on the relative quantum yields for photochemical *trans-cis* and *cis-trans* isomerisation, $\phi_{t\rightarrow c}$ and $\phi_{c\rightarrow t}$. For simplicity, expression of these quantum yields relative to one another, and to a standard value, has been undertaken and presented in Table 5.8. The new values for quantum yields, $\phi_{t\rightarrow c}^{rel}$ and $\phi_{c\rightarrow t}^{rel}$, are related to the largest observed photochemical rate constant in this study, 273/19 $k_{-1}(h\nu)$, which becomes unity. From this point onwards, comparison of photochemical data will be conducted using these relative quantum yields.

5.5.2 Effect of Structural Change on *Cis-Trans* Photoisomerisation

It is initially worth taking a moment to consider the relative quantum yields presented in Table 5.8. If photo-isomerisation is the only decay channel for the excited state, and *trans-cis* and *cis-trans* isomerisation proceed *via* the same transition state (TS), then $\phi_{t\rightarrow c} + \phi_{c\rightarrow t} = 1$. Without a method of directly determining absolute quantum yields, only ϕ_{isom}^{rel} in each isomerisation direction is available. However, if $\phi_{t\rightarrow c}+\phi_{c\rightarrow t} = 1$, then an increase in $\phi_{t\rightarrow c}$ must be accompanied by a decrease in $\phi_{c\rightarrow t}$. In the case of this study, $\phi_{t\rightarrow c}^{rel}+\phi_{c\rightarrow t}^{rel}$ will equal a constant if the absolute quantum yields for photo-isomerisation sums to unity. This is clearly not the case, so *cis-trans* and *trans-cis* isomerisation must proceed *via* different transition states. Of course this assumption relies upon the assumption that no other decay routes are available to the excited molecules. If more than one de-excitation route is available to the excited state *trans* or *cis* isomer, the

Molecule	$k_1(h\nu)$ /10^{-6} $s^{-1}moll^{-1}cm$	$\phi^{rel}_{t\rightarrow c}$	$k_{-1}(h\nu)$ /10^{-6} $s^{-1}moll^{-1}cm$	$\phi^{rel}_{c\rightarrow t}$	$\phi^{rel}_{t\rightarrow c}/\phi^{rel}_{c\rightarrow t}$
273/10	2.3	0.16	4.1	0.29	0.55
273/19	5.8	0.41	14.0	1.00	0.41
269/52	0.8	0.06	1.1	0.08	0.73
269/56	2.5	0.18	7.3	0.52	0.35
271/64	3.3	0.24	5.5	0.39	0.61
284/43	8.5	0.61	8.5	0.61	1.00
273/5	2.9	0.21	7.6	0.54	0.39
273/6	3.6	0.26	5.4	0.39	0.67
273/8	2.4	0.17	7.6	0.54	0.31
273/13	2.5	0.18	7.9	0.56	0.32

Table 5.8: Relative quantum yeild values for the *cis* and *trans* isomers of each molecule. Data are relative to 273/19 $k_{-1}(h\nu)$.

difference in the relative quantum yields could be accountable. However, no alternative evidence is available to support this and the assumption of separate transition states will be used to discuss the difference in ϕ^{rel}_{isom}.

To interpret ϕ^{rel}_{isom} values requires a knowledge of the ground and excited state potential energy surfaces (PES). Given the complexity of the molecules studied, even calculation of potential energy curves along a reaction coordinate would be extremely time-consuming. Performing calculations to this extent, and for excited state transition state structures of the molecules studied, was deemed far outside the scope of this project. Referring to Section 4.4.1, the number of possible minima on the ground state PES for dyebase 273/10 was shown to be at least four for the *trans* isomer alone. It is not surprising, therfore, that the data suggest more than one excited state TS is present.

It is clear from examining the relative quantum yields presented in Table 5.8 that structural diversity leads to a large degree of variation in the values, ranging from 0.06 to 1.00. Therefore, the excited state reaction coordinate is influenced to a large degree by modifying the structues. One striking observation is that all molecules demonstrate $\phi^{rel}_{c\rightarrow t} > \phi^{rel}_{t\rightarrow c}$ with the exception of 284/43, where the relative quantum yields are equal. Although no information is available for the ground and excited state PES, it is possible to infer some conclusions from this fact. At the instant a molecule undergoes irradiation the ground state (GS) structure is projected onto the excited state PES, and can be described as the Franck-Condon (FC) geometry for each isomer. After this, the molecular geometry will change until it reaches a transtion state (local minimum) close

to the FC geometry. The transition state accessed by excitation to the FC geometry, followed by relaxation, will hereafter be labelled *cis* TS and *trans* TS for the respective *cis* and *trans* isomers. Given $\phi_{c\rightarrow t}^{rel}$ is consistently larger than $\phi_{t\rightarrow c}^{rel}$ it is evident that *cis* TS bears more resemblance to *trans* GS than *trans* TS does to *cis* GS in each case. To illustrate this principle, Figue 5.8 gives a simple representation of the reaction coordinate, *vs.* energy for the expected species.

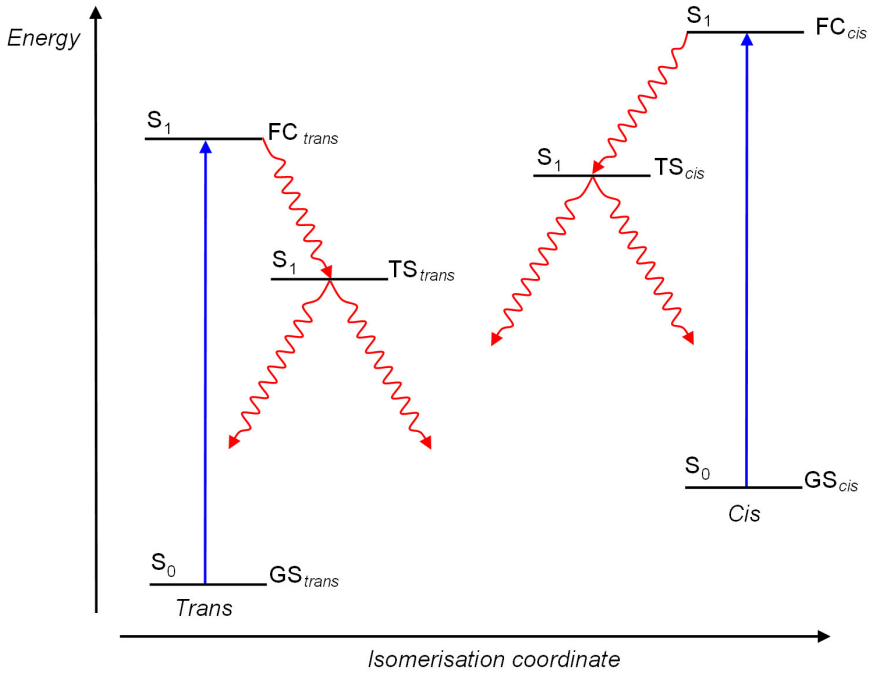

Figure 5.8: Simple representation of the isomerisation coordinate, where GS = Ground State, FC = Frank Condon state, and TS = Transition State. Two separate excited transition state structures, TS_{trans} and TS_{cis}, are shown.

Figue 5.8 can be used to help understand other observations in ϕ_{isom}^{rel}. The dyebases show an increase in both of the relative quantum yields when modified into reactive dyes. This indicates that the geometry of both *trans* TS and *cis* TS is more similar to the Frank-Condon geometry for the respective isomer in the dyebase, than observed for the dye. 'Second leg' dyes show little variation in $\phi_{t\rightarrow c}^{rel}$ and $\phi_{c\rightarrow t}^{rel}$ between each dye, suggesting the nature of the group is not particularly influential on the relationship of *trans* TS and *cis* TS with their ground state structures. One surprising observation is the difference in $\phi_{t\rightarrow c}^{rel}$ between dyebases 271/64 and 284/43. The move of both sulfonate groups from the **AC** to the **BD** positions on the naphthalene ring has produced significant changes in the relative quantum yields. This is further proof that it is extremely difficult to gain a full understanding of the excited state kinetics presented here without information on the excited and ground state potential energy surfaces. Only unsophisticated conclusions can be drawn from comparision of the photochemical

rate constants after conversion into relative quantum yields. Where possible, a more detailed investigation of photochemical rates is undertaken in the sections that follow.

5.5.3 Effect of Structural Change on *Cis-Trans* Thermal Isomerisation

Thermal decay of the *cis* isomer is of particular interest to the dye chemist, since this value pertains to the length of time the unwanted product will persist once removed from the light source. In contrast to the photochemical rates, kinetic data for thermal *cis* isomer decay show more dependence upon molecular structure. Although Tait noticed kinetic differences on the scale of nearly four orders of magnitude between certain structures, the group responsible for greatly extended thermal decays was identified as a methyl group on the nitrogen linking the chlorotriazine to the chromophore, and has not been studied within this work. Aside from these extreme values, Tait found that dyes without the methyl group on the linking nitrogen displayed $k_{-1}(\Delta)$ values spanning up to two orders of magnitude; a result in accordance with the present data. Evidently these rates show more dependence on electronic structure and steric effects than do the photochemical rate constants. Some simple observations can be made before an in depth analysis of structural effects is undertaken. The dyebases display shorter thermal decay half-lifes than the dyes. Furthermore, *cis* isomers of compounds containing a methyl group *ortho* to the azo bond take longer to decay than equivalent structures with a ureido group. Rates of thermal reversal for the second leg structures are quite variable, the nature of the terminal group affecting thermal kinetics much more than for the photochemical rates in these compounds. An interesting point to note is the effect of hydrolysing the chlorine group from the triazine ring. This modification appears to alter the thermal rate without affecting the photochemical rates of the system. Further analysis of thermal rates relating to each of the contrasting structures is conducted in the following sections.

5.5.4 Comparison of Dye and Dyebase Kinetics

Although the reactive dye is the form of the colourant to be applied to fabrics, it is interesting to investigate the changes induced when the chlorotriazine group is bonded to the dyebase (the azo chromophore). Hence, dye and dyebase pairs 273/10 and 273/19, and 269/52 and 269/56 are compared here to explain the effects of adding the reactive component to the chromophore. The data for these dyes is presented in the upper half of Table 5.7.

5.5.4.1 Effect of the Reactive Group on Photoisomerisation

For both dyebases, the conversion to a reactive dye results in an approximate 2.5-3.0× increase in $\phi^{rel}_{t\rightarrow c}$. Furthermore, the rise observed in $\phi^{rel}_{c\rightarrow t}$ is more pronounced than the increase in $\phi^{rel}_{t\rightarrow c}$. Referring once more to Figure 5.8, *trans* TS and *cis* TS of a dyebase must resemble their respective Frank-Condon excited state geometries more than the reactive dyes, resulting in a reduced probability of isomerisation after internal conversion, instead vibrationally relaxing into the same potential energy surface minimum from which they were excited. Conversely, the TS structures in the reactive dye will show greater differences from the FC geometries than their respective dyebases, allowing a greater number of isomerisation events to occur in each direction, leading to the elevated ϕ^{rel}_{isom} values. The other interesting observation is the larger increase in $\phi^{rel}_{c\rightarrow t}$ from dyebase to reactive dye compared with the rise in $\phi^{rel}_{t\rightarrow c}$. This indicates *cis* TS in the reactive dye loses more of its similarity to *cis* FC than does *trans* TS to *trans* FC. Hence, a greater increase in the quantum yield for *cis-trans* isomerisation is seen. A significant hypsochromic shift is apparent in the UV-vis absorption spectrum following addition of the chlorotriazine group to a dyebase (Figure 4.3), a clear indication that the excited state electronic structure of the dye differs from the unreactive chomophore. A change in the observed kinetics is therefore not an unexpected observation.

5.5.4.2 Effect of the Reactive Group on Thermal Isomerisation

For both dye/dyebase pairs, an approximate six-fold decrease is observed in $k_{-1}(\Delta)$, the thermal decay rate constant, following the addition of the chlorotriazine ring to the dyebase. It is evident that the reactive group increases the thermal barrier to isomerisation, extending the lifetime of the *cis* isomer; a particularly undesirable consequence of this chemical modification of the chromophore. The *cis* isomer of a reactive dye with sufficient length and flexibility to contort has been shown to form favourable interactions between aromatic group substituents that are remote in the *trans* isomer.[30] Stabilisation of a *cis* isomer can increase the thermal decay barrier which it must overcome to revert to the more stable *trans* geometry. Figure 5.9 shows the *trans* and *cis* structures for each dye and dyebase, labelled a–h. Examination of the *cis* isomer structures shows the addition of the chlorotriazine ring does not lead to any more intramolecular interactions than those observed in the chromophore. Despite this fact, the change in $k_{-1}(\Delta)$ after structural modification is distinct and must be attributed to an alteration of the π electron structure of the molecule. The presence of a chlorotriazine group is clearly instrumental in changing the ground state electronic structure of the molecule, raising the energy barrier to thermal reversal.

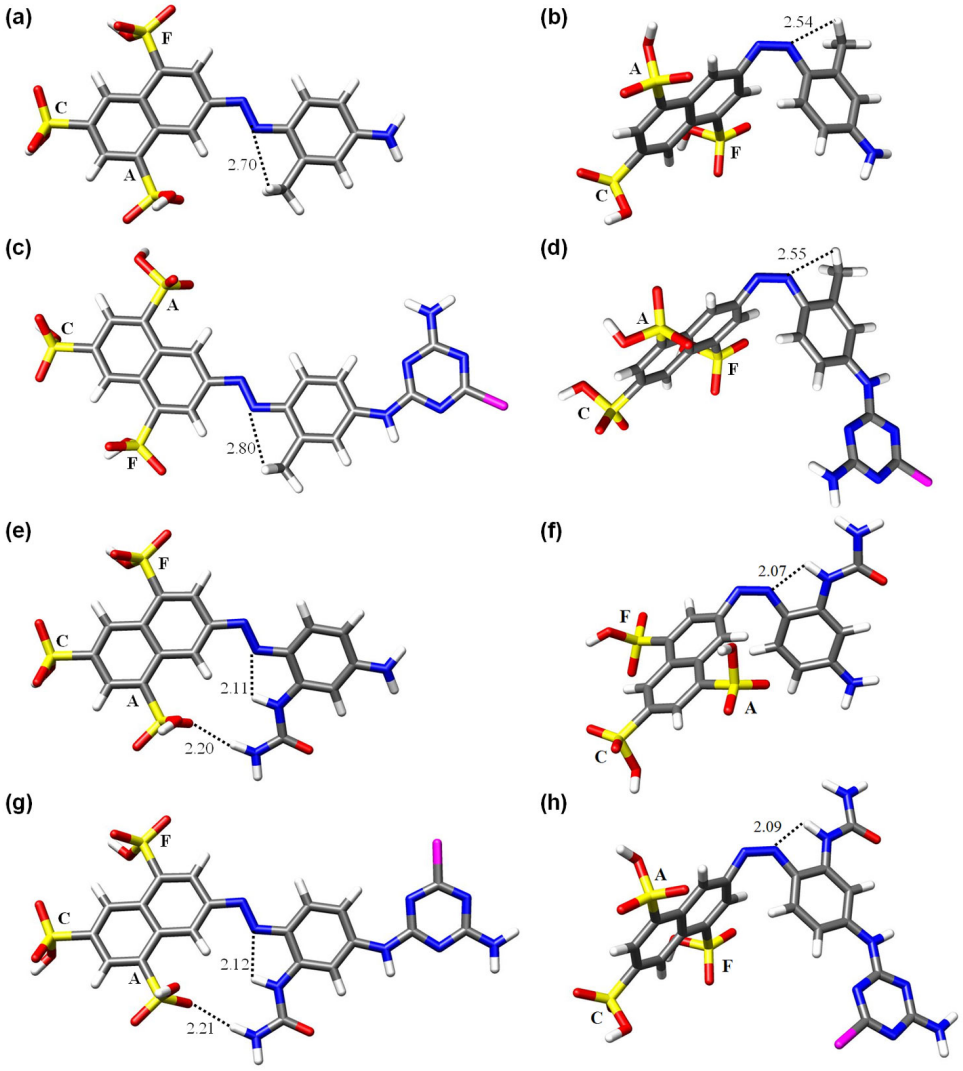

Figure 5.9: Minimum energy stuctures of the dye and dyebases (a) *trans* 273/10, (b) *cis* 273/10, (c) *trans* 273/19, (d) *cis* 273/19, (e) *trans* 269/52, (f) *cis* 269/52†, (g) *trans* 269/56, (h) *cis* 269/56†. Distances (Å) are presented for interactions <3 Å. †Structure expected from experimental data, refer to Section 4.4.3.1

5.5.5 Effect of Methyl and Ureido Substituents

The purpose of altering the benzene ring substituent was to investigate the effects of groups proximal to the azo linkage, and opposing the naphthalene group. Many current commercial dyes incorporate a ureido or chemically similar group in this position. The effect of adding such a group is observed through comparing the isomerisation rates of dyebases 273/10 and 269/52, and dyes 273/19 and 269/56, data for which are repeated in Table 5.9, with relative quantum yields stated instead of corrected photochemical rate constants.

Molecule/Structure	ϵ_{t}^{irr} /$M^{-1}cm^{-1}$	$^{a}k_1(h\nu)$ /$10^{-4}s^{-1}$	$^{a}\phi_{t\rightarrow c}^{rel}$	$^{a}k_{-1}(h\nu)$ /$10^{-4}s^{-1}$	$^{a}\phi_{c\rightarrow t}^{rel}$	$^{b}k_{-1}(\Delta)$ /$10^{-4}s^{-1}$	$^{b}t_{1/2}$ Cis
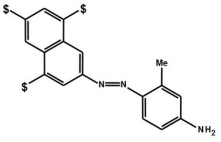 273/10	1620	36	0.16	86	0.29	6.7	1040
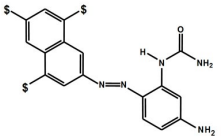 269/52	7950	64	0.06	116	0.08	74.7	90
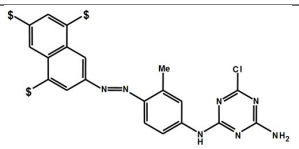 273/19	730	42	0.41	162	1.00	1.2	5800
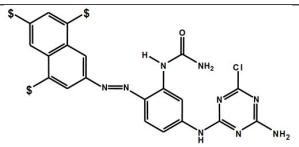 269/56	4333	106	0.18	307	0.52	11.2	620

Table 5.9: Rates of isomerisation for the photoisomers containing methyl and ureido substituents, arranged by dyebase/dye pairs.
^{a}standard deviation = 18%. ^{b}standard deviation = 5%.

5.5.5.1 Effect on the Photoisomerisation Rate

Comparison of the dyes, and of the dyebases, shows $\phi_{t\rightarrow c}^{rel}$ to be approximately 2.5× greater in the methyl containing molecules, and $\phi_{c\rightarrow t}^{rel}$ 2-3× greater. Hence, the *trans* TS and *cis* TS structures are closer to their respective ground state starting geometries in compounds containing a ureido group than those with a methyl group in the same position. For the methyl substituted molecules there is a greater likelihood that the *cis* TS will relax to *trans* GS, and *vice versa*, hence giving a greater chance of isomerisation after photon absorption. It is difficult to glean any further conclusions from the photochemical data presented in the table.

5.5.5.2 Effect on the Thermal Rate

An approximate increase of one order of magnitude is seen in $k_{-1}(\Delta)$ when the methyl is replaced with a ureido group. Calculated structures of the *cis* isomers presented in Figure 5.9 may be used to attempt an explanation of the experimental observations. In the *cis* isomer of the ureido substituted molecules, the ureido NH proton interacts with the closest azo nitrogen atom, the dyebase demonstrating a hydrogen-bonding distance of 2.07 Å, the dye 2.09 Å. This hydrogen bonding interaction forms a pseudo 5-membered ring between the ureido NH and the azo bond and is likely to reduce π

electron density in the –N=N– bond when compared with the equivalent methyl containing molecule. This is shown by a lengthening of the azo bond for both the dye and dyebase, although the magnitude of this change is small (0.004, 0.007 Å respectively). The inferred weaker azo bond in the ureido containing molecules allows a lower energy route for thermal isomerisation to the more stable *trans* isomer, consistent with the increased rate of thermal decay observed for the ureido compound compared with its methyl equivalent. The effect of the *ortho* substituent is certainly not steric in nature, given the increase in rate for molecules containing the larger ureido group. In this case an electronic effect is present through intramolecular interaction of the substituent with the azo bond.

Nishimura and Sueyoshi have commented on the effects of methyl and chloro substituents *ortho* to the azo bond, postulating that the effect of these components affect the π electron structure of the *cis* isomer, causing a change in $k_{-1}(\Delta)$.[79,80,94] In donor/acceptor aromatic azo dyes, *ortho* methyl groups were seen to accelerate thermal *cis* isomer decay when positioned on the donor side of the molecule, with a slight retarding effect when positioned on the acceptor side. This effect became more remarkable when the solvent polarity was increased. Conversely, placing an *ortho* chlorine group on the donor side retarded the rate, whereas placing it on the acceptor side raises the rate. The observations suggest delocalisation of the π electrons is important in rate controlling factors. At this point, an unsubstituted dye would be a useful measure against the ureido and methyl groups used in this study. However, this is not available so discussion of the two substituents studied must suffice.

To conclude, replacing the methyl substituent *ortho* to the azo bond with a ureido group has the effect of reducing the energy barrier to isomerisation of the *cis* isomer, allowing a more rapid thermal decay. It also serves to reduce both $\phi^{rel}_{t\rightarrow c}$ and $\phi^{rel}_{c\rightarrow t}$. It would be interesting to further investigate effects observed here by investigating the properties of protonated analogues to confirm a slower rate of thermal decay in the absence of any *ortho* substituent on the benzene ring.

5.5.6 Second Leg Effects

Reactive dye B275 (Figure 5.7) is a commercial yellow azo dye. Kinetic measurements performed by Tait for this dye are presented at the top of Table 5.10. Each of the dyes presented alongside B275 in this table are based on this reactive chromophore, with modification of the terminal amine on the chlorotriazine ring. The concept of adding a 'second leg' to the point where B275 terminates in a primary amine group is to investigate how elongating the structure of B275 affects the characteristics of

isomerisation. Presently, only the effect of changing substituents close to the azo bond have been investigated. From a simplistic viewpoint, the addition of a large group on the reactive component may be expected to influence the kinetics by interacting with other components of the structure, especially in the *cis* isomer where the molecule will have sufficient length and flexibility for each end to interact. In the case of 273/5, also a commercial dye, bonding to cellulose occurs through the terminal vinyl sulfone, rather than through elimination of the triazine chlorine atom. In doing so it forms a strong, covalent carbon-oxygen bond to the substrate. Therefore, it is important to investigate such moleucles to determine how the extension of the structure impacts on the properites.

Molecule/Structure	$\epsilon_{\mathbf{t}}^{\mathbf{irr}}$ /$\mathbf{M^{-1}cm^{-1}}$	$^{a}\mathbf{k_1(h\nu)}$ /$\mathbf{10^{-4}s^{-1}}$	$^{a}\phi_{t\rightarrow c}^{rel}$	$^{a}\mathbf{k_{-1}(h\nu)}$ /$\mathbf{10^{-4}s^{-1}}$	$^{a}\phi_{c\rightarrow t}^{rel}$	$^{b}\mathbf{k_{-1}(\Delta)}$ /$\mathbf{10^{-4}s^{-1}}$	$^{b}\mathbf{t_{1/2}}$ **Cis**
B275 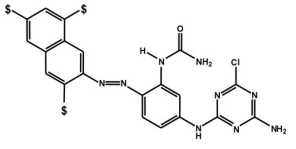	1850	10	0.09	40	0.36	2	3540
273/5 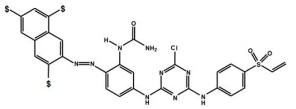	1788	53	0.21	123	0.54	11.1	620
273/6 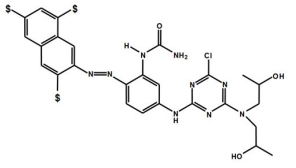	916	33	0.26	46	0.39	1.1	6200
273/8 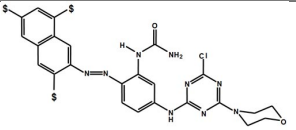	1073	25	0.17	78	0.54	4.1	1700

Table 5.10: Rates of isomerisation for each of the photoisomers in the 'second leg' study.
^{a}standard deviation = 18%. ^{b}standard deviation = 5%, except B275, where ^{a}standard deviation = 18%. ^{b}standard deviation = 7%

The relative quantum yield for *trans-cis* photo-isomerisation, $\phi_{t\rightarrow c}^{rel}$, for each of the new dyes differs to that of B275, with values ranging from 2-3× that of the parent molecule. In contrast, $\phi_{c\rightarrow t}^{rel}$ shows less variation, 273/6 being almost identical to B275. Despite the distinct difference in the nature of the additional groups, $\phi_{c\rightarrow t}^{rel}$ for dyes 273/5 and 273/8 is the same. Of the four sets of ϕ_{isom}^{rel} presented, B275 displays the best characteristics for a dye chromophore with the smallest $\phi_{t\rightarrow c}^{rel}$, and a $\phi_{c\rightarrow t}^{rel}$ value comparable to the others, giving a $\phi_{t\rightarrow c}^{rel}/\phi_{c\rightarrow t}^{rel}$ ratio of 0.25 compared with the range of 0.31-0.67 displayed by the 'second leg' dyes. As with all dyes studied, the lack of detailed information

regarding the ground and excited state potential energy surfaces makes it difficult to interpret structural effects on the relative quantum yields displayed by these dyes. The addition of the 'second leg' appears to change the structure of *trans* TS to a certain extent, moving it further from FC *trans*. The nature of *cis* TS is influenced to a lesser degree by the presence of the new groups.

The variation in the 'second legs' used is mirrored in the thermal decay characteristics of these molecules. Although the groups are remote from the area of greatest geometrical rearrangement upon isomerisation, each group bears influence on the energy barrier to thermal reversal. An obvious trend, for example an overall increase or decrease in the rate of thermal *cis* decay upon addition of a large group to B275, can not be extracted from these data. In two cases the rate was seen to increase, one by 2× and one over 5×. For 273/6, the isomerisation slowed down by a factor of two. The aromatic nature of the additional components on 273/5 could well be the reason for it having the fastest *cis* isomer decay of the studied dyes, due to possible conjugation through the aromatic system. Due to the aliphatic nature of substituents used in the other two dyes, the chlorotriazine ring is less likely to experience a strong influence on its π electron structure. This is likely to explain the small change in rate, approximately 2× greater or smaller than B275, compared to the 5× difference for 273/5. The calculated structures for the *cis* isomers of each of the dyes, including B275, are presented in Figure 5.10.

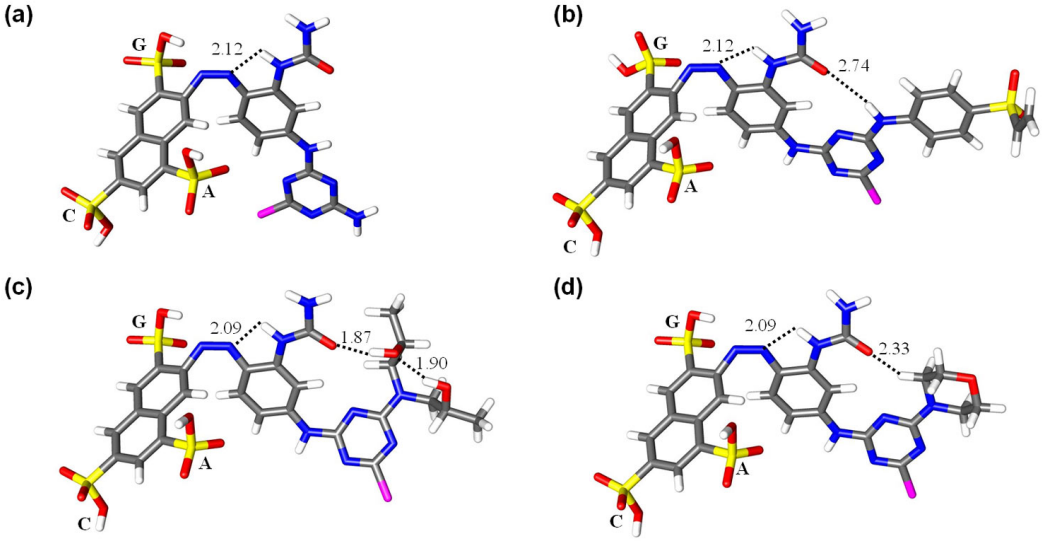

Figure 5.10: Minimum energy stuctures of the 'second leg' dyes (a) *cis* B275†, (b) *cis* 273/5, (c) *cis* 273/6, (d) *cis* 273/8. Distances (Å) are presented for interactions <3 Å.
†Calculation performed on behalf of K.M. Tait by Dr. P.R. Richardson, University of Edinburgh.

Across the *cis* isomer structures, the structural arrangement of the naphthalene and benzene ring components is consistent. Beyond this, similarity of 'second leg' dyes with B275 begins to change. The extended structure of the second leg dyes differ to B275 with a 180° torsion of the amine bridge and chlorotriazine ring bringing the second leg close to the ureido group in each case. In 273/6, the OH groups on the isopropyl alcohol group align to hydrogen bond internally, and with the carbonyl oxygen of the ureido group. If the ureido group is responsible for affecting the π electron density in the azo bond, this hydrogen bonding interaction may be perturbed slightly due to the oxygen–hydrogen bond formed with one of the hydroxyl groups of the second leg. This is of course highly speculative. In general the structures do not convey a great deal of information regarding why such changes have been observed in the thermal decay of the *cis* isomers for each of the dyes. It it clear that further interactions are present in these structures due to the extra groups, but the implications of these interactions can not be clearly rationalised through studying the rate of thermal *cis* isomer decay.

In conclusion, the addition of a 'second leg' to a dye appears to have the effect of increasing the quantum yield for the *trans-cis* photo-isomerisation, without greatly affecting $\phi^{rel}_{c\rightarrow t}$. However, the thermal rates show a greater degree of variation which can only be assigned to the second leg groups affecting the overall π structure of the molecule, the greatest difference demonstrated by 273/5 with an aromatic second leg.

5.5.7 Effect of Hydrolysing the Chlorotriazine Group

In Chapter 4, an investigation into the impact of hydrolysing the chlorine atom of 273/8 (forming 273/13) on the NMR spectrum and structure was conducted. This provides another route to examining the changes in the kinetic properties produced by modifying parts of the molecule distant from the azo bond area.

Molecule/Structure	ϵ^{irr}_{t} /$M^{-1}cm^{-1}$	$^{a}k_1(h\nu)$ /$10^{-4}s^{-1}$	$^{a}\phi^{rel}_{t\rightarrow c}$	$^{a}k_{-1}(h\nu)$ /$10^{-4}s^{-1}$	$^{a}\phi^{rel}_{c\rightarrow t}$	$^{b}k_{-1}(\Delta)$ /$10^{-4}s^{-1}$	$^{b}t_{1/2}$ Cis
273/8 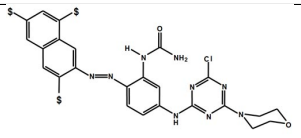	1073	25	2.4	78	7.6	4.1	1700
273/13 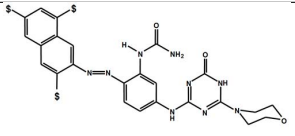	930	24	2.5	73	7.9	10.8	640

Table 5.11: Rates of isomerisation for each of the photoisomers of after hydrolysing the chlorotriazine group.
[a]standard deviation = 18%. [b]standard deviation = 5%.

The experimental data for the two dyes are presented in Table 5.11. Examining the UV-vis spectrum of each *trans* isomers presented in Figure 4.3 shows the two dyes to have very similar spectra, the hydrolysed dye demonstrating reduced ϵ_t at λ_{max}. The dyes both have a similar molar absorption coefficent at λ_{irr}, with minor deviation between the *trans* and *cis* isomers (refer to Table 5.4). Examination of the relative quantum yield values reveal the photochemical properties of both dyes to be identical within the stated bounds of experimental error. Therefore, hydrolysing the chlorine atom has no effect on $\phi^{rel}_{t\rightarrow c}$ and $\phi^{rel}_{c\rightarrow t}$ for the otherwise unaltered chromophore, suggesting the excited state potential energy surface for each molecule is identical. Clearly, the electronic effect of the chlorine or hydrolysed tautomeric system in an area somewhat remote from the point of large-scale geometrical change exhibits limited influence on *trans* TS and *cis* TS in relation to the ground state geometries.

The major difference observed between the two dyes, as with many of the molecules studied, can be found in the thermal isomerisation characteristics. For 273/13, $k_{-1}(\Delta)$ is 2.5× greater than the equivalent chlorine substituted dye, leading to an accelerated conversion of *cis* back to the more stable *trans* geometry. It is interesting that such a small change in the molecule at a point remote from the greatest geometrical change can introduce an increase in the rate of thermal decay without affecting the photochemical rates. Clearly the structural change is influential on the shape of the ground state potential energy surface. Minimum energy structures for the *cis* isomer of each dye are presented in Figure 5.11, showing both *cis* isomers to be extremely similar. Furthermore, the azo bond lengths and angles presented in Table 4.15 for both *cis* isomers are extremely similar, preventing an obvious structural cause to the difference in thermal rates of isomerisation from being identified.

Although the result of this study is interesting with respect to the substitution of a chlorine atom, expecially since chlorine elimination occurs during the dying process, the expected tautomeric structure is not representative of a free dye, or one bound to a fibre. The accelerated thermal decay of this molecule only serves to highlight the importance of subtle changes in the molecular structure on the kinetic behaviour of the molecule.

5.5.8 Effects of the Naphthyl Sulfonation Pattern

Due to other substantial structural changes, the **ACF** pattern utilised for the dye and dyebases could not be compared with the **ACG** pattern seen in the 'second leg' dyes. However, the comparison may still be made with previous results,[30] and is discussed later in Section 5.6.2. Two candidates, dyebases 271/64 and 284/43, with changes in

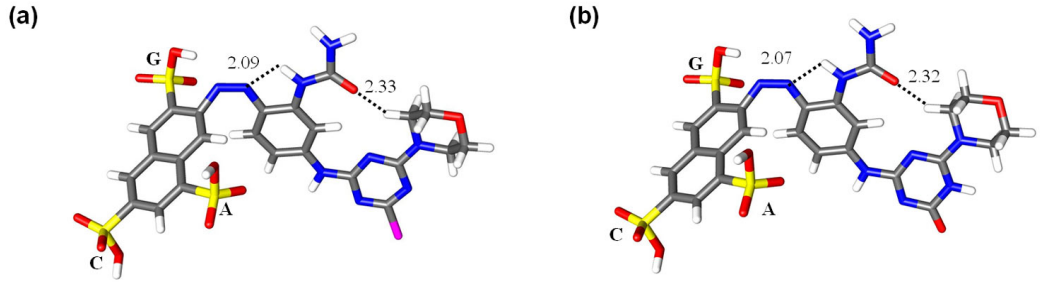

Figure 5.11: Minimum energy stuctures of the *cis* isomerers of 'second leg' structures containing chlorinated or hydrolysed triazine groups (a) *cis* 273/8, (b) *cis* 273/13. Distances (Å) are presented for interactions <3 Å.

Molecule/Structure	$\epsilon_{\mathbf{t}}^{\mathbf{irr}}$ /$\mathbf{M^{-1}cm^{-1}}$	$^{a}\mathbf{k_1(h\nu)}$ /$\mathbf{10^{-4}s^{-1}}$	$^{a}\phi_{t\rightarrow c}^{rel}$	$^{a}\mathbf{k_{-1}(h\nu)}$ /$\mathbf{10^{-4}s^{-1}}$	$^{a}\phi_{c\rightarrow t}^{rel}$	$^{b}\mathbf{k_{-1}(\Delta)}$ /$\mathbf{10^{-4}s^{-1}}$	$^{b}\mathbf{t_{1/2}}$ **Cis**
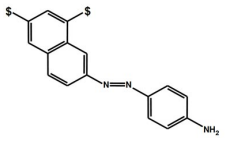 271/64/	1520	51	0.24	128	0.39	1.6	4500
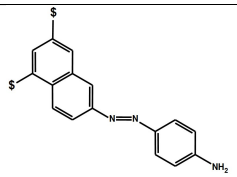 284/43	520	44	0.61	121	0.61	1.1	6300

Table 5.12: Rates of isomerisation for each of the photoisomers with **AC** and **BD** naphthyl sulfonation pattern.
^{a}standard deviation = 18%, ^{b}standard deviation = 5%.

the naphthalene substitution pattern were investigated in this study. This was to look into the importance of sulfonate positions distant from the azo group, and the effect this has on the quantum yields and thermal rates of isomerisation. Results for these two dyes are summarised in Table 5.12.

The two dyes contain only two naphthyl sulfonate groups, neither of them adjacent to the azo linkage, with a *para*-amino benzene group on the other side of the azo bond. Sulfonate groups are positioned **AC** in 271/64, and **BD** in 284/43. In fact, rather than the single changes made in other dyes within this work, this involves two changes in the structure. Examining the relative quantum yields shows this stuctural change to have a bearing on the excited state potential energy surface. Quantum yield differences in the two dyebases are distinct, with a greater change between $\phi_{t\rightarrow c}^{rel}$ at 2.5× larger in the **BD** molecule, than between $\phi_{c\rightarrow t}^{rel}$ at 1.5× greater in **BD**. The photoisomerisation quantum yields for dyebase 284/43 are equal, whereas $\phi_{c\rightarrow t}^{rel}$ is over 1.5× greater than the *trans-cis* quantum yield in 271/64. Evidently the changes in position of the naphthyl sulfonate groups are important for altering the photochemical properties of the dye.

The *cis* isomer half lifes are longer than for the other dyebases presented here, which is likely to be an influence of these molecules lacking substituents ortho to the azo bond. The half life of thermal *cis* isomer decay for dyebase 284/43 is 1.4× longer than 271/64. This is not as great a change as those observed in other systems and reflects the fact that sulfonate groups positions more distant from the azo bond do not greatly influence the ground state potential energy surface. The difference may be attributable to the difference in the *cis* isomer geometries of these two dyes. In Chapter 4, the ^{1}H NMR spectra and structures showed the molecules to display contrasting orientations of the naphthyl and phenyl rings around the azo bond. It is perfectly feasible that isomerisation to the different orientations proceed by a different route on the ground state PES, giving rise to the observed differences in the rates of thermal decay. This may also be explain the differences in the excited state PES.

5.6 Discussion of All Kinetic Data

Kinetic results obtained by Tait[30] are presented in this section and incorporated with current dye results to facilitate further analysis, and substantiate some conclusions. Given the advances in obtaining values for ϵ_{cis} described in this work (Section 5.3.5), and with access to the dye samples studied by Tait, data for ϵ_{cis} were collected to complement Tait's work by allowing calculation of $k_{-1}(h\nu)/\epsilon_c^{irr}$, hence adding $\phi_{c\rightarrow t}^{rel}$ to the discussion. The entire set of results is compiled in Table 5.13. In-depth discussion of the structural features is contained in the cited reference. The sections following will consider structural changes relevant to the current work, and briefly summarise previous observations on substituent effects not studied here. Examining the data, the value of $\phi_{c\rightarrow t}^{rel}$ is found to exceed that of $\phi_{t\rightarrow c}^{rel}$ in all cases except that of dye 178/3, where an identical result is seen. At no point does $\phi_{c\rightarrow t}^{rel}$ drop below that of $\phi_{t\rightarrow c}^{rel}$ for a given molecule. All values of ϕ_{isom}^{rel} are calculated relative to 273/19 which was identified to have the largest corrected photochemical rate constant of all dyes in the present study. It is clear from the relative quantum yield values exceeding unity in the previous study that the transition state structures in the present work are more representative of the ground state starting geometries, than some of those stated here. Ultimately, it highlights the fact we are only able to state data derived from the current study relative to a single value, and not to absolute quantum yields for these dyes. Alongside discussion of the quantum yield data, a greater amount of variability is present in the rate of thermal decay for these dyes compared with those in Section 5.5. Reasons for the extremely long decays are discussed within sections that follow.

Molecule/Structure	ϵ_t^{irr} /$M^{-1}cm^{-1}$	$^a k_1(h\nu)$ /$10^{-4}s^{-1}$	$^a\phi_{t\rightarrow c}^{rel}$	$^a k_{-1}(h\nu)$ /$10^{-4}s^{-1}$	$^a\phi_{c\rightarrow t}^{rel}$	$^b k_{-1}(\Delta)$ /$10^{-4}s^{-1}$	$^b t_{1/2}$ Cis
178/1 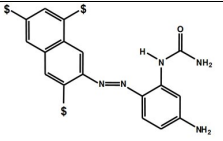	3330	>120	0.26	>210	>0.71	180	40
B275 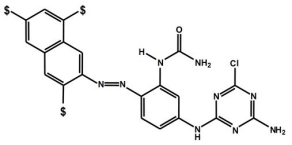	1850	10	0.09	40	0.36	2	3540
178/2 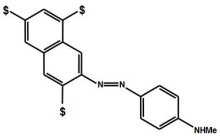	1220	190	1.14	190	1.29	10	520
178/11 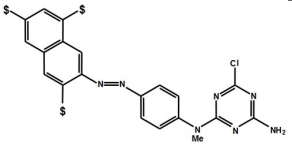	1995	50	0.18	120	0.43	0.024	290020
178/3 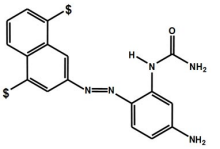	5340	90	0.12	90	0.12	160	40
178/9 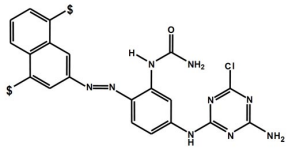	3967	120	0.21	170	0.26	10	620
178/5 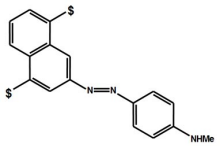	1890	7	0.03	20	0.06	5	1310
178/7 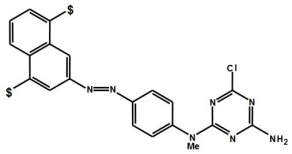	1224	60	0.35	260	1.50	0.25	28640

Table 5.13: Rates of isomerisation for each of the photoisomers studied by Tait,[30] grouped by dyebase/dye pairs.
[a]standard deviation = 18%. [b]standard deviation = 7%.

5.6.1 Dye versus Dyebase

As discussed in Section 5.5.4, adding a chlorotriazine ring to the dyebase had the effect of increasing the relative quantum yields, $\phi_{t\rightarrow c}^{rel}$ and $\phi_{c\rightarrow t}^{rel}$. This extra ring is also

responsible for a six-fold reduction in the thermal *cis* decay rate constant in the two systems studied indicating the reactive group has a strong influence on the ground state potential energy surface. Previous studies, data for which are reproduced in Table 5.13 arranged as pairs of dyebases with their respective dyes, may be used to see if this trend is general. Pairs 178/3 and 178/9, and 178/5 and 178/7 demonstrate a rise in $\phi^{rel}_{t\rightarrow c}$ and $\phi^{rel}_{c\rightarrow t}$, as expected from the two pairs studied earlier. However, the other two systems demonstrate the opposite effect. It is clear that a simple trend can not be applied to the photochemical rate constants for conversion of a dyebase to a dye. The postulate made earlier that *trans* TS and *cis* TS resemble their respective ground state geometries in a dyebase more than in the reactive chromophore cannot be applied to all systems. For two it is the reverse. Further explanation can not be attempted due to the unkown nature of the ground and excited state potential energy surfaces.

The thermal rate constant follows expectation well, with the dye demonstrating a longer *cis* decay time than the dyebase. This is where comparability becomes limited. There is no trend in the differences between each dye and dyebase pair. Where the molecules studied in Section 5.5.4 demonstrated a 6× increase in the thermal decay half life, the four pairs in Table 5.13 show 90, 500, 16, and 20 fold increases in $t_{1/2}$ following chlorotriazine addition. The dyes exhibiting especially long half lives, 178/7 and 178/11, were shown to have a sufficient level of flexibility for interactions between otherwise remote sites in the *cis* isomer. This was associated with the presence of a methyl group on the amine group linking the benzene and chlorotriazine components, a highly unexpected and undesirable occurence. Only simple conclusions regarding the thermal *cis* isomer decay can be taken away from comparing the six dyebase/dye systems studied here. The addition of a reactive component will extend the thermal half life of the photochemically generated *cis* isomer by a variable amount that is highly sensitive to structural changes.

5.6.2 Naphthyl Sulfonation Patterns

The use of two simple dyebases, with a disubstituted naphthyl ring containing either **AC** or **BD** sulfonate groups, demonstrated the effect of remote sulfonate groups to be more influential on ϕ^{rel}_{isom} than on the thermal isomerisation rates. The rates of thermal decay were elongated compared to other dyebases studied, a likely influence of the lack of any substituents *ortho* to the azo bond. Despite the use of both ACG and ACF sulfonated naphthyl groups in the other dyes discussed in Section 5.5, full analysis of these group effects could not be resolved due to additional differences in the substituted chlorotriazine rings. However, **ACF** dye 269/56 was synthesised as a structural variant of B275, the **ACG** substituted equivalent. Tait identified inequalities in the kinetic data

Molecule/ Structure	ϵ $^{irr}_{t}$ /$M^{-1}cm^{-1}$	$^{a}k_1(h\nu)$ /$10^{-4}s^{-1}$	$^{a}\phi^{rel}_{t\rightarrow c}$	$^{a}k_{-1}(h\nu)$ /$10^{-4}s^{-1}$	$^{a}\phi^{rel}_{c\rightarrow t}$	$^{b}k_{-1}(\Delta)$ /$10^{-4}s^{-1}$	$^{b}t_{1/2}$ Cis
B275 (**ACG**) 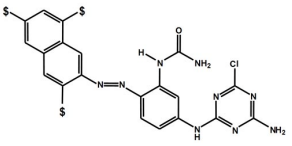	1850	10	0.09	40	0.36	2	3540
178/9 (**AF**) 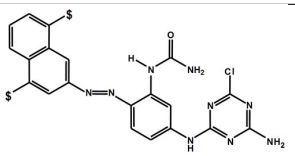	3967	120	0.21	170	0.26	10	620
269/56 (**ACF**) 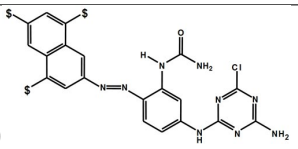	4333	106	0.18	307	0.52	11.2	620

Table 5.14: Rates of isomerisation for each of the photoisomers with a varied naphthyl sulfonation pattern.
269/56: ^{a}standard deviation = 18%, ^{b}standard deviation = 5%; B275 and 178/9: ^{a}standard deviation = 18%. ^{b}standard deviation = 7%

of B275, and the corresponding **AF** substituted dye, 178/9. Although the contrast in the results was ascribed to the movement of sulfonate **G** to the **F** position, the influence of additionally removing the **C** sulfonate from 178/9 could not ruled out of the argument due to a lack of experimental data. The data for 269/56 may be amalgamated with these results to provide a greater understanding of sulfonate pattern effects.

5.6.2.1 The Influence of Sulfonation Pattern on Structure

To assist our understanding of the kinetic data, the *cis* and *trans* structures for each of the dyes are presented, with labelled distances appropriate to the discussion, in Figure 5.12. Since the structural data for B275 and 178/9 are not discussed in Chapeter 4, a brief discussion is conducted here. To simplify the comparision of each structure, naphthalene groups are arranged uniformly in the figure. Although only the NMR data of dye 269/56 were discussed in Chapter 4, the other two dye structures were found to correlate well with experimental NMR data.[30] Of particular note is the *trans* structure of B275 which contrasts with the other two dyes. The NMR signal for the ureido NH_2 group appears as two separate, broad proton signals in the *trans* isomer, resolving to a single signal in the *cis*. This is apparent from the close proximity of the protons to the **G** sulfonate, the favourable hydrogen bond of only 1.98 Å slowing rotation to the extent two peaks apear in the *trans* spectrum. Although a favourable hydrogen bonding interaction between sulfonate **A** and the NH_2 protons is present in the calculated *trans* structures of 178/9 and 269/56, the distance is greater than that observed in B275 and

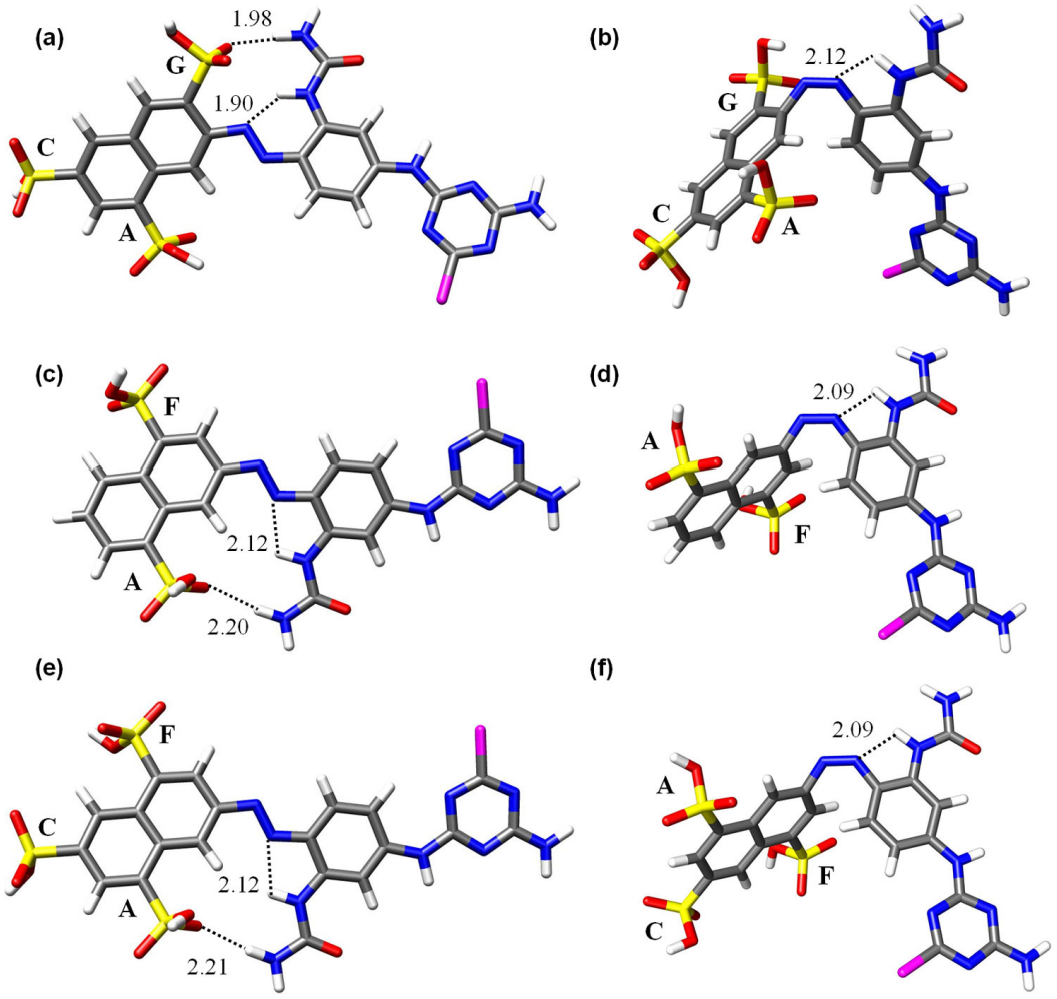

Figure 5.12: *Trans* and *cis* isomer structures of the three sulfonate substituted dyes, (a) *trans* B275†, (b) *cis* B275†, (c) *trans* 178/9†, (d) *cis* 178/9†, (e) *trans* 269/56 (f) *cis* 269/56. Distances (Å) are presented for interactions <3 Å.
†Calculations performed on behalf of K.M. Tait by Dr. P.R. Richardson, University of Edinburgh.

the ^{1}H NMR peak appears as a singlet. Each molecule incorporates this interaction with the closest sulfonate. As such, the group closest to the ureido protons in B275, **G**, causes the significant difference in *trans* structure when compared to the near identical structures of 178/9 and 269/56 that must take on an alternative orientation to benefit from a similar hydrogen bonding interaction. Further to the favourable NH_2-sulfonate hydrogen bonding in the *trans* isomer, the ureido NH, in all cases, aligns to one of the azo nitrogen atoms, offering additional H-bonding stabilisation. For 178/9 and 269/56, the hydrogen coordinates with the azo nitrogen on the benzene side of the molecule, displaying a distance of 2.12 Å. This forms a pseudo five-membered ring, affording some stabilisation. Conversely, due to its different orientation around the azo bond, the ureido hydrogen on B275 coordinates with the naphthyl side azo nitrogen with a bonding distance of 1.90 Å, forming a pseudo six-membered ring which is likely to bring

about even more stability in this molecule. This significantly shorter hydrogen bonding interaction is identified in the ^{1}H NMR spectrum of *trans* B275 by the ureido proton appearing at the deshielded value of 11.6 ppm. The same proton appears around 9 ppm in the the other two dyes.

Each *cis* isomer for the three dyes takes on a very similar structure. The ureido NH_2–sulfonate hydrogen bond identified in the *trans* isomers has been eliminated due to the twisted nature of a *cis* isomer. All three contain a pseudo five-membered ring created by the ureido NH proton and the phenyl-side azo nitrogen, with a distance of 2.12 Å in B275, and a shorter distance of 2.09 Å in the **ACF** and **AF** dyes. Figure 5.12 illustrates the *cis* structures with naphthalene groups orientated in a congruous manner. The **C** sulfonate of 269/56 and B275 appears remote from the rest of the molecule, preventing any possible interactions from occurring, and hence is not expected to influence the rate of thermal *cis* isomer decay. In 269/56 and 178/9, the only other obvious difference in the *cis* isomer structures is the position of sulfonate group in the **G** or **F** position on the naphthyl ring.

5.6.2.2 Correlating Isomerisation Rates with Structural Information

For convenience, data for the three dyes have been arranged into Table 5.14. The apparent difference in the structure of *trans* B275 appears to follow through into the isomerisation properties. The value of $\phi^{rel}_{t\rightarrow c}$ for the **ACG** sulfonated dye is approximately half that of the **AF** and **ACF** dyes, which hold a broadly similar value. The *ortho* sulfonate appears to reduce the probability that an excited *trans* molecule will undergo isomerisation, compared to a dye containing a proton in this position. This suggests *trans* TS bears a closer resemblance to *trans* FC than for the **F** substituted dyes. The *cis-trans* quantum yield, $\phi^{rel}_{c\rightarrow t}$, is not quite as simple to interpret since the value of B275 lies between those of the other two dyes. The lack of the **C** sulfonate has induced a smaller $\phi^{rel}_{c\rightarrow t}$ than in the dyes with a **C** sulfonate. Where B275 and 269/56 display large differences in the photo-isomerisation quantum yields, 178/9 does not, the values of $\phi^{rel}_{t\rightarrow c}$ and $\phi^{rel}_{c\rightarrow t}$ being quite close. This is reflected in the amount of *cis* isomer present at the PSS, where B275 has 15%, 269/56 has 20% and 178/9 has 40%. The smaller difference in forward and reverse ϕ^{rel}_{isom} for 178/9 allows a greater level of *cis* isomer to build up at the photostationary state. As usual, ϕ^{rel}_{isom} in each dye is weighted in the *cis-trans* direction, but to a lesser degree in the case of 178/9.

The thermal decay rate constants for the **AF** and **ACF** dyes are identical. The lack of any difference between the two dyes adds an great level of support to the argument that the **C** sulfonate does not greatly influence the thermal kinetics, which is inferred

in Section 5.5.8 by moving the **A** and **C** sulfonates to the **B** and **D** positions. This is borne out in the optimised geometries of the *trans* and *cis* isomers presented in Figure 5.14, where very little difference can be identified between the **AF** and **ACF** structures. B275 displays a $k_{-1}(\Delta)$ value 5× smaller than the other dyes, leading to a proportionately longer decay of the *cis* isomer. The difference between the *cis* isomer of B275 and the other dyes is the **G** sulfonate *ortho* to the azo bond, which appears to influence the hydrogen bonding between the ureido NH and the azo bond, lengthening the interaction by 0.03 Å. The longer H–bond suggests a change in the characteristics of the azo bond which could indeed affect the rate of thermal *cis* isomer decay. Furthermore, the *trans* isomer geometry of B275 differs from the **AF** and **ACF** dyes. This implies the mechanism by which *cis* B275 reverts to *trans* will be different to that of the other two analogues, the data suggesting it experiences a higher energy barrier to isomerisation. All that can be gathered through speculative discussion is that a sulfonate *ortho* to the azo bond is responsible for increasing the *cis* isomer half life. Calculated structures demonstrate this effect to be independent of the presence of the ureido group in the dyes investigated, which does not interact with the sulfonate groups in the *cis* isomer of each dye.

A more solid conclusion may now be drawn regarding the influence of sulfonate pattern on thermal *cis-trans* isomerisation. Groups remote from the azo bond are not expected to greatly affect the thermal decay of any *cis* isomer formed through photoisomerisation. When looking to alter a dye to change the characteristics of thermal isomerisation, removing the **C** sulfonate should be considered a redundant strategy. From a design perspective, this position, remote from the azo bond, may be used for a sulfonate solubilising group without introducing dramatic and unwanted changes in the rate of thermal decay. Naturally, the use of computational chemistry to predict structures prior to dye synthesis would be advantageous, allowing potentially unwanted interactions to be identified in advance. The use of a naphthyl sulfonate group *ortho* to the azo bond bears potential problems. In B275, the **G** sulfonate has an unfavourable influence on thermal decay, prolonging the life of the *cis* isomer. This perturbation is not observed in the **AF** and **ACF** dyes as a sulfonate proximal to the azo bond is not present.

5.6.3 Linking group

This is a structural effect that has not been studied specifically as part of this thesis. However, the data gathered help support claims made by Tait regarding the effect on rate of changing the substituent on the amine linking the benzene and chlorotriazine groups. The reactive dyes that contained a methyl group here (refer to Table

5.13) demonstrated substantially longer thermal decay times when compared to those containing a proton. It should be noted that this comparison was made to dyes that contained a ureido group *ortho* to the azo bond, which in itself is responsible for accelerating thermal decay. The observation that a change in the substitution of the benzene ring was made along with the addition of a methyl group to the linking amine makes it difficult to relate changes in the photochemical quantum yields of isomerisation observed in these molecules to a particular structural feature. However, the increase in *cis* decay time for these dyes was not in proportion with the equivalent dyebases that also lacked a ureido group. This effect was determined to be structural: the extended structure of the reactive dye was, in the *cis* form, able to twist further allowing two groups that were normally remote to be well within interacting distance. As an example, previously calculated *trans* and *cis* structures of 178/11 are presented in Figure 5.13, allowing the interaction in the *cis* isomer to be visualised. The molecule is highly contorted to allow this interaction. The additional stabilisation this affords is likely to lower the energy of the *cis* isomer relative to the GS transition state structure, therfore increasing the energy barrier for transition back to the *trans* geometry and providing such contrasting kinetics. Tait noted that reactive dyes containing a proton on the linking amine, rather than the methyl group, do not demonstrate such contorted *cis* isomers, leading to thermal *cis* isomer decay times that are significantly shorter than for molecules containing a methyl amine. The theory that a methylated amine allows distortion of the molecular geometry is further supported by the reactive dyes presented in this thesis, since the thermal decays remain short in comparison, and no interactions are observed between substituents bound on opposite sides of the azo bond in the *cis* isomer. Evidently the use of a methyl group in this position gives rise to a thermally stable *cis* isomer and should be avoided at all costs if a dye is to demonstrate rapid return to the *trans* isomer.

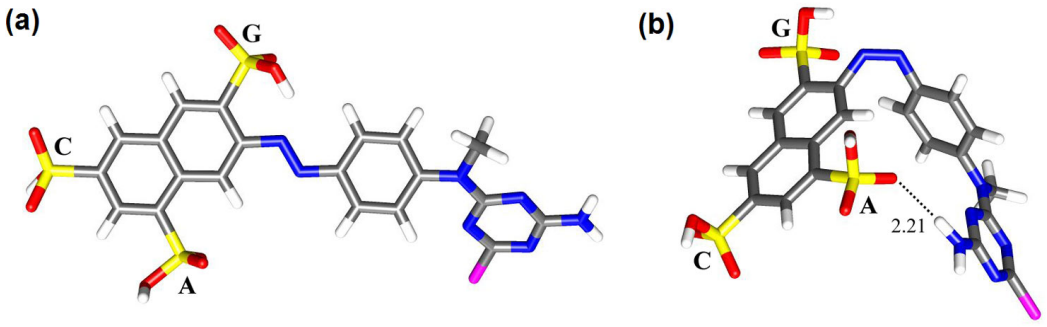

Figure 5.13: Dye 178/11 (a) *trans*† and (b) *cis*†. Distances (Å) are presented for interactions <3 Å.
†Calculations performed on behalf of K.M. Tait by Dr. P.R. Richardson, University of Edinburgh.

5.6.4 Benzene Ring Substituent

Two benzene ring substituents, a methyl and a ureido group, were investigated as discussed in Section 5.5.5. Tait attempted to investigate the influence of benzene ring substitution by comparing an unsubstituted dye to one containing a ureido group *ortho* to the azo bond. However, in each case compared there was an additional change in the structure brought about by adding a methyl group to the nitrogen of the terminal (dyebase) or linking (reactive dye) amine in the molecule with a hydrogen *ortho* to the azo bond, implications of which have been discussed in Section 5.6.3. Essentially, the methyl group here allows an additional degree of flexibility in a reactive dye that allows a naphthalene sulfonate group to interact with components of the chlorotriazine ring in the *cis* isomer. Therefore, discussion regarding the effects of benzene ring substitution could not be related entirely to a single modification. The study concluded that the ureido group held an electronic effect through hydrogen bonding to the nearest azo nitrogen in the *cis* isomer, which increased the rate of thermal decay when compared with a molecule containing a proton in this position. Analysing the corrected photochemical rate constants for *trans-cis* isomerisation proved inconclusive as no trend could be extracted from the examples used.

If we ignore the dyes that show interaction, and focus instead on the dyebases, it is possible to add to the discussion presented in Section 5.5.5. The best molecules to compare are 269/52 containing a ureido group, 273/10 with a methyl, and 178/5, with a proton. This study does not rule out the effect of a missing **C** sulfonate, and the additional methyl group at the point where a chlorotriazine ring would be attached to the dye. However, it has already been shown in Section 5.6.2 that the **C** sulfonate does not affect the thermal kinetics. Assuming the methyl group on the terminal amine does not affect isomerisation in the dyebase structure, we can compare the effect of having a ureido, methyl, or proton on the benzene ring *ortho* to the azo bond. Results are summarised in Table 5.15.

Photo-isomerisation quantum yields for 269/52 and 178/5, the ureido and protonated dyebases, are fairly similar, and somewhat lower than the methyl substituted dyebase for $\phi^{rel}_{t\rightarrow c}$, and much lower in $\phi^{rel}_{c\rightarrow t}$. No trend can be extracted from this data since the similarity of the first two molecules mentioned may be due to the lack of a **C** sulfonate group in 178/5 which was shown to reduce $\phi^{rel}_{c\rightarrow t}$ (Section 5.6.2.2).

Examination of the thermal *cis* isomer decay data is more fruitful in this study. Section 5.5.5 identified the rate of thermal *cis* isomer decay to be highly dependent upon the electronic nature of the substituent. The ureido group appears to weaken the azo bond

Molecule/Structure	ϵ_{t}^{irr} /$M^{-1}cm^{-1}$	$^{a}k_1(h\nu)$ /$10^{-4}s^{-1}$	$^{a}\phi_{t\rightarrow c}^{rel}$	$^{a}k_{-1}(h\nu)$ /$10^{-4}s^{-1}$	$^{a}\phi_{c\rightarrow t}^{rel}$	$^{b}k_{-1}(\Delta)$ /$10^{-4}s^{-1}$	$^{b}t_{1/2}$ Cis
273/10 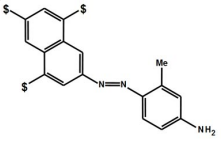	1620	36	0.16	86	0.29	6.7	1040
269/52 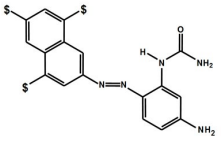	7950	64	0.06	116	0.08	74.7	90
178/5 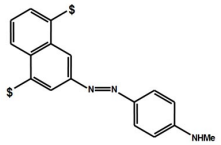	1890	7	0.03	20	0.06	5	1310

Table 5.15: Rates of isomerisation for each of the photoisomers with a varied benzene ring substituent.
273/10, 269/52: ^{a}standard deviation = 18%, ^{b}standard deviation = 5%; 178/5: ^{a}standard deviation = 18%. ^{b}standard deviation = 7%

somewhat, leading to a faster conversion back to *trans*, which is certainly desirable in a photochromic dye. Regarding the literature discussion (Section 5.5.5) on the electronic effect of the *ortho* substituent, it is expected that the substituted dyes will display an accelerated *cis* isomer decay compared to a protonated equivalent. Comparing the three dyebases, this is seen to be true:

$$t_{1/2} = \begin{matrix}\text{Proton} \\ (1310\text{ s})\end{matrix} > \begin{matrix}\text{Methyl} \\ (1040\text{ s})\end{matrix} > \begin{matrix}\text{Ureido} \\ (90\text{ s})\end{matrix}$$

This information helps to eliminate the possibility that steric hindrance from the *ortho* group occurs during isomerisation, since the rate increases in this example as the substituent gets larger. The effect must be derived from an alteration in the π electron structure of the azo bond, due to electronic differences in the nearby groups. Given the slight differences in the structures of 178/5 and 273/10, the rate of *cis* decay is quite similar. This suggests that either the *ortho* methyl does not greatly contribute to changing the ground state potential energy barrier to isomerisation in the protonated dye, or the methyl amine and missing **C** sulfonate of 178/5 accelerate the thermal *cis* decay of this particular dyebase to a rate more comparable to 273/10. The trend remains as anticipated, leading to the conclusion that thermal *cis* isomer decay is strongly dependent upon the electronic nature of the substituent and its effects on the local bonding in each molecule. This is supportive of research conducted by Nishimura *et. al,*[79,80,94] and of the conclusions formed in Section 5.5.5. It does however contrast with the results presented in Section 5.6.2 where an *ortho* sulfonate group leads to extended *cis* isomer decay times, the reason for which is anticipated to be a strong steric component.

5.7 Temperature Dependence of Thermal *Cis* Isomer Decay

The combination of NMR spectroscopy and *in situ* laser irradiation yields a great deal of information with respect to the kinetics of the dyes studied here. However, many of the discussions rely on speculation regarding potential energy surfaces, and often the energy barrier to *cis-trans* thermal isomerisation. As a trial for the *in situ* system, thermal isomerisation in dyebase 273/10, and 'second leg' dyes 273/6 and 273/8 was monitored at progressively elevated temperatures to see if the barrier could be experimentally determined using this technique. The low temperature limit was the freezing point of d_6-DMSO, with the upper limit determined by the longevity of the *cis* isomer of a particular dye at elevated temperature being sufficient for the technique to be applied effectively. Typically 6 or 7 experiments were performed at 5 K increments, with a suitable amount of time allowed for the irradiated systems to equilibrate to the new temperature between runs. This was found to produce a suitable number of values for fitting. Both the Arrhenius and Eyring Equations were used to derive thermodynamic parameters for the dyes. The Arrhenius equation is presented as Equation 5.19, where k is the rate constant, R is the universal gas constant with a value of 8.314 $JK^{-1}mol^{-1}$, T is the temperature in Kelvin, A is the steric factor and assumed to be constant over the temperature range studied, and E_a is the activation energy. A straight line plot of $\ln k$ *vs.* $1/T$ allows E_a to be calculated from the gradient, and A from the value of y at $x = 0$.

$$k = Ae^{-E_a/RT} \tag{5.19}$$

The barrier to a process can also be studied using transition state theory. The rate constant for a process, k, is defined in Equation 5.20, where k_B is the Boltzmann constant, h is Planck's constant, T is the temperature in Kelvin, and $K^{\ddagger}$ is the equilibrium constant between the activated complex and the reactants.

$$k = \frac{k_B T}{h} K^{\ddagger} \tag{5.20}$$

The equilibrium constant is related to the Gibbs free energy, $\Delta G^{\ddagger}$, as $\Delta G^{\ddagger} = -RTlnK^{\ddagger}$, which in turn is related to the activation enthalpy and entropy, $\Delta H^{\ddagger}$ and $\Delta S^{\ddagger}$, as $\Delta G^{\ddagger} = \Delta H^{\ddagger} - T\Delta S^{\ddagger}$. This allows Equation 5.20 to be written as:

$$k = \frac{k_B T}{h} e^{\frac{-\Delta H^{\ddagger}}{RT} + \frac{\Delta S^{\ddagger}}{R}} \tag{5.21}$$

Taking the natural log of k and rearranging the terms gives Equation 5.22, known as the Eyring equation. A plot of $\ln(k/T)$ *vs.* $1/T$ allows $\Delta H^{\ddagger}$ to be derived from the gradient, and $\Delta S^{\ddagger}$ from the graphical intercept with the y axis. These two values allow

Gibbs free energy of activation, $\Delta G^{\ddagger}$ to be calculated using the relationship stated earlier.

$$ln\frac{k}{T} = -\frac{\Delta H^{\ddagger}}{R} \times \frac{1}{T} + ln\frac{k_B}{h} + \frac{\Delta S^{\ddagger}}{R} \tag{5.22}$$

For a unimolecular reaction, the activation energy calculated using the Arrhenius equation is linked to the activation enthalpy, $\Delta H^{\ddagger}$ by the following relationship:

$$E_a = \Delta H^{\ddagger} + RT \tag{5.23}$$

This arises from the fact that the pre-exponential factor is slightly temperature dependent, although the Arrhenius equation assumes it to be constant. $\Delta H^{\ddagger}$ relates to T=0 K.

Graphs fitting the temperature dependent rate data for dyebase 273/10 to Equations 5.19 and 5.22 are presented in Figure 5.14. A good linear fit to both the Arrhenius Equation and Eyring Equation is apparent from the data (R=0.999 for both), demonstrating the applicability of this technique to thermal energy barrier calculation. The other two systems studied were treated in the same way and yielded equally good fits (not shown). All data were collected in d_6-DMSO to allow for comparison between values. Studies have shown activation energies of thermal azo isomerisation to display high sensitivity to the solvent environment.[61,78,79,99] The studies additionally report these activation energies to range from *ca.* 35 to over 100 kJ mol^{-1}. The data for the three dyes are presented in Table 5.16.

Molecule	$\boldsymbol{E_a}$/ **kJmol^{-1}**	**Steric Factor/ s^{-1}**	$\boldsymbol{\Delta H^{\ddagger}}$/ **kJmol^{-1}**	$\boldsymbol{\Delta S^{\ddagger}}$/ **JK^{-1}mol^{-1}**	$\boldsymbol{\Delta G^{\ddagger}_{298K}}$/ **kJmol^{-1}**
273/6	90.0	4.49×10^{11}	+87.4	-30.6	+96.5
273/8	82.6	3.50×10^{10}	+80.0	-51.8	+95.4
273/10	76.7	2.10×10^{10}	+74.2	-56.0	+90.8

Table 5.16: Activation Energy parameters for three of the 273 dyes, obrained in d_6-DMSO. E_a and the steric factor derived from the Arrhenius equation. $\Delta H^{\ddagger}$, $\Delta S^{\ddagger}$ and $\Delta G^{\ddagger}_{298K}$ derived from the Eyring equation.

As expected, dye 273/6 with the smallest rate constant for themal *cis* isomer decay demonstrates the largest activation energy, the trend of increasing rate constants from 273/6 to 273/10 is mirrored with decreasing activation energy for the molecules, the values for which exist within the experimental ranges found by other groups (see above). In view of the steric factors reported for thermal azo *cis-trans* isomerisation, ranging from 2.3×10^5 to 2.5×10^{12} s^{-1},[99] steric factors for the three molecules do not greatly differ from one another. The Arrhenius steric factor is related to $\Delta S^{\ddagger}$, and the activation energy to $\Delta H^{\ddagger}$. An increase in the steric factor corresponds to a decrease in $\Delta S^{\ddagger}$,

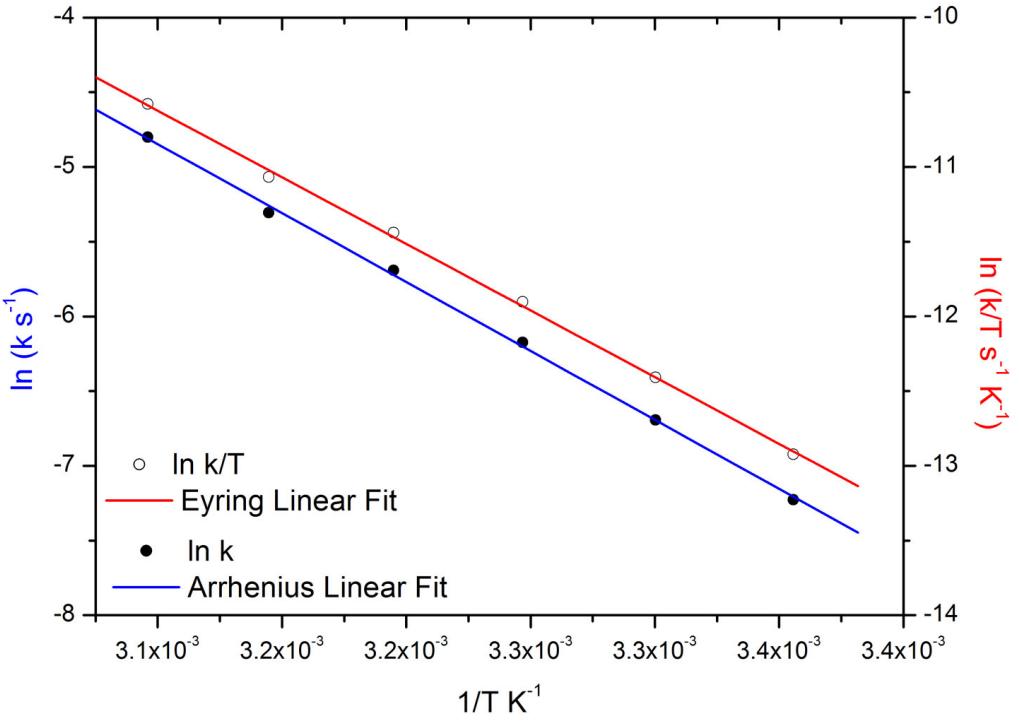

Figure 5.14: Graph showing the temperature dependence of the rate constant of 273/10 in d_6-DMSO with base.

showing the decrease in disorder between the *cis* isomer and activated complex of 273/6 is less than the other two dyes, which show similar entropy changes. $\Delta G^{\ddagger}_{298K}$ is almost identical for the 'second leg' dyes, with a small change for dyebase 273/10. This is not surprising given the similar structures 273/6 and 273/8, which contrast with the smaller dyebase.

Combining the experimentally determined value of E_a with the energy difference between the *cis* and *trans* isomers derived from *ab initio* calculations can provide a greater level of understanding with respect to the ground state potential energy curve along a reaction coordinate. A crude diagram using these details has been constructed in Figure 5.15 for 273/10. The calculated energy difference between the *trans* and *cis* isomers is less than the difference between the *cis* isomer and ground state transition state. It is clear that thermal isomerisation only occurs in the *cis-trans* direction since the *trans-cis* thermal energy barrier is much greater.

In conclusion, the use of NMR with *in situ* laser irradiation has been used to photogenerate azo *cis* isomers and follow their thermal decay over a range of temperatures to gain insightful data on the energy barrier for three of the dyes studied here. The excellent fit of data to the Arrhenius and Eyring Equations suggest that this method is ideal for determining thermal energy barriers. The high resolution of NMR used for determining kinetic parameters is additive in the goodness of fit, since the ambiguities

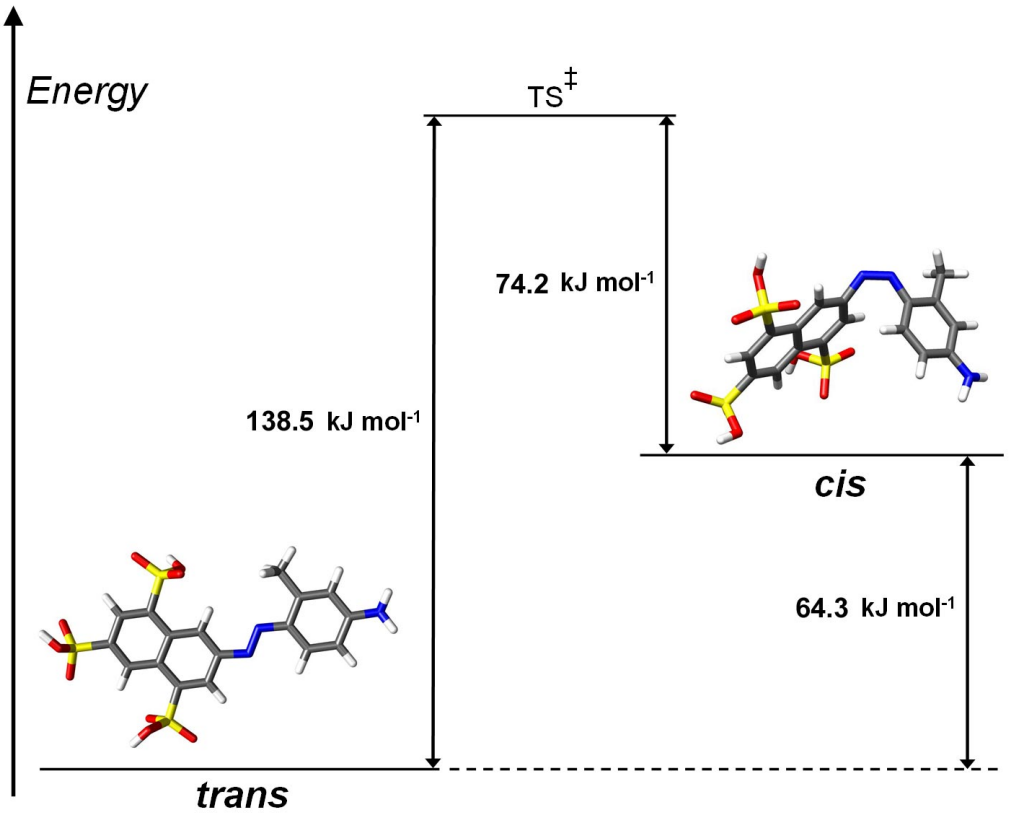

Figure 5.15: Schematic of the 273/10 *trans* and *cis* isomers, and ground state transition state energy differences.

such as peak deconvolution in UV-vis are not allowed to creep in for each measurement. It is clear that this method can be used to derive fundamental thermodynamic data related to the ground state transition state structure which could be combined with data from structural calculations to give a better picture of thermal *cis-trans* isomerisation. Further work in calculating the energy barrier along a reaction coordinate for simple azo molecules could now be performed for comparison with the values determined experimentally by this method. This could provide important information on the mechanism of isomerisation as there is still controversy as to whether this proceeds *via* torsion or inversion about the azo bond.

5.8 Conclusions

Results discussed in this chapter have further demonstrated the application of NMR with *in situ* laser irradiation to the kinetic investigation of the photo and thermal isomerisation rates of azo dyes. Through the application of thermal *cis* isomer decay results derived using the high resolution NMR technique, it has been possible to obtain molar absorption coefficients of even the shortest-lived *cis* isomers in this study. Additionally, with access to samples studied by Tait[30] previously unavailable data has

been obtained producing comparable rates of *cis-trans* photoisomerisation. Despite the presence of distinctly different molar absorption coefficients for the *cis* and *trans* isomers in some of the dyes studied, the influence of a time-dependent photokinetic factor has been found to be negligible when fitting the data to a first order equilibrium model. The apparent absence of any influence stems from the limited fractional concentration of *cis* isomer at the photostationary state, leading only to very small changes in the molar absorption coefficient for the irradiated solution.

Repeatability studies have demonstrated the results obtained within this study to be comparable with the previously reported results used extensively in this work to support and expand our knowledge of the yellow dye chromophore kinetics. In all cases, for the dyes studied in DMSO in this work, the photochemical contribution to *cis-trans* isomerisation is greater than the thermal contribution. The excited state kinetics represented in this work by relative quantum yields of photoisomerisation, ϕ_{isom}^{rel}, show a high degree of variation with molecular structure. Additionally, the fact $\phi_{t\rightarrow c}^{rel}$ and $\phi_{c\rightarrow t}^{rel}$ for each dye do not sum to a constant value indicates *trans-cis* and *cis-trans* isomerisation proceed *via* different transition states on the excited state potential energy surface. Some simple information about the structures of the transition state, relative to the Franck-Condon structures, can be derived from comparing the relative quantum yields for the processes.

Structural modification is seen to have a profound effect on the rate of thermal *cis* isomer decay. Dyes created through addition of a chlorotriazine ring to the dyebase exhibit an undesirable reduction in $k_{-1}(\Delta)$ leading to an extension of *cis* isomer longevity. Although the ratio of this reduction in rate is consistent within the dyes synthesised for this study, previous work shows a high degree of variability, with a great deal of sensitivity to other substituent effects. The electronic nature of substituents on the benzene ring *ortho* to the azo bond has a prominent influence on thermal *cis* isomer decay. A ureido group has a significant ability to accelerate the process leading to faster reversion to the *trans* isomer. Cross comparison of molecules from both studies has shown the presence of an *ortho* naphthyl sulfonate to greatly affect the kinetics of thermal reversal by slowing down the rate of *cis* isomer decay compared to that of a *meta* sulfonate. Sulfonates placed in other positions on the naphthyl ring do not inherently affect the thermal rate, unless intramolecular interaction can occur through further structural modification, such as adding a methyl group to the linking N atom. The influence of substituents *ortho* to the azo bond is highly consistent with observations from many other research groups. Modification of the chlorotriazine component, through hydrolysing the chlorine group on the ring, or through modifying the terminal

–NH_2 into a larger group, have been shown to affect the decay. These molecules are a first step towards simulating dyes bound to fibres and demonstrate high variability in thermal decay for modifications so distant from the point of greatest geometry change. It would be extremely interesting to bond one of the dyes to a short cellulose chain to study the effects on the kinetics of the dye using NMR.

The technique of NMR with *in situ* laser irradiation has, for the first time, been extended to determining the energy barrier to thermal isomerisation for a number of dyes. Rate constants obtained through monitoring *cis* isomer decay after *in situ* irradiation over a range of temperatures demonstrate an excellent fit to the Arrhenius and Eyring equations, allowing useful thermodynamic activation parameters to be derived. The energy barrier and frequency factor are in agreement with reports from studies conducted on similar azo dyes using spectrophotometric techniques. For the three systems studied, the data appear consistent, the energy barrier increasing as the rate of room temperature thermal decay decreases. The excellent fits obtained commend the technique for application to other molecules. However, time constraints have prevented measurements on the other dyes contained in this study.

Ab initio calculations have been used to interpret features of the NMR spectra and have assisted in explaining some of the kinetic observations. Advances in computer technology allow calculations on such large and complex molecules to be conducted without a great computational cost. However, with so many degrees of freedom, locating the lowest energy minimum for the structure under investigation can be prone to error, and requires a significant amount of user input and successive calculations in search of minima. The extension of this work to dyes with flexible 'second legs' lengthens the time spent processing, and time the user must spend manually adjusting the calculation to probe for minima. Despite the cumbersome nature of these large structural calculations, features of the calculated data appear consistent with the experimental kinetic results and provide insight into the conformation of the photo-induced species.

It is a hope that the combined efforts in this area will assist in setting the trajectory for future yellow azo dye synthesis. The results allow more thoughtful design to be applied to the dye, and the substituents it should contain to improve light-stable characteristics. However, modification of multiple substituents can produce structures that suffer a great deal from photochromism, through interactions that may not initially be perceived when the dye synthesis is planned on paper. For certain components it has already been observed that *cis* isomers in these yellow dyes adopt structures which form particularly stable intramolecular interactions, raising the potential energy barrier to isomerisation and producing undesirable photochromic behaviour. Prior to conducting synthesis and

analytical work upon dyes predicted to bear beneficial properties, it would be convenient to use structural calculations to investigate whether the *cis* isomer structures suffer from unwanted stabilisation. The results presented here clearly show good interplay between theoretical and experimental data. Performing theoretical calculations prior to experimental research would allow an informed opinion to be formed on whether the synthesis is worthwhile, saving time and resources in the future.

Chapter 6

Observation of Uncharacteristic Behaviour In A Yellow Azo Dyebase

6.1 Introduction

This chapter reports on a yellow azo dyebase, similar in structure to those examined in earlier chapters but displaying uncharacteristic behaviour compared with the others. The dyebase structure, used in a current commercially available azo dye product, is presented in Figure 6.1. The molecule consists of an **AF** sulfonated naphthyl group, ^{1}H NMR signals for which were discussed in Section 4.3.5. Differences between the dyebase shown in Figure 6.1 and those studied in Chapters 4 & 5 are seen on the phenyl ring. A methoxy substituent is present and the terminal NH_2 of the ureido group has been replaced with a methyl group, forming an acetylamido group. Although the changes appear trivial in nature, some interesting physical and, of even greater relevance to industry, chemical behaviour has been recorded for this dyebase. Rationalisation of this unusual behaviour has been conducted using one- and two-dimensional NMR techniques, results of which are described herein.

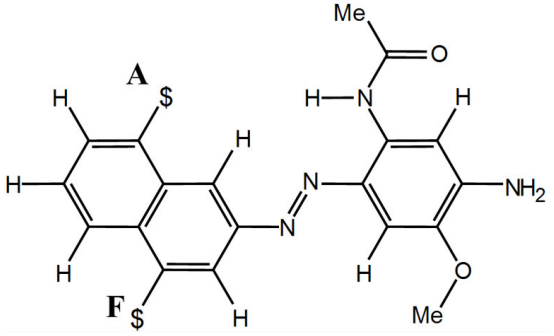

Figure 6.1: The chemical structure of dyebase 283/26.

6.2 Experimental

Procedures outlined in Chapter 4 for the study of azo molecules were adopted in the study of 283/26. UV-vis spectroscopy was employed to decide on the most suitable irradiation wavelength through acquiring the molar absorption coefficients for the available laser lines, and calculating possible sample concentrations from this. This was based on the constant absorption conditions used in Section 4.2.3.

A 5 μl aliquot of aqueous base (Na_2CO_3, 0.1 M) was added to the sample in d_6-DMSO prior to the irradiation studies in order to ensure presence of an azonium species did not restrict observation of the *cis* isomer (Section 4.2.2). For 1D ^{1}H NMR spectra recorded at low sample concentration, presaturation of the significant water signal, combined with 512 scans, was necessary to give a spectrum with sufficient signal to noise to conduct the analysis. Two dimensional ^{1}H-^{1}H NOESY experiments were recorded using a phase-sensitive pulse sequence (noesyph, Bruker). These studies were conducted at 298 K, and used a high sample concentration (10 mM, d_6-DMSO) due to the low sensitivity of the technique. Later characterisation studies resorted to more complex NMR techniques that are reported in Appendix E since they were not conducted by the Author.

Ab initio (DFT) calculations were carried out at the B3LYP/6-31G(d,p) level of theory/basis set using the method described in Section 3.5. The torsions around the azo bond were adjusted to probe the possible conformations. These structures could then be compared with NMR data, including the NOESY results, to look for conformations consistent with the experimental data.

6.3 UV-visible Spectroscopy of 283/26

The UV-visible spectrum of 283/26 is shown in Figure 6.2. The available laser lines at which the solution can be irradiated whilst maintaining a feasible sample concentration for NMR are highlighted in the figure by arrows. The sample concentrations for lines at 530 and 568 nm, based on the requirement of 50% light transmission at a depth of 2 mm used for the molecules in Chapters 4 & 5, are listed in Table 6.1. Irradiation at 530 nm requires a concentration that would limit the time-resolution of any kinetic data acquired by NMR, since a very large number of scans are demanded to gain appreciable signal to noise at such a low concentration. Therefore, 568 nm irradiation was used for the initial photochemical studies to take advantage of the higher sample concentration afforded by this wavelength.

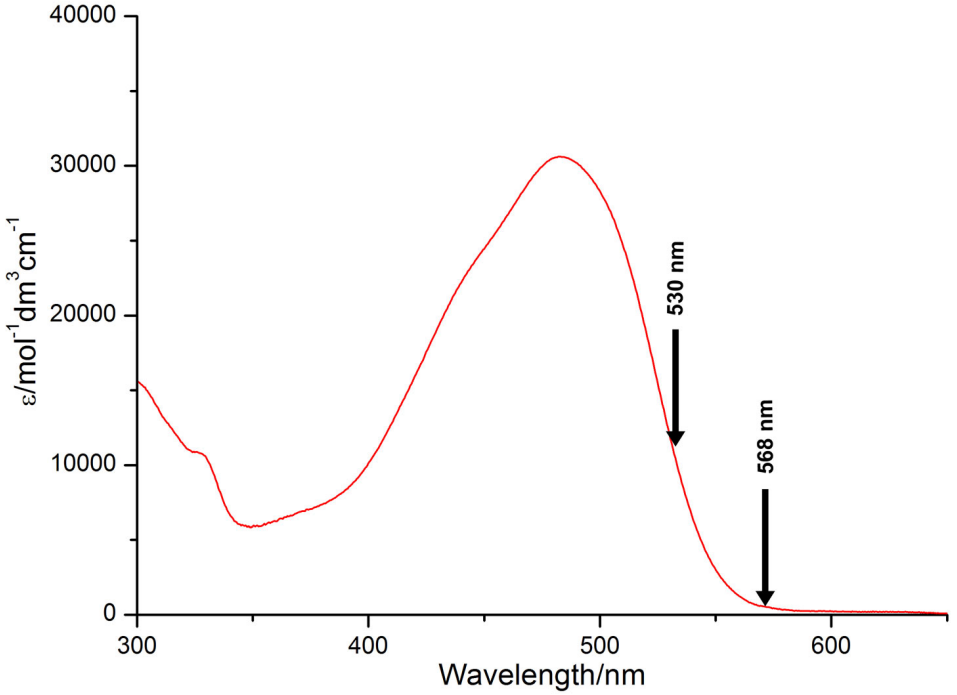

Figure 6.2: UV-vis spectrum of 283/26 in DMSO. The arrows indicate the two possible wavelengths on the bathochromic tail of the spectrum for which laser irradiation lines are available with the current setup.

Irradiation Wavelength, λ_{irr}/nm	Molar Absorption Coefficient, ϵ_{irr}/mol^{-1}lcm^{-1}	Concentration/mM
530	12060	0.13
568	615	2.52

Table 6.1: Sample conditions required for the irradiation wavelengths highlighted by arrows in Figure 6.2.

6.4 NMR Observations on a Sample of 283/26

6.4.1 Proton Numbering Scheme

In order to ensure consistency with the proton numbering scheme used for the molecules in Chapter 4, a similar scheme was applied to dye 283/26. The naphthyl and phenyl ring proton labels used in the earlier chapter are maintained here. However, the methyl resonances present in this molecule adopt numbers used for different protons in the other dyes (since a comparison of these signals is not required). This numbering scheme is shown in Figure 6.3.

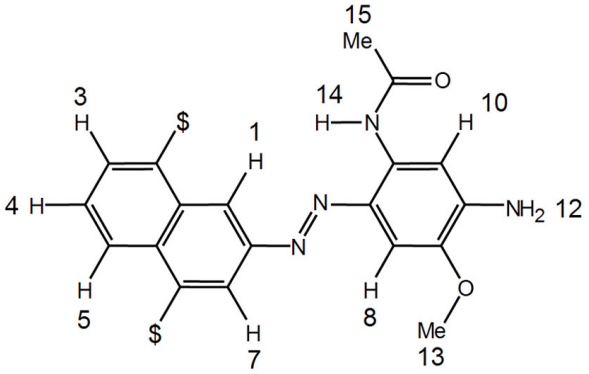

Figure 6.3: The proton numbering scheme applied to the structure shown in Figure 6.1.

6.4.2 Observation of Unusual Sample Behaviour by NMR

The sample of 283/26 was prepared in d_6-DMSO and treated in the typical manner used for the dyes presented in the earlier photoisomerisation studies in Chapters 4 & 5. This involved preparing the sample one day in advance of the study, and leaving it in darkness overnight to ensure any photoisomers had decayed back to the *trans* geometry. However, when the sample was monitored the following day, a large number of proton signals were present, many of which could not be atrributed to the structure shown in Figure 6.3. On closer examination of the spectrum, some of the signals appeared to mirror one another, albeit with different intensities, suggesting two very similar species were present in the solution. The extensive characterisation work conducted in Chapter 4 suggest these new signals to bear no resemblance to the *cis* isomers seen for other molecules. It must therefore be another species. Industrial collaborators, DyStar UK ltd, informed us that this had been previously noted and rationalised by them as slow rotameric behaviour which was deemed worthy of further investigation.

The intensity of the two sets of signals observed in the initial experiment was in a ratio of approximately 7:3. However, when the sample was analysed after having spent several days in darkness, a change in the peak intensities to give a ratio of 1:9 was observed. Clearly the sample was slowly changing in solution, and did not appear to be demonstrating the assumed behaviour of two rotamers. In fact, interpretations of the NMR spectra described later reveal the presence of two chemically different species in the solution. A time series for this change in the aromatic region of the ^{1}H NMR spectrum is presented in Figure 6.4, with spectra recorded immediately following preparation, and at various times following dissolution. Although not shown in the figure, the aliphatic region of the spectrum also contains duplicates of the two expected methyl peaks, the intensity of which is also dependent upon the time spent in solution.

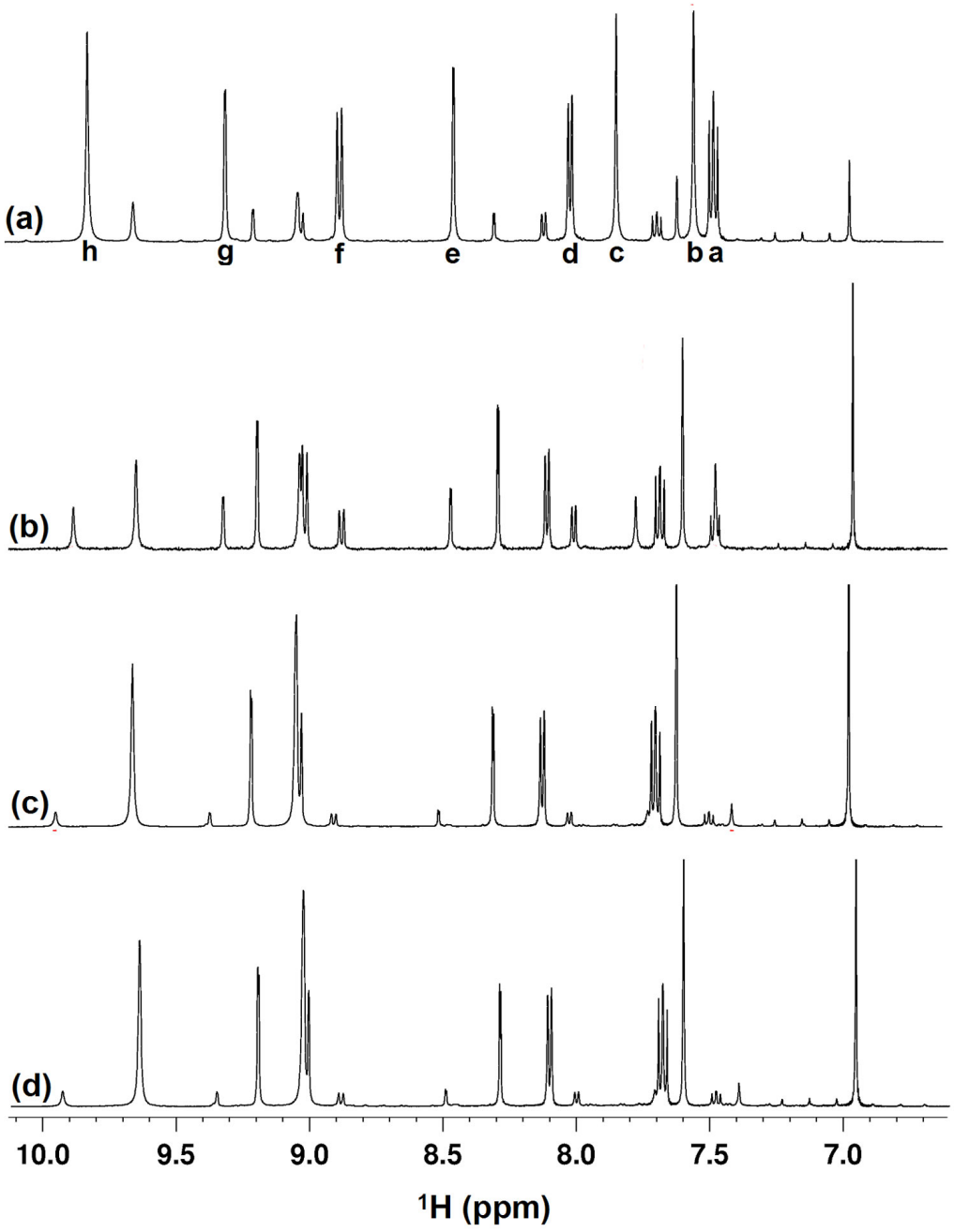

Figure 6.4: ^{1}H NMR spectrum of the aromatic signals of 283/26 in d_6-DMSO (10 mM) at varying times following sample preparation: (a) one hour, (b) one day, (c) 7 days, and (d) 15 days.

A sample containing both species was irradiated to investigate the respective photostabilities. After a significant period of irradiation at 568 nm, no new signals were identified in the spectrum indicating that photoisomerisation was not occuring in either species. This potentially very interesting result given the desirabiity of a non-photochromic azo dye, prompted further investigation, as presented in the following sections. Initially, interpretation of the NMR spectra will be considered.

6.4.3 Assignment of the Inital Species

6.4.3.1 1D ^{1}H NMR Interpretation

Since two distinct species are present for the sample designated 283/26, they shall be labelled species **A** and species **B** within this chapter, **A** representing the inital species present upon dissolving the sample, and **B** the product species derived over time. Species **A** is assigned within this section since it relates to the structure numbered in Figure 6.3. The proton signals referred to in this assignment are those labelled in the NMR spectrum in Figure 6.4 (a). The signals for species **B** are only present at minimal intensity in this spectrum. Although the **AF** sulfonated naphthyl group was not explicitly examined in this work, it has been studied previously,[30] and the **ACF** group examined in Chapter 4 was determined to have a similar proton pattern. This allows some of the signals in the spectrum of dye 283/26 to be assigned immediately and with confidence.

A summary of the previous assignments of sulfonated naphthyl group protons is available in Figure 4.19, and will shed light on the assignments made here. Examining Figure 6.4 (a), peaks **a**, **d** and **f** form the triplet and two doublets expected for the three adjacent protons of the naphthyl ring. The triplet is easily assigned to proton 4, situated between two protons to give the peak multiplicity observed. By analogy to earlier assignments, proton 5 positioned next to the sulfonate on the adjacent ring is expected to show a larger chemical shift than proton 3, indicating signal **f** is proton 5 and signal **d** is proton 3. By analogy once more, protons 1 and 7 are assigned to signals **g** and **e** respectively, each demonstrating a *meta* coupling constant of 1.83 Hz.

In contrast to the dyes examined in Chapter 4, the protonation pattern of the phenyl ring prevents unequivocal assignment using coupling constants since the substitution pattern causes both signals to appear as a singlet. However, the chemical shifts are expected to be similar, the local shielding environments causing proton 10 to experience slightly less shielding than proton 8. Therefore, singlet **b** is assigned to proton 8, and **c** to proton 10. This assignment is later confirmed by examining cross peaks for each proton in a NOESY spectrum. The remaining peak in the aromatic region of the spectrum is **h** which, given the deshielded chemical shift, must be proton 14 of the NH group adjacent to the azo bond. Two methyl signals are present in the aliphatic region of this spectrum at 2.32 ppm and 3.97 ppm, (not shown) each a sharp singlet indicating no coupling with any other protons. Because of the chemical inequivalence of the two groups, the less shielded signal is assigned to protons 13 of the methoxy group, and the more shielded signal to COMe protons 15.

Surprisingly, no signal is observed for the terminal amine group in species **A**. This is quite unexpected since the terminal NH_2 signal was present for all dyes studied in Chapter 4. The remainder of the assignments are consistent with the structure shown in Figure 6.3, so it seems unlikely that this structure is incorrect. Further experiments have provided an explanation for this observation, as discussed below. The assignments for species **A** are summarised in Table 6.2.

species **A**	Proton Assignment
a	4
b	8
c	10
d	3
e	7
f	5
g	1
h	14
OMe	13
COMe	15

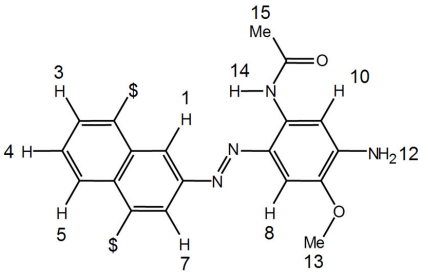

Table 6.2: ^{1}H NMR assignments for species **A** observed in the NMR spectrum of 283/26 after 0.5 days in solution. Peak labels relate to those shown in Figure 6.4 (a).

6.4.3.2 2D ^{1}H–^{1}H NOESY Observations

Two-dimensional ^{1}H–^{1}H NOESY experiments were performed to try and gain more information on the two species. 2D NOESY is a powerful tool that yields information on how the the protons are correlated through space rather than through bonds. A 2D spectrum was recorded four hours following sample preparation at 10 mM in d_6-DMSO, and another after five days in solution to give information relating to species **B** only. In the former case, cross peaks relating to both species were observed since the lengthy NOESY experiment allowed time for a proportion of **A** to undergo a change to **B**. Comparison of the initial NOESY spectrum with that recorded after 5 days showed all NOEs relating to **B** to be present in the initial NOESY spectrum, meaning only one spectrum needs presenting for analysis.

A mixing time of one second was used for the NOESY experiment in the hope that exchange cross-peaks would also be visible as the sample converted between the two species. The intensity of EXSY peaks in the NOESY spectrum depends on the rate of exchange and the mixing time used. These EXSY peaks evolve from the same pulse program when a longer mixing time is used. The aim was to allow correlation of a

proton peak of each species relating to the same proton during the conversion from **A** to **B**. Unfortunately, no peaks were oberserved for the interconversion of species. However, the majority of the 1D spectrum was easily assigned so the lack of these data is not a great problem.

The 2D ^{1}H–^{1}H NOESY spectrum showing both species in a solution of d_6-DMSO is shown in Figure 6.5. One of the most striking features of the NOESY spectrum is the sign of the NOE cross-peaks. As alluded to in Section 2.2.4.2, small molecules will demonstrate positive NOEs, and much larger molecules negative NOEs. The sign of the NOE is judged from the phase of the diagonal, which is always negative. In the NOESY spectrum presented in Figure 6.5, the red contours represent negative levels. Hence, the cross-peaks observed here are indicative of a molecule, or indeed two molecules, much larger than the expected structure and tumbling slowly in solution. However, the one-dimensional data are highly consistent with a smaller molecule. Negative NOEs observed here suggest that the molecule is tumbling very slowly in solution, mimicking a much larger molecule, indicating that an appreciable amount of aggregation is present for both **A** and **B**.

Each NOE cross-peak shown in Figure 6.5 has been labelled to simplify referencing within the text. Cross-peaks [a]-[f] correspond to species **A**, and [g]-[m] correspond to **B**. A discussion of cross-peaks relating to **A** will be conducted here, and those relating to **B** in a later section. The proton numbers described here are shown in Figure 6.3. Cross-peaks [a], [b] and [c] all relate to an interaction of proton 14 with other protons in the sample. Peak [a] corresponds with proton 1, [b] with 7, and [c] with proton 10 of the phenyl ring. This is interesting behaviour. In each case the intensity of the cross-peak is not as great as some of the others observed in the spectrum. However, it confirms the assignment of signal **h** applied in Section 6.4.3 as proton 14, since it appears to be in the correct location given by its proximity to other confirmed proton signals. Furthermore, it highlights certain behavioural characteristics in the sample. Since it appears to have access to both protons 1 and 7 of the naphthyl ring, this ring must either be able to rotate freely around the naphthyl C-N bond, or two very similar conformations of the dye are present in solution for species **A**. Since aggregation appears to be operative in this sample, the latter scenario is feasible since rotation is more likely to be restricted in an aggregate. Peaks [d] and [e] show through-space correlation of proton 4 with protons 5 and 3 respectively. This is expected since these naphthyl protons are adjacent to one another. The final signal for **A** is [f], describing a through-space interaction of proton 8 with the protons of the methoxy group, confirming the earlier assignment of peak **b** in Figure 6.4 (a) to proton 8. Assignment of the NOEs are summarised in Table 6.3.

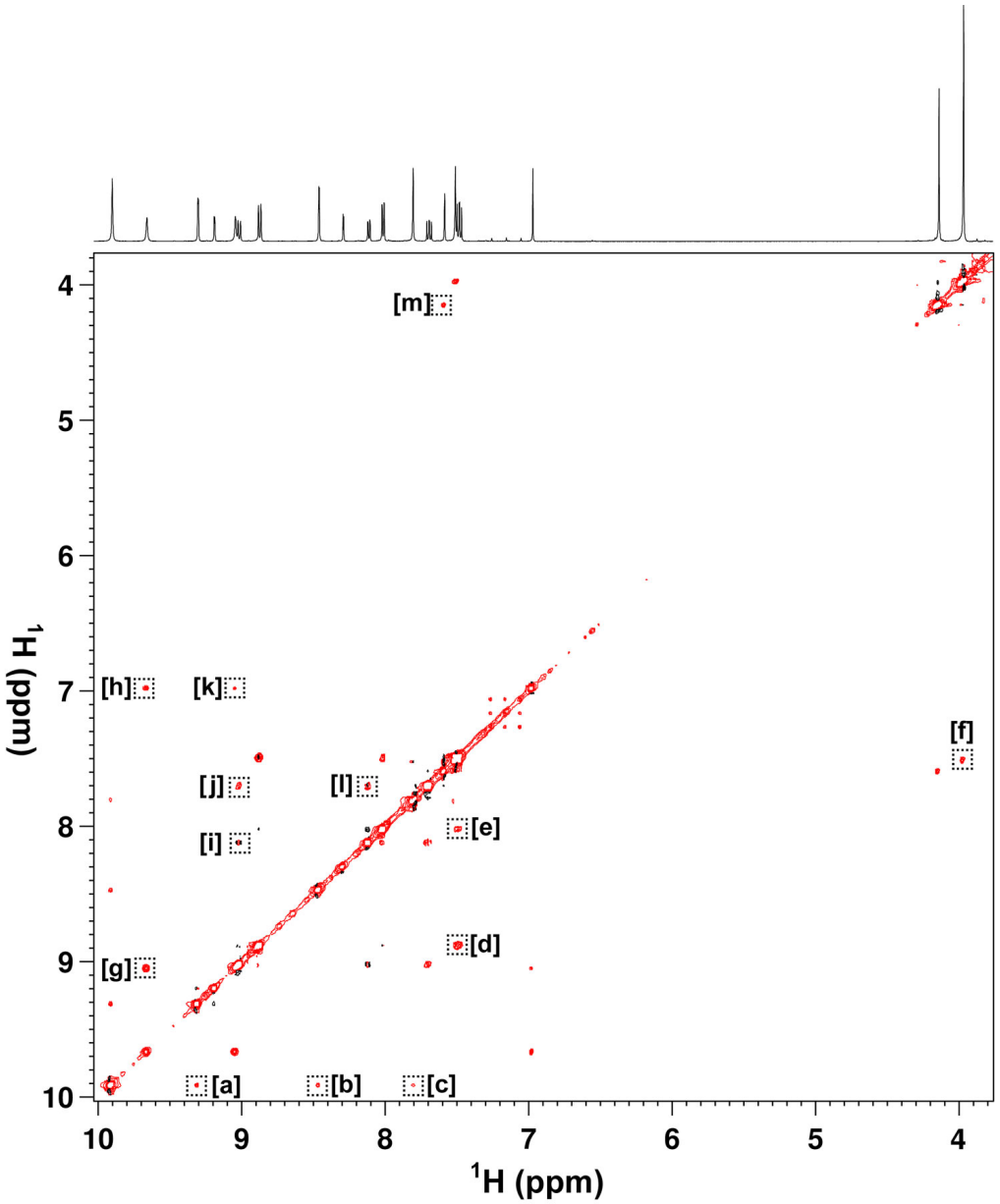

Figure 6.5: The 500 MHz ^{1}H–^{1}H NOESY spectrum of 283/26 recorded at 298 K over an 8 hour period, starting 4 hours after sample preparation in d_6-DMSO. An appreciable presence of both species is seen in the spectrum. Black contours represent positive levels, red contours negative.

6.4.3.3 Low Concentration NMR Studies

The NOESY spectrum presented earlier showed negative NOEs for the protons that are spatially near, indicating the molecule to be aggregated. Furthermore, as the sample changed from species **A** to **B**, peaks **b**, **c** and **h** (Figure 6.4 (a)) are seen to drift as the concentration of **A** decays over time. The change in chemical shift as a function of concentration has previously been used to monitor the aggregation of samples in solution,[100] adding further support to the claim of aggregation. The initial irradiation study was conducted at a concentration of 2.5 mM, and the two dimensional studies at

NOE	Signals†	Proton Interaction
[a]	**g** – **h**	1 – 14
[b]	**e** – **h**	7 – 14
[c]	**c** – **h**	10 – 14
[d]	**a** – **f**	4 – 5
[e]	**d** – **a**	3 – 4
[f]	**b** – **OMe**	8 – 13

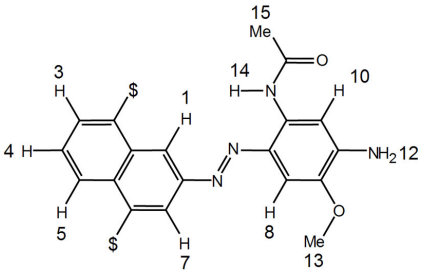

Table 6.3: ^{1}H-^{1}H NOE assignments for species **A** observed in the NMR spectrum of 283/26 recorded between 4-12 hours following sample preparation.
† Peaks labels relate to those in Figure 6.4 (a).

10 mM. No differences were observed in these spectra. Further experiments have been conducted at lower concentrations and are presented in this section. Figure 6.6 is the ^{1}H NMR spectrum of dye 283/26 recorded at the time of preparation in d_6-DMSO: (a) corresponds to 0.25 mM and (b) to 0.10 mM. At such low concentrations the spectra require a large number of scans to obtain sufficient signal to noise for analysis.

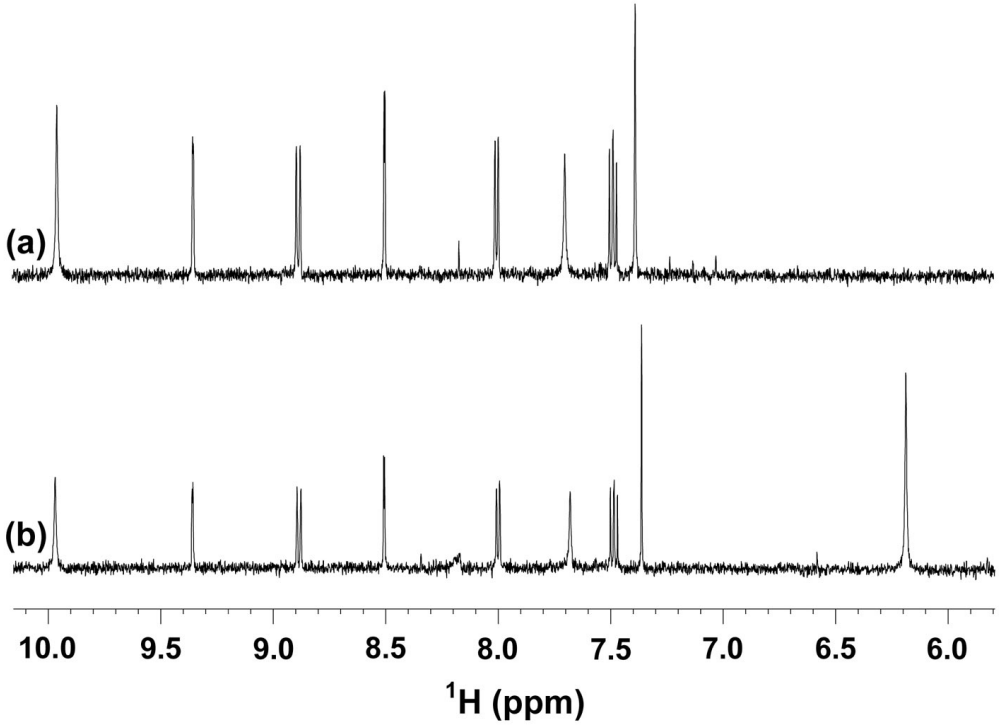

Figure 6.6: ^{1}H NMR spectrum of 283/26 recorded immediately following preparation in d_6-DMSO to ensure the presence of species **A** alone, (a) at 0.25 MM, and (b) at 0.10 mM.

The difference between spectra recorded at 0.25 mM and 0.10 mM is quite clear. Examining Figure 6.6 shows no change is apparent for the signals present at higher concentrations, but at low concentration an additional peak appears at 6.2 ppm, a location

highly consistent with the terminal amine protons of this sample. Measuring samples at concentrations between the two shown in the figure did not provide any more detail: the peak was only observed at 0.1 mM. Repeat measurements using solvents from different sources were performed to confirm the lack of this peak in higher concentration samples, and its appearance upon sufficient dilution. Aggregation of the dyebase is clearly preventing nuclear magnetic resonance from being observed in the terminal amine protons until high enough dilution is achieved. It is plausible that the amine group is somehow involved in the aggregation, inhibiting its rotation and causing the signal to broaden into the baseline.

A further observation was made regarding the rate of conversion of species **A** to **B** for a sample at high dilution such as this. Examination of the sample after one week in solution showed little conversion to have occurred, which is in contrast to the relatively high concentration of species **B** seen in a 10 mM sample after seven days in solution (Figure 6.4 (c)). This concentration dependence suggests the conversion process to be bimolecular. The rate of conversion increases with increased concentration of species **A**. Given the acidic isolation conditions of the dyebase, the increased concentration of **A** will also increase the concentration of acid in solution, making an acid catalysed conversion a possible explanation.

6.4.4 Photoisomerisation of Species A

Aggregation of species **A** appears to limit the observation of the terminal amine group until high enough dilution is present in solution. Using the low concentration of 0.1 mM to study the sample with limited aggregation allows the photochromism in the sample to be revisited. Species **A** was irradiated at the shorter wavelength of 530 nm to investigate whether a non-photochromic species had been found, or whether the aggregation present at higher concentration was also responsible for restricting photoisomerisation of the *trans* isomer. A sample of the species **A** was indeed observed to undergo photoisomerisation.

Figure 6.7 (a) is the ^{1}H NMR spectrum of species **A** at 0.10 mM in d_6-DMSO. For the purposes of convenience, the peak labelling applied in this figure has been changed from that used in Figure 6.4 to accommodate the additional amine peak observed at low concentration, and to allow continuous alphabetical labelling of the *cis* isomer species. A discussion of the *trans* isomer assignments is conducted in Section 6.4.3. To avoid repetition, the new peak labels and corresponding proton numbers are summarised with the *cis* isomer assignments in Table 6.4.

Figure 6.7 (b) is the 530-nm photostationary state ^{1}H NMR spectrum of 283/26 species

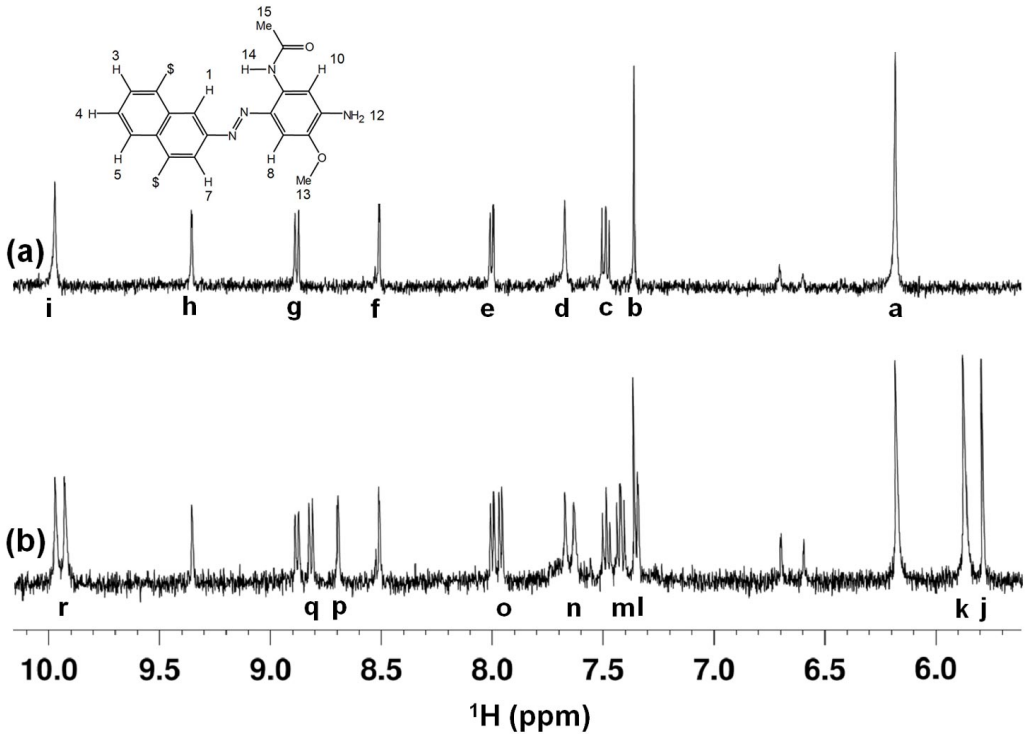

Figure 6.7: The ^{1}H NMR Spectra of 286/26 species **A** (0.10 mM) in d_6-DMSO (a) prior to irradiation and (b) during irradiation at the 530-nm PSS.

A at 0.10 mM in d_6-DMSO. Nine new proton resonances can be identified in the aromatic region, along with two new signals in the aliphatic region (not shown). Since all *cis* isomer signals have been shown to always move to lower ppm than the corresponding *trans* signals, much of the assignment can be performed with ease. Triplet **m** can be reliably assigned to proton 4, centred between protons 3 and 5 of the naphthyl group and paired with signal **c** ($\Delta\delta = 0.07$ ppm). Doublet **q** must be paired with signal **g** as proton 5 as it is the only doublet in this region, leaving doublet **o** to be paired with *trans* signal **e** as naphthyl proton 3 ($\Delta\delta = 0.06$ and 0.03 ppm respectively). Due to its intensity compared with the other signals, *cis* signal **k** can be paired with *trans* **a**, corresponding to the terminal amine resonance ($\Delta\delta = 0.31$ ppm). Signal **r** must be paired with *trans* **i** since no other *trans* isomer signals are present at such a deshielded location, giving a 0.04 ppm change in the chemical shift for proton 14.

The aliphatic signals (not shown) also demonstrate new *cis* isomer peaks, the methoxy group proton chemical shift moving by 1.10 ppm, and the methyl protons of the acetylamido group changing by 0.02 ppm. In both cases the *cis* isomer signals demonstrate the expected increased shielding. The PSS spectrum of species **A** in d_6-DMSO irradiated with 530 nm light is composed of 51% *cis* isomer. A summary of the assignments for each isomer, and their proton chemical shift differences, is presented in Table 6.4.

Trans Signal	*Cis* Signal	Proton Assignment	$\Delta\delta$/ppm
a	k	12	0.31
b	j	8	1.57
c	m	4	0.07
d	n	10	0.04
e	o	3	0.03
f	l	7	1.17
g	q	5	0.06
h	p	1	0.66
i	r	14	0.04
OMe	OMe	13	1.10
COMe	COMe	15	0.02

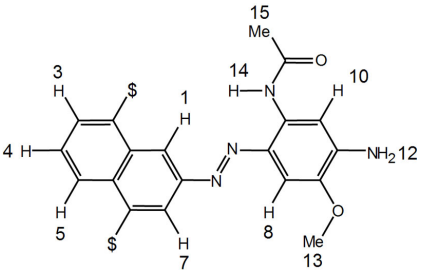

Table 6.4: ^{1}H NMR assignments for the *trans* and *cis* isomers of species **A** (283/26) in d_6-DMSO, and the difference in chemical shift between each isomer, $\Delta\delta$. Peak labels refer to those used in Figure 6.7.

As with previous sections of this work, the chemical shift differences can be rationalised using geometry optimised structural calculations. Figure 6.8 shows the minimum energy *trans* and *cis* isomer structure for species **A**. The *trans* isomer structure is the minimum energy calculation obtained from the four possible orientations of the aryl group around the C–N bond. However, with access to the NOESY spectrum of this isomer, further insight is obtained. Proton 14 of the acetylamido group shows cross-peaks with protons 1 and 7 of a similar intensity to each other. From previous observations of the chemical shift of proton 14 of a ureido group, it was observed that the chemical shift of proton 14 when in close proximity to the naphthyl azo nitrogen is about 12 ppm, whereas the chemical shift was approximately 9 ppm when proton 14 was close to the phenyl azo nitrogen. Given the chemical shift of proton 14 in species **A** is *ca.* 10 ppm, and an NOE is seen between this proton and each of the naphthyl protons *ortho* to the azo bond, it is likely that two possible conformations can be populated: that shown in Figure 6.8 (a), and another involving a rotation of the naphthyl group around the C–N bond by 180° to give proton 14 access to proton 7. This alternative conformation (not shown) is calculated to be 2.6 kJ mol^{-1} higher in energy than the minimum energy structure shown. The two conformers must be rotating faster than the NMR timescale can observe to produce these two peaks.

The *cis* isomer of species **A** (Figure 6.8 (b)) shows a good deal of correlation to the observed $\Delta\delta$ values shown in Table 6.4. Proton 7 appears to sit in the shielding cone of electrons of the opposing phenyl ring, and consequently demonstrates a much larger change in chemical shift to that seen for proton 1 which points away from this area.

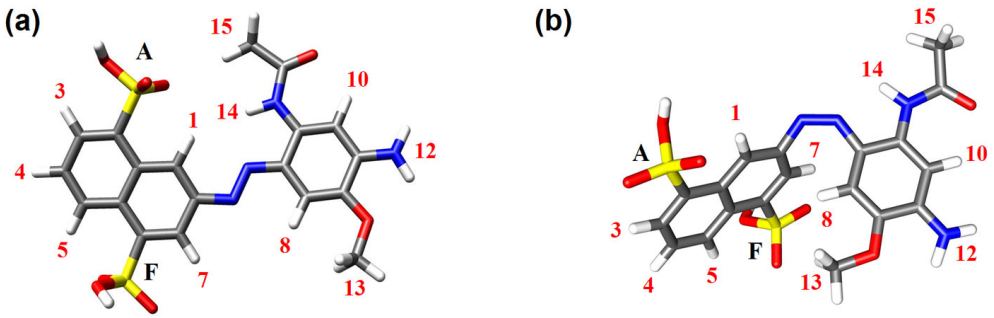

Figure 6.8: Minimum energy stuctures for species **A** of 283/26 (a) *trans* and (b) *cis*. Calculations were conducted at the B3LYP/6-31g(d,p).

Proton 8 demonstrates the largest $\Delta\delta$ for all protons, which ties in well with its position pointing towards the naphthyl ring. Furthermore, the protons of the methoxy group point towards proton 8 and the naphyl group, supported by a large $\Delta\delta$ (1.10 ppm) from the *trans* isomer indicative of a large increase in the shielding of the protons. Protons 3, 4 and 5 of the naphthyl ring demonstrate only minor changes in their chemical shift upon isomerisation, as do protons 10 and 14. Such changes tie in well with all the photoisomers observed in Chapter 4, and with the calculated structure of the *cis* isomer of species **A**.

The initial species present in the sample of 283/26 has been fully characterised as the expected structure following synthesis. Following the observation of aggregation, the photoisomerisation experiments were revisited with an awareness of the concentration dependence. Kinetic data could not be obtained due to the poor time-resolution associated with such a low concentration sample, but the photoisomer of this dyebase could still be observed and characterised. The issue of chemical conversion of the sample will now be addressed.

6.4.5 Characterisation of the Product, Species B

With the structure and behaviour of the initial species and its photoisomer fully characterised, determination of the reaction product remains. As stated earlier, the initial thoughts suggested a second rotamer species to be present, exchanging with species **A** at a slow enough rate on the NMR timescale to show up as two discrete sets of signals. However, several observations appear to contradict this rationalisation of the behaviour, leading to another explanation being sought.

6.4.5.1 UV-visible Spectroscopy

To replicate the earlier conditions used for NMR where the highest rate of conversion was observed, a sample of 283/26 was made up in DMSO at a concnetration of 10 mM. This sample was allowed to sit for two weeks ensuring the formation of a high

proportion of species **B**. Through measurement of equivalent proton signals in the NMR spectrum of a 10 mM sample after two weeks, the proportion of species **A** in the UV-vis spectrum was estimated at 11%. The high concentration sample was diluted prior to analysis by UV-vis.

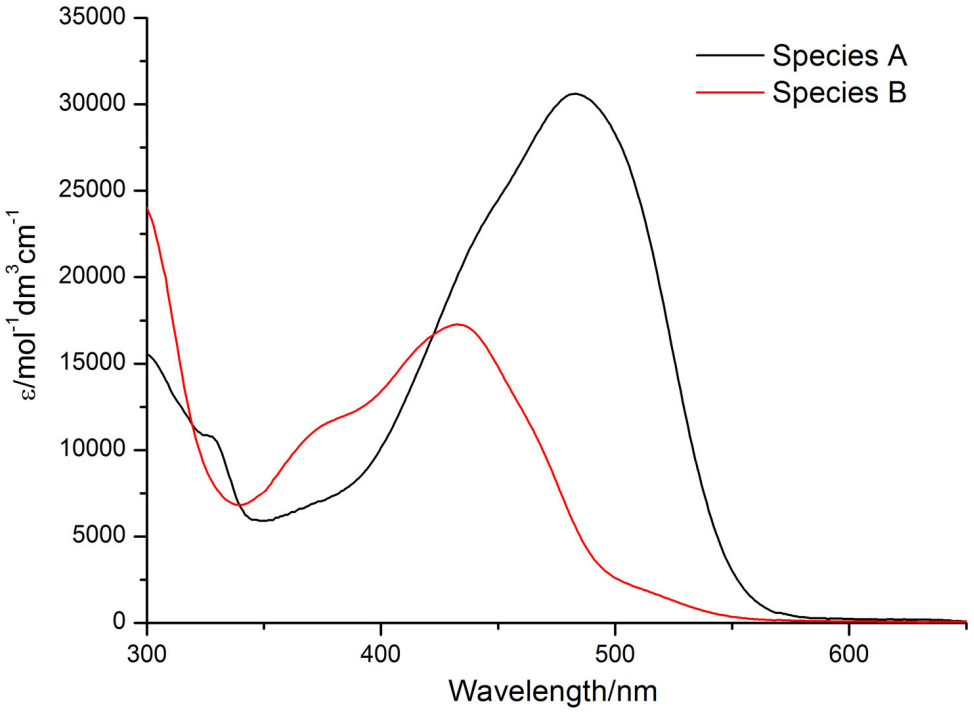

Figure 6.9: UV-vis spectra of species **A** and **B** in DMSO solution. NMR measurements predict 11% **A** will be present in the spectrum of **B**.

Figure 6.9 shows an overlay of the UV-vis spectra of species **A** and species **B**. The difference in spectra is striking. The spectrum of species **A** contains a band with λ_{max} of 482 nm, with the shoulder of an unresolved band on the hypsochromic side, and some further transitions in the UV. The spectrum of species **B** contains a band with λ_{max} at 431 nm with an overlapping band peaking at 381 nm. Further peaks begin to appear in the UV region for **B**. The absorption of the DMSO solvent prevented measurements below 290 nm. In addition to the differences in absorption maxima, the intensity of the visible band of **A** is much higher than **B**, giving it a stronger colour. The hypsochromic shift in **B** shows a loss of the extended conjugation in the molecule which is more indicative of a chemical, rather than conformational, change. Therefore, the properties of the chromophore have changed, possibly from a change involving the azo bond since the hypsochromic shift of the main band reports a decrease in the extended conjugation of the molecule.

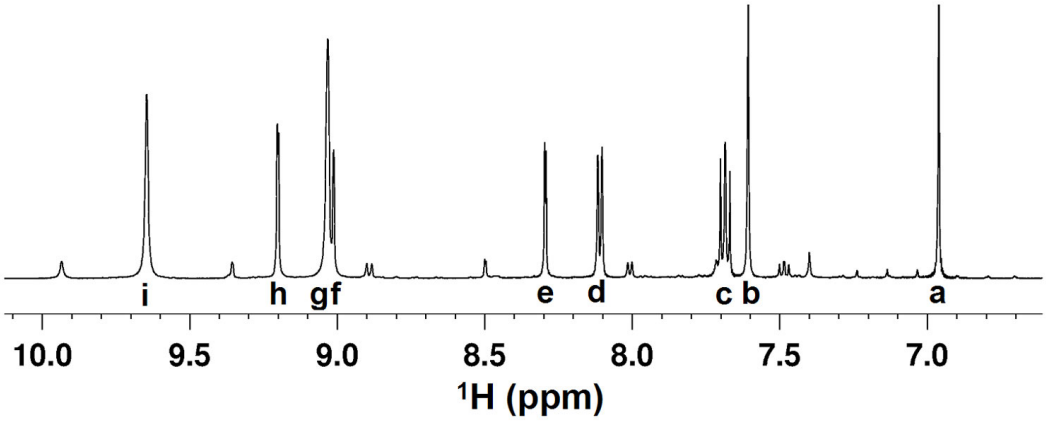

Figure 6.10: ^{1}H NMR spectrum of the aromatic signals of species **B** in d_6-DMSO (10 mM) 15 days after preparation.

6.4.5.2 One- and Two-Dimensional ^{1}H NMR Observations

To assist the reader, Figure 6.4 (d) showing the aromatic peaks for species **B** is reproduced as Figure 6.10, peak labels for which are also included. The majority of signals can be assigned through comparison with those given for species **A**, suggesting the structure of the product bears some strong similarities to the starting material. Where the structure can be easily identified, the proton numbers applied to **A** will be used in this assignment. For instance, several signals can be assigned to an **AF** sulfonated naphthyl group: triplet **c**, and doublets **d** and **f**, which is overlapping with signal **g**, can be assigned with confidence to protons 4, 3 and 5, respectively. An examination of the earlier ^{1}H–^{1}H NOESY spectrum (Figure 6.5) shows correlations [j] and [l] to link proton 4 with protons 5 and 3, respectively. Furthermore, [i] shows an NOE between protons 3 and 5. Based on the NMR evidence presented earlier regarding the proton pattern for an **AF** sulfonated naphthyl group, protons 1 and 7 must correspond to signals **h** and **e**, respectively.

The two methyl signals in the aliphatic region are present at different chemical shifts from those in **A**, with the methoxy group proton signal becoming less shielded by 0.17 ppm, and the acetyl protons less shielded by 0.36 ppm. The two sharp singlets **a** and **b** belong to the two protons on the phenyl ring. An examination of the earlier ^{1}H–^{1}H NOESY spectrum shows a correlation between the methoxy group protons and signal **b**, labelled [m]. This indicates that signal **b** corresponds to proton 8, undergoing a small chemical shift from the initial species ($\Delta\delta$ = +0.07 ppm). However, peak **a** corresponding to proton 10 has undergone a significant change in its shielding environment by moving to much lower ppm ($\Delta\delta$ = -0.83 ppm).

Two signals, **g** and **i**, remain to be assigned. These peaks are broader than the other

signals suggesting they are labile. This is confirmed by adding D_2O to the sample and observing the disappearance of these signals due to proton exchange with deuterons. Cross-peak [g] in the 2D ^1H–^1H NOESY spectrum suggests the labile protons are spatially near. However, given the labile nature of the two proton peaks, caution should be taken with this observation since the water present in the solvent can cause modulation of exchange between labile protons which could be well separated. Cross-peaks [h] and [k] show proximity of proton 10 to each of these broad peaks. This evidence indicates signals **g** and **i** belong to the terminal amine protons which is experiencing restricted rotation. Heating the sample to 75°C showed the two peaks to move to higher ppm and broaden, although they were far from coalescing (data not shown). The NOE assignments are presented in Table 6.5. Table 6.6 shows the assignments made for each proton signal of species **B**, and how the chemical shift of directly comparable signals vary from those presented for **A**.

NOE	Signal†	Proton Interaction
[g]	**g** – **i**	12 – 12
[h]	**a** – **i**	10 – 12
[i]	**d** – **f**	3 – 5
[j]	**c** – **f**	4 – 5
[k]	**a** – **i**	10 – 12
[l]	**c** – **d**	3 – 4
[m]	**b** – **OMe**	8 – 13

Table 6.5: ^1H-^1H NOE assignments for species **B** observed in the NMR spectrum of 283/26 recorded between 4-12 hours following sample preparation.
† Peak labels relate to those labelled in Figure 6.10.

The NOE data presented in Figure 6.5 showed all cross-peaks as negative, indicating that both species are aggregating in solution. Following on from the low concentration studies performed for species **A**, the product species was investigated to look for concentration effects related to aggregation. The main point to note from the one-dimensional NMR studies is that two broad peaks are present for the terminal amine. It is unusual that the group should be rotating slowly on the NMR timescale, and that the signals appear at an electron withdrawn location compared with terminal amine signals of similar molecules examined earlier. Investigation at low concentration showed the two labile peaks to disappear below 0.2 mM. In contrast to species **A**, the signals did not coalesce elsewhere in the spectrum at the concentrations used ($\geq$ 50 μM). The evidence indicates the molecule is disaggregating over the concentration range studied, but has not been studied at a low enough concentration for full dispersion to occur, at which point a single amine peak should appear.

Species **A** Signal	Species **B** Signal	Proton Assignment	$\Delta\delta$/ppm
a	c	4	+0.21
b	b	8	+0.07
c	a	10	-0.83
d	d	3	+0.10
e	e	7	-0.17
f	f	5	+0.14
g	h	1	-0.11
h	$*$	14	$*$
$*$	g	12	$*$
$*$	i	12	$*$
COMe	COMe	15	+0.36
OMe	OMe	13	+0.17

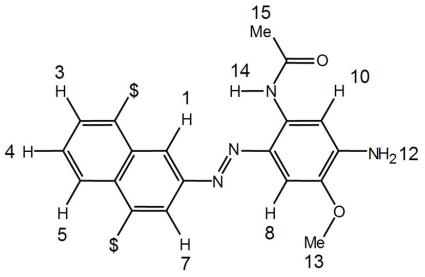

Table 6.6: ^{1}H NMR assignments for species **A** and **B** observed in the NMR spectrum of 283/26 after 0.5 days in d_6-DMSO solution (10 mM). Chemical shift differences are given as $\Delta\delta$, measured from the same spectrum since drift in some signals was observed over time. Peak labels for **A** are taken from Figure 6.4 (a) and **B** from Figure 6.10. $*$ Not available.

A summary of the major changes that have occurred in the ^{1}H NMR spectrum between the two species are illustrated in Figure 6.11. Since a large change has occurred in the chemical shift of proton 10, and the terminal amine remains intact, the change in environment must be from a change in the the nature of the adjacent acetylamido group. This is evidenced by the apparent loss of proton 14 from species **A** upon converison. The presence of an intact naphthyl group, and signals present for the phenyl and methoxy protons, suggest this change to affect the acetylamido group only. One possible suggestion would involve this group dropping off into solution, although presence of the methyl group indicates this is unlikely.

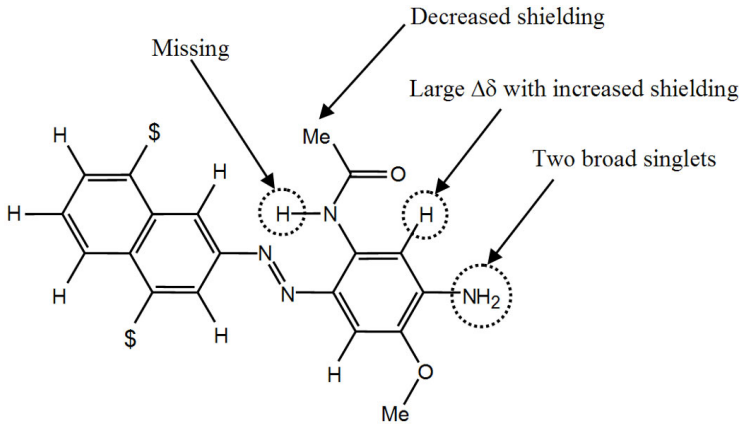

Figure 6.11: Significant changes in the NMR signals for the protons of species **A** going to species **B**.

6.4.5.3 Chemically Induced Changes in 283/26

In an attempt to isolate the product species, the reaction was found to accelerate using aqueous HCl. Of even greater relevance, species **B** could be driven back to **A** by adding NaOH. The change between the two species is clearly dictated by the pH of the solution, and is fully reversible. Therefore, this change is not quite as destructive as initially perceived. The differences observed in the UV-vis spectra of the initial and final species indicate a change in the chromophore properties that involve the loss of some conjugation in the molecule, provided by the azo bridge. Given the reversible nature of this process, and the observations in the ^{1}H NMR spectra, a cyclisation involving dehydration of the molecule is a plausible proposal. Examining the literature, the formation of 1,2,4-benzotriazinium dyestuffs has been patented,[101] making cyclisation the best explanation for what is being observed by NMR and UV-vis in solution. The proposed interconversion is shown in Figure 6.12.

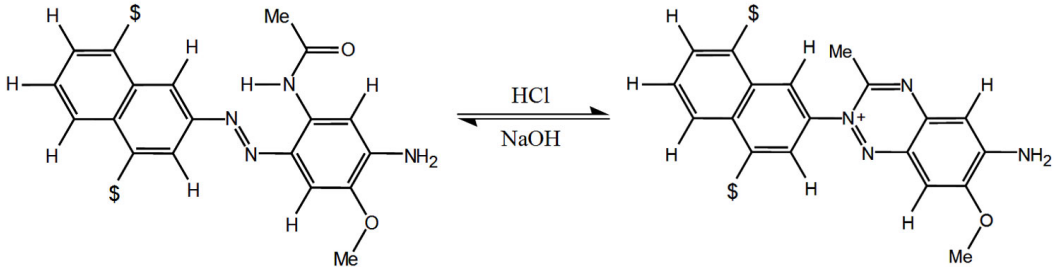

Figure 6.12: Scheme showing the chemical interconversion of species **A** and **B**.

6.4.5.4 2D Heteronuclear Correlated Experiments

To confirm the proposed structure of species **B**, a number of two-dimensional heteronuclear NMR correlation experiments were performed by Dr. John Parkinson at Strathclyde University. A summary of the supporting points will be highlighted in the text; full experimental details and spectra from these experiments are available in Appendix E.

Characterisation was performed using heteronuclear single quantum correlation (HSQC) and heteronuclear multiple bond correlation (HMBC) experiments. These are essentially heteronuclear COSY experiments that complement each other in the information they provide. The HSQC experiment produces a 2D spectrum with a ^{1}H and a heteroatom axis, allowing identification of protons bound to specific heteroatoms. Unlike homonuclear experiments, diagonal peaks do not exist since the frequency range for each nucleus is different. Cross-peaks will be present for protons directly bound to a heteroatom being studied. Both ^{1}H–^{13}C and ^{1}H–^{15}N HSQC experiments were performed to examine the immediate connectivity of the protons in the molecule. The

HMBC experiment extends the evolution time used in the HSQC pulse program to produce proton correlations with heteroatoms more than one bond away. The evolution time can be adjusted to produce correlations with heteroatoms up to five bonds apart. When used in conjunction with HSQC experiments, this is a powerful tool for identifying the connectivity atoms in a molecule. Both ^{1}H–^{13}C and ^{1}H–^{15}N were performed, allowing characterisation of the product species. The notable results from the study are summarised below.

The [^{1}H–^{15}N] HSQC experiment identifies labile peaks **g** and **i** to bond to a single nitrogen, confirming existance of a single amine group that further correlations confirm to be positioned *ortho* to proton 10. The proton signal belonging to methyl protons 15 shows a three-bond correlation with two nitrogen atoms. One of the two nitrogen atoms shows HMBC correlation with proton 10 indicating it is bonded to the phenyl ring; the other shows correlations to protons 1 and 7, proving it to be one of the former azo nitrogen atoms, a result that can only derive from a cyclised structure. This key result confirms the structure proposed in Figure 6.12.

6.4.6 Structural Calculation of Species B

The structure of species **B** has been calculated using the same methodology as that employed for the other dyes, with the addition of a positive charge in this case. Views of the minimum energy conformation of this structure are shown in Figure 6.13, allowing visualisation of the product species created by the cyclisation reaction.

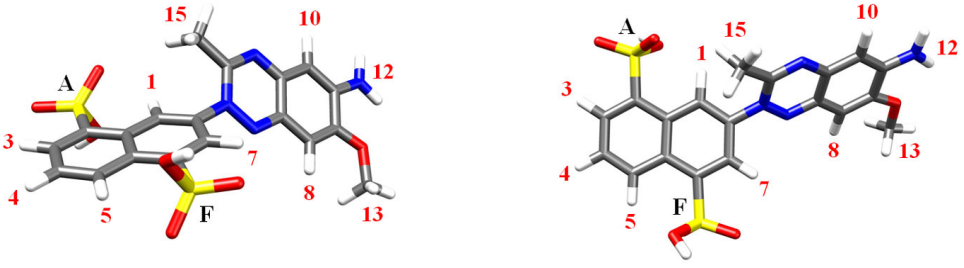

Figure 6.13: Two views of the minimum energy structure of species **B** obtained using the B3LYP/6-31G(d,p) level of theory/basis set. Proton numbers are labelled in red.

In contrast to the planar geometry seen for an azo *trans* isomer, the figure clearly displays the twist present between the two fused ring systems of this molecule. The torsional angle between the planes of the two aromatic groups is 124°. This twist presumably avoids steric hindrance between the methyl group (containing protons 15) and the naphthyl protons *ortho* to the azo bond. With the aid of this structure, an attempt can be made to explain some of the observed changes in chemical shift ($\Delta\delta$ in Table 6.6) between species **B** and the *trans* isomer of species **A**.

Investigating the naphthyl proton $\Delta\delta$ values shows protons 1 and 7 to experience an increase in shielding, and the remaining three protons to become subject to greater electron withdrawal. Given the presence of a positive charge on the former naphthyl azo nitrogen there ought to be an inductive effect present that would withdraw some electron density from the surrounding protons. The proximal protons are protons 15 of the methyl group bound to the heterocyclic ring, and protons 1 and 7 of the naphthyl group. The methyl protons behave as expected, showing a +0.36 ppm change in chemical shift, although it must be noted that the environment has changed from an acetylamido group to a fused hetercyclic ring system. Protons 1 and 7 exhibit more shielding ($\Delta\delta$ = -0.11, -0.07 respectively), even though they should demonstrate a reduction. In light of the calculated structure, an explanation is suggested by analogy with the effect of *trans-cis* isomerisation on $\Delta\delta$ values. On photoisomerisation of a *trans* azo species, protons in the *cis* isomer that point towards a region of high electron density on the opposing phenyl ring show a substantial reduction in their chemical shift caused by increased shielding. A similar effect can be seen in the structure of species **B**. Both naphthyl protons *ortho* to the inter-ring bond should experience additional shielding from the electron cloud above and below the heterocyclic ring. The observation that additional shielding for protons 1 and 7 in species **B** is not substantial compared with *trans* **A** is probably due to the positive charge on the adjacent heterocyclic ring causing electron withdrawal through the bonds, thus compensating for the aromatic shielding. Since the shielding cone of the heterocycle only influences protons 1 and 7 on the naphthyl group, protons 3, 4 and 5 only incur electron withdrawal from the distant positive charge, each experiencing some deshielding.

The remaining $\Delta\delta$ values are somewhat easier to explain. In the *cis* isomer of azo species **A**, proton 8 points towards the shielding cone of electrons from the naphthyl ring, experiencing a large amount of beneficial shielding and consequently demonstrating a large $\Delta\delta$. A similarly large change is seen for the methoxy group proton signal. With the positive charge present on the neighboring ring, proton 8 shows a small change in chemical shift of +0.08 ppm. Similarly, the protons of the methoxy group are less shielded by 0.17 ppm. The remaining peak to discuss is proton 10, adjacent to the acetylamido group in species **A**. A consequence of the large structural change in the vicinity of proton 10 is a much reduced chemical shift ($\Delta\delta$ = -0.83 ppm) on cyclisation to form species **B**.

6.5 Conclusions

This chapter has reported two interesting features relating to an azo dyebase. The first observation has been the effect of aggregation on this dyebase in d_6-DMSO, preventing photoisomerisation and causing a terminal amine signal to elude detection at high concentration. Such an effect has not been apparent in molecules studied earlier in Chapter 4 and in other work,[30] all of which demonstrated photoisomerisation at the chosen concentration. This type of behaviour could result in a molecule being falsely identified as non-photochromic.

The second, and quite unusual, feature of dyebase 283/26 is the chemical conversion observed in solution, bringing into question the overall stability of the unit for use in a dye. The apparent degradation was rationalised as a cyclisation effect, brought about by acidic isolation conditions for this molecule. Although stable as a solid, this molecule was slowly driven towards a 1,2,4-benzotriazinium compound in solution. Further work demonstrated that this acid-catalysed process could be reversed by addition of base to the solution.

To observe the *cis* isomer of the initial species, low concentration ($\leq$0.1 mM) had to be used. Consequently, a large number of scans had to be averaged to build up an appreciable signal to noise ratio, hence restricting the time-resolution for monitoring the kinetics of this system; no information regarding photo- and thermal isomerisation rates could be derived. This serves to highlight one of the limitations in using NMR as a detection method since it is inherently insensitive. Although the *in situ* technique proved incapable of studying the kinetics of photoisomerisation here, it did enable the *cis* isomer of the dyebase to be both observed and characterised. Furthermore, NMR studies not only identified the chemical instability of the dyebase, but also made apparent the aggregation present in the sample. Two-dimensional correlation experiments played a crucial role in confirming the structure of the product species following chemical conversion from the dyebase.

To summarise, the *in situ* NMR technique was used to observe the photoisomer of dyebase 283/26, but unable to follow the kinetics due to unfavourable sample conditions. However, the high resolution afforded by this method, and the numerous types of experiment available, led to the observation and characterisation of reversible cyclisation in this sample that had previously gone undetected. This again serves to highlight the strengths of NMR spectroscopic monitoring with *in situ* irradiation over techniques such as UV-visible spectroscopy.

Chapter 7

Conclusions

The work presented in this thesis has used the technique of NMR spectroscopy coupled with *in situ* irradiation to study *cis-trans* isomerisation in azo dyes from both a structural and kinetic viewpoint. This has provided an insight into the effect of structural modification on the rates of isomerisation for a series of yellow azo dyes. Furthermore, strengths and weaknesses of this technique have been identified and reviewed. A summary of conclusions is presented below.

The somewhat uncommon approach of monitoring samples whilst they undergo irradiation, afforded by the *in situ* nature of the technique, has allowed NMR spectra of otherwise inaccessible photoisomers of a number of yellow azo dyes to be obtained. A significant observation derived from this work is that all azo dyes here have demonstrated photoisomerisation to a varying degree: in none of the cases was a non-photochromic molecule discovered. Furthermore, the *cis* isomer proton signal is always more shielded than the respective *trans* signal.

A *trans* isomer ^{1}H NMR spectral fingerprint has been identified and characterised for the five differently sulfonated naphthyl groups found in these yellow azo dye structures, the assignment of which was critical for accurate evaluation of the structural effects of isomerisation. Through careful interpretation of the isomerisation-induced change in chemical shift for each proton, $\Delta\delta$, differentiation of alternative torsional conformers of the *cis* isomer species has been achieved for the first time using NMR. The asymmetry in $\Delta\delta$ for naphthyl protons *ortho* to the azo bond acts as a reporter for the relative twist of the naphthyl and phenyl rings. Whether a proton points towards or away from the opposing phenyl ring can be read from the relative magnitudes of $\Delta\delta$; the proton pointing towards the ring experiences a larger change in chemical shift compared with the proton pointing away from the ring. A reduction in the aysmmetry of $\Delta\delta$ is indicative of an equilibrium between two similar energy torsional conformers that interconvert rapidly on the NMR time-scale.

Ab initio (DFT) calculations have proved effective in predicting the structures of the photoisomers. The most significant outcome of the theoretical studies is the extremely good agreement between the *in vacuo* calculated *cis* isomer structure, and the solvated structure inferred by the chemical shifts. The combination of theoretical and experimental work has, therefore, provided a clear insight into the molecular structure of the unstable *cis* isomers.

For dyes bearing a ureido group, the torsional conformation of the *trans* isomer is governed by a hydrogen-bonding interaction of the ureido terminal amine and a sulfonate group. For the **ACG** sulfonate pattern, the amine protons H-bond to the **G** sulfonate; **ACF** molecules with the **A** sulfonate producing different torsional conformations around the aryl C–N bond. The addition of a fiber-reactive (chlorotriazine) group to a dyebase does not have a major structural influence on the conformation of the molecule. The dyes containing a 'second leg' on the reactive group all showed the same torsional configuration of the chlorotriazine relative to the adjacent phenyl ring in both the *trans* and *cis* isomers.

NMR coupled with *in situ* irradiation has provided a clear route to investigating the rates of photo- and thermal isomerisation. This is afforded by the high spectral resolution, and the ability to record and process data efficiently using a pseudo 2D acquisition. By careful control of the experimental conditions it has been possible to compare the experimental kinetic results with those presented by K.M. Tait,[30] providing a wider perspective on the effect of structure on the rates of isomerisation, and allowing systematic trends to be identified.

The kinetic data obtained for each dye consisted of rate constants for the reversible photoisomerisation, and the rate constant for thermal *cis* isomer decay. The measured photoisomerisation rate constants yield values for the relative quantum yields of *trans-cis* and *cis-trans* photoisomerisation, $\phi^{rel}_{t\rightarrow c}$ and $\phi^{rel}_{c\rightarrow t}$. In all cases observed in this study, and in previous studies, $\phi^{rel}_{c\rightarrow t}$ was greater than or equal to $\phi^{rel}_{t\rightarrow c}$. No obvious correlation was found between the structural variation in the molecules and ϕ^{rel}_{isom}. However, it is apparent that photoisomerisation of the *cis* and *trans* isomers proceed *via* different transition states on the excited state potential energy surface.

A number of thermal kinetic effects have been identified to arise from modifying different parts of the dye structure. Changing the sulfonation pattern of otherwise equivalent dyes influences the rate of thermal isomerisation. The presence of a sulfonate in the **C** position has little effect on the rate of thermal *cis* isomer decay. In contrast, the presence of a **G** sulfonate group, *ortho* to the azo bond, increases the lifetime of the

cis isomer as a result of intramolecular interaction that inhibits reversion to the *trans* isomer. Variation of the phenyl ring substituents lead to significant changes in the rate of thermal isomerisation. A decreases in the *cis* isomer lifetime is observed when a methyl group is placed *ortho* to the azo bond instead of a proton. In a more extreme case, thermal *cis* decay is further accelerated when this group is replaced with the larger ureido group, the NH proton of which hydrogen bonds to the azo bond and weakens it.

For each of the dyes studied, the addition of a chlorotriazine group to the dyebase retards the thermal decay of the *cis* isomer. The observed change in the rate is highly sensitive to the overall dye structure. Further modification of this chlorotriazine group *via* the introduction of a 'second leg' demonstrates that groups distant from the point of greatest geometric change affect the kinetics of thermal isomerisation. Since calculated structures show little intramolecular interaction to be present between the 'second leg' and the main dye structure in the *cis* isomers, and little difference in the azo bond lengths and angles, this influence on the rate must largely be due to more subtle electronic effects of the groups.

The activation energy of thermal *cis* isomer decay was determined for three molecules using NMR. The *in situ* technique allows the kinetics to be monitored at higher temperatures for these systems since detection is possible immediately after terminating the irradiation. The measured activation energies correlate well with previously reported values for azo molecules, the value increasing for the molecules with longer *cis* isomer lifetimes. Values for the pre-exponential factor also fit with reported results, and were very similar in value, varying by approximately one order of magnitude.

For a particular molecule in this study, an acetylamido substituted dyebase, aggregation prevented photoisomer formation at the desired concentration for NMR measurements. On resorting to lower sample concentration, the *in situ* technique was used to successfully observe and characterise the *cis* isomer, but kinetic measurements were not possible due to the long acquisition time at the concentration employed. Uniquely amongst the molecules studied here, the *trans* isomer of this dyebase was found to be thermally unstable at room temperature as a result of an acid-catalysed cyclisation reaction.

^{1}H NMR spectroscopy has proved its worth in the study of photochromic systems. The resolution is superior to the available optical techniques, allowing the species present in solution to be observed and characterised. The pseudo 2D NMR technique used in these studies provides a system for successful acquisition of time-dependent concentration data relating to a multi-component system. The limitations of this technique stem

from the time required to acquire enough spectra to model a kinetic process, and the low sample concentrations needed to allow the passage of light through the sample.

In summary, NMR spectroscopic monitoring of samples undergoing *in situ* irradiation has been demonstrated as a particularly effective tool for observing and structurally characterising azo *cis* isomer species, following the kinetics of photoisomerisation, and investigating thermodynamics of thermal *cis* isomer decay. In combination with *ab initio* (DFT) calculations, the NMR data were useful in predicting *cis* isomer geometries using a comparison of the isomerisation-induced chemical shift changes. The application of the *in situ* technique was only limited in one case, which prevented acquisition of kinetic data due to the very low concentrations. The studies performed in this work, when combined with previous observations, have allowed a rigorous and systematic approach to studying the effect of structural modification on the kinetics of photoisomerisation. It is hoped that this work, and further use of the technique, will provide an effective approach in the design of new dye molecules, and open up further opportunities in the study of photochromic systems.

Bibliography

1. P. F. Gordon and P. Gregory, *Organic Chemistry in Color*, 1983.

2. R. Christie, *Colour Chemistry*, RSC Publications, 2001.

3. S. A. Ahmed, A. A. Abdel-Wahab, and H. Dürr, *CRC Handbook of Organic Photochemistry and Photobiology*, CRC Press, 2004.

4. P. Ball and C. H. Nicholls, *Dyes Pigments*, 1985, **6**, 13–25.

5. Y. Okada, A. Sugane, F. Fukuoka, and Z. Morita, *Dyes Pigments*, 1998, **39**, 1–23.

6. P. Hunt, D. R. Worrall, F. Wilkinson, and S. N. Batchelor, *J. Am. Chem. Soc.*, 2002, **124**, 8532–8533.

7. S. N. Batchelor, D. Carr, C. E. Coleman, L. Fairclough, and A. Jarvis, *Dyes Pigments*, 2003, **59**, 269–275.

8. P. Aranyosi, Z. Csepregi, I. Rusznak, L. Toke, and A. Vig, *Dyes Pigments*, 1998, **37**, 33–45.

9. N. Katsuda, T. Omura, and T. Takagishi, *Dyes Pigments*, 1998, **36**, 231–241.

10. A. Bozzi, T. Caronna, F. Fontana, B. Marcandalli, and E. Selli, *J. Photochem. Photobiol. A*, 2002, **152**, 193–197.

11. L. Antonov and D. Nedeltcheva, *Chem. Soc. Rev.*, 2000, **29**, 217–227.

12. K. M. Tait, J. A. Parkinson, S. P. Bates, W. J. Ebenezer, and A. C. Jones, *J. Photochem. Photobiol. A*, 2003, **154**, 179–188.

13. S. Delbaere, C. Bochu, N. Azaroual, G. Buntinx, and G. Vermeersch, *J. Chem. Soc. Perkin. Trans 2*, 1997, **1**, 1499–1501.

14. W. P. Aue, E. Bartholdi, and R. R. Ernst, *J. Chem. Phys.*, 1976, **64**, 2229–2246.

15. D. Williams and I. Fleming, *Spectroscopic Methods in Organic Chemistry*, McGraw-Hill, 1995.

16. P. Atkins and J. de Paula, *Physical Chemistry*, Oxford University Press, 2002.

17. P. Hore, *Nuclear Magnetic Resonance*, Oxford University Press, 1995.

18. P. Hore, J. Jones, and S. Wimperis, *NMR: The Toolkit*, Oxford University Press, 2000.

19. T. D. W. Claridge, *High-Resolution NMR Techniques In Organic Chemistry*, Elsevier, 1999.

20. M. J. Thrippleton and J. Keeler, *Angew. Chem. Int. Ed.*, 2003, **42**, 3938 – 3941.

21. S. Delbaere, J.-C. Micheau, and G. Vermeersch, *Org. Lett.*, 2002, **4**, 3143–3145.

22. D. Venec, S. Delbaere, J. C. Micheau, M. Frigoli, C. Moustrou, A. Samat, and G. Vermeersch, *J. Photochem. Photobiol. A*, 2006, **183**, 70–78.

23. S. Delbaere, J. Berthet, M. A. Salvador, G. Vermeersch, and M. M. Oliveira, *Int. J. Photoenergy*, 2006, **2**, 1–7.

24. J. Berthet, J. C. Micheau, G. Vermeersch, and S. Delbaere, *Tetrahedron Lett.*, 2006, **47**, 2485–2488.

25. S. Magennis, F. Mackay, A. Jones, K. Tait, and P. Sadler, *Chem. Mat.*, 2005, **17**, 2059–2062.

26. I. Kuprov and P. J. Hore, *J. Mag. Res.*, 2004, **171**, 171–175.

27. I. Kuprov and P. J. Hore, *J. Mag. Res.*, 2004, **168**, 1–7.

28. K. H. Mok and P. J. Hore, *Methods*, 2004, **34**, 75–87.

29. I. Kuprov, M. Goez, P. A. Abbott, and P. J. Hore, *Rev. Sci. Instrum.*, 2005, **76**, 84103–84107.

30. K. M. Tait *The Novel Application of NMR spectroscopy and in-situ Laser Irradiation for the Study of Cis-trans Isomerisation in Azo Dyes.* PhD thesis, The University of Edinburgh, 2003.

31. S. Delbaere, B. Luccioni-Houze, C. Bochu, Y. Teral, M. Campredon, and G. Vermeersch, *J. Chem. Soc. Perkin. Trans 2*, 1998, **5**, 1153–1157.

32. C. J. Cramer, *The Essentials of Computational Chemistry. Theories and Models*, J. Wiley & Sons, 2002.

33. J. A. Pople, D. P. Santry, and G. A. Segal, *J. Chem. Phys.*, 1965, **43**, 129–135.

34. P. Hohenberg and W. Kohn, *Phys. Rev.*, 1964, **136**(3B), B864–B871.

35. W. Kohn and L. J. Sham, *Phys. Rev.*, 1965, **140**(4A), A1133–A1138.

36. A. D. Becke, *Phys. Rev. A*, 1988, **38**, 3098–4001.

37. J. P. Perdew and Y. Wang, *Phys. Rev. B*, 1992, **45**, 13244–13249.

38. A. D. Becke, *J. Chem. Phys.*, 1993, **98**, 5648–5652.

39. C. Lee, W. Yang, and R. G. Parr, *Phys. Rev. B*, 1988, **37**, 785–789.

40. P. C. Hariharan and J. A. Pople, *Theor. Chem. Acc.*, 1973, **28**, 213–222.

41. J. Park and J. Shore, *Coloration Technology*, 1999, **115**, 157–167.

42. J. A. Delaire and K. Nakatani, *Chemical Reviews (Washington, D. C.)*, 2000, **100**, 1817–1845.

43. R. H. El Halabieh, O. Mermut, and C. J. Barrett, *Pure Appl. Chem.*, 2004, **76**, 1445–1465.

44. K. G. Yager and C. J. Barrett, *J. Photochem. Photobiol. A*, 2006, **182**, 250–261.

45. O. N. Oliveira, Jr., D. S. dos Santos, Jr., D. T. Balogh, V. Zucolotto, and C. R. Mendonca, *Adv. Colloid Interface Sci.*, 2005, **116**, 179–192.

46. Z. F. Liu, K. Hashimoto, and A. Fujishima, *Nature*, 1990, **347**, 658–660.

47. P. Rochon, E. Batalla, and A. Natansohn, *Appl. Phys. Lett.*, 1995, **66**, 136–138.

48. J. Henzl, M. Mehlhorn, H. Gawronski, K.-H. Rieder, and K. Morgenstern, *Angew. Chem. Int. Ed.*, 2006, **45**, 603–606.

49. D. Rottger and H. Rau, *J. Photochem. Photobiol. A*, 1996, **101**, 205–214.

50. D. Junge and D. McGrath, *J. Am. Chem. Soc.*, 1999, **121**, 4912–4913.

51. M. S. Vollmer, T. D. Clark, C. Steinem, and M. R. Ghadiri, *Angew. Chem. Int. Ed.*, 1999, **38**, 1598–1601.

52. C. Steinem, A. Janshoff, M. Vollmer, and M. Ghadiri, *Langmuir*, 1999, **15**, 3956–3964.

53. J. Griffiths, *Chem. Soc. Rev*, 1972, **1**, 481–493.

54. H. Knoll, *CRC handbook of organic photochemistry and photobiology*, CRC Press, 2004.

55. C. L. Forber, E. C. Kelusky, N. J. Bunce, and M. C. Zerner, *J. Am. Chem. Soc.*, 1985, **107**, 5884–5890.

56. S. Malkin and E. Fischer, *J. Phys. Chem.*, 1962, **66**, 2482–2486.

57. E. Fischer, M. Frankel, and R. Wolovsky, *J. Chem. Phys.*, 1955, **23**, 1367–1367.

58. T. Fujino, S. Y. Arzhantsev, and T. Tahara, *J. Phys. Chem. A*, 2001, **105**, 8123–8129.

59. T. Fujino, S. Y. Arzhantsev, and T. Tahara, *Bull. Chem. Soc. Jpn.*, 2002, **75**, 1031–1040.

60. G. S. Hartley, *J. Chem. Soc*, 1938, p. 633.

61. P. D. Wildes, D. G. Whitten, J. G. Pacifici, and J. Irick, Gether, *J. Am. Chem. Soc.*, 1971, **93**, 2004–2008.

62. P. Bortolus and S. Monti, *J. Phys. Chem.*, 1979, **83**, 648–652.

63. P. Bortolus and M. Monti, *J. Phys. Chem.*, 1987, **91**, 5046–5050.

64. H. Rau and E. Lueddecke, *J. Am. Chem. Soc.*, 1982, **104**, 1616–1620.

65. T. Fujino and T. Tahara, *J. Phys. Chem. A*, 2000, **104**, 4203–4210.

66. S. Monti, G. Orlandi, and P. Palmieri, *Chem. Phys.*, 1982, **71**, 87–99.

67. I. K. Lednev, T.-Q. Ye, R. E. Hester, and J. N. Moore, *J. Phys. Chem.*, 1996, **100**, 13338–13341.

68. I. K. Lednev, T.-Q. Ye, L. C. Abbott, R. E. Hester, and J. N. Moore, *J. Phys. Chem. A*, 1998, **102**, 9161–9166.

69. T. Schultz, J. Quenneville, B. Levine, A. Toniolo, T. J. Martinez, S. Lochbrunner, M. Schmitt, J. P. Shaffer, M. Z. Zgierski, and A. Stolow, *J. Am. Chem. Soc.*, 2003, **125**, 8098–8099.

70. P. Cattaneo and M. Persico, *Phys. Chem. Chem. Phys.*, 1999, **1**, 4739–4743.

71. T. Ishikawa, T. Noro, and T. Shoda, *J. Chem. Phys.*, 2001, **115**, 7503–7512.

72. C. Ciminelli, G. Granucci, and M. Persico, *Chem. Eur. J.*, 2004, **10**, 2327–2341.

73. A. Cembran, F. Bernardi, M. Garavelli, L. Gagliardi, and G. Orlandi, *J. Am. Chem. Soc.*, 2004, **126**, 3234–3243.

74. L. Gagliardi, G. Orlandi, F. Bernardi, A. Cembran, and M. Garavelli, *Theor. Chem. Acc.*, 2004, **111**, 363–372.

75. E. W.-G. Diau, *J. Phys. Chem. A*, 2004, **108**, 950–956.

76. C. Crecca and A. Roitberg, *J. Phys. Chem. A*, 2006, **110**, 8188–8203.

77. E. R. Talaty and J. C. Fargo, *Chem. Commun.*, 1967, **2**, 65–66.

78. T. Asano, T. Okada, S. Shinkai, K. Shigematsu, Y. Kusano, and O. Manabe, *J. Am. Chem. Soc.*, 1981, **103**, 5161–5165.

79. N. Nishimura, T. Sueyoshi, H. Yamanaka, E. Imai, S. Yamamoto, and S. Hasegawa, *Bull. Chem. Soc. Jpn.*, 1976, **49**, 1381–1387.

80. N. Nishimura, S. Kosako, and Y. Sueishi, *Bull. Chem. Soc. Jpn.*, 1984, **57**, 1617–1625.

81. K. S. Schanze, T. F. Mattox, and D. G. Whitten, *J. Org. Chem.*, 1983, **48**, 2808–2813.

82. T. Asano, T. Yano, and T. Okada, *J. Am. Chem. Soc.*, 1982, **104**, 4900–4904.

83. M. J. Frisch, G. W. Trucks, H. B. Schlegel, G. E. Scuseria, M. A. Robb, J. R. Cheeseman, J. A. Montgomery, Jr., T. Vreven, K. N. Kudin, J. C. Burant, J. M. Millam, S. S. Iyengar, J. Tomasi, V. Barone, B. Mennucci, M. Cossi, G. Scalmani, N. Rega, G. A. Petersson, H. Nakatsuji, M. Hada, M. Ehara, K. Toyota, R. Fukuda, J. Hasegawa, M. Ishida, T. Nakajima, Y. Honda, O. Kitao, H. Nakai, M. Klene, X. Li, J. E. Knox, H. P. Hratchian, J. B. Cross, V. Bakken, C. Adamo, J. Jaramillo, R. Gomperts, R. E. Stratmann, O. Yazyev, A. J. Austin, R. Cammi, C. Pomelli, J. W. Ochterski, P. Y. Ayala, K. Morokuma, G. A. Voth, P. Salvador, J. J. Dannenberg, V. G. Zakrzewski, S. Dapprich, A. D. Daniels, M. C. Strain, O. Farkas, D. K. Malick, A. D. Rabuck, K. Raghavachari, J. B. Foresman, J. V. Ortiz, Q. Cui, A. G. Baboul, S. Clifford, J. Cioslowski, B. B. Stefanov, G. Liu, A. Liashenko, P. Piskorz, I. Komaromi, R. L. Martin, D. J. Fox, T. Keith, M. A. Al-Laham, C. Y. Peng, A. Nanayakkara, M. Challacombe, P. M. W. Gill, B. Johnson, W. Chen, M. W. Wong, C. Gonzalez, and J. A. Pople, Gaussian 03, Revision B.02, Gaussian, Inc., Wallingford, CT, Gaussian, Inc., Wallingford, CT, 2004.

84. L. C. Abbott, S. N. Batchelor, J. Oakes, B. C. Gilbert, A. C. Whitwood, J. R. Lindsay Smith, and J. N. Moore, *J. Phys. Chem. A*, 2005, **109**, 2894–2905.

85. E. F. Petterson, T. D. Goddard, C. C. Huang, G. S. Couch, D. M. Greenblatt, E. C. Meng, and T. E. Ferrin, *J. Comp. Chem.*, 2004, **25**, 1605–1612.

86. A. Sanchez and R. H. De Rossi, *J. Org. Chem.*, 1993, **58**, 2094–2096.

87. A. M. Sanchez and R. H. Rossi, *J. Org. Chem.*, 1995, **60**, 2974–2976.

88. A. M. Sanchez, M. Barra, and R. H. de Rossi, *J. Org. Chem.*, 1999, **64**, 1604–1609.

89. W. J. Ebenezer, *Personal Communication*, 2005.

90. K. M. Tait, J. A. Parkinson, A. C. Jones, W. J. Ebenezer, and S. P. Bates, *Chem. Phys. Lett.*, 2003, **374**, 372–380.

91. L. C. Abbott, S. N. Batchelor, J. Oakes, J. R. Lindsay Smith, and J. N. Moore, *J. Phys. Chem. A*, 2004, **108**, 10208–10218.

92. M. Skowronek, I. Roterman, L. Konieczny, B. Stopa, J. Rybarska, B. Piekarska, A. Gorecki, and M. Krol, *Comput. Chem. (Oxford)*, 2000, **24**, 429–450.

93. S. Bell, A. Bisset, and T. Dines, *J. Ram. Spec.*, 1998, **29**, 447–462.

94. T. Sueyoshi, N. Nishimura, S. Yamamoto, and S. Hasegawa, *Chem. Lett.*, 1974, **10**, 1131–1134.

95. Z. F. Liu, K. Morigaki, T. Enomoto, K. Hashimoto, and A. Fujishima, *J. Phys. Chem.*, 1992, **96**, 1875–1880.

96. K. Yoshida, T. Koujiri, T. Horii, and Y. Kubo, *Bull. Chem. Soc. Jpn.*, 1990, **63**, 1658–1664.

97. M. R. Massafra, E. Selli, S. Salsa, and B. Marcandalli, *Dyes Pigments*, 1998, **40**, 171–180.

98. E. Remi, A. Rockenbauer, L. Korecz, I. Rusznak, and A. Vig, *Radiat. Phys. Chem.*, 1999, **55**, 555–558.

99. K. Matczyszyn, W. Bartkowiak, and J. Leszczynski, *THEOCHEM*, 2001, **565-566**, 53–57.

100. K. Hamada, M. Nishizawa, and M. Mitsuishi, *Dyes Pigments*, 1991, **16**, 165–171.

101. K. Leverenz and K. Schundehutte, 1,2,4-benzotriazinium Dyestuffs. Patent Specification GB1384223, 1973.

Appendix A
Correction of Previously Published Work

Tables containing the required correction for signals observed in work published by K.M. Tait are tabulated below (Section 4.3.5.1). Proton numbering has been changed to correlate with that adopted in Chapter 4.

Trans Signal	*Cis* Signal	Proton Assignment	Changed Assignment?	$\Delta\delta$/ppm
a	j	12	No	0.20
b	i	9/10	No	0.34
c	m	4	No	0.07
d	k	8/11	No	0.90
e	n	5	Yes: 3	0.04
f	l	1	Yes: 7	1.23
g	p	3	Yes: 5	0.09
h	o	7	Yes: 1	0.75

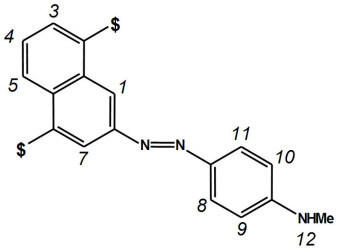

Table A.1: Changes in the ^{1}H NMR assignments of the *trans* and *cis* isomers of 178/5 in d_6-DMSO. Spectra to which these peaks correspond are available in the cited reference.[30]

Trans Signal	*Cis* Signal	Proton Assignment	Changed Assignment?	$\Delta\delta$/ppm
a	l k	13	No	0.10 0.16
b	m	4	No	0.12
c	i	9/10	No	0.67
d	n	5	Yes: 3	0.10
e	j	8/11	No	0.80
f	∗	1	Yes: 7	∗
g	p	3	Yes: 5	0.16
h	o	7	Yes: 1	0.87

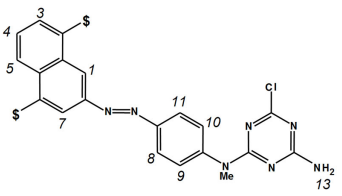

Table A.2: Changes in the ^{1}H NMR assignments for the *trans* and *cis* isomers of 178/7 in d_6-DMSO. Spectra to which these peaks correspond are available in the cited reference.[30]
∗ Unobtainable.

Trans Signal	*Cis* Signal	Proton Assignment	Changed Assignment?	$\Delta\delta$/ppm
a	m	12	No	0.20
b	l	9	No	0.70
c	o	15	No	0.11
d	q	4	No	0.05
e	n	8	No	1.55
f	∗	10	No	∗
g	s	5	Yes: 3	0.02
h	r	1	Yes: 7	0.76
i	u	3	Yes: 5	0.07
j	∗	14	No	∗
k	∗	7	Yes: 1	∗

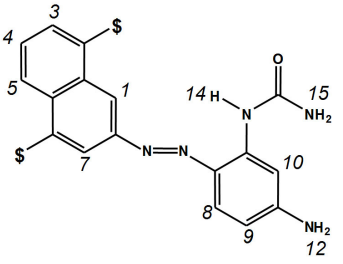

Table A.3: Changes in the ^{1}H NMR assignments for the *trans* and *cis* isomers of 178/3 in d_6-DMSO. Spectra to which these peaks correspond are available in the cited reference.[30]
∗ Unobtainable.

Trans Signal	*Cis* Signal	Proton Assignment	Changed Assignment?	$\Delta\delta$/ppm
a	n	15	No	0.17
b	p	4	No	0.08
c	$*$	13	No	$*$
d	$*$	9	No	$*$
e	$*$	12	No	$*$
f	m	8	No	1.60
g	q	5	Yes: 3	0.04
h	o	10	Yes 7	1.32
i	r	1	Yes: 10	0.14
j	s	3	Yes: 5	0.13
k	t	7	No	0.21
l	$*$	7	Yes: 1	$*$

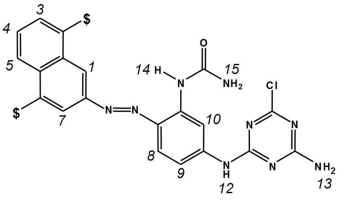

Table A.4: Changes in the ^{1}H NMR assignments for the *trans* and *cis* isomers of 178/9 in d_6-DMSO. Spectra to which these peaks correspond are available in the cited reference.[30]

$*$ Unobtainable.

Appendix B
^{1}H NMR Spectra and Assignments

This appendix contains the proton assignments and chemical shifts for the dyes and their photoisomers described within the thesis.

Dyebase 271/64 Spectral Assignment

The ^{1}H NMR Spectra of 271/64 (1.00 mM) in d_6-DMSO (a) prior to irradiation and (b) during irradiation at the 530-nm PSS. Spectra recorded at 298 K. ^{1}H NMR assignments for the *trans* and *cis* isomers are given in the table, along with chemical shifts and $\Delta\delta$ values.

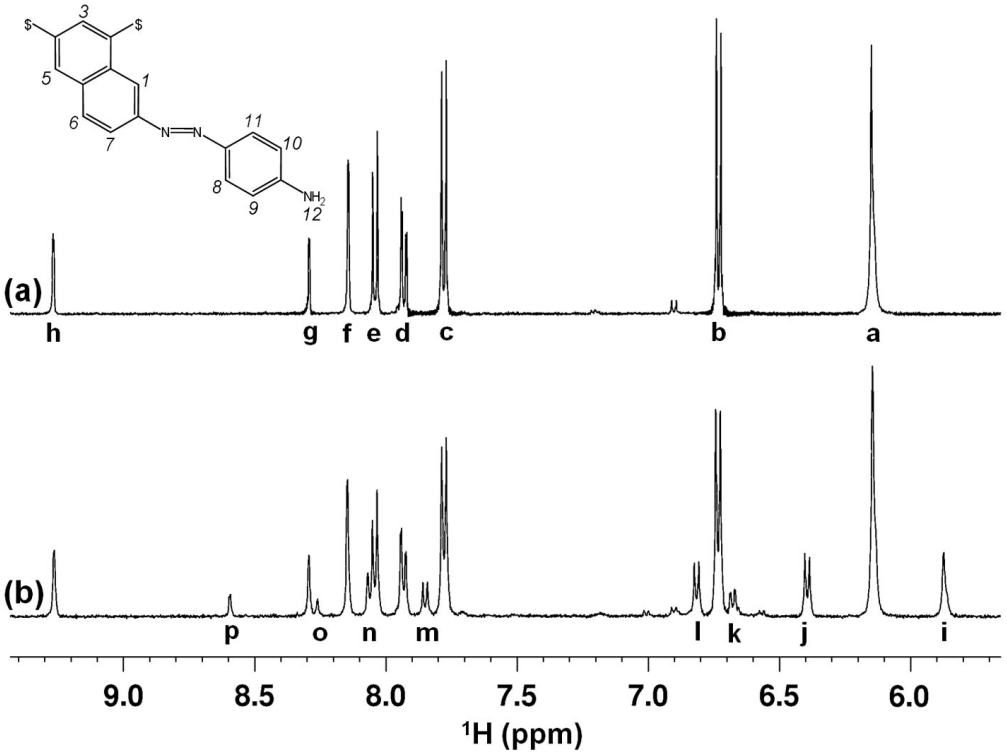

Trans Signal	*Trans* chemical shift δ_t/ppm	*Cis* Signal	*Cis* chemical shift δ_c/ppm	Proton Assignment	$\Delta\delta$/ppm
a	6.15	i	5.87	12	0.28
b	6.73	j	6.39	9/10	0.34
c	7.76	l	6.80	8/11	0.96
d	7.93	k	6.68	7	1.25
e	8.04	m	7.85	6	0.19
f	8.15	n	8.07	5	0.08
g	8.29	o	8.26	3	0.03
h	9.27	p	8.59	1	0.68

Dyebase 284/43 Spectral Assignment

The ^{1}H NMR Spectra of 284/43 (2.90 mM) in d_6-DMSO (a) prior to irradiation and (b) during irradiation at the 530-nm PSS. ^{1}H NMR assignments for the *trans* and *cis* isomers are given in the table, along with chemical shifts and $\Delta\delta$ values.

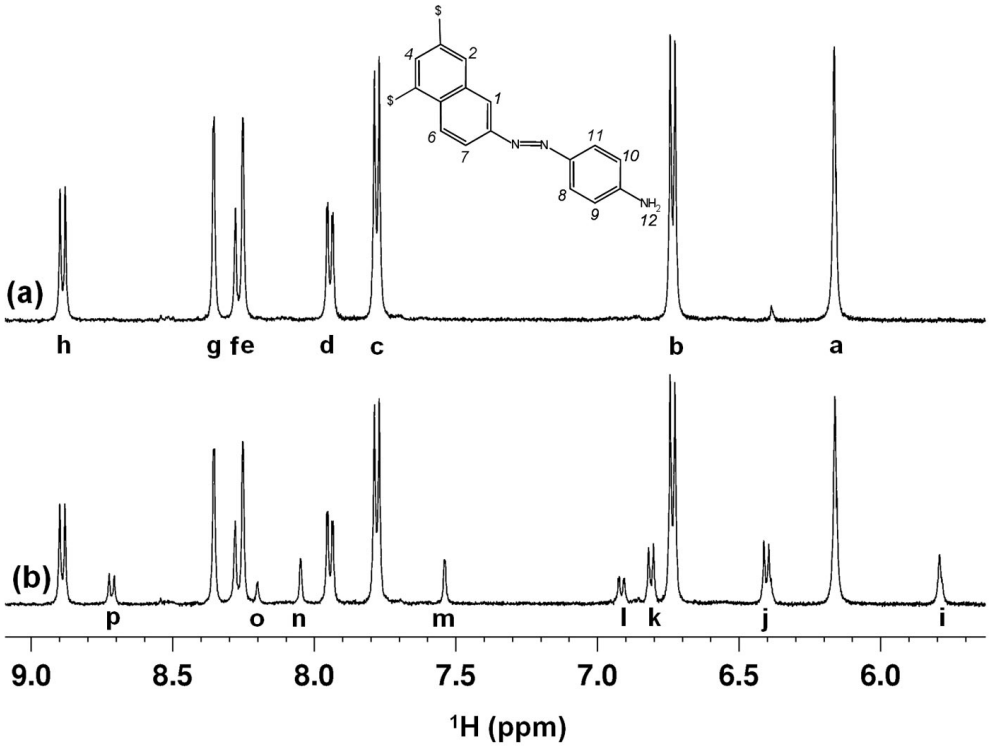

Trans Signal	*Trans* chemical shift δ_t/ppm	*Cis* Signal	*Cis* chemical shift δ_c/ppm	Proton Assignment	$\Delta\delta$/ppm
a	6.16	i	5.79	12	0.37
b	6.74	j	6.40	9/10	0.34
c	7.78	k	6.81	8/11	0.97
d	7.95	l	6.92	7	1.03
e	8.25	n	8.05	2	0.20
f	8.28	o	8.20	4	0.08
g	8.35	m	7.54	1	0.81
h	8.89	p	8.71	6	0.18

Dyebase 273/10 Spectral Assignment

The ^{1}H NMR Spectra of 273/10 (0.93 mM) in d_6-DMSO (a) prior to irradiation and (b) during irradiation at the 530-nm PSS. Spectra recorded at 298 K. ^{1}H NMR assignments for the *trans* and *cis* isomers are given in the table, along with chemical shifts and $\Delta\delta$ values.

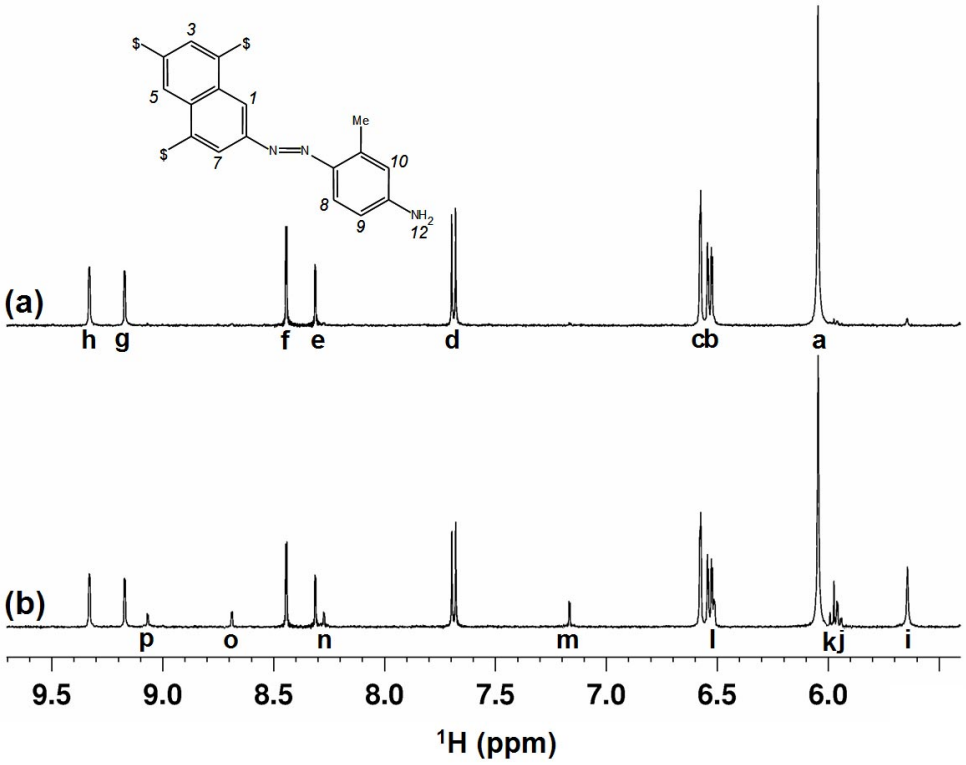

Trans Signal	*Trans* chemical shift δ_t/ppm	*Cis* Signal	*Cis* chemical shift δ_c/ppm	Proton Assignment	$\Delta\delta$/ppm
a	6.05	i	5.64	12	0.41
b	6.53	j	5.95	9	0.58
c	6.58	l	6.51	10	0.07
d	7.69	k	5.98	8	1.71
e	8.31	n	8.27	3	0.04
f	8.44	m	7.17	7	1.27
g	9.17	p	9.06	5	0.11
h	9.33	o	8.69	1	0.64
Me	2.64	Me	2.48	Me	0.16

Dye 273/19 Spectral Assignment

The ^{1}H NMR Spectra of 273/19 (2.06 mM) in d_6-DMSO (a) prior to irradiation and (b) during irradiation at the 530-nm PSS. Spectra recorded at 298 K. ^{1}H NMR assignments for the *trans* and *cis* isomers are given in the table, along with chemical shifts and $\Delta\delta$ values.

$*$ = Unobtainable.

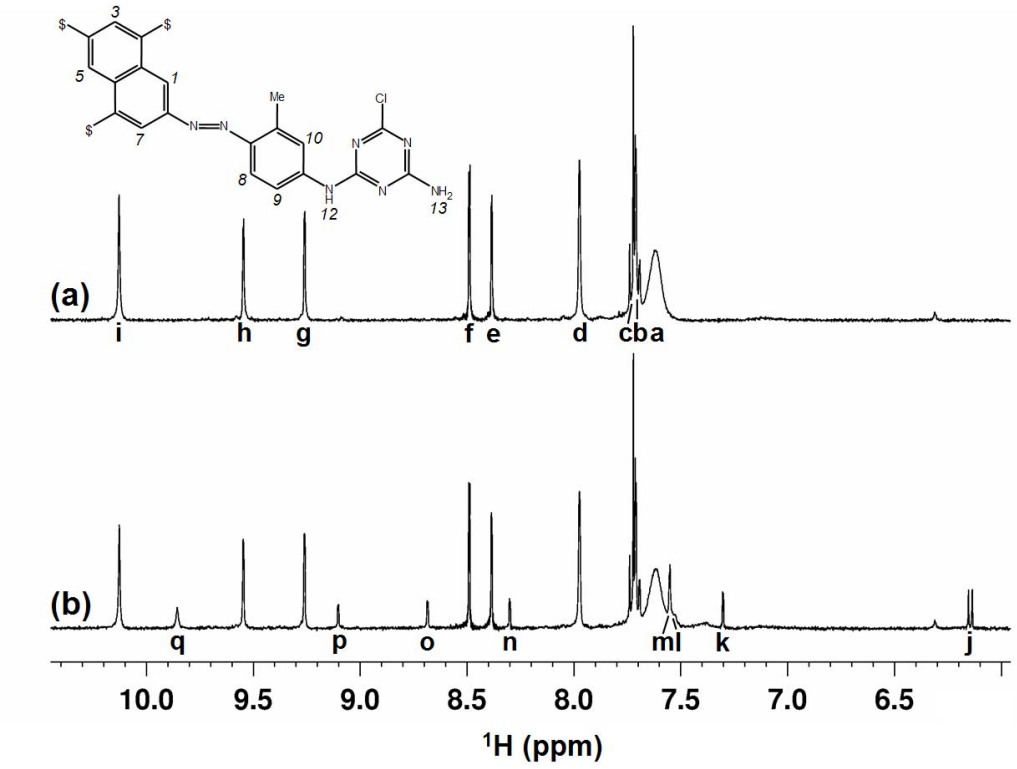

Trans Signal	*Trans* chemical shift δ_t/ppm	*Cis* Signal	*Cis* chemical shift δ_c/ppm	Proton Assignment	$\Delta\delta$/ppm
a	7.62	l	7.53	13	0.09
b	7.70	$*$	$*$	9	$*$
c	7.73	j	6.15	8	1.58
d	7.97	m	7.55	10	0.42
e	8.38	n	8.30	3	0.08
f	8.49	k	7.30	7	1.19
g	9.26	p	9.11	5	0.15
h	9.55	o	8.69	1	0.86
i	10.13	q	9.87	12	0.26
Me	2.79	Me	2.43	Me	0.36

Dyebase 269/52 Spectral Assignment

The ^{1}H NMR Spectra of 269/52 (0.19 mM) in d_6-DMSO (a) prior to irradiation and (b) during irradiation at the 530-nm PSS. Spectra recorded at 298 K. ^{1}H NMR assignments for the *trans* and *cis* isomers are given in the table, along with chemical shifts and $\Delta\delta$ values.

$*$ = Unobtainable.

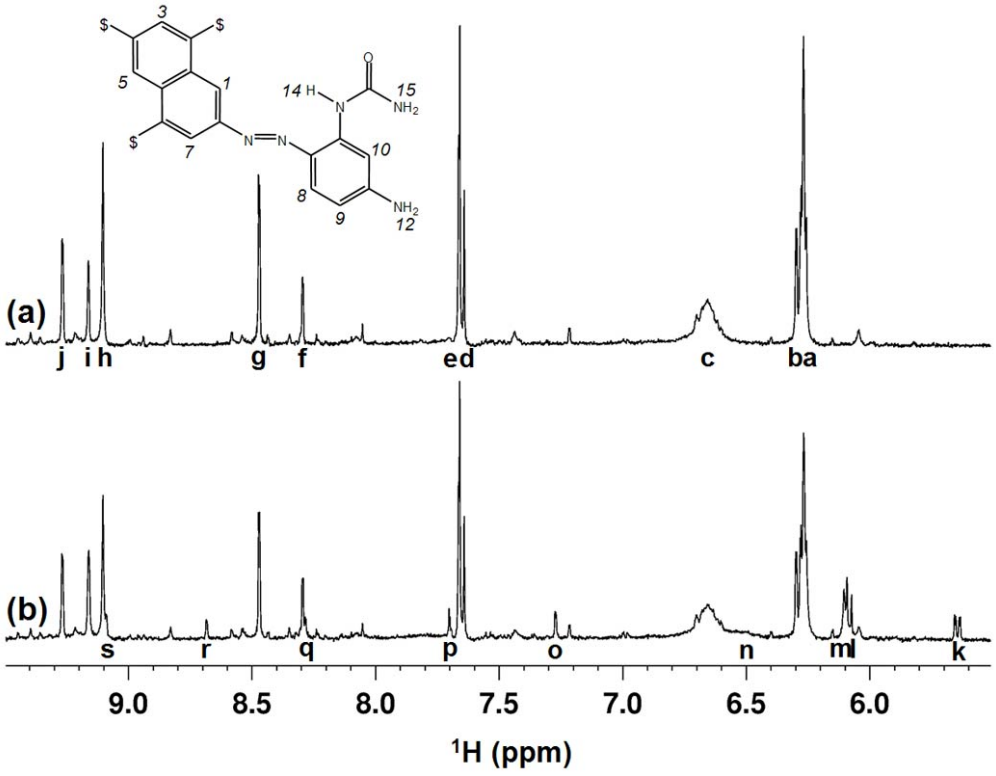

Trans Signal	*Trans* chemical shift δ_t/ppm	*Cis* Signal	*Cis* chemical shift δ_c/ppm	Proton Assignment	$\Delta\delta$/ppm
a	6.27	m	6.10	12	0.17
b	6.29	k	5.65	9	0.64
c	6.66	n	6.53	15	0.13
d	7.65	l	6.08	8	1.57
e	7.67	o	7.27	10	0.40
f	8.30	q	8.29	3	0.01
g	8.47	p	7.71	7	0.76
h	9.10	$*$	$*$	14	$*$
i	9.16	$*$	$*$	5	$*$
j	9.27	r	8.68	1	0.59

Dye 269/56 Spectral Assignment

The ^1H NMR Spectra of 269/56 (0.35 mM) in d_6-DMSO (a) prior to irradiation and (b) during irradiation at the 530-nm PSS. Spectra recorded at 298 K. ^{1}H NMR assignments for the *trans* and *cis* isomers are given in the table, along with chemical shifts and $\Delta\delta$ values.

$*$ = Unobtainable.

† Superimposed *cis* signals.

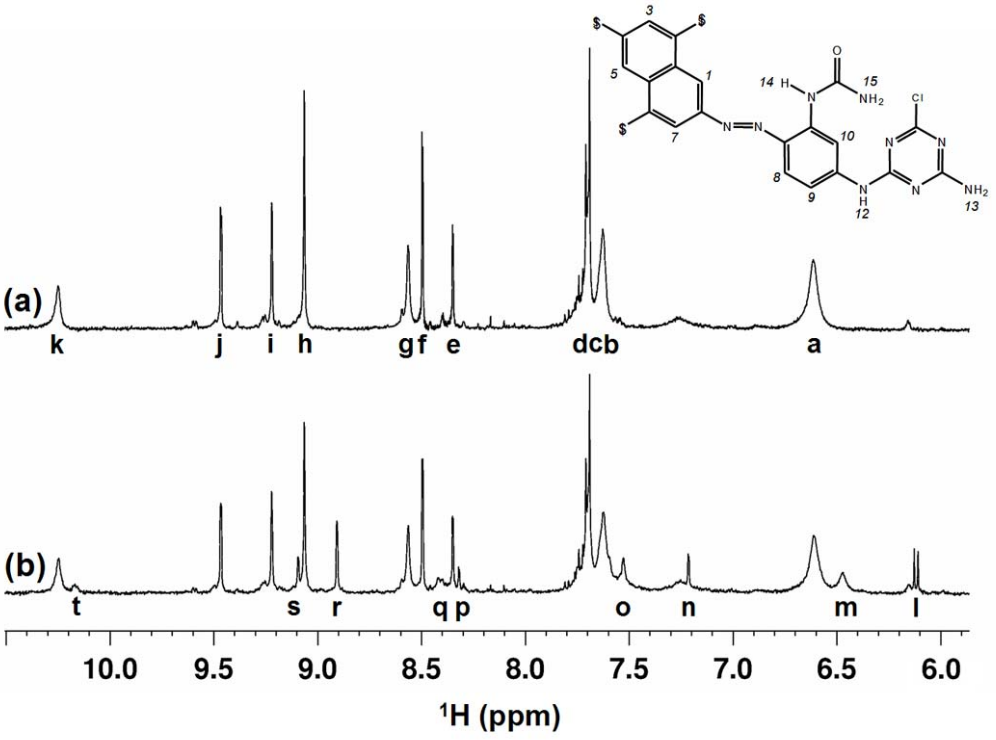

Trans Signal	*Trans* chemical shift δ_t/ppm	*Cis* Signal	*Cis* chemical shift δ_c/ppm	Proton Assignment	$\Delta\delta$/ppm
a	6.61	m	6.47	15	0.14
b	7.62	$*$	$*$	13	$*$
c	7.67	o	7.53	9	0.14
d	7.70	l	6.12	8	1.58
e	8.35	p	8.32	3	0.03
f	8.50	n	7.22	7	1.28
g	8.56	q	8.42	10	0.14
h	9.06	r†	8.91	14	0.15
i	9.22	s	9.10	5	0.12
j	9.47	r†	8.91	1	0.56
k	10.25	t	10.17	12	0.08

Dye 273/5 Spectral Assignment

The ^{1}H NMR Spectra of 273/5 (0.84 mM) in d_6-DMSO (a) prior to irradiation and (b) during irradiation at the 530-nm PSS. Spectra recorded at 298 K. ^{1}H NMR assignments for the *trans* and *cis* isomers are given in the table, along with chemical shifts and $\Delta\delta$ values.

$*$ = Unobtainable.

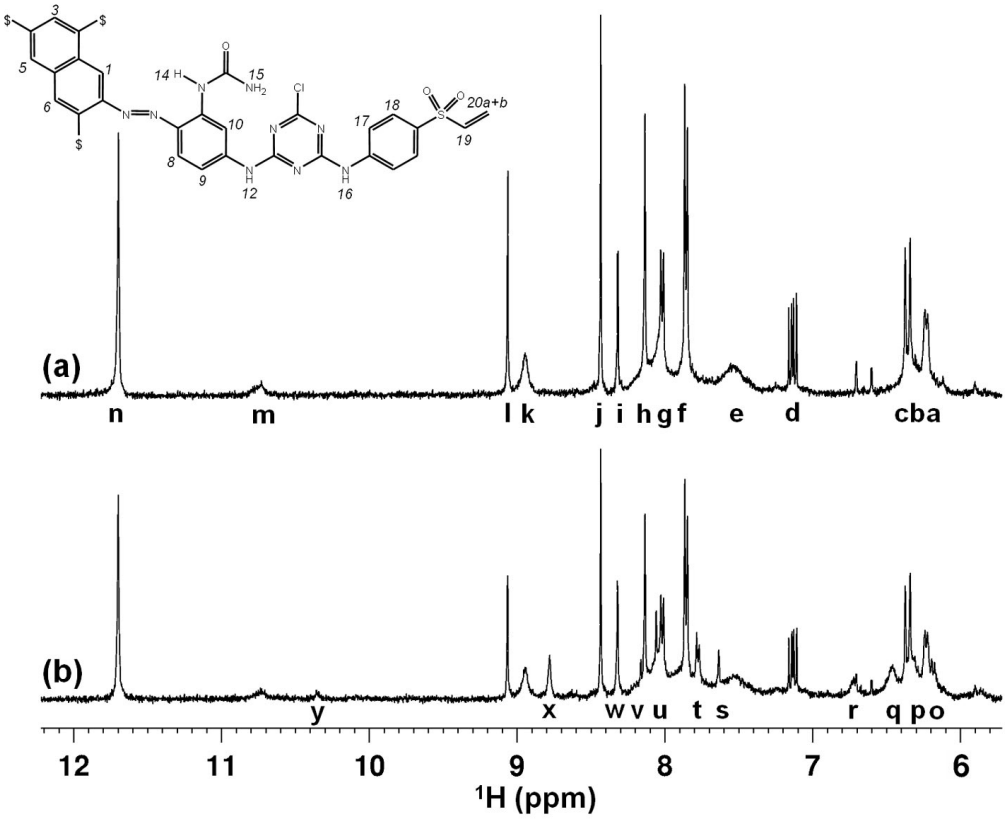

Trans Signal	*Trans* chemical shift δ_t/ppm	*Cis* Signal	*Cis* chemical shift δ_c/ppm	Proton Assignment	$\Delta\delta$/ppm
a	6.22	o	6.19	20_Z	0.03
b	6.32	q	6.44	15	-0.12
c	6.36	$*$	$*$	20_E	$*$
d	7.14	$*$	$*$	19	$*$
e	7.53	q	6.44	15	1.09
f	7.86	t	7.76	18	0.10
g	8.01	$*$	$*$	17	$*$
h	8.14	u	8.06	5	0.08
i	8.32	v	8.16	3	0.16
j	8.44	w	8.32	6	0.12
k	8.94	$*$	$*$	10	$*$
l	9.07	s	7.63	1	1.44
m	10.74	y	10.36	12/16	0.38
n	11.70	x	8.78	14	2.92

Dye 273/6 Spectral Assignment

The ^{1}H NMR Spectra of 273/6 (1.64 mM) in d_6-DMSO (a) prior to irradiation and (b) during irradiation at the 530-nm PSS. Spectra recorded at 298 K. ^{1}H NMR assignments for the *trans* and *cis* isomers are given in the table, along with chemical shifts and $\Delta\delta$ values.

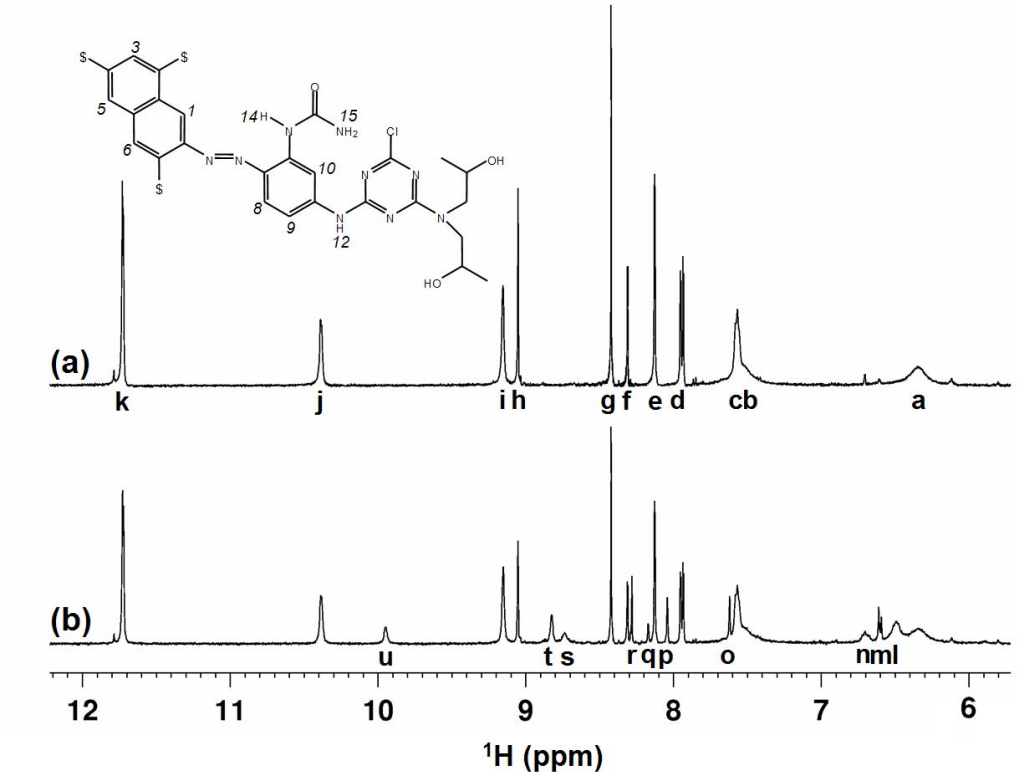

Trans Signal	*Trans* chemical shift δ_t/ppm	*Cis* Signal	*Cis* chemical shift δ_c/ppm	Proton Assignment	$\Delta\delta$/ppm
a	6.35	l	6.48	15	-0.13
b	7.53	l	6.48	15	1.05
c	7.57	n	6.70	9	0.87
d	7.94	m	6.60	8	1.34
e	8.13	p	8.04	5	0.09
f	8.31	q	8.16	3	0.15
g	8.43	r	8.28	6	0.15
h	9.05	o	7.62	1	1.43
i	9.16	s	8.73	10	0.43
j	10.38	u	9.94	12	0.44
k	11.72	t	8.83	14	2.89

Dye 273/8 Spectral Assignment

The ^{1}H NMR Spectra of 273/8 (1.40 mM) in d_6-DMSO (a) prior to irradiation and (b) during irradiation at the 530-nm PSS. Spectra recorded at 298 K. ^{1}H NMR assignments for the *trans* and *cis* isomers are given in the table, along with chemical shifts and $\Delta\delta$ values.

$*$ = Unobtainable.

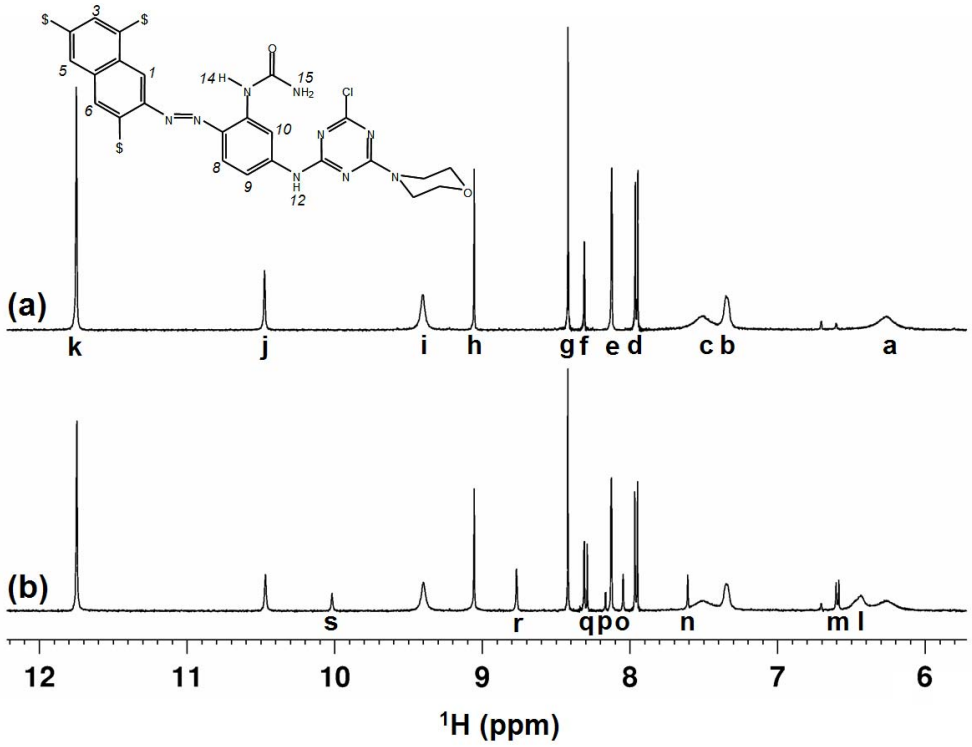

Trans Signal	*Trans* chemical shift δ_t/ppm	*Cis* Signal	*Cis* chemical shift δ_c/ppm	Proton Assignment	$\Delta\delta$/ppm
a	6.30	l	6.43	15	-0.13
b	7.35	$*$	$*$	9	$*$
c	7.51	l	6.43	15	1.08
d	7.96	m	6.60	8	1.36
e	8.12	o	8.05	5	0.07
f	8.31	p	8.17	3	0.14
g	8.42	q	8.29	6	0.13
h	9.06	n	7.61	1	1.45
i	9.40	$*$	$*$	10	$*$
j	10.47	s	10.02	12	0.45
k	11.75	r	8.77	14	2.98

Dye 273/13 Spectral Assignment

The ^{1}H NMR Spectra of 273/13 (1.62 mM) in d_6-DMSO (a) prior to irradiation and (b) during irradiation at the 530-nm PSS. Spectra recorded at 298 K. ^{1}H NMR assignments for the *trans* and *cis* isomers are given in the table, along with chemical shifts and $\Delta\delta$ values.

$*$ = Unobtainable.

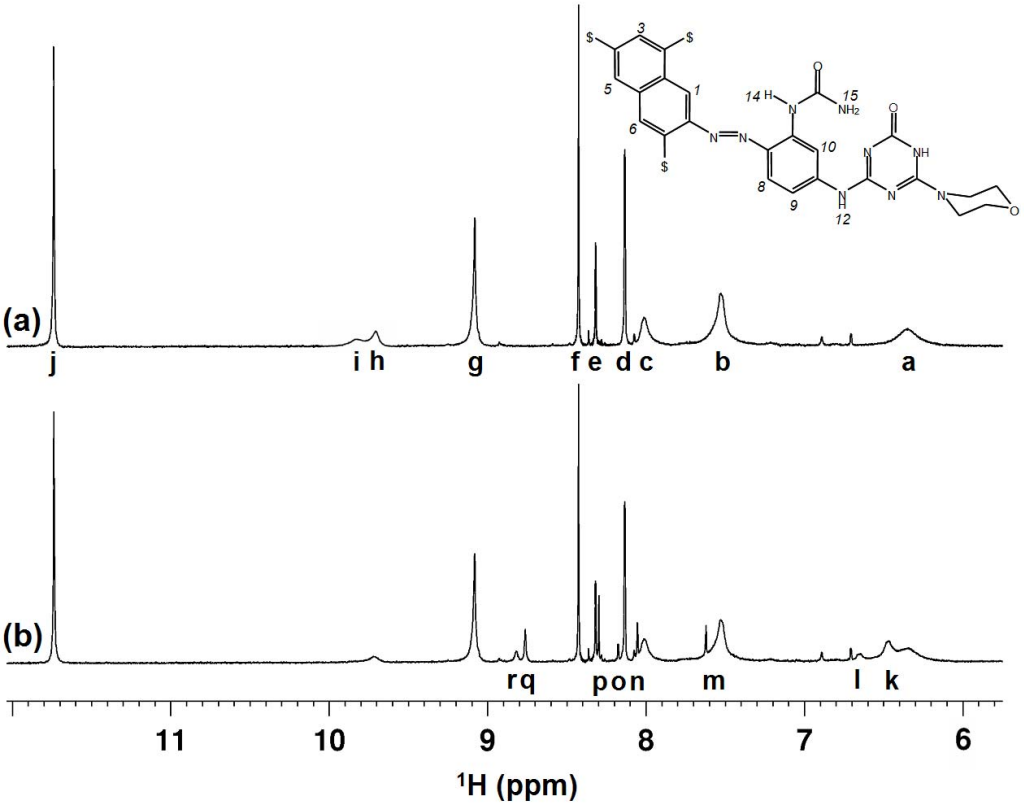

Trans Signal	*Trans* chemical shift δ_t/ppm	*Cis* Signal	*Cis* chemical shift δ_c/ppm	Proton Assignment	$\Delta\delta$/ppm
a	6.33	k	6.46	15	-0.13
b	7.52	k $*$	6.46 $*$	15 9	1.06 $*$
c	8.01	$*$	$*$	8	$*$
d	8.13	n	8.05	5	0.08
e	8.32	o	8.17	3	0.15
f	8.43	p	8.30	6	0.13
g	9.08	m r	7.64 8.82	1 7	1.44 0.26
h	9.71	$*$	$*$	12	$*$
i	9.85	$*$	$*$	Hydroxyl	$*$
j	11.74	q	8.76	14	2.98

Dyebase 283/26 Species A Spectral Assignment

The ^{1}H NMR Spectra of 286/26 Species **A** (0.10 mM) in d_6-DMSO (a) prior to irradiation and (b) during irradiation at the 530-nm PSS. Spectra recorded at 298 K. ^{1}H NMR assignments for the *trans* and *cis* isomers are given in the table, along with chemical shifts and $\Delta\delta$ values.

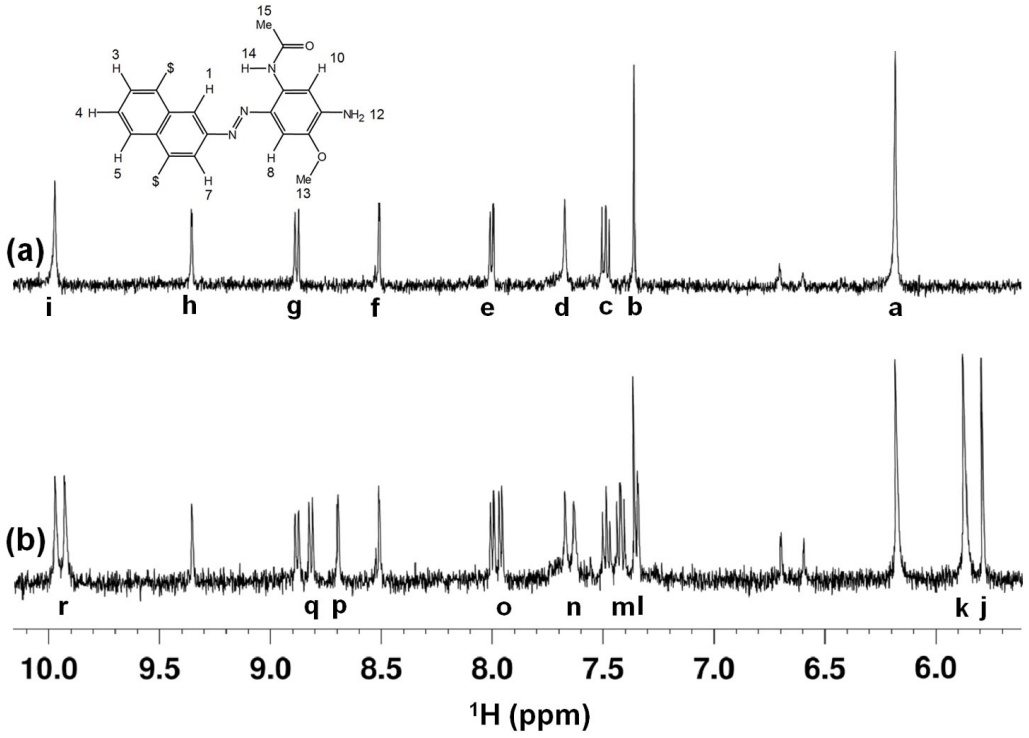

Trans Signal	*Trans* chemical shift δ_t/ppm	*Cis* Signal	*Cis* chemical shift δ_c/ppm	Proton Assignment	$\Delta\delta$/ppm
a	6.18	k	5.87	12	0.31
b	7.36	j	5.79	8	1.57
c	7.49	m	7.42	4	0.07
d	7.68	n	7.64	10	0.04
e	8.00	o	7.97	3	0.03
f	8.51	l	7.35	7	1.17
g	8.88	q	8.82	5	0.06
h	9.36	p	8.70	1	0.66
i	9.97	r	9.93	14	0.04
OMe	3.90	OMe	2.80	13	1.10
COMe	2.24	COMe	2.22	15	0.02

Appendix C
Minimum Energy Structures

This appendix contains figures for all the structures presented within the thesis. Cartesian coordinate matrices are available in Appendix D.

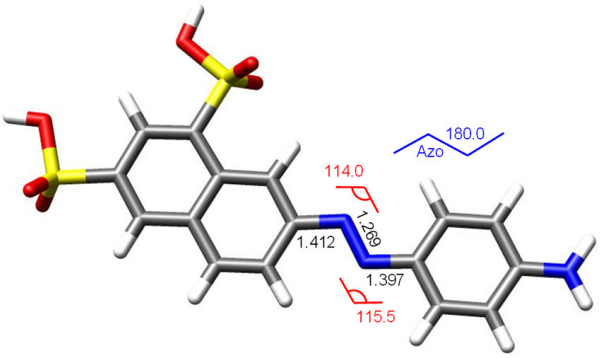

Figure C.1: Minimum energy structure of the *trans* isomer of molecule 271/64 calculated at the B3LYP/6-31G(d,p) level of theory. Bond lengths are stated in Angtroms, and angles in degrees.

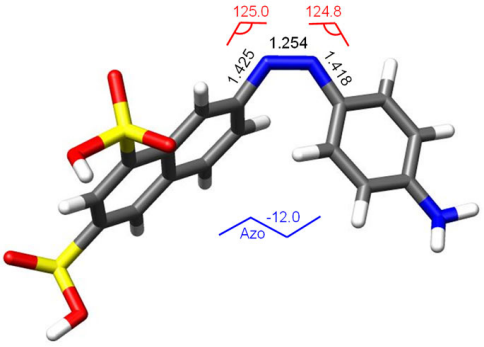

Figure C.2: Minimum energy structure of the *cis* isomer of molecule 271/64 calculated at the B3LYP/6-31G(d,p) level of theory. Bond lengths are stated in Angstroms, and angles in degrees.

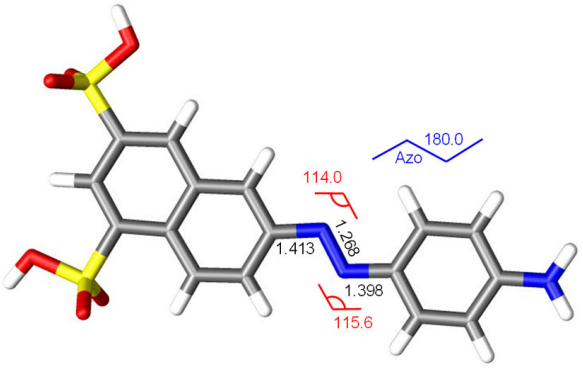

Figure C.3: Minimum energy structure of the *trans* isomer of molecule 284/43 calculated at the B3LYP/6-31G(d,p) level of theory. Bond lengths are stated in Angstroms, and angles in degrees.

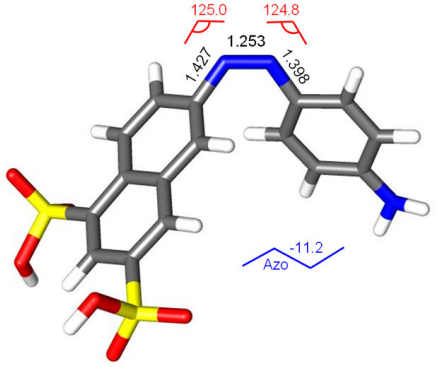

Figure C.4: Minimum energy structure of the *cis* isomer of molecule 284/43 calculated at the B3LYP/6-31G(d,p) level of theory. Bond lengths are stated in Angstroms, and angles in degrees.

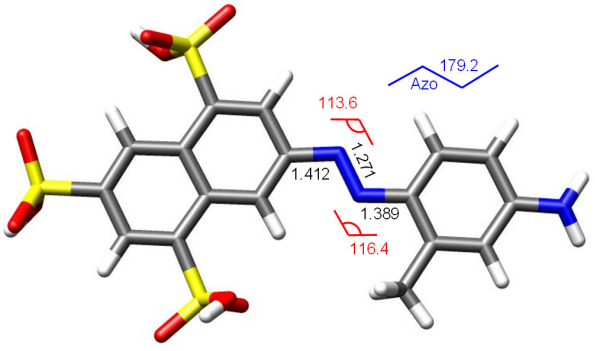

Figure C.5: Minimum energy structure of the *trans* isomer of molecule 273/10 calculated at the B3LYP/6-31G(d,p) level of theory. Bond lengths are stated in Angstroms, and angles in degrees.

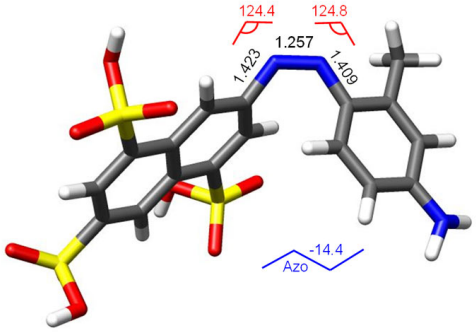

Figure C.6: Minimum energy structure of the *cis* isomer of molecule 273/10 calculated at the B3LYP/6-31G(d,p) level of theory. Bond lengths are stated in Angstroms, and angles in degrees.

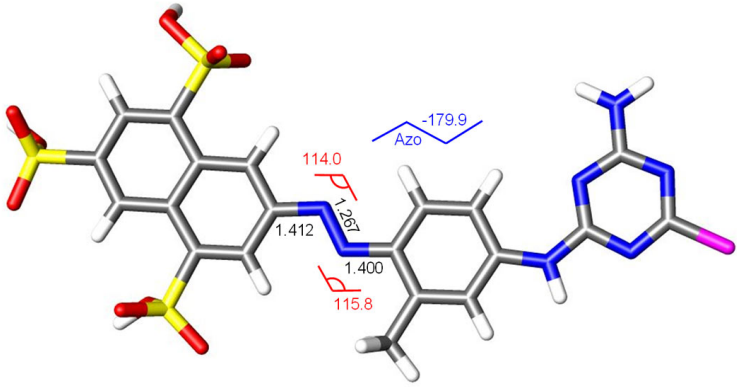

Figure C.7: Minimum energy structure of the *trans* isomer of molecule 273/19 calculated at the B3LYP/6-31G(d,p) level of theory. Bond lengths are stated in Angstroms, and angles in degrees.

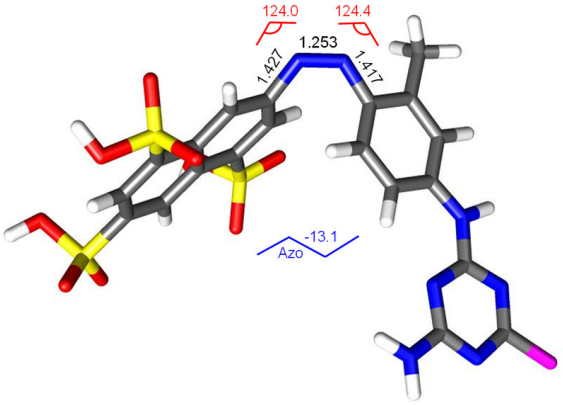

Figure C.8: Minimum energy structure of the *cis* isomer of molecule 273/19 calculated at the B3LYP/6-31G(d,p) level of theory. Bond lengths are stated in Angstroms, and angles in degrees.

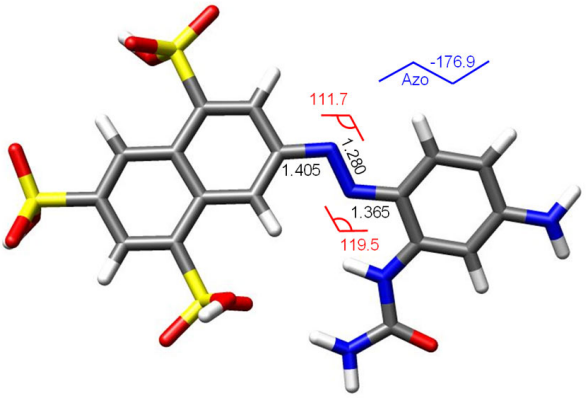

Figure C.9: Minimum energy structure of the *trans* isomer of molecule 269-52 calculated at the B3LYP/6-31G(d,p) level of theory. Bond lengths are stated in Angstroms, and angles in degrees.

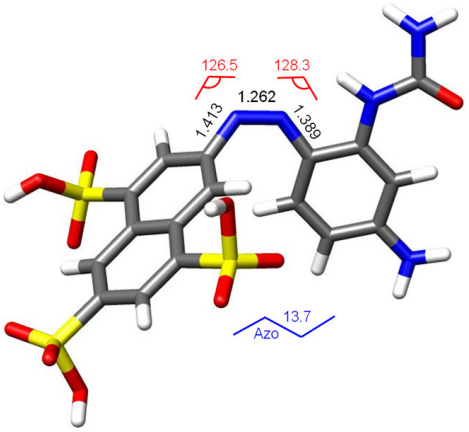

Figure C.10: Minimum energy structure of the *cis* isomer of molecule 269-52 that most closely matches experimental data, calculated at the B3LYP/6-31G(d,p) level of theory. Bond lengths are stated in Angstroms, and angles in degrees.

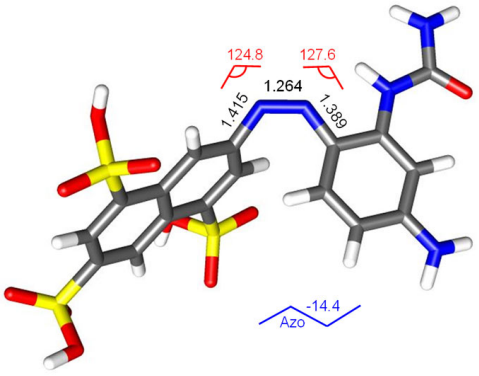

Figure C.11: Minimum energy structure of the *cis* isomer of molecule 269-52 calculated at the B3LYP/6-31G(d,p) level of theory. Bond lengths are stated in Angstroms, and angles in degrees.

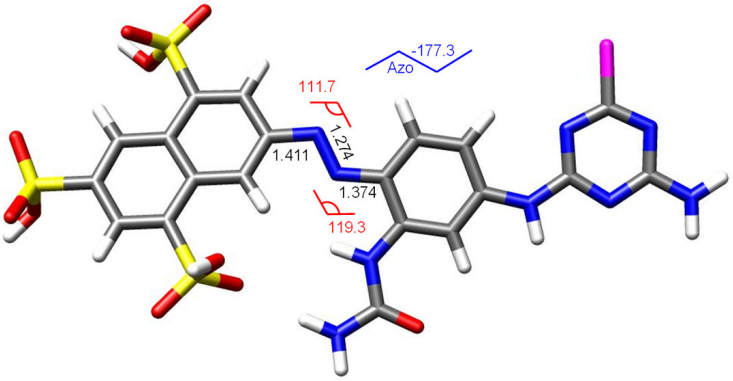

Figure C.12: Minimum energy structure of the *trans* isomer of molecule 269-56 calculated at the B3LYP/6-31G(d,p) level of theory. Bond lengths are stated in Angstroms, and angles in degrees.

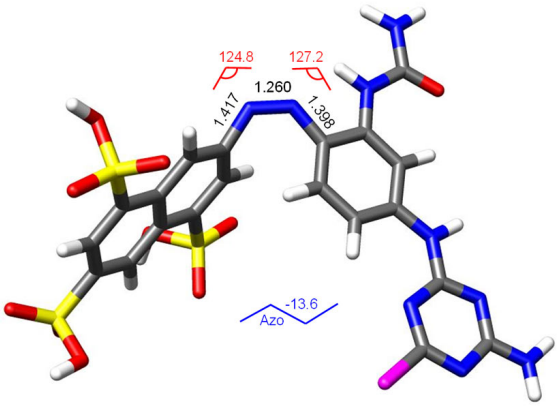

Figure C.13: Minimum energy structure of the *cis* isomer of molecule 269-56 that most closely matches experimental data, calculated at the B3LYP/6-31G(d,p) level of theory. Bond lengths are stated in Angstroms, and angles in degrees.

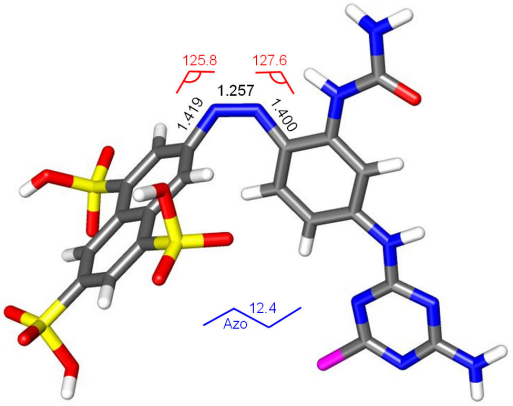

Figure C.14: Minimum energy structure of the *cis* isomer of molecule 269-56 calculated at the B3LYP/6-31G(d,p) level of theory. Bond lengths are stated in Angstroms, and angles in degrees.

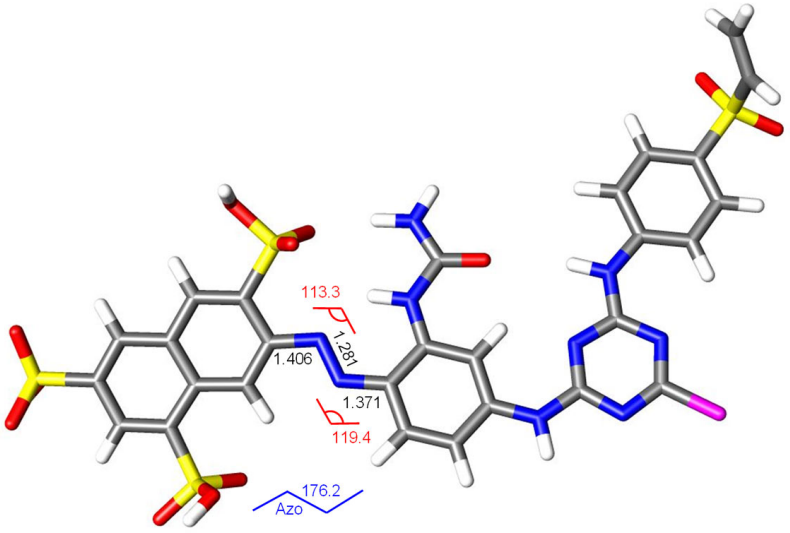

Figure C.15: Minimum energy structure of the *trans* isomer of molecule 273/5 calculated at the B3LYP/6-31G(d,p) level of theory. Bond lengths are stated in Angstroms, and angles in degrees.

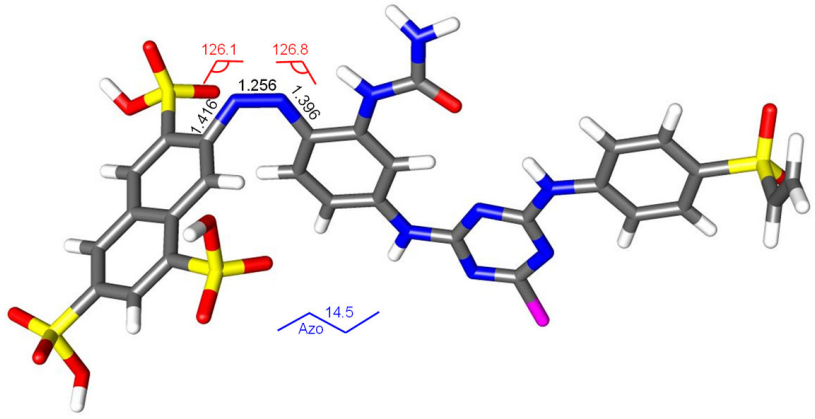

Figure C.16: Minimum energy structure of the *cis* isomer of molecule 273/5 calculated at the B3LYP/6-31G(d,p) level of theory. Bond lengths are stated in Angstroms, and angles in degrees.

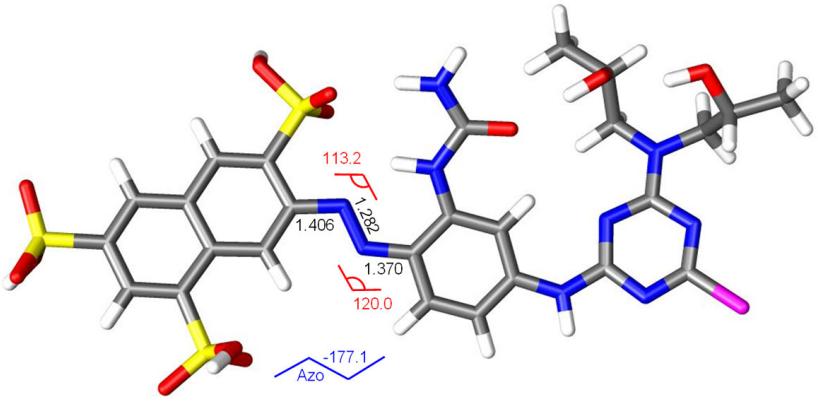

Figure C.17: Minimum energy structure of the *trans* isomer of molecule 273/6 calculated at the B3LYP/6-31G(d,p) level of theory. Bond lengths are stated in Angstroms, and angles in degrees.

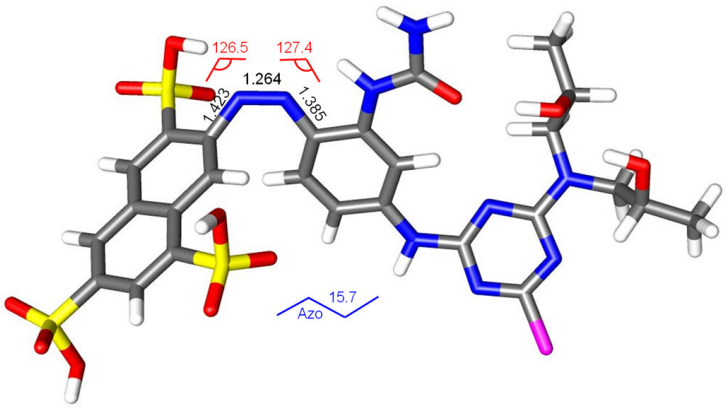

Figure C.18: Minimum energy structure of the *cis* isomer of molecule 273/6 calculated at the B3LYP/6-31G(d,p) level of theory. Bond lengths are stated in Angstroms, and angles in degrees.

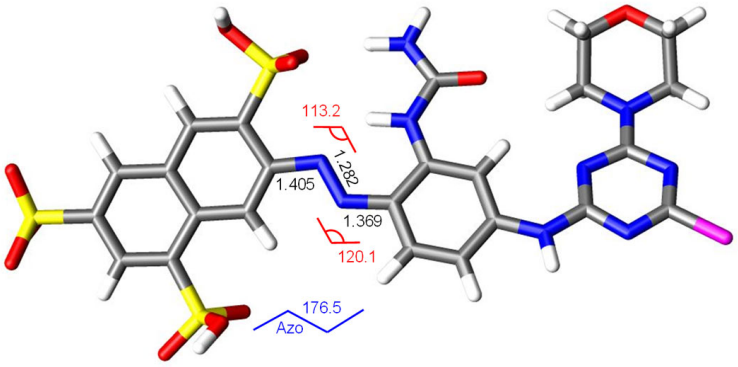

Figure C.19: Minimum energy structure of the *trans* isomer of molecule 273/8 calculated at the B3LYP/6-31G(d,p) level of theory. Bond lengths are stated in Angstroms, and angles in degrees.

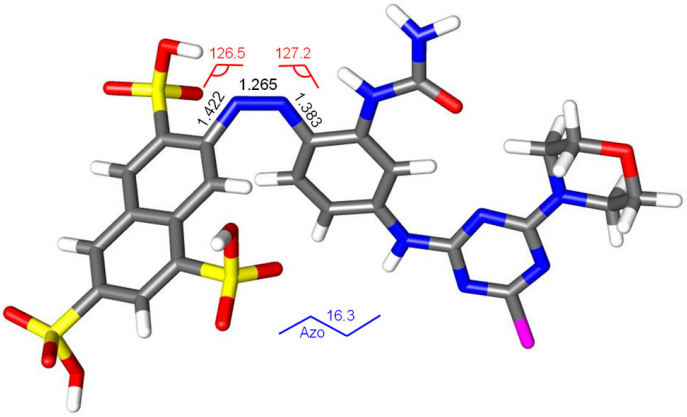

Figure C.20: Minimum energy structure of the *cis* isomer of molecule 273/8 calculated at the B3LYP/6-31G(d,p) level of theory. Bond lengths are stated in Angstroms, and angles in degrees.

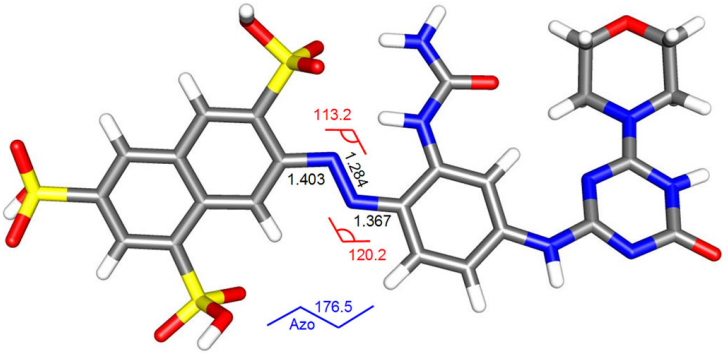

Figure C.21: Minimum energy structure of the *trans* isomer of molecule 273/13 calculated at the B3LYP/6-31G(d,p) level of theory. Bond lengths are stated in Angstroms, and angles in degrees.

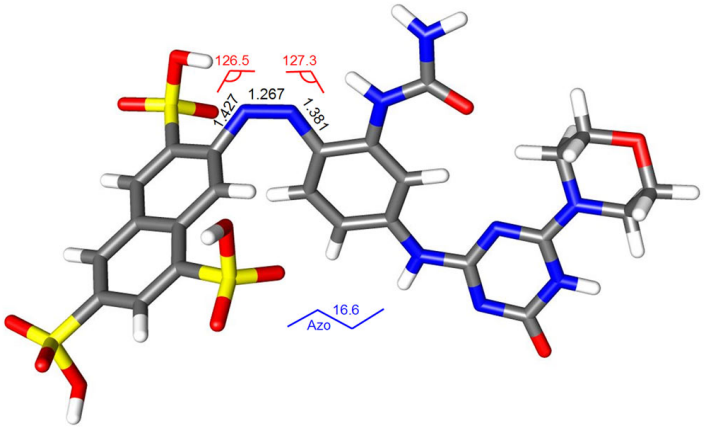

Figure C.22: Minimum energy structure of the *cis* isomer of molecule 273/13 calculated at the B3LYP/6-31G(d,p) level of theory. Bond lengths are stated in Angstroms, and angles in degrees.

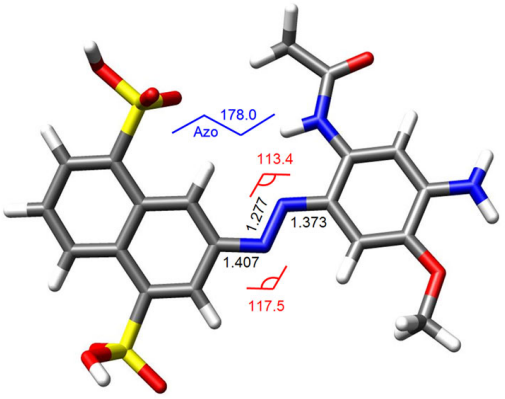

Figure C.23: Minimum energy structure of the *trans* isomer of molecule 283/26 species **A** calculated at the B3LYP/6-31G(d,p) level of theory. Bond lengths are stated in Angstroms, and angles in degrees.

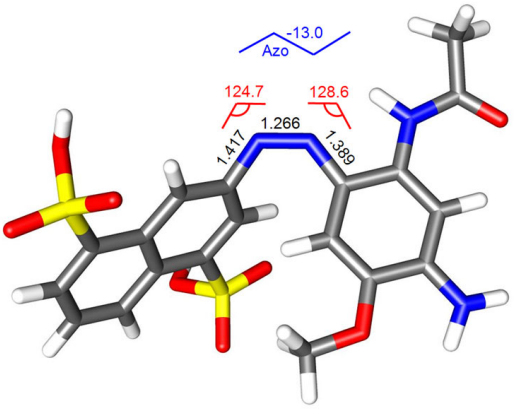

Figure C.24: Minimum energy structure of the *cis* isomer of molecule 283/26 species **A** calculated at the B3LYP/6-31G(d,p) level of theory. Bond lengths are stated in Angstroms, and angles in degrees.

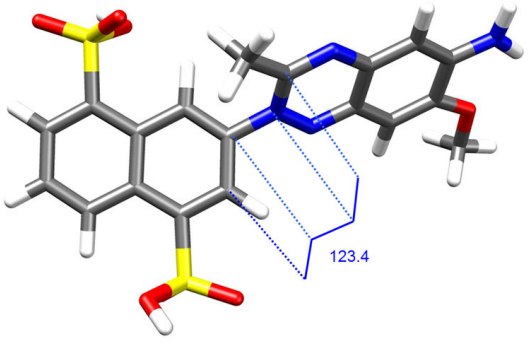

Figure C.25: Minimum energy structure of 283/26 species **B** calculated at the B3LYP/6-31G(d,p) level of theory. Bond angles are stated in degrees.

Appendix D: Cartesian Coordinates for the Structures Presented in Appendix C

This appendix contains the Cartesian coordinate matrices for the calculated structures presented within chapters of this thesis.

Table D.1: Cartesian coordinates for *trans* 271/64. Optimised at the B3LYP/6-31G(d,p) level of theory. (Figure C.1)

Atom Number	Atom	X Coordinate	Y Coordinate	Z Coordinate
1	C	-2.398030	0.803216	-0.073082
2	C	-3.570078	0.078818	-0.107427
3	C	-3.496215	-1.330409	-0.119605
4	C	-2.284218	-1.988015	-0.097958
5	C	-1.077066	-1.257171	-0.062735
6	C	-1.109370	0.179189	-0.049324
7	C	0.120122	0.880354	-0.013875
8	C	1.327839	0.202956	0.007478
9	C	1.355666	-1.222018	-0.005925
10	C	0.182326	-1.924023	-0.040079
11	N	2.480451	1.018092	0.042266
12	N	3.571283	0.370184	0.061197
13	C	4.731701	1.147883	0.095797
14	C	4.762986	2.559224	0.110437
15	C	5.967170	3.231530	0.145014
16	C	7.193511	2.521607	0.166479
17	C	7.161027	1.110664	0.151815
18	C	5.948537	0.444029	0.117101
19	S	-2.450989	2.597899	-0.056619
20	O	-1.954223	3.104507	1.220232
21	O	-1.895755	3.129340	-1.298819
22	O	-4.086998	2.788645	-0.092710
23	H	-4.255694	3.746721	-0.087180
24	S	-4.951742	-2.368788	-0.163625
25	O	-5.072521	-3.114724	1.086107
26	O	-5.014074	-3.089899	-1.432070
27	O	-6.083313	-1.173498	-0.178105
28	H	-6.954539	-1.605547	-0.202586
29	H	-4.529067	0.573545	-0.124808
30	H	-2.242361	-3.072975	-0.107683
31	H	0.155627	1.962322	-0.002385
32	H	2.318159	-1.718212	0.011523
33	H	0.190400	-3.010378	-0.050601
34	H	3.823567	3.099688	0.093961
35	H	5.984321	4.318423	0.156127
36	H	8.093369	0.552979	0.167957
37	H	5.911400	-0.640660	0.105546

Continued on following page

Table D.1 – continued from previous page

Atom Number	Atom	X Coordinate	Y Coordinate	Z Coordinate
38	N	8.382585	3.196075	0.200726
39	H	8.408409	4.201001	0.211233
40	H	9.258757	2.703377	0.216205

Table D.2: Cartesian coordinates for *cis* 271/64. Optimised at the B3LYP/6-31G(d,p) level of theory. (Figure C.2)

Atom Number	Atom	X Coordinate	Y Coordinate	Z Coordinate
1	C	-1.799126	1.076365	0.030875
2	C	-2.926936	0.307832	0.197354
3	C	-2.909890	-1.034397	-0.242356
4	C	-1.799473	-1.587023	-0.837374
5	C	-0.633548	-0.807838	-1.018643
6	C	-0.609072	0.563711	-0.587780
7	C	0.564455	1.323142	-0.804480
8	C	1.690754	0.740030	-1.362217
9	C	1.662184	-0.615755	-1.797079
10	C	0.523442	-1.359658	-1.634393
11	N	2.786907	1.580370	-1.710946
12	N	3.985145	1.357811	-1.415946
13	C	4.421806	0.376002	-0.490438
14	C	3.728820	-0.067811	0.653708
15	C	4.325419	-0.954456	1.534853
16	C	5.625747	-1.449139	1.298681
17	C	6.326403	-0.986422	0.165979
18	C	5.742160	-0.067370	-0.688260
19	S	-1.785474	2.771624	0.627622
20	O	-0.899656	2.865819	1.789845
21	O	-1.637452	3.674848	-0.502194
22	O	-3.318102	2.936568	1.196054
23	H	-3.237503	3.025917	2.161433
24	S	-4.368301	-2.031692	-0.022737
25	O	-4.241436	-3.236035	-0.833595
26	O	-5.565194	-1.193703	-0.092183
27	O	-4.172859	-2.438463	1.563996
28	H	-5.065604	-2.464797	1.951240
29	H	-3.822220	0.723092	0.640727
30	H	-1.821545	-2.618735	-1.172263
31	H	0.605910	2.374370	-0.547588
32	H	2.541991	-1.040189	-2.267826
33	H	0.488930	-2.390832	-1.973672
34	H	2.739367	0.310832	0.877239
35	H	3.787861	-1.272826	2.424097
36	H	7.337158	-1.338887	-0.020604
37	H	6.289015	0.323934	-1.540089
38	N	6.186870	-2.384775	2.143940
39	H	5.793558	-2.467544	3.069549
40	H	7.189782	-2.492656	2.114286

Table D.3: Cartesian coordinates for *trans* 284/43. Optimised at the B3LYP/6-31G(dp) level of theory. (Figure C.3)

Atom Number	Atom	X Coordinate	Y Coordinate	Z Coordinate
1	C	-1.816855	-1.605076	-0.000003
2	C	-3.146630	-1.258754	0.000000
3	C	-3.560683	0.094077	0.000001
4	C	-2.602683	1.082560	-0.000002
5	C	-1.203001	0.789838	-0.000005
6	C	-0.821119	-0.593922	-0.000006
7	C	0.552185	-0.937633	-0.000010
8	C	1.532747	0.035924	-0.000011
9	C	1.151820	1.407978	-0.000011
10	C	-0.170719	1.771879	-0.000008
11	N	2.868129	-0.426319	-0.000015
12	N	3.734742	0.499582	0.000021
13	C	5.068329	0.078507	0.000015
14	C	5.496056	-1.266223	0.000008
15	C	6.841534	-1.573026	0.000001
16	C	7.818730	-0.546922	-0.000001
17	C	7.389897	0.797367	0.000005
18	C	6.038144	1.096032	0.000015
19	S	-4.469275	-2.460578	0.000004
20	O	-5.203450	-2.392353	-1.260265
21	O	-5.203441	-2.392355	1.260278
22	O	-3.543168	-3.822533	0.000000
23	H	-4.153453	-4.580125	0.000002
24	S	-3.092573	2.811044	-0.000002
25	O	-2.706321	3.441420	-1.259882
26	O	-2.706313	3.441422	1.259875
27	O	-4.723293	2.593584	0.000003
28	H	-5.127378	3.478535	0.000004
29	H	-1.516414	-2.645410	-0.000004
30	H	-4.612737	0.345481	0.000003
31	H	0.851790	-1.980824	-0.000012
32	H	1.934995	2.156337	-0.000012
33	H	-0.426178	2.824382	-0.000009
34	H	4.746764	-2.049454	0.000010
35	H	7.164167	-2.611226	-0.000002
36	H	8.127583	1.595025	0.000003
37	H	5.697221	2.126454	0.000021
38	N	9.150448	-0.859086	-0.000009
39	H	9.459151	-1.815772	-0.000013
40	H	9.852188	-0.139225	-0.000010

Table D.4: Cartesian coordinates for *cis* 284/43. Optimised at the B3LYP/6-31G(dp) level of theory. (Figure C.4)

Atom Number	Atom	X Coordinate	Y Coordinate	Z Coordinate
1	C	-0.709969	1.246000	-0.785577
2	C	-1.972651	1.429900	-0.277611
3	C	-2.749922	0.353573	0.206629
4	C	-2.220671	-0.914907	0.158242
5	C	-0.917756	-1.178731	-0.371448
6	C	-0.151877	-0.058190	-0.844247
7	C	1.155856	-0.258337	-1.347943
8	C	1.702142	-1.527581	-1.402539
9	C	0.924993	-2.640336	-0.984317
10	C	-0.334069	-2.471743	-0.460288
11	N	2.922866	-1.798672	-2.089110
12	N	4.033449	-1.285671	-1.816550
13	C	4.316206	-0.526484	-0.649825
14	C	3.743802	-0.699851	0.625525
15	C	4.194977	0.042190	1.704273
16	C	5.218323	1.002074	1.549026
17	C	5.807292	1.156089	0.277878
18	C	5.381714	0.380366	-0.787399
19	S	-2.656305	3.077344	-0.206130
20	O	-1.569943	4.036738	-0.341494
21	O	-3.618867	3.154346	0.893962
22	O	-3.534053	3.105313	-1.596330
23	H	-4.436248	3.371173	-1.347430
24	S	-3.193514	-2.300234	0.768382
25	O	-2.511454	-2.896590	1.917868
26	O	-3.620345	-3.113538	-0.358621
27	O	-4.529598	-1.545455	1.352668
28	H	-4.456790	-1.571036	2.322569
29	H	-0.133891	2.097772	-1.131122
30	H	-3.732837	0.534112	0.620296
31	H	1.725814	0.597244	-1.694965
32	H	1.351046	-3.633616	-1.082272
33	H	-0.885746	-3.342064	-0.127360
34	H	2.965795	-1.436361	0.783717
35	H	3.761948	-0.119662	2.687812
36	H	6.616964	1.868219	0.144314
37	H	5.853399	0.469646	-1.760732
38	N	5.677907	1.720339	2.634169
39	H	5.071544	1.785621	3.437944
40	H	6.200291	2.562506	2.444930

Table D.5: Cartesian coordinates for *trans* 273/10. Optimised at the B3LYP/6-31G(d,p) level of theory. (Figure C.5)

Atom Number	Atom	X Coordinate	Y Coordinate	Z Coordinate
1	C	-2.564004	1.013862	-0.296286
2	C	0.728917	0.848611	-0.446283
3	C	1.189399	-0.461484	-0.540219
4	C	2.560188	-1.569942	-0.509944
5	C	3.074532	-1.418871	-0.349242
6	C	4.438439	-0.097024	-0.229328
7	C	5.315745	0.059701	-0.063343
8	C	4.789057	-1.040759	-0.013767
9	C	3.438651	-2.345808	-0.125937
10	C	-3.249179	-2.523666	-0.286407
11	N	-2.355468	-0.990092	0.160142
12	N	-4.400389	0.192548	0.237579
13	C	-2.305656	0.310343	0.425611
14	C	-2.838359	1.632623	0.511094
15	C	-7.447906	1.803696	0.708431
16	C	-7.988537	0.705949	0.822456
17	C	-7.714638	-0.604929	0.732848
18	C	-7.933776	-0.791061	0.539206
19	S	-8.654465	2.716935	-0.180197
20	O	-3.115573	2.861794	0.957950
21	O	-4.036411	3.596208	-0.373396
22	O	-1.960782	2.856869	-1.518076
23	H	-4.018247	3.306599	-2.196450
24	S	-4.723005	-0.677756	-0.728978
25	O	-5.825452	0.416443	-1.535483
26	O	-5.313107	-2.071717	-1.049556
27	O	-1.072508	-0.400185	0.817944
28	H	-0.543393	0.251804	0.767622
29	S	4.844489	-4.223906	-0.454778
30	O	5.457044	-4.366292	-1.583194
31	O	3.018565	-5.103519	-0.334065
32	O	6.665069	-4.321556	0.917935
33	H	6.990622	-4.972439	0.748834
34	H	7.232158	1.709468	-0.507055
35	H	2.165536	-2.550338	-0.627741
36	H	2.728946	1.040486	0.045561
37	H	1.368434	-3.196182	-0.076932
38	H	1.671671	2.809987	0.775026
39	H	3.435947	-1.458039	0.816565
40	H	6.964700	-1.788046	0.472413
41	N	5.824171	0.902306	0.978652
42	H	6.609694	1.813233	1.262428
43	H	5.210004	0.127426	1.285583
44	C	6.235053	2.830060	0.390600
45	H	7.294491	3.758393	0.513927
46	H	6.120655	2.804019	1.138571
47	H	5.881310	2.853518	-0.585385

Table D.6: Cartesian coordinates for *cis* 273/10. Optimised at the B3LYP/6-31G(d,p) level of theory. (Figure C.6)

Atom Number	Atom	X Coordinate	Y Coordinate	Z Coordinate
1	C	-2.201996	1.552464	-0.012058
2	C	-3.308778	0.791035	0.281340
3	C	-3.194933	-0.611542	0.231163
4	C	-2.019323	-1.235142	-0.118976
5	C	-0.874774	-0.466038	-0.438639
6	C	-0.942402	0.971435	-0.375609
7	C	0.208518	1.737332	-0.680991
8	C	1.408279	1.132358	-1.007030
9	C	1.479150	-0.284525	-1.116513
10	C	0.371913	-1.044495	-0.845139
11	N	2.476052	1.953814	-1.465647
12	N	3.679749	1.805239	-1.135247
13	C	4.126385	1.012132	-0.059670
14	C	5.443009	0.491584	-0.174442
15	C	5.968890	-0.234785	0.886163
16	C	5.256753	-0.420691	2.087875
17	C	3.977645	0.162237	2.213246
18	C	3.424049	0.854820	1.153914
19	S	-2.433123	3.327642	0.123672
20	O	-1.327151	3.949730	0.852504
21	O	-3.808771	3.587361	0.528730
22	O	-2.250004	3.705552	-1.465574
23	H	-1.995185	4.644544	-1.513571
24	S	-4.625992	-1.610946	0.614869
25	O	-5.837528	-0.854404	0.301936
26	O	-4.397767	-2.951928	0.097985
27	O	-4.525732	-1.677583	2.254217
28	H	-5.375228	-1.347950	2.595583
29	S	0.594413	-2.822382	-0.990987
30	O	0.075060	-3.511897	0.191327
31	O	1.950770	-3.081358	-1.454826
32	O	-0.460638	-3.106854	-2.217252
33	H	-0.856170	-3.983061	-2.059859
34	H	-4.250552	1.265901	0.529671
35	H	0.172956	2.817132	-0.644329
36	H	2.398965	-0.764510	-1.426738
37	H	-1.981031	-2.315470	-0.138356
38	H	2.454321	1.321733	1.278513
39	H	3.435947	0.076508	3.150881
40	H	6.964700	-0.661176	0.793020
41	N	5.824171	-1.098635	3.142706
42	H	6.609694	-1.700090	2.946097
43	H	5.210004	-1.438573	3.867140
44	C	6.235053	0.677619	-1.443162
45	H	7.294491	0.468167	-1.275663
46	H	6.120655	1.695591	-1.823551
47	H	5.881310	0.005530	-2.233561

Table D.7: Cartesian coordinates for *trans* 273/19. Optimised at the B3LYP/6-31G(d,p) level of theory. (Figure C.7)

Atom Number	Atom	X Coordinate	Y Coordinate	Z Coordinate
1	C	-4.100974	-0.364718	0.072561
2	C	-3.324801	-1.381063	0.105837
3	C	-3.861111	-2.536616	0.169116
4	C	-5.073018	-2.688063	0.201784
5	C	-5.803580	-1.669428	0.183163
6	C	-5.348955	-0.537384	0.106226
7	C	-3.553529	0.785945	0.013730
8	C	-2.345815	0.933731	-0.020137
9	C	-1.590463	-0.079658	0.010044
10	C	-2.077052	-1.205790	0.077331
11	N	-0.336724	-0.021615	-0.016190
12	N	0.071897	1.026644	-0.081157
13	C	1.312402	1.122404	-0.111520
14	C	2.088540	0.140025	-0.080773
15	C	3.309145	0.282612	-0.114055
16	C	3.785651	1.440149	-0.180160
17	C	3.010214	2.422697	-0.210933
18	C	1.781889	2.290397	-0.178621
19	N	4.999832	1.693577	-0.218022
20	H	5.222335	2.564483	-0.261930
21	C	5.990832	0.984600	-0.209658
22	N	7.019512	1.612685	-0.258877
23	C	7.976325	0.931692	-0.251337
24	N	8.036704	-0.241242	-0.203624
25	C	6.955433	-0.765980	-0.157712
26	N	5.901247	-0.196171	-0.157848
27	S	-2.913926	-3.828658	0.132934
28	O	-2.118028	-3.808285	1.162439
29	O	-2.457201	-3.978239	-1.066520
30	O	-3.874091	-4.901259	0.370582
31	H	-3.721791	-5.189080	1.172340
32	S	-7.379763	-1.864284	0.245064
33	O	-7.713254	-2.961224	-0.368066
34	O	-7.953490	-0.736478	-0.028770
35	O	-7.507545	-2.128132	1.680664
36	H	-8.147555	-2.704521	1.769532
37	S	-4.417600	2.130360	-0.056393
38	O	-5.376234	2.022982	-0.929286
39	O	-3.608814	3.141493	-0.095295
40	O	-5.030728	2.051667	1.270344
41	H	-5.783420	2.478634	1.228310
42	H	-5.464291	-3.566806	0.225791
43	H	-5.952161	0.209989	0.056981
44	H	-1.955455	1.812445	-0.063558
45	H	-1.466742	-1.949202	0.116139
46	H	1.703437	-0.742110	-0.030306
47	H	3.900830	-0.472954	-0.090989
48	H	3.383638	3.313289	-0.262338
49	C	0.981525	3.366110	-0.214455
50	H	1.504601	4.183432	-0.267165
51	H	0.418171	3.413897	0.577057
52	H	0.383185	3.335685	-0.980696
53	Cl	9.342166	1.680304	-0.312711
54	N	6.938801	-1.961656	-0.106662
55	H	6.157080	-2.395875	-0.079506
56	H	7.714308	-2.408491	-0.112757

Table D.8: Cartesian coordinates for *cis* 273/19. Optimised at the B3LYP/6-31G(d,p) level of theory. (Figure C.8)

Atom Number	Atom	X Coordinate	Y Coordinate	Z Coordinate
1	C	2.434377	0.156393	0.770740
2	C	2.737816	0.872714	-0.440308
3	C	3.727224	0.310916	-1.315280
4	C	4.383928	-0.858580	-1.018456
5	C	4.077583	-1.516020	0.190711
6	C	3.122166	-1.048355	1.060976
7	C	1.442287	0.723651	1.633844
8	C	0.766730	1.874075	1.318545
9	C	1.066145	2.558457	0.110030
10	C	2.065886	2.088606	-0.719468
11	N	0.530509	3.855468	-0.150529
12	N	-0.689066	4.136517	-0.088728
13	C	-1.729572	3.176910	-0.016162
14	C	-1.729619	1.978436	-0.751447
15	C	-2.830798	1.136005	-0.763440
16	C	-3.966635	1.479736	-0.009500
17	C	-3.975415	2.693917	0.703119
18	C	-2.892190	3.563820	0.695032
19	N	-5.124364	0.702962	0.067458
20	H	-5.881378	1.081762	0.621707
21	C	-5.453311	-0.519262	-0.455670
22	N	-6.705832	-0.918758	-0.121832
23	C	-7.023812	-2.098745	-0.622032
24	N	-6.287394	-2.895721	-1.376596
25	C	-5.061705	-2.389005	-1.641504
26	N	-4.590952	-1.202938	-1.207850
27	S	4.024774	1.103406	-2.905150
28	O	4.507047	2.467942	-2.689983
29	O	2.893726	0.830735	-3.776842
30	O	5.299057	0.238881	-3.469620
31	H	6.069162	0.832686	-3.431528
32	S	4.942994	-3.029022	0.582831
33	O	5.282322	-3.736980	-0.650887
34	O	4.252516	-3.696999	1.676675
35	O	6.342129	-2.374777	1.154626
36	H	7.061931	-2.965393	0.869858
37	S	0.969480	-0.051144	3.185770
38	O	0.746099	-1.485770	3.007955
39	O	-0.045205	0.776099	3.825151
40	O	2.397908	0.125652	3.980242
41	H	2.450237	-0.588711	4.640750
42	H	5.104679	-1.285282	-1.703597
43	H	2.889814	-1.619111	1.949929
44	H	0.025201	2.266986	2.003175
45	H	2.325769	2.679131	-1.589220
46	H	-0.870199	1.722719	-1.360266
47	H	-2.830185	0.226597	-1.345096
48	H	-4.862485	2.967515	1.269754
49	C	-2.937032	4.862824	1.457657
50	H	-3.966014	5.136653	1.703214
51	H	-2.477007	5.666158	0.876453
52	H	-2.377218	4.792413	2.397527
53	Cl	-8.630320	-2.683610	-0.233941
54	N	-4.249881	-3.138261	-2.410390
55	H	-3.310300	-2.829588	-2.595193
56	H	-4.562748	-4.047095	-2.709264

Table D.9: Cartesian coordinates for *trans* 269/52. Optimised at the B3LYP/6-31G(dp) level of theory. (Figure C.9)

Atom Number	Atom	X Coordinate	Y Coordinate	Z Coordinate
1	C	-4.100974	-0.364718	0.072561
2	C	-3.324801	-1.381063	0.105837
3	C	-3.861111	-2.536616	0.169116
4	C	-5.073018	-2.688063	0.201784
5	C	-5.803580	-1.669428	0.183163
6	C	-5.348955	-0.537384	0.106226
7	C	-3.553529	0.785945	0.013730
8	C	-2.345815	0.933731	-0.020137
9	C	-1.590463	-0.079658	0.010044
10	C	-2.077052	-1.205790	0.077331
11	N	-0.336724	-0.021615	-0.016190
12	N	0.071897	1.026644	-0.081157
13	C	1.312402	1.122404	-0.111520
14	C	2.088540	0.140025	-0.080773
15	C	3.309145	0.282612	-0.114055
16	C	3.785651	1.440149	-0.180160
17	C	3.010214	2.422697	-0.210933
18	C	1.781889	2.290397	-0.178621
19	S	4.999832	1.693577	-0.218022
20	O	5.222335	2.564483	-0.261930
21	O	5.990832	0.984600	-0.209658
22	O	7.019512	1.612685	-0.258877
23	H	7.976325	0.931692	-0.251337
24	S	8.036704	-0.241242	-0.203624
25	O	6.955433	-0.765980	-0.157712
26	O	5.901247	-0.196171	-0.157848
27	O	-2.913926	-3.828658	0.132934
28	H	-2.118028	-3.808285	1.162439
29	S	-2.457201	-3.978239	-1.066520
30	O	-3.874091	-4.901259	0.370582
31	O	-3.721791	-5.189080	1.172340
32	O	-7.379763	-1.864284	0.245064
33	H	-7.713254	-2.961224	-0.368066
34	H	-7.953490	-0.736478	-0.028770
35	H	-7.507545	-2.128132	1.680664
36	H	-8.147555	-2.704521	1.769532
37	H	-4.417600	2.130360	-0.056393
38	H	-5.376234	2.022982	-0.929286
39	H	-3.608814	3.141493	-0.095295
40	H	-5.030728	2.051667	1.270344
41	N	-5.783420	2.478634	1.228310
42	H	-5.464291	-3.566806	0.225791
43	C	-5.952161	0.209989	0.056981
44	O	-1.955455	1.812445	-0.063558
45	N	-1.466742	-1.949202	0.116139
46	H	1.703437	-0.742110	-0.030306
47	H	3.900830	-0.472954	-0.090989
48	N	3.383638	3.313289	-0.262338
49	H	0.981525	3.366110	-0.214455
50	H	1.504601	4.183432	-0.267165

Table D.10: Cartesian coordinates for the minimum energy *cis* isomer of 269/52. Optimised at the B3LYP/6-31G(d,p) level of theory. (Figure C.11)

Atom Number	Atom	X Coordinate	Y Coordinate	Z Coordinate
1	C	-2.704164	1.653789	-0.002415
2	C	-3.897393	1.006264	0.216843
3	C	-3.929775	-0.398196	0.124215
4	C	-2.810643	-1.132979	-0.194512
5	C	-1.577722	-0.481578	-0.435883
6	C	-1.496135	0.952874	-0.329107
7	C	-0.257922	1.600739	-0.555426
8	C	0.886640	0.881840	-0.852081
9	C	0.812739	-0.533324	-0.998704
10	C	-0.379288	-1.178371	-0.800810
11	N	2.052741	1.579036	-1.246578
12	N	3.215695	1.342711	-0.810893
13	C	3.566920	0.586044	0.299848
14	C	4.966488	0.256822	0.363737
15	C	5.468136	-0.458085	1.447245
16	C	4.620728	-0.816625	2.509377
17	C	3.254178	-0.433869	2.487477
18	C	2.749009	0.244581	1.403483
19	S	-2.757211	3.438880	0.177001
20	O	-1.626705	3.925513	0.968425
21	O	-4.115298	3.830830	0.532521
22	O	-2.467357	3.835235	-1.392266
23	H	-2.135689	4.751086	-1.403602
24	S	-5.474392	-1.249639	0.408909
25	O	-6.583883	-0.360585	0.066877
26	O	-5.364689	-2.592233	-0.141954
27	O	-5.459012	-1.370624	2.048298
28	H	-6.295623	-0.984164	2.360682
29	S	-0.336915	-2.966064	-0.989442
30	O	-0.989791	-3.625199	0.142846
31	O	1.007870	-3.356102	-1.390549
32	O	-1.347817	-3.105524	-2.276733
33	H	-1.840604	-3.938605	-2.166771
34	H	-4.794813	1.571104	0.439805
35	H	-0.182599	2.676485	-0.481128
36	H	1.692390	-1.099516	-1.280253
37	H	-2.885324	-2.210187	-0.248853
38	H	1.713988	0.558862	1.418629
39	H	2.616797	-0.664023	3.335693
40	H	6.518733	-0.713492	1.464412
41	N	5.741164	0.667554	-0.711637
42	H	5.215216	1.250199	-1.357020
43	C	7.110294	0.508847	-0.891922
44	O	7.855111	-0.066032	-0.110374
45	N	7.569559	1.107960	-2.049030
46	H	6.945400	1.244954	-2.830561
47	H	8.517248	0.855136	-2.285711
48	N	5.123483	-1.487341	3.589144
49	H	6.043701	-1.893521	3.527796
50	H	4.488977	-1.919461	4.241420

Table D.11: Cartesian coordinates for *cis* 269/52 predicted by NMR. Optimised at the B3LYP/6-31G(dp) level of theory. (Figure C.10)

Atom Number	Atom	X Coordinate	Y Coordinate	Z Coordinate
1	C	1.488710	-1.614058	-0.521908
2	C	2.799518	-1.914561	-0.238458
3	C	3.683804	-0.861013	0.067311
4	C	3.276991	0.452929	0.072811
5	C	1.934196	0.782393	-0.233379
6	C	0.990792	-0.267053	-0.528706
7	C	-0.357024	0.057986	-0.808379
8	C	-0.786391	1.377428	-0.827015
9	C	0.145712	2.423958	-0.591755
10	C	1.448725	2.128309	-0.284337
11	N	-2.050381	1.755885	-1.331323
12	N	-3.174000	1.373458	-0.903750
13	C	-3.466355	0.721310	0.287017
14	C	-4.813491	0.219979	0.355487
15	C	-5.264024	-0.423631	1.505021
16	C	-4.421015	-0.544214	2.621021
17	C	-3.113366	0.007212	2.585898
18	C	-2.655052	0.614241	1.441190
19	S	0.427745	-3.022504	-0.867286
20	O	-0.780037	-2.925834	-0.061979
21	O	1.251568	-4.229184	-0.881201
22	O	-0.034732	-2.734882	-2.416840
23	H	0.498893	-3.315101	-2.986786
24	S	5.389444	-1.244663	0.429271
25	O	5.765455	-2.474148	-0.268709
26	O	6.172159	-0.023681	0.305636
27	O	5.277568	-1.627695	2.024229
28	H	5.731619	-2.481379	2.134509
29	S	2.508297	3.539028	0.063057
30	O	3.294835	3.313691	1.276617
31	O	1.723233	4.756025	-0.088727
32	O	3.535045	3.391960	-1.211840
33	H	4.406668	3.712076	-0.917153
34	H	3.146158	-2.940810	-0.263909
35	H	-1.074704	-0.727785	-1.002350
36	H	-0.182180	3.454762	-0.657197
37	H	3.992122	1.226171	0.316970
38	H	-1.662221	1.042770	1.439372
39	H	-2.482019	-0.048945	3.467399
40	H	-6.269050	-0.822319	1.521100
41	N	-5.597427	0.407748	-0.773041
42	H	-5.099601	0.907425	-1.503837
43	C	-6.915835	0.021595	-0.978569
44	O	-7.577228	-0.647953	-0.197088
45	N	-7.407442	0.430017	-2.204113
46	H	-7.026523	1.249282	-2.654621
47	H	-8.403588	0.302188	-2.300936
48	N	-4.875564	-1.147242	3.762620
49	H	-5.721084	-1.694279	3.714617
50	H	-4.206878	-1.436121	4.459093

Table D.12: Cartesian coordinates for *trans* 269/56. Optimised at the B3LYP/6-31G(dp) level of theory.

Atom Number	Atom	X Coordinate	Y Coordinate	Z Coordinate
1	C	-4.100974	-0.364718	0.072561
2	C	-3.324801	-1.381063	0.105837
3	C	-3.861111	-2.536616	0.169116
4	C	-5.073018	-2.688063	0.201784
5	C	-5.803580	-1.669428	0.183163
6	C	-5.348955	-0.537384	0.106226
7	C	-3.553529	0.785945	0.013730
8	C	-2.345815	0.933731	-0.020137
9	C	-1.590463	-0.079658	0.010044
10	C	-2.077052	-1.205790	0.077331
11	N	-0.336724	-0.021615	-0.016190
12	N	0.071897	1.026644	-0.081157
13	C	1.312402	1.122404	-0.111520
14	C	2.088540	0.140025	-0.080773
15	C	3.309145	0.282612	-0.114055
16	C	3.785651	1.440149	-0.180160
17	C	3.010214	2.422697	-0.210933
18	C	1.781889	2.290397	-0.178621
19	N	4.999832	1.693577	-0.218022
20	H	5.222335	2.564483	-0.261930
21	C	5.990832	0.984600	-0.209658
22	N	7.019512	1.612685	-0.258877
23	C	7.976325	0.931692	-0.251337
24	N	8.036704	-0.241242	-0.203624
25	C	6.955433	-0.765980	-0.157712
26	N	5.901247	-0.196171	-0.157848
27	S	-2.913926	-3.828658	0.132934
28	O	-2.118028	-3.808285	1.162439
29	O	-2.457201	-3.978239	-1.066520
30	O	-3.874091	-4.901259	0.370582
31	H	-3.721791	-5.189080	1.172340
32	S	-7.379763	-1.864284	0.245064
33	O	-7.713254	-2.961224	-0.368066
34	O	-7.953490	-0.736478	-0.028770
35	O	-7.507545	-2.128132	1.680664
36	H	-8.147555	-2.704521	1.769532
37	S	-4.417600	2.130360	-0.056393
38	O	-5.376234	2.022982	-0.929286
39	O	-3.608814	3.141493	-0.095295
40	O	-5.030728	2.051667	1.270344
41	H	-5.783420	2.478634	1.228310
42	H	-5.464291	-3.566806	0.225791
43	H	-5.952161	0.209989	0.056981
44	H	-1.955455	1.812445	-0.063558
45	H	-1.466742	-1.949202	0.116139
46	H	1.703437	-0.742110	-0.030306
47	H	3.900830	-0.472954	-0.090989
48	H	3.383638	3.313289	-0.262338
49	N	0.981525	3.366110	-0.214455
50	H	1.504601	4.183432	-0.267165
51	C	0.418171	3.413897	0.577057
52	O	0.383185	3.335685	-0.980696
53	N	9.342166	1.680304	-0.312711
54	H	6.938801	-1.961656	-0.106662
55	H	6.157080	-2.395875	-0.079506
56	Cl	6.157080	-2.395875	-0.079506
57	N	6.157080	-2.395875	-0.079506

Continued on following page

Table D.12 – continued from previous page

Atom Number	Atom	X Coordinate	Y Coordinate	Z Coordinate
58	H	6.157080	-2.395875	-0.079506
59	H	7.714308	-2.408491	-0.112757

Table D.13: Cartesian coordinates for the minimum energy *cis* isomer of 269/56. Optimised at the B3LYP/6-31G(dp) level of theory.

Atom Number	Atom	X Coordinate	Y Coordinate	Z Coordinate
1	C	2.441899	-0.262549	1.810177
2	C	3.435995	0.665075	2.010694
3	C	4.233660	1.048734	0.914197
4	C	4.060917	0.507151	-0.337689
5	C	3.050682	-0.461303	-0.559553
6	C	2.191835	-0.856401	0.527726
7	C	1.155291	-1.792636	0.297588
8	C	0.970982	-2.356488	-0.954034
9	C	1.852560	-2.029849	-2.017251
10	C	2.838112	-1.095712	-1.824974
11	N	0.095983	-3.453843	-1.161510
12	N	-1.143690	-3.455833	-0.951870
13	C	-1.970147	-2.352308	-0.707193
14	C	-3.253607	-2.700637	-0.176352
15	C	-4.194186	-1.699193	0.060854
16	C	-3.910516	-0.366016	-0.267966
17	C	-2.674914	-0.020685	-0.859119
18	C	-1.731062	-1.008557	-1.058443
19	N	-4.922867	0.551960	0.014748
20	H	-5.751577	0.168984	0.451438
21	C	-5.025285	1.906144	-0.166511
22	N	-4.017788	2.589156	-0.741385
23	C	-4.266843	3.888090	-0.849132
24	N	-5.339306	4.552230	-0.473566
25	C	-6.284367	3.755931	0.091082
26	N	-6.180758	2.431831	0.268295
27	S	1.470144	-0.687116	3.262267
28	O	0.054482	-0.621754	2.935068
29	O	2.031458	0.015103	4.413674
30	O	1.819951	-2.281393	3.448649
31	H	2.467589	-2.349790	4.171247
32	S	5.527494	2.255957	1.166910
33	O	5.963402	2.203704	2.562216
34	O	6.468448	2.154791	0.061708
35	O	4.682425	3.652673	0.989201
36	H	4.841190	4.178200	1.792621
37	S	3.843296	-0.712129	-3.266828
38	O	3.987677	0.734538	-3.430919
39	O	3.390548	-1.538636	-4.376772
40	O	5.282680	-1.281955	-2.715616
41	H	5.980562	-0.723450	-3.103126
42	H	3.610885	1.079587	2.996432
43	H	0.485328	-2.067259	1.101262
44	H	1.740012	-2.518573	-2.977944
45	H	4.698755	0.833319	-1.147523
46	H	-0.795778	-0.737660	-1.529786
47	H	-2.481729	1.001545	-1.146598
48	H	-5.144729	-1.978011	0.496066

Continued on following page

Table D.13 – continued from previous page

Atom Number	Atom	X Coordinate	Y Coordinate	Z Coordinate
49	N	-3.482372	-4.045078	0.084393
50	H	-2.693532	-4.628429	-0.175072
51	C	-4.636734	-4.635963	0.583254
52	O	-5.619894	-4.021137	0.973731
53	N	-4.549198	-6.012624	0.649650
54	H	-3.935157	-6.514548	0.025168
55	H	-5.427254	-6.464019	0.857386
56	Cl	-2.995157	4.839198	-1.591359
57	N	-7.415088	4.362404	0.499370
58	H	-8.138077	3.821346	0.942963
59	H	-7.503226	5.359149	0.392436

Table D.14: Cartesian coordinates for the *cis* isomer of 269/56 predicted by NMR. Optimised at the B3LYP/6-31G(dp) level of theory.

Atom Number	Atom	X Coordinate	Y Coordinate	Z Coordinate
1	C	3.976557	0.530221	-1.311516
2	C	4.856866	-0.440303	-0.896454
3	C	4.635244	-1.057691	0.349784
4	C	3.580334	-0.709943	1.161004
5	C	2.670314	0.294641	0.750395
6	C	2.850501	0.939244	-0.527114
7	C	1.938831	1.940385	-0.940066
8	C	0.852257	2.285893	-0.156756
9	C	0.679549	1.684250	1.121353
10	C	1.566345	0.731760	1.549811
11	N	0.074517	3.410948	-0.528454
12	N	-1.184771	3.448720	-0.518365
13	C	-2.062930	2.366269	-0.407168
14	C	-3.397378	2.739276	-0.041985
15	C	-4.386217	1.760235	0.038993
16	C	-4.094927	0.427400	-0.286781
17	C	-2.799776	0.059043	-0.714404
18	C	-1.812883	1.023739	-0.760505
19	N	-5.161513	-0.464780	-0.173488
20	H	-6.032045	-0.066961	0.155346
21	C	-5.275164	-1.810502	-0.404794
22	N	-4.218488	-2.509305	-0.858749
23	C	-4.488404	-3.795960	-1.037068
24	N	-5.618795	-4.435678	-0.829139
25	C	-6.607992	-3.623855	-0.372577
26	N	-6.492389	-2.309142	-0.143507
27	S	4.319906	1.234042	-2.927008
28	O	3.095384	1.289409	-3.717464
29	O	5.526157	0.619368	-3.478084
30	O	4.716561	2.755054	-2.448130
31	H	5.415022	3.068129	-3.050765
32	S	5.773353	-2.321342	0.900588
33	O	7.097766	-2.073876	0.328699
34	O	5.579315	-2.506739	2.330541
35	O	5.178632	-3.628015	0.108842
36	H	5.933213	-4.011180	-0.371653
37	S	1.243378	0.051445	3.184303
38	O	1.289208	-1.410897	3.151001
39	O	0.095998	0.746758	3.751948

Continued on following page

Table D.14 – continued from previous page

Atom Number	Atom	X Coordinate	Y Coordinate	Z Coordinate
40	O	2.604149	0.561261	3.946606
41	H	2.846586	-0.133091	4.585979
42	H	5.706288	-0.711163	-1.511928
43	H	2.069545	2.445136	-1.888100
44	H	-0.140126	1.984979	1.762384
45	H	3.449288	-1.220641	2.105187
46	H	-0.832455	0.741332	-1.120842
47	H	-2.597465	-0.960513	-1.005334
48	H	-5.381761	2.058908	0.339938
49	N	-3.616249	4.081250	0.235165
50	H	-2.795205	4.647555	0.044416
51	C	-4.822540	4.700196	0.553803
52	O	-5.883246	4.110570	0.712890
53	N	-4.713160	6.061771	0.669923
54	H	-3.834967	6.553402	0.665571
55	H	-5.537286	6.549767	0.978792
56	Cl	-3.154916	-4.767664	-1.627107
57	N	-7.799487	-4.204240	-0.138219
58	H	-8.560196	-3.652490	0.221128
59	H	-7.899622	-5.194935	-0.284104

Table D.15: Cartesian coordinates for *trans* 273/5. Optimised at the B3LYP/6-31G(dp) level of theory. (Figure C.15)

Atom Number	Atom	X Coordinate	Y Coordinate	Z Coordinate
1	C	-6.669714	1.725789	2.426005
2	C	-7.949894	1.400521	2.806758
3	C	-8.447429	0.108712	2.522414
4	C	-7.688094	-0.822480	1.855241
5	C	-6.369856	-0.498724	1.452061
6	C	-5.817474	0.796389	1.739874
7	C	-4.494801	1.078146	1.337804
8	C	-3.727343	0.139821	0.660354
9	C	-4.298609	-1.138061	0.375712
10	C	-5.579611	-1.450063	0.757349
11	N	-2.389667	0.348838	0.280936
12	N	-2.056961	1.585391	0.258195
13	C	-0.758665	1.928072	-0.019834
14	C	0.375167	1.064691	-0.235261
15	C	1.620367	1.645835	-0.493140
16	C	1.783003	3.031457	-0.542221
17	C	0.674605	3.890108	-0.331411
18	C	-0.552778	3.332837	-0.075730
19	N	3.017858	3.632122	-0.793342
20	H	3.043469	4.642972	-0.821018
21	C	4.250876	3.062046	-0.997241
22	N	4.377336	1.745574	-0.976817
23	C	5.620504	1.276878	-1.180984
24	N	6.702384	2.048220	-1.401370
25	C	6.424220	3.347741	-1.396192
26	N	5.260965	3.944004	-1.207438
27	Cl	7.787659	4.409201	-1.678481
28	N	5.692980	-0.081299	-1.146136
29	H	4.781844	-0.498720	-0.970454
30	C	6.762909	-0.972322	-1.301866
31	C	6.442427	-2.340874	-1.214210
32	C	7.428667	-3.305267	-1.356682
33	C	8.747859	-2.905646	-1.587602
34	C	9.078976	-1.551994	-1.663188
35	C	8.093177	-0.578758	-1.523860
36	S	10.027219	-4.145293	-1.784088
37	O	11.312293	-3.522260	-1.427456
38	O	9.562737	-5.381331	-1.131881
39	C	10.068233	-4.439939	-3.551630
40	H	10.401423	-3.588927	-4.137691
41	C	9.770021	-5.637199	-4.043999
42	H	9.840314	-5.838885	-5.108554
43	H	9.458390	-6.442913	-3.386488
44	S	-6.123474	3.386111	2.845755
45	O	-7.240757	4.094303	3.466224
46	O	-4.812119	3.316889	3.469323
47	O	-5.894487	4.049529	1.361226
48	H	-6.646788	4.643794	1.195819
49	S	-10.111542	-0.310216	3.017098
50	O	-10.491261	-1.540727	2.338770
51	O	-10.947751	0.888164	2.968648
52	O	-9.864121	-0.649983	4.604779
53	H	-10.525878	-0.141693	5.105912
54	S	-3.305458	-2.319988	-0.537081
55	O	-3.069929	-1.857887	-1.901689
56	O	-2.199119	-2.766966	0.308658
57	O	-4.336037	-3.592977	-0.639491

Continued on following page

Table D.15 – continued from previous page

Atom Number	Atom	X Coordinate	Y Coordinate	Z Coordinate
58	H	-4.581548	-3.670029	-1.578132
59	H	-8.572397	2.133935	3.306116
60	H	-4.032284	2.028815	1.563837
61	H	-5.995928	-2.424647	0.535633
62	H	-8.101713	-1.800439	1.632419
63	H	-1.424414	3.954211	0.097468
64	H	0.798387	4.968276	-0.365703
65	H	2.461417	0.999009	-0.648098
66	N	0.220712	-0.305966	-0.171887
67	H	-0.736341	-0.604792	0.013789
68	C	1.212777	-1.294874	-0.317497
69	O	2.401025	-1.071440	-0.543983
70	N	0.718052	-2.552152	-0.174519
71	H	1.376074	-3.304868	-0.286995
72	H	-0.262162	-2.758618	-0.026375
73	H	5.412961	-2.634873	-1.027354
74	H	7.190837	-4.359895	-1.272979
75	H	10.113503	-1.260570	-1.809655
76	H	8.341602	0.471492	-1.577662

Table D.16: Cartesian coordinates for *cis* 273/5. Optimised at the B3LYP/6-31G(dp) level of theory. (Figure C.16)

Atom Number	Atom	X Coordinate	Y Coordinate	Z Coordinate
1	C	5.300771	-1.529784	-1.403098
2	C	6.363026	-2.383184	-1.217542
3	C	7.454187	-1.963929	-0.424888
4	C	7.485597	-0.714684	0.148675
5	C	6.401673	0.175928	-0.039050
6	C	5.262025	-0.219160	-0.819927
7	C	4.191768	0.690087	-0.972194
8	C	4.230730	1.951435	-0.393885
9	C	5.381930	2.337462	0.358088
10	C	6.427573	1.469464	0.544458
11	N	3.300875	2.948535	-0.774564
12	N	2.055291	2.894968	-0.625613
13	C	1.346783	2.000443	0.179364
14	C	-0.048340	1.922270	-0.118384
15	C	-0.882817	1.102687	0.640351
16	C	-0.366689	0.401982	1.733642
17	C	0.998746	0.532899	2.082765
18	C	1.833353	1.313029	1.312635
19	N	-1.150955	-0.428169	2.537477
20	H	-0.686408	-0.900508	3.301890
21	C	-2.486115	-0.732226	2.464851
22	N	-3.241214	-0.197745	1.515855
23	C	-4.535783	-0.563808	1.536205
24	N	-5.083088	-1.406186	2.432097
25	C	-4.207498	-1.860722	3.322204
26	N	-2.919717	-1.592455	3.422032
27	Cl	-4.853976	-2.962034	4.519336
28	N	-5.275253	0.003999	0.543950
29	H	-4.709343	0.607153	-0.045282
30	C	-6.632493	-0.091618	0.206112
31	C	-7.041697	0.647884	-0.920404

Continued on following page

Table D.16 – continued from previous page

Atom Number	Atom	X Coordinate	Y Coordinate	Z Coordinate
32	C	-8.364018	0.623431	-1.337228
33	C	-9.290938	-0.144516	-0.627309
34	C	-8.899072	-0.873469	0.496097
35	C	-7.572538	-0.854563	0.918773
36	S	-11.002203	-0.181002	-1.159290
37	O	-11.822476	-0.558011	0.003309
38	O	-11.263747	1.052949	-1.919364
39	C	-11.066275	-1.556511	-2.306642
40	H	-10.886748	-2.525629	-1.851299
41	C	-11.378423	-1.358518	-3.582676
42	H	-11.468862	-2.191716	-4.272974
43	H	-11.559785	-0.356421	-3.958936
44	S	3.950531	-2.161866	-2.404775
45	O	4.326294	-3.480550	-2.908686
46	O	2.693637	-1.928480	-1.711218
47	O	3.963507	-1.130401	-3.682427
48	H	4.378895	-1.599446	-4.426688
49	S	8.831831	-3.073250	-0.185017
50	O	9.939725	-2.310657	0.371594
51	O	8.992282	-3.913180	-1.371062
52	O	8.220855	-4.038063	0.996877
53	H	8.375592	-4.956585	0.714366
54	S	5.367408	3.969534	1.107647
55	O	5.722678	5.002432	0.138768
56	O	4.164977	4.061274	1.922863
57	O	6.656164	3.833396	2.123661
58	H	7.269155	4.545497	1.870728
59	H	6.364724	-3.359902	-1.687388
60	H	3.318286	0.414107	-1.547832
61	H	7.276452	1.762023	1.150257
62	H	8.344050	-0.410701	0.738453
63	H	2.863488	1.443460	1.615271
64	H	1.385055	0.030239	2.964527
65	H	-1.921200	1.025235	0.379903
66	N	-0.517975	2.677725	-1.185976
67	H	0.209130	3.244823	-1.609613
68	C	-1.820817	2.790903	-1.659703
69	O	-2.772451	2.118351	-1.278536
70	N	-1.938890	3.721667	-2.670725
71	H	-2.891923	3.930656	-2.926487
72	H	-1.286257	4.488525	-2.740332
73	H	-6.312560	1.246500	-1.460144
74	H	-8.687279	1.206000	-2.192747
75	H	-9.638891	-1.438483	1.052870
76	H	-7.262038	-1.412997	1.789942

Table D.17: Cartesian coordinates for *trans* 273/6. Optimised at the B3LYP/6-31G(dp) level of theory. (Figure C.17)

Atom Number	Atom	X Coordinate	Y Coordinate	Z Coordinate
0	C	6.184426	1.431672	0.157219
1	C	7.532002	1.166085	0.208293
2	C	7.974586	-0.173847	0.128846
3	C	7.087443	-1.218030	0.022279
4	C	5.696278	-0.958635	-0.029143
5	C	5.204533	0.390386	0.027092
6	C	3.812837	0.612321	-0.029227
7	C	2.913661	-0.441039	-0.136383
8	C	3.423398	-1.774573	-0.188904
9	C	4.771639	-2.028332	-0.139653
10	N	1.516733	-0.282587	-0.157647
11	N	1.148523	0.921267	-0.398884
12	C	-0.182385	1.244438	-0.392848
13	C	-1.315428	0.408181	-0.075975
14	C	-2.601757	0.955546	-0.142961
15	C	-2.791530	2.298978	-0.484027
16	C	-1.682752	3.133633	-0.776996
17	C	-0.420848	2.602376	-0.731962
18	N	-4.042152	2.896472	-0.504450
19	H	-4.058301	3.908217	-0.508421
20	C	-5.318450	2.376724	-0.401555
21	N	-5.540009	1.077633	-0.543213
22	C	-6.840323	0.707820	-0.428497
23	N	-7.847742	1.579708	-0.145531
24	C	-7.465835	2.835123	-0.058421
25	N	-6.247963	3.336761	-0.181376
26	Cl	-8.736848	4.004439	0.263979
27	N	-7.185464	-0.585317	-0.621720
28	C	-8.608252	-0.963321	-0.537921
29	H	-9.204218	-0.179966	-1.011578
30	H	-8.735211	-1.887699	-1.108097
31	C	-9.114528	-1.190632	0.902131
32	H	-8.877818	-0.285898	1.481760
33	O	-8.543399	-2.339790	1.503394
34	H	-7.578344	-2.223609	1.588767
35	C	-10.626627	-1.394032	0.902317
36	H	-11.146214	-0.513423	0.512948
37	H	-10.970076	-1.580916	1.922679
38	H	-10.897108	-2.263173	0.292544
39	C	-6.226741	-1.563612	-1.153028
40	H	-6.513797	-1.800954	-2.187836
41	H	-5.247290	-1.087713	-1.177272
42	C	-6.141948	-2.874142	-0.349640
43	H	-7.129928	-3.343610	-0.318741
44	O	-5.823456	-2.631468	1.015391
45	H	-4.920143	-2.262924	1.063087
46	C	-5.154724	-3.842485	-1.005683
47	H	-5.108119	-4.766854	-0.423640
48	H	-4.150330	-3.409588	-1.048977
49	H	-5.463329	-4.096029	-2.025587
50	S	5.720450	3.165838	0.251003
51	O	6.933766	3.956403	0.445773
52	O	4.765567	3.465415	-0.803537
53	O	4.881205	3.211096	1.661439
54	H	5.457363	3.631274	2.323247
55	S	9.725789	-0.517399	0.195680
56	O	9.901256	-1.947485	0.401697

Continued on following page

Table D.17 – continued from previous page

Atom Number	Atom	X Coordinate	Y Coordinate	Z Coordinate
57	O	10.382759	0.472414	1.047814
58	O	10.147700	-0.162319	-1.351883
59	H	10.912005	0.438322	-1.302182
60	S	2.249695	-3.118532	-0.365936
61	O	1.462772	-3.226927	0.862908
62	O	1.597803	-3.077722	-1.671473
63	O	3.250220	-4.418541	-0.376382
64	H	3.202436	-4.792460	-1.273743
65	H	8.242149	1.976877	0.322945
66	H	3.403777	1.612739	-0.001703
67	H	5.140773	-3.045388	-0.180873
68	H	7.454230	-2.238332	-0.017106
69	H	0.452230	3.204711	-0.957478
70	H	-1.839156	4.174704	-1.041966
71	H	-3.450158	0.339271	0.093692
72	N	-1.079578	-0.901045	0.307025
73	H	-0.092875	-1.164762	0.287684
74	C	-2.015576	-1.837570	0.744299
75	O	-3.226663	-1.604327	0.811787
76	O	-1.477667	-3.033019	1.085193
77	O	-2.114909	-3.729800	1.434086
78	O	-0.483739	-3.228275	1.053083

Table D.18: Cartesian coordinates for *cis* 273/6. Optimised at the B3LYP/6-31G(dp) level of theory. (Figure C.18)

Atom Number	Atom	X Coordinate	Y Coordinate	Z Coordinate
0	C	-4.465928	-1.344674	1.162743
1	C	-5.570550	-2.150570	1.016954
2	C	-6.628559	-1.723411	0.184768
3	C	-6.586070	-0.515214	-0.469617
4	C	-5.454590	0.325069	-0.329069
5	C	-4.349225	-0.079394	0.496564
6	C	-3.230560	0.778587	0.614583
7	C	-3.185510	1.987125	-0.063376
8	C	-4.302249	2.384624	-0.856289
9	C	-5.399504	1.577094	-0.995547
10	N	-2.211959	2.985160	0.220715
11	N	-0.958343	2.824819	0.258802
12	C	-0.230434	1.760142	-0.244947
13	C	1.120152	1.689150	0.234706
14	C	1.990507	0.711161	-0.243800
15	C	1.547264	-0.187894	-1.221226
16	C	0.234144	-0.083118	-1.749612
17	C	-0.629887	0.869331	-1.268998
18	N	2.330821	-1.222836	-1.701463
19	H	1.848051	-1.970377	-2.183536
20	C	3.673295	-1.513721	-1.539057
21	N	4.516662	-0.598012	-1.083351
22	C	5.805792	-1.012811	-0.990271
23	N	6.210279	-2.279451	-1.283179
24	C	5.256087	-3.059816	-1.741654
25	N	3.976075	-2.775331	-1.922032
26	Cl	5.737599	-4.691318	-2.173382
27	N	6.763262	-0.137418	-0.609157

Continued on following page

Table D.18 – continued from previous page

Atom Number	Atom	X Coordinate	Y Coordinate	Z Coordinate
28	C	8.164528	-0.594925	-0.550888
29	H	8.353729	-1.244363	-1.408534
30	H	8.801285	0.289584	-0.639277
31	C	8.526470	-1.344629	0.748389
32	H	7.804617	-2.166045	0.867957
33	O	8.518028	-0.495873	1.884038
34	H	7.616157	-0.158468	2.037092
35	C	9.930202	-1.932650	0.642899
36	H	9.997137	-2.655735	-0.175408
37	H	10.186931	-2.436546	1.577819
38	H	10.667074	-1.139453	0.475271
39	C	6.487761	1.300997	-0.496539
40	H	6.987649	1.814655	-1.330604
41	H	5.413622	1.442778	-0.611770
42	C	6.952790	1.935155	0.826306
43	H	8.028402	1.774725	0.945173
44	O	6.373623	1.279745	1.949869
45	H	5.414584	1.450481	1.947766
46	C	6.671892	3.439277	0.831232
47	H	7.008433	3.871271	1.777496
48	H	5.601421	3.638886	0.720650
49	H	7.201666	3.945256	0.017141
50	S	-3.159308	-1.984516	2.216207
51	O	-1.884814	-1.849947	1.527411
52	O	-3.603044	-3.252300	2.789060
53	O	-3.132838	-0.882109	3.434406
54	H	-3.585686	-1.284590	4.195714
55	S	-8.063884	-2.771201	0.002648
56	O	-8.266587	-3.534963	1.232814
57	O	-9.131827	-1.984518	-0.596006
58	O	-7.493579	-3.825492	-1.121602
59	H	-7.743291	-4.717073	-0.820808
60	S	-4.229075	3.934749	-1.763835
61	O	-5.554510	4.241282	-2.278013
62	O	-3.067469	3.858590	-2.647036
63	O	-3.939168	4.976542	-0.559648
64	H	-3.138093	4.622554	-0.089985
65	H	-5.630629	-3.094918	1.545401
66	H	-2.391272	0.492999	1.234216
67	H	-6.231154	1.904962	-1.610891
68	H	-7.420626	-0.202451	-1.088462
69	H	-1.609571	0.973106	-1.715669
70	H	-0.075090	-0.744688	-2.552799
71	H	2.993033	0.644841	0.140011
72	N	1.472172	2.615834	1.211618
73	H	0.739653	3.301116	1.371954
74	C	2.677207	2.744369	1.874721
75	O	3.648785	2.016446	1.673712
76	N	2.715103	3.785906	2.765179
77	H	1.870749	4.200853	3.128408
78	H	3.526870	3.809091	3.363013

Table D.19: Cartesian coordinates for *trans* 273/8. Optimised at the B3LYP/6-31G(dp) level of theory. (Figure C.19)

Atom Number	Atom	X Coordinate	Y Coordinate	Z Coordinate
0	C	5.569355	-1.475424	0.359970
1	C	6.927975	-1.279458	0.433850
2	C	7.452185	0.013357	0.208887
3	C	6.635978	1.074927	-0.101485
4	C	5.235486	0.885917	-0.186768
5	C	4.658723	-0.408383	0.054131
6	C	3.258143	-0.556118	-0.024920
7	C	2.432164	0.514133	-0.344344
8	C	3.026694	1.789862	-0.589086
9	C	4.384831	1.973011	-0.513554
10	N	1.030516	0.432069	-0.391435
11	N	0.599661	-0.768106	-0.528211
12	C	-0.746235	-1.019775	-0.517698
13	C	-1.839735	-0.103296	-0.289115
14	C	-3.154573	-0.594337	-0.316256
15	C	-3.404986	-1.947157	-0.567468
16	C	-2.334745	-2.851334	-0.798707
17	C	-1.049044	-2.384669	-0.764048
18	N	-4.679974	-2.492139	-0.637824
19	H	-4.740785	-3.441037	-0.983711
20	C	-5.930360	-1.993917	-0.340410
21	N	-6.076056	-0.804069	0.223719
22	C	-7.361333	-0.446934	0.464705
23	N	-8.436623	-1.218100	0.148043
24	C	-8.121841	-2.373548	-0.397324
25	N	-6.922324	-2.856169	-0.674667
26	Cl	-9.473065	-3.417729	-0.813705
27	N	-7.596941	0.740775	1.057892
28	C	-8.947707	1.250810	1.304359
29	C	-9.067418	2.658642	0.713682
30	O	-8.057898	3.523484	1.212203
31	C	-6.756946	3.029215	0.903725
32	C	-6.531438	1.643358	1.504604
33	S	5.000394	-3.150963	0.674748
34	O	6.170104	-4.002834	0.878436
35	O	3.898505	-3.114768	1.622309
36	O	4.349795	-3.563011	-0.775598
37	H	4.981576	-4.161318	-1.210634
38	S	9.217520	0.263023	0.302462
39	O	9.526168	1.558047	-0.285888
40	O	9.902086	-0.959076	-0.117044
41	O	9.411612	0.377353	1.929773
42	H	10.121290	-0.243773	2.170272
43	S	1.946410	3.148318	-1.039704
44	O	1.322065	2.908244	-2.337201
45	O	1.146692	3.526712	0.124384
46	O	3.029540	4.362942	-1.254121
47	H	3.035793	4.556176	-2.207927
48	H	7.587445	-2.112672	0.647331
49	H	2.783432	-1.505593	0.179766
50	H	4.818196	2.947790	-0.699252
51	H	7.066391	2.053220	-0.288101
52	H	-0.204766	-3.045638	-0.925239
53	H	-2.540203	-3.900764	-0.986454
54	H	-3.971687	0.085646	-0.153395
55	N	-1.540463	1.221228	-0.047270
56	H	-0.540813	1.427495	-0.074603

Continued on following page

Table D.19 – continued from previous page

Atom Number	Atom	X Coordinate	Y Coordinate	Z Coordinate
57	C	-2.431550	2.273512	0.217178
58	O	-3.653182	2.152865	0.255132
59	N	-1.799787	3.455905	0.443332
60	H	-2.396432	4.255490	0.575336
61	H	-0.802227	3.590993	0.332513
62	H	-9.115798	1.294756	2.388814
63	H	-9.673467	0.569636	0.862443
64	H	-10.028245	3.101747	0.991171
65	H	-9.013449	2.598849	-0.385872
66	H	-6.038461	3.738237	1.320110
67	H	-6.609150	2.986313	-0.186188
68	H	-5.561134	1.255778	1.208698
69	H	-6.576319	1.710236	2.600255

Table D.20: Cartesian coordinates for *cis* 273/8. Optimised at the B3LYP/6-31G(dp) level of theory. (Figure C.20)

Atom Number	Atom	X Coordinate	Y Coordinate	Z Coordinate
0	C	-3.867047	-1.328639	1.207095
1	C	-4.944248	-2.173788	1.080229
2	C	-6.011676	-1.805283	0.232152
3	C	-6.006216	-0.614543	-0.454932
4	C	-4.904052	0.266483	-0.332935
5	C	-3.788632	-0.079244	0.506155
6	C	-2.699501	0.817926	0.605118
7	C	-2.693806	2.011338	-0.101020
8	C	-3.820530	2.350391	-0.906973
9	C	-4.888842	1.502587	-1.030500
10	N	-1.758030	3.049440	0.163559
11	N	-0.499440	2.932669	0.214614
12	C	0.262782	1.883298	-0.266894
13	C	1.610677	1.850209	0.227246
14	C	2.506756	0.879857	-0.228421
15	C	2.099019	-0.022613	-1.217781
16	C	0.789916	0.054849	-1.765433
17	C	-0.104234	0.980921	-1.293096
18	N	2.907555	-1.024876	-1.728543
19	H	2.462548	-1.682498	-2.356055
20	C	4.236257	-1.346098	-1.540456
21	N	5.027912	-0.582331	-0.801311
22	C	6.308016	-1.021478	-0.709198
23	N	6.767851	-2.152538	-1.307552
24	C	5.858916	-2.793626	-2.011104
25	N	4.587067	-2.479507	-2.194395
26	Cl	6.401798	-4.257360	-2.813943
27	N	7.185794	-0.297843	0.015185
28	C	8.581585	-0.702331	0.202542
29	C	8.913467	-0.690115	1.697072
30	O	8.624464	0.569361	2.287031
31	C	7.246639	0.899513	2.143282
32	C	6.840821	0.965919	0.672021
33	S	-2.545624	-1.895730	2.283324
34	O	-1.273895	-1.750619	1.591882
35	O	-2.955890	-3.155232	2.898552
36	O	-2.552933	-0.752542	3.462961

Continued on following page

Table D.20 – continued from previous page

Atom Number	Atom	X Coordinate	Y Coordinate	Z Coordinate
37	H	-2.991924	-1.142773	4.238557
38	S	-7.408860	-2.906512	0.071811
39	O	-7.586972	-3.648635	1.319079
40	O	-8.501871	-2.172111	-0.547392
41	O	-6.804476	-3.968422	-1.027428
42	H	-6.996113	-4.860308	-0.687832
43	S	-3.795989	3.880323	-1.850413
44	O	-5.129509	4.132067	-2.373979
45	O	-2.631254	3.821209	-2.731228
46	O	-3.541436	4.958303	-0.670909
47	H	-2.734343	4.635611	-0.187119
48	H	-4.976807	-3.103724	1.635955
49	H	-1.852839	0.577143	1.233771
50	H	-5.728389	1.786834	-1.656665
51	H	-6.848176	-0.346494	-1.084618
52	H	-1.081279	1.060185	-1.750734
53	H	0.506987	-0.611122	-2.574930
54	H	3.499615	0.828740	0.181628
55	N	1.938167	2.811565	1.171655
56	H	1.170550	3.451213	1.350739
57	C	3.141228	3.006620	1.838998
58	O	4.101781	2.249774	1.781307
59	N	3.132263	4.130151	2.637362
60	H	2.522019	4.905982	2.427003
61	H	4.033602	4.369071	3.021983
62	H	9.229219	0.013992	-0.320697
63	H	8.728388	-1.690962	-0.229776
64	H	9.981854	-0.870410	1.845912
65	H	8.348824	-1.489470	2.204332
66	H	7.099376	1.873437	2.615266
67	H	6.618502	0.161192	2.666002
68	H	5.776712	1.160288	0.578539
69	H	7.396876	1.774653	0.178230

Table D.21: Cartesian coordinates for *trans* 273/13. Optimised at the B3LYP/6-31G(dp) level of theory. (Figure C.21)

Atom Number	Atom	X Coordinate	Y Coordinate	Z Coordinate
0	C	-5.378827	1.407926	0.374823
1	C	-6.7307	1.173355	0.458743
2	C	-7.219942	-0.133143	0.234028
3	C	-6.376035	-1.170222	-0.085721
4	C	-4.982482	-0.941222	-0.181857
5	C	-4.440252	0.368353	0.058073
6	C	-3.045628	0.556451	-0.032596
7	C	-2.191193	-0.488858	-0.362386
8	C	-2.752404	-1.780192	-0.606489
9	C	-4.103965	-2.002485	-0.51943
10	H	-7.411571	1.987116	0.679853
11	H	-2.596498	1.518749	0.16994
12	H	-4.511071	-2.988646	-0.704532
13	H	-6.779732	-2.159963	-0.271729
14	N	-0.794502	-0.367436	-0.422717
15	N	-0.398583	0.846798	-0.557905
16	C	0.937224	1.137468	-0.561126
17	C	2.061082	0.254447	-0.342592
18	C	3.359969	0.779065	-0.393948
19	C	3.573083	2.139473	-0.651808
20	C	2.470834	3.011572	-0.866906
21	C	1.199753	2.510361	-0.813653
22	H	0.335652	3.147554	-0.965596
23	H	2.644437	4.065888	-1.059274
24	H	4.197747	0.121878	-0.245457
25	N	1.798877	-1.077507	-0.089668
26	H	0.804951	-1.311075	-0.117562
27	C	2.713713	-2.096532	0.207585
28	O	3.930722	-1.937398	0.278408
29	N	2.115632	-3.297601	0.427787
30	H	2.733614	-4.075665	0.586367
31	H	1.125408	-3.465429	0.296809
32	S	-4.854867	3.097122	0.693496
33	O	-6.046824	3.916181	0.903669
34	O	-3.749684	3.087988	1.63787
35	O	-4.219995	3.532388	-0.757023
36	H	-4.869198	4.114698	-1.188041
37	S	-8.976166	-0.433123	0.341095
38	O	-9.253311	-1.73486	-0.248274
39	O	-9.698742	0.770219	-0.069059
40	O	-9.155585	-0.557968	1.969617
41	H	-9.877346	0.046123	2.217271
42	S	-1.638888	-3.105795	-1.073211
43	O	-1.031987	-2.84324	-2.374646
44	O	-0.819716	-3.470028	0.082005
45	O	-2.689798	-4.349353	-1.285613
46	H	-2.702859	-4.533023	-2.241191
47	N	4.824316	2.723464	-0.747054
48	H	4.846195	3.671988	-1.099765
49	C	6.113172	2.282326	-0.491133
50	N	6.26985	1.076045	0.093646
51	C	7.529995	0.71584	0.319923
52	N	8.550157	1.543102	-0.035215
53	C	8.338606	2.831714	-0.635409
54	N	7.034299	3.160768	-0.860131
55	O	9.319124	3.508125	-0.884628
56	N	7.794812	-0.478529	0.899547

Continued on following page

Table D.21 – continued from previous page

Atom Number	Atom	X Coordinate	Y Coordinate	Z Coordinate
57	C	9.139983	-1.01072	1.123071
58	C	9.16079	-2.507614	0.782625
59	O	8.169395	-3.222221	1.491302
60	C	6.866611	-2.732791	1.169615
61	C	6.726756	-1.26345	1.543127
62	H	9.432009	-0.863176	2.172157
63	H	9.870596	-0.508122	0.485827
64	H	10.12842	-2.934211	1.062229
65	H	9.023452	-2.628243	-0.304571
66	H	6.151918	-3.330249	1.738102
67	H	6.657175	-2.867753	0.098956
68	H	5.75867	-0.885755	1.22838
69	H	6.826886	-1.15053	2.631675
70	H	9.516258	1.347457	0.181671

Table D.22: Cartesian coordinates for *cis* 273/13. Optimised at the B3LYP/6-31G(dp) level of theory. (Figure C.22)

Atom Number	Atom	X Coordinate	Y Coordinate	Z Coordinate
0	C	-3.808655	-1.368615	1.112031
1	C	-4.93016	-2.142318	0.926322
2	C	-5.976671	-1.653334	0.113828
3	C	-5.907089	-0.415171	-0.479993
4	C	-4.758886	0.392963	-0.296817
5	C	-3.662129	-0.075768	0.506831
6	C	-2.525228	0.750217	0.665963
7	C	-2.455747	1.993279	0.05411
8	C	-3.564814	2.453362	-0.716012
9	C	-4.677852	1.67651	-0.89747
10	H	-5.012256	-3.10863	1.410115
11	H	-1.690616	0.415443	1.26714
12	H	-5.502212	2.052371	-1.494943
13	H	-6.733637	-0.054274	-1.083149
14	N	-1.463737	2.953519	0.390719
15	N	-0.211071	2.765929	0.41334
16	C	0.490155	1.729463	-0.169596
17	C	1.848711	1.600457	0.282242
18	C	2.690197	0.633376	-0.268872
19	C	2.223565	-0.172263	-1.317319
20	C	0.903589	0.004631	-1.81956
21	C	0.061215	0.924279	-1.252483
22	H	-0.922281	1.077841	-1.675753
23	H	0.573134	-0.582692	-2.670838
24	H	3.687598	0.505133	0.110939
25	N	2.235301	2.471209	1.292036
26	H	1.492508	3.11726	1.540981
27	C	3.46812	2.59811	1.914813
28	O	4.42101	1.847222	1.741022
29	N	3.508913	3.641237	2.814503
30	H	2.884928	4.428974	2.722848
31	H	4.429441	3.843859	3.172874
32	S	-2.523739	-2.082667	2.144058
33	O	-1.240826	-1.947663	1.471734
34	O	-2.999565	-3.364273	2.658241
35	O	-2.483114	-1.035885	3.409894

Continued on following page

Table D.22 – continued from previous page

Atom Number	Atom	X Coordinate	Y Coordinate	Z Coordinate
36	H	-2.955882	-1.458953	4.147412
37	S	-7.431855	-2.660957	-0.122112
38	O	-7.65204	-3.481587	1.068111
39	O	-8.482867	-1.82452	-0.682103
40	O	-6.886447	-3.67168	-1.297966
41	H	-7.131101	-4.573536	-1.025397
42	S	-3.457939	4.045855	-1.542161
43	O	-4.777994	4.41237	-2.031527
44	O	-2.30483	3.987678	-2.438275
45	O	-3.133513	5.014868	-0.287785
46	H	-2.347529	4.605328	0.165692
47	N	2.96701	-1.161391	-1.930393
48	H	2.472736	-1.742544	-2.596106
49	C	4.284118	-1.584775	-1.821872
50	N	5.118663	-0.884037	-1.024587
51	C	6.365952	-1.345479	-0.9688
52	N	6.719589	-2.44312	-1.689523
53	C	5.803071	-3.149359	-2.541782
54	N	4.531764	-2.654863	-2.561116
55	O	6.228222	-4.104138	-3.163798
56	N	7.280103	-0.724553	-0.186672
57	C	8.659383	-1.179731	-0.001706
58	C	9.04806	-1.051097	1.478016
59	O	8.836719	0.258641	1.965769
60	C	7.462058	0.624635	1.852194
61	C	7.008352	0.5989	0.398709
62	H	9.337777	-0.574617	-0.618916
63	H	8.770249	-2.226738	-0.290768
64	H	10.112399	-1.271892	1.598666
65	H	8.46812	-1.781598	2.065495
66	H	7.364164	1.634668	2.253717
67	H	6.834434	-0.050525	2.452759
68	H	5.947684	0.817525	0.328295
69	H	7.570252	1.350502	-0.173098
70	H	7.666943	-2.788033	-1.735815

Table D.23: Cartesian coordinates for *trans* 283/26 **A**. Optimised at the B3LYP/6-31G(d,p) level of theory. (Figure C.23)

Atom Number	Atom	X Coordinate	Y Coordinate	Z Coordinate
1	C	-2.987408	1.995847	0.183505
2	C	-4.334225	2.264866	0.087115
3	C	-5.244776	1.20797	-0.120999
4	C	-4.803489	-0.091831	-0.216404
5	C	-3.422285	-0.401789	-0.118958
6	C	-2.470518	0.662034	0.073791
7	C	-1.090419	0.366698	0.138694
8	C	-0.620286	-0.930905	0.015847
9	C	-1.548462	-1.993786	-0.125723
10	C	-2.894454	-1.731743	-0.194417
11	H	-4.690735	3.284064	0.159958
12	H	-0.363493	1.154196	0.273285
13	H	-1.176259	-3.009246	-0.18998
14	H	-5.518129	-0.886118	-0.388022
15	H	-6.303308	1.428786	-0.207653
16	N	0.735667	-1.304467	0.049552
17	N	1.538048	-0.318861	-0.084191
18	C	2.883939	-0.583156	-0.01994
19	C	3.753848	0.531876	-0.219909
20	C	5.136016	0.345428	-0.155514
21	C	5.668767	-0.923932	0.096602
22	C	4.792825	-2.043513	0.283504
23	C	3.433816	-1.867469	0.226402
24	H	5.788206	1.195079	-0.302135
25	H	2.736867	-2.683826	0.362252
26	N	3.157435	1.764128	-0.477486
27	H	2.145142	1.716433	-0.499407
28	C	3.757417	2.988147	-0.702686
29	O	4.968803	3.16306	-0.69678
30	C	2.782174	4.117531	-0.986534
31	H	2.866547	4.393003	-2.042831
32	H	3.084829	4.987684	-0.399656
33	H	1.738637	3.876881	-0.770461
34	O	5.445754	-3.227578	0.504699
35	C	4.652266	-4.393448	0.68145
36	H	5.351587	-5.21644	0.832966
37	H	4.036678	-4.594147	-0.20387
38	H	4.000806	-4.301685	1.558914
39	N	7.011328	-1.133296	0.196902
40	H	7.648827	-0.411241	-0.096053
41	H	7.344235	-2.083735	0.216924
42	S	-1.8344	3.332646	0.514877
43	O	-0.855948	3.413735	-0.564928
44	O	-1.389551	3.27908	1.908925
45	O	-2.806689	4.651403	0.388084
46	H	-2.834195	5.045653	1.277169
47	S	-3.962141	-3.160149	-0.397664
48	O	-4.889598	-2.932221	-1.496114
49	O	-3.148659	-4.372157	-0.317254
50	O	-4.871169	-3.10662	0.975035
51	H	-4.500939	-3.770369	1.581442

Table D.24: Cartesian coordinates for *cis* 283/26 **A**. Optimised at the B3LYP/6-31G(d,p) level of theory. (Figure C.24)

Atom Number	Atom	X Coordinate	Y Coordinate	Z Coordinate
1	C	3.90162	-0.877626	0.210889
2	C	4.952123	-0.028416	0.484695
3	C	4.793526	1.360652	0.314875
4	C	3.597019	1.874786	-0.13091
5	C	2.499766	1.024876	-0.425964
6	C	2.631917	-0.397786	-0.24634
7	C	1.528191	-1.243725	-0.522614
8	C	0.313801	-0.733963	-0.944379
9	C	0.181738	0.66412	-1.173341
10	C	1.238933	1.499307	-0.916025
11	H	5.89237	-0.442528	0.829169
12	H	1.611393	-2.312593	-0.383629
13	H	-0.752412	1.069114	-1.543523
14	H	3.490098	2.945476	-0.246146
15	N	-0.701705	-1.63546	-1.349805
16	N	-1.915572	-1.560708	-0.99639
17	C	-2.478152	-0.788851	0.011919
18	C	-3.91023	-0.773859	-0.012416
19	C	-4.621704	-0.072727	0.96069
20	C	-3.948292	0.589754	1.992788
21	C	-2.51979	0.538803	2.051262
22	C	-1.811367	-0.136173	1.085523
23	H	-0.7369	-0.19831	1.158182
24	H	-5.701529	-0.055471	0.909182
25	N	-4.527507	-1.472846	-1.048622
26	H	-3.852421	-1.962691	-1.628539
27	C	-5.871726	-1.618761	-1.318173
28	O	-6.764028	-1.0788	-0.677996
29	S	4.213227	-2.616731	0.505157
30	O	3.120167	-3.238871	1.255616
31	O	5.58853	-2.775432	0.963248
32	O	4.097058	-3.154887	-1.046959
33	H	3.817358	-4.0866	-1.003079
34	S	0.916872	3.24957	-1.151532
35	O	1.249563	3.961432	0.075108
36	O	-0.381934	3.408646	-1.803068
37	O	2.05839	3.683813	-2.253287
38	H	1.608739	3.749483	-3.113193
39	N	-4.611868	1.256244	2.976946
40	H	-5.594896	1.446507	2.872422
41	H	-4.076403	1.838684	3.600541
42	H	5.621369	2.025117	0.537641
43	O	-1.985219	1.20343	3.121491
44	C	-0.568854	1.322133	3.196473
45	H	-0.363235	1.913978	4.088797
46	H	-0.166415	1.838136	2.316315
47	H	-0.091183	0.340106	3.297063
48	C	-6.168585	-2.546442	-2.485709
49	H	-7.058243	-2.180967	-3.000542
50	H	-6.391662	-3.547463	-2.100925
51	H	-5.340865	-2.627269	-3.195308

Table D.25: Cartesian coordinates for 283/26 species **B**. Optimised at the B3LYP/6-31G(d,p) level of theory. (Figure C.25)

Atom Number	Atom	X Coordinate	Y Coordinate	Z Coordinate
1	C	3.022072	0.247928	2.549308
2	C	4.388976	0.403711	2.553577
3	C	5.060019	0.737451	1.356397
4	C	4.36275	0.922592	0.18599
5	C	2.947473	0.78408	0.153368
6	C	2.25059	0.42669	1.359032
7	C	0.841158	0.266635	1.328368
8	C	0.143092	0.51136	0.172716
9	C	0.791457	0.870543	-1.026473
10	C	2.159501	0.993532	-1.022581
11	S	2.242881	-0.124451	4.126098
12	O	1.067133	0.725095	4.277726
13	O	3.274435	-0.213684	5.151074
14	O	1.666246	-1.639525	3.864034
15	S	2.899149	1.391374	-2.617076
16	O	3.970586	0.445943	-2.884952
17	O	1.826181	1.629059	-3.579887
18	O	3.569955	2.844691	-2.262493
19	N	-1.296693	0.362849	0.156822
20	N	-1.737348	-0.479635	-0.784439
21	C	-3.040672	-0.683333	-0.857667
22	C	-3.544149	-1.578826	-1.850341
23	C	-4.88825	-1.818122	-1.906795
24	C	-5.808486	-1.168223	-0.966189
25	C	-5.31136	-0.284701	-0.002544
26	C	-3.946088	-0.026149	0.065974
27	N	-7.108842	-1.460959	-1.087336
28	O	-5.518526	-2.629226	-2.770478
29	C	-4.744208	-3.335053	-3.754766
30	N	-3.440695	0.850495	0.967226
31	C	-2.143928	1.053831	1.007027
32	C	-1.599187	2.078277	1.957487
33	H	4.939348	0.277301	3.478989
34	H	0.317844	-0.045005	2.220665
35	H	0.229092	1.040106	-1.936526
36	H	4.898398	1.17088	-0.720867
37	H	6.138476	0.852065	1.366819
38	H	2.216462	-2.25697	4.377854
39	H	3.2895	3.46985	-2.954926
40	H	-2.83871	-2.046166	-2.524606
41	H	-5.976741	0.212705	0.694059
42	H	-7.413135	-2.102178	-1.805172
43	H	-7.797916	-1.050835	-0.475573
44	H	-5.461911	-3.915807	-4.33121
45	H	-4.027108	-4.003591	-3.268943
46	H	-4.223291	-2.6294	-4.408909
47	H	-2.438188	2.687014	2.293424
48	H	-1.131935	1.621297	2.835456
49	H	-0.849417	2.712817	1.478798

Appendix E
Characterisation of 283/26 B

The work presented in this appendix was conducted by Dr. John Parkinson at Strathclyde University.

Structural confirmation of D304/71 from NMR data assignments

Introduction

In order to prove that reaction product **2** (D304/71) is formed from **1**, an NMR sample of pure **2** was prepared from material supplied by Dystar.

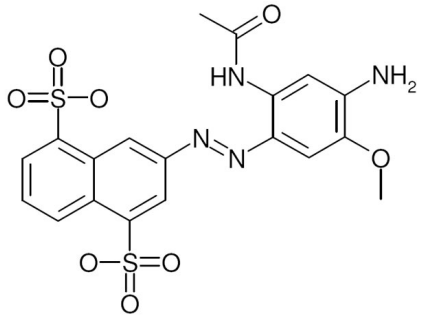

1

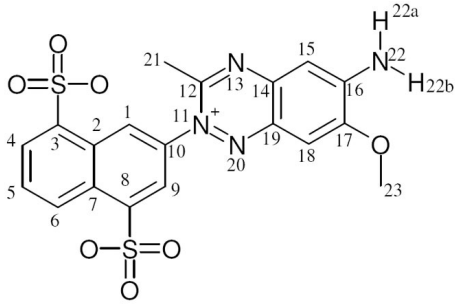

2

Experimental

Sample Preparation: For the purposes of allowing the accumulation of ^{15}N NMR data, a sample of D304/71 was prepared to provide adequate natural abundance ^{15}N for short-term acquisition of ^{15}N-related data. 29.93 mg of **2** were dissolved in 550 μL d_6-DMSO (Sigma-Aldrich, U.K.) to provide a final concentration of **2** at 114 mM. At this concentration, ^{15}N was present at a level of 0.42 mM (^{15}N at a natural abundance of 0.37%), allowing for ^{1}H-detected ^{15}N inverse experiments to be completed with a 1-2 hour experimental period. The sample was admitted to a 5 mm NMR tube (tube code: 535-PP, Wilmad Glass, NJ, USA).

Data acquisition: NMR data were acquired on a Bruker AVANCE400 NMR spectrometer operating at a proton resonance frequency of 400.13 MHz (field = 9.4 T) and equipped with an auto-tune broadband observation probe fitted with an actively

shielded z-gradient coil (BBFO-z-ATM). All data were accumulated under full automation using IconNMR under TOPSPIN (version 1.3, Bruker Biospin) running on a Hewlett Packard HP XW4100 personal computer operating under Windows XP. NMR data were acquired according to the following experimental protocols. 1D ^{1}H NMR spectra were acquired using a single pulse-acquire pulse sequence (zg30: d1-p1-aq) optimised for a 30° proton pulse (p1 = 4 μs), a relaxation delay d1 of 2 s. Data were acquired using 8 transients into 32 K data points (aq = 2 s) over a ^{1}H frequency width equivalent to 20 ppm centred at 6.175 ppm. 1D ^{13}C-{^{1}H} NMR data were acquired using a powergated decoupling pulse sequence (zgpg30: d1-p1-aq) where d1 = 0.7 s and p1 was optimised for a 30° carbon pulse (p1 = 2.6 μs). Data were acquired with 256 transients into 16 K data points over a ^{13}C frequency width equivalent to 238 ppm (aq = 0.3 s). 2D [^{1}H, ^{13}C] HSQC NMR data were acquired in a phase-sensitive mode with F2 sweep-width optimisation and gradient selection using a sensitivity improved, echo-antiecho pulse scheme (hsqcetgpsi). The evolution period was optimised for $^{1}J_{CH}$ = 145 Hz. Data were accumulated into 1 K data points over a ^{1}H [F2] frequency width equivalent to 8.90 ppm centred at 6.07 ppm with 2 transients for each of 256 t_1 increments for a ^{13}C [F1] frequency width equivalent to 165.7 ppm centred at 75 ppm. 2D [^{1}H, ^{13}C] HMBC NMR data were acquired without decoupling during acquisition in magnitude mode with F2 sweep-width optimisation and gradient selection using a low pass J-filter for suppression of one-bond ($^{1}J_{CH}$) couplings (hmbcgplpndqf). The evolution period was optimised for a long range $^{n>1}J_{CH}$ coupling of 7 Hz. Data were accumulated into 4 K data points over a ^{1}H [F2] frequency width equivalent to 8.30 ppm centred at 6.114 ppm with 8 transients for each of 128 t_1 increments for a ^{13}C [F1] frequency width equivalent to 222 ppm centred at 100 ppm. 2D [^{1}H, ^{15}N] HSQC NMR data were acquired in a phase-sensitive mode with F2 sweep-width optimisation and gradient selection using a sensitivity improved, echoantiecho pulse scheme (hsqcetgpsi). The evolution period was optimised either for $^{1}J_{NH}$ = 90 Hz or for $^{3}J_{NH}$ = 9 Hz (two separate data sets were acquired). Data were accumulated into 1 K data points over a ^{1}H [F2] frequency width equivalent to 8.45 ppm centred at 6.09 ppm with 8 transients for each of 128 t_1 increments for a ^{15}N [F1] frequency width equivalent to 400 ppm centred at 200 ppm. 2D [^{1}H, ^{15}N] HMBC NMR data were acquired without decoupling during acquisition in magnitude mode with F2 sweep-width optimisation and gradient selection using a low pass J-filter for suppression of one-bond ($^{1}J_{CH}$) couplings and optimised for a range of long range couplings (3-16 Hz) according to the CIGAR-HMBC protocol[1] (hmbcacgplpndqf). Data were accumulated into 1 K data points over a ^{1}H

[1]Hadden CE, Martin GE, Krishnamurthy VV. Constant time inverse-detection gradient accordion rescaled heteronuclear multiple bond correlation spectroscopy: CIGAR-HMBC *Magn. Reson. Chem.* **38**, 143-147, 2000.

[F2] frequency width equivalent to 8.45 ppm centred at 6.09 ppm with 16 transients for each of 128 t_1 increments for a ^{15}N [F1] frequency width equivalent to 400 ppm centred at 200 ppm. 2D [^1H, ^1H] NOESY NMR data were acquired phase-sensitive with an Echo-Antiecho-TPPI mode of acquisition and F2 frequency width optimisation using a standard pulse scheme (noesyetgp). Data were accumulated into 2 K data points over a ^1H [F2/F1] frequency width equivalent to 8.45 ppm centred at 6.09 ppm with 4 transients for each of 256 t_1 increments. A mixing time of 800 ms was used to allow for the evolution of the NOE response.

Results

The 1D ^1H NMR spectrum of **2** (Figure E.1) is labelled A-K.

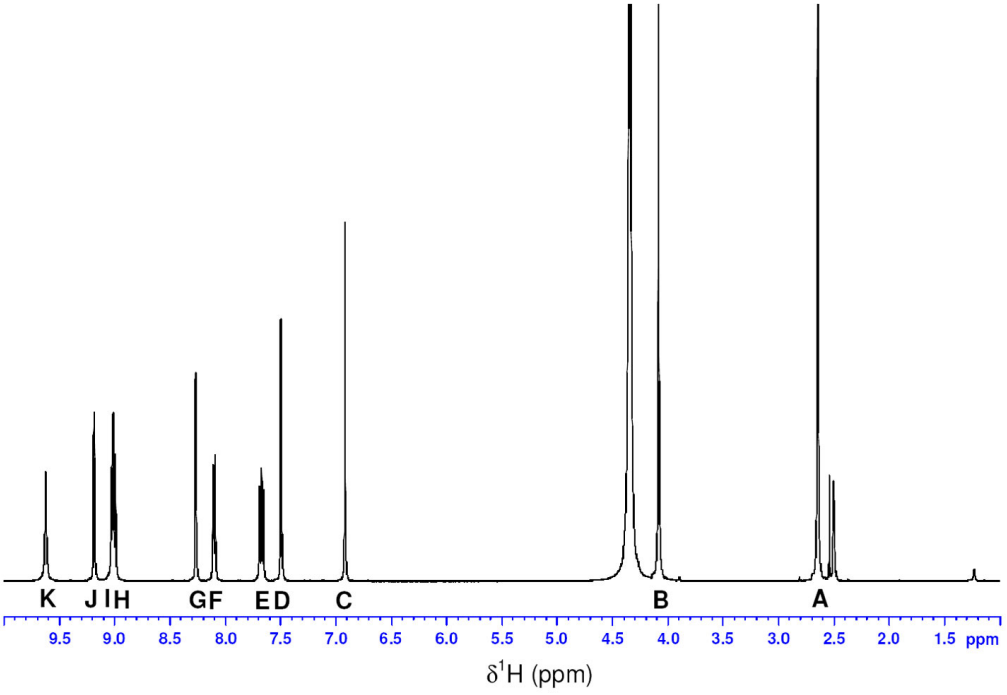

Figure E.1: ^1H NMR spectrum of **2** acquired at 400 MHz

A and **B** integrate to three proton equivalents each and correspond to methyl-21 (**A**) and methyl-23 (**B**). The remaining signals integrate to one proton equivalent each: **C/D** correspond to H-15 or H-18; **E** is assigned to H-5; **F/H** are assigned to H-4 or H-6; **G/J** correspond to H-1 or H-9; **I/K** are assigned to H-22a or H-22b. 2D [^1H, ^{13}C]HSQC NMR data allowed for the assignment of ^{13}C resonances associated with directly bonded H-C pairs (Table E.1) and 2D [^1H, ^{13}C] HMBC NMR data (Figure E.2) allowed for the assignment of quaternary carbon signals. Proton resonance **A** (H-21) showed $^3J_{HC}$ coupling to ^{13}C signal **r** (155.3 ppm) assigned to C-12. Proton resonance **B** (H-23) showed $^3J_{HC}$ coupling to ^{13}C signal **q** (154.3 ppm) assigned to C-17. Proton resonance

C (H-15 or H-18) also showed a strong $^{3}J_{HC}$ response to ^{13}C signal **q**. In the 2D [^{1}H, ^{15}N] HMBC data (Figure E.3), proton signal **C** (H-15) showed long-range responses to two ^{15}N centres at δ^{15}N = 28.1 ppm and δ^{15}N = 335.6 ppm. The ^{15}N response at 28.1 ppm also showed $^{1}J_{NH}$ coupling to proton signals **I** and **K**, which are know to exchange out on shaking the sample with D2O. Hence the signal at δ^{15}N = 28.1 ppm was assigned to N-22 and from this, the proton signal at **C** was assigned to H-15. By elimination proton signal **D** was assigned to H-18. This assignment was confirmed by the presence of an NOE (Figure E.4) between H-18 and the methoxy methyl-23, placing these features of the molecule in close proximity to one another. H-18 showed a ^{15}N coupling to a signal at δ^{15}N = 90.58 ppm which was assigned to N-20. Assignment of H-18 and H-15 allowed for the assignment of quaternary carbons C14, C16, C17 and C19 via 2JHC and $^{3}J_{HC}$ couplings. The response between H-15 (signal C) and the ^{15}N signal at δ^{15}N = 335.6 ppm enabled this nitrogen response to be assigned to N-13, which also couples to H-21 (signal **A**). The latter signal also showed a coupling to a ^{15}N signal at δ^{15}N = 233.2 ppm which was therefore assigned to N-11. This assignment was confirmed by the fact that the ^{15}N signal for N-11 also showed correlations to proton signals **G** and **J**, which corresponded to naphthyl protons H-1 or H-9. By comparison with related structures that possess the **AF** sulphonation pattern present in **2**, the related signal at higher proton chemical shift was assigned to H-1 and the signal at lower shift to H-9. By the same token the assignment of signals associated with H-4 and H-6 were made on the basis of precedent: H-4 was assigned to the respective signal at lower chemical shift and H-6 to the signal at higher chemical shift. Signals for H-5, H-9 and H-1 all showed correlations to a ^{13}C signal at δ^{13}C= 129.70 ppm, which was therefore assigned to C-7 on the basis that $^{3}J_{HC}$ couplings from this carbon atom would be expected to occur to each of these protons. Signals for H-9 and H-1 both showed a ^{13}C correlation to a signal at δ^{13}C = 137.35 ppm, which was therefore assigned to C-10. H-9 showed a ^{13}C correlation to a signal at δ^{13}C = 146.30 ppm, which was thus assigned to C-8. This was confirmed by the $^{3}J_{HC}$ coupling between H-6 and C-8. C-3 was expected to resonate at a similar chemical shift to that of C-8 (being bound to a sulphonate group) and hence the ^{13}C signal at δ^{13}C = 144.48 ppm was assigned to C-3 since it showed $^{3}J_{HC}$ coupling to both H-5 and H-1. Finally C-2 was assigned to the signal at δ^{13}C = 128.96 ppm, which showed a strong $^{3}J_{HC}$ correlation to H-4.

Table E.1: ^{1}H, ^{13}C and ^{15}N chemical shift assignments for the NMR responses displayed by **2** (D304/71).

Position	**Chemical Shift (ppm)**		
	^{1}H	^{13}C	^{15}N
1	9.19	125.96	
2		128.96	
3		144.48	
4	8.10	125.43	
5	7.67	126.38	
6	9.00	129.00	
7		129.70	
8		146.30	
9	8.26	121.83	
10		137.35	
11			233.2
12		155.3	
13			335.6
14		142.9	
15	6.90	101.3	
16		156.55	
17		154.3	
18	7.49	105.07	
19		140.36	
20			90.58
21	2.65	23.37	
22			28.1
22a	9.62		
22b	9.02		
23	4.08	57.57	

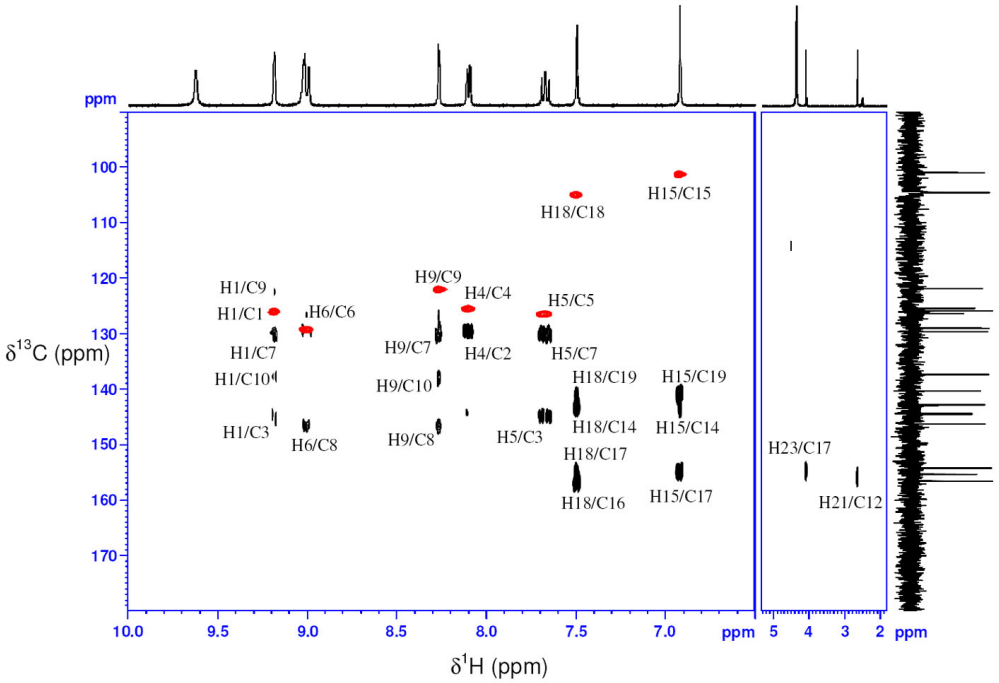

Figure E.2: Composite 2D [^{1}H, ^{13}C] HSQC (red) and HMBC (black) NMR data for 2 acquired at a magnetic field strength of 9.4 T.

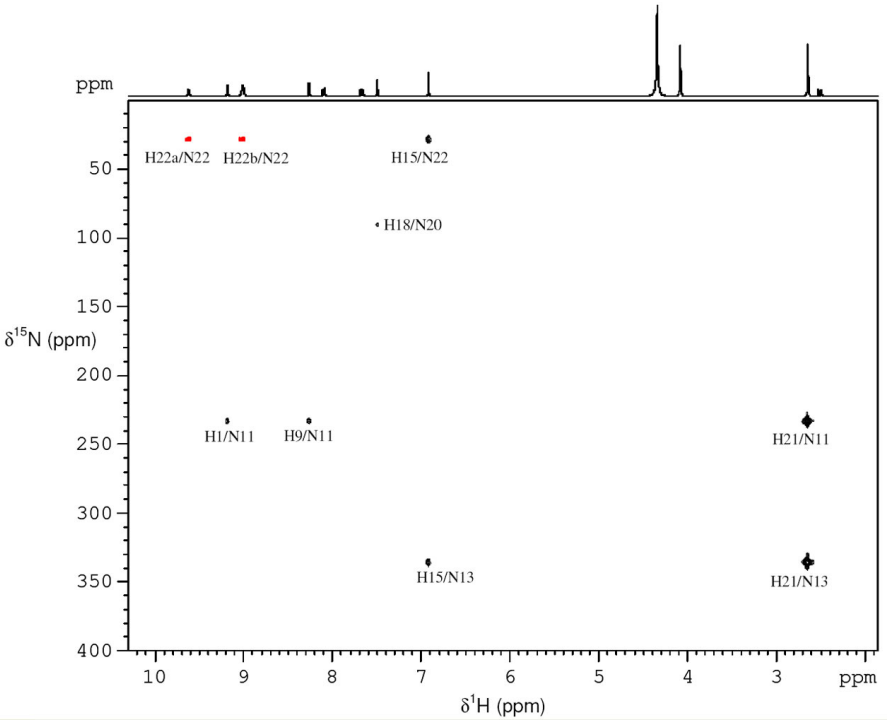

Figure E.3: Composite 2D [^{1}H, ^{15}N] HSQC (red) and HMBC (black) NMR data for 2 acquired at a magnetic field strength of 9.4 T.

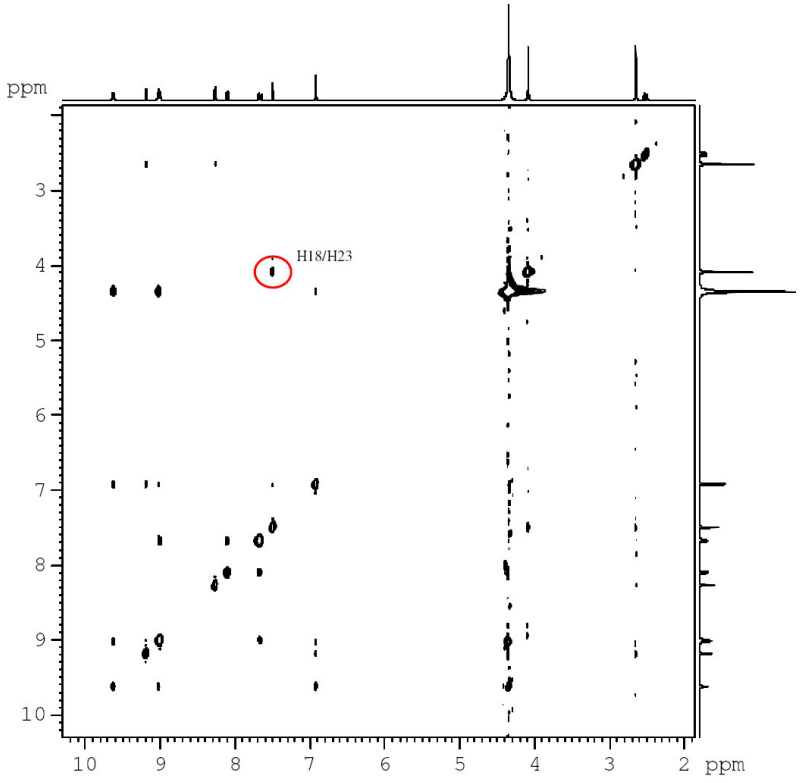

Figure E.4: 800 ms 2D [^{1}H, ^{1}H] NOESY NMR data for 2 acquired at a magnetic field strength of 9.4 T.

Conferences and Courses

Postgraduate Courses and Lectures

Introduction to HTML

UNIX I

UNIX II

Poster Production

Effective Writing

Time Management

Thesis Writing Workshop

Project Management in the Real World

Laser Spectroscopy

Nuclear Magnetic Resonance

Postgraduate NMR Workshop

Departmental Colloquium

Conferences and Meetings

Presentation at XXII International Conference on Photochemistry; Cairns, Australia.

Annual presentation to the Materials and Physical Chemistry Section; School of Chemistry.

Annual presentation and poster session at Firbush Point Field Centre to the combined physical chemistry departments of Edinburgh and Herriot Watt Universities.

Representative Publications

K. M. Tait, J. A. Parkinson, D. I. Gibson, P. R. Richardson W. J. Ebenezer, M. G. Hutchings and A. C. Jones. *Structural characterisation of the photoisomers of reactive sulfonated azo dyes by NMR spectroscopy and DFT calculations.*
Photochemical and Photobiological Science (In press, March 2007)